MODELLING AEROSOL-CLOUD-PRECIPITATION INTERACTIONS FOR WEATHER MODIFICATION IN EAST AFRICA

By

NGAINA, JOSHUA NDIWA

I80/95907/2014

Department of Meteorology
School of Physical Sciences
University of Nairobi.

A thesis submitted in fulfilment of the requirements for the degree of

Doctor of Philosophy (Ph.D.) in Meteorology

Department of Meteorology

University of Nairobi, Kenya.

June 2015.

DECLARATION

This thesis is my original work and has not been presented for a degree in any other University

Signature ---

Joshua Ndiwa Ngaina **Date**

Department of Meteorology,
University of Nairobi.

This thesis has been submitted for examination with our approval as University supervisors.

Signature ---

Prof. Nzioka J. Muthama **Date**

Department of Meteorology,
University of Nairobi.

Signature ---

Prof. Joseph M. Ininda **Date**

Department of Meteorology,
University of Nairobi.

Signature ---

Dr. Alfred O. Opere **Date**

Department of Meteorology,
University of Nairobi.

DEDICATION

To my dear father Mr. Patrick Kisembe Ngaina, HSC who has inculcated in me a desire for academic excellence; my mother Fridah Kisembe, for her love and prayers and to all my brothers, sisters and friends for their support.

ACKNOWLEDGEMENT

Thanks to the **Almighty Lord** for seeing me through the University education this far and successive completion of this Doctorate thesis. May His Holy Name be glorified forever.

The success of this PhD study would not have been realized without the support obtained from various individuals and institutions. Therefore, I wish to acknowledge unreservedly those individuals and institutions who contributed directly or indirectly towards the successful completion of this study.

I am particularly grateful of the University of Nairobi (UoN) and all the staff of the Department of Meteorology for creating an enabling environment during the entire period of this study. I am also grateful to my three supervisors and mentors Prof. Nzioka J. Muthama, Prof. Joseph M. Ininda and Dr. Alfred O. Opere, of the UoN for their invaluable encouragement and guidance throughout this study.

I further wish to make a special mention of the following individuals and institutions and their respective staff for their contribution towards the completion of the study. Dr. Elijah Mukhala and Mr. Nicholas Maingi of World Meteorological Organisation (WMO) Regional Office for Eastern and Southern Africa for their moral support in my quest for Ph.D. studies; Susy Ngaina (UoN), Mr. Bethwel Mutai (UoN) and Janet Jerotich (UoN) who meticulously read through my draft thesis and made useful suggestions. I also wish to thank sincerely all those not mentioned here but who provided support in one way or another. Please accept my sincere thanks. Your contribution is highly valued.

Last but not least, I wish to appreciate most sincerely the patience and moral support from my parents, Mr. and Mrs Patrick Ngaina; my sisters Judith, Susy, Vellah and Caro; my brothers Ken, James, David and Leonard; My Nephew Paul and Ian and all my friends. Your prayers and encouragement gave me extra energy and courage to move on.

ABSTRACT

Precipitation enhancement is one of the possible measures to improve on the available fresh water in East Africa (EA). The existing gap in knowledge not only on suitable conditions but also Aerosol-Cloud-Precipitation (ACP) interactions limits the success of precipitation enhancement through weather modification. This study aimed at modelling the effects of aerosols on clouds and precipitation for weather modification in EA.

Aerosol and cloud data were retrieved from Moderate Resolution Imaging Spectroradiometer (MODIS). It comprised of Aerosol Optical Depth (AOD), Fine Mode Fraction (FMF), Cloud Top Pressure (CTP), Cloud Top Temperature (CTT) and Cloud Optical Depth (COD). Precipitation data comprised of 3B42 product sourced from Tropical Rainfall Measuring Mission (TRMM), and comprised of 3B42 product. The Weather Research and Forecasting model (WRF) initial and boundary conditions utilized the National Centers for Environmental Prediction Final (NCEP FNL) data. The daily datasets from MODIS and TRMM spanned the period 2001-2012 (12 years). The spatial and temporal analysis utilized the time series and Principal Component Analysis (PCA). The relationship between aerosol, clouds and precipitation were based Hybrid Single-Particle Lagrangian Integrated Trajectory (HYSPLIT) and Multiple Linear Regression (MLR) analysis. Suitable weather modification conditions were identified using Greater Horn of Africa (GHA) consensus forecast, CAPE and COD and CTP. Evaluation of WRF to simulations of Deep Convective Clouds (DCCs) was based on updrafts/downdrafts and precipitation. Aerosols effects on precipitation modification were simulated based on microphysical properties, precipitation, and convective strength under low, intermediate, and high Cloud Condensation Nuclei (CCN) and Cloud Droplet Number Concentration (CDNC) scenarios.

In EA, time series (trend and seasonality), Hovmoller and PCA analysis of aerosol, clouds, and precipitation showed a high spatial and temporal variability. The PCA analysis yielded 13, 20, 11, 9 and 16 Principal Components (PCs) during MAM for AOD, FMF, CTT, OLR and TRMM 3B42 respectively. Similarly, PCA analysis yielded 14, 18, 10, 10 and 17 PCs during OND for AOD, FMF, CTT, OLR and TRMM 3B42 respectively. The explained variance during both MAM and OND were all greater than 57%.

The MLR analysis showed that all aerosol and cloud variables with strong factor loading in EA had a positive relationship with rainfall. The backward trajectory indicated differences in origins of transported particles in the atmosphere with strong vertical mixing inland with mixed aerosols due to mountain blocking systems. GHA consensus forecast verification indicated less reliability due to lower Critical Success Index (CSI) and Heidke Skill score (HSS). However, verified consensus forecast for MAM 2012 indicated a likelihood of Near Normal (NN) to Below Normal (BN) rainfall and thus suitable for precipitation enhancement. Areas located centrally to EA exhibited optimal seedable temperatures of -5°C to -25°C. DCCs dominated pentad 29 (CTP > 440MB, COD>23 and meridional/zonal transition in CAPE >1000J/kg) over Mt. Kenya catchment. Therefore, Mt. Kenya catchment was selected as representative of seedable conditions in EA.

Evaluation of the efficiency of WRF microphysics shows that Morrison scheme simulated the initiation of downdraft cumulus core almost at the same time as observed. The initiation of several updrafts and its associated downdrafts with strong downdrafts below the updraft cores were comparable to the observed. Accumulated precipitation based on TRMM 3B42 and WRF model output for Mt. Kenya Region were also found to be comparable to the 24h simulation. Observed and model simulated the initiation of downdraft Cores was comparable. Microphysical properties (vertical profiles of mass concentrations of five hydrometeors of cloud water, rainwater, ice-crystal snow and graupel) showed the complex relationship under three aerosol scenarios. Precipitation increased with increase in CDNC and CCN from maritime/clean to continental/polluted conditions and reduced/suppressed at highly polluted conditions (CDNC>1600cm^{-3}, CCN>2000cm^{-3}). Accumulated total precipitation exhibited a complex variation (non-linear relationship) under CDNC and CCN scenarios. The mean of core updraft and maximal vertical velocity increased under intermediate and low CCN scenarios and decreased under high CCN scenarios. The response of precipitation to increase in aerosol concentration (CDNC and CCN) was non-monotonic.

The study indicates the possibility of enhancing precipitation in locations with similar conditions to Mt. Kenya catchment. Increasing the available fresh water in EA will spur sustainable development. However, critical issues remain yet to be solved and require stronger scientific evidence/support. These include improvement of the predictability of seasonal rainfall and development of cloud-resolving models for the region. Further, It will be necessary to develop relevant policies to address the benefits, risks, and ethical issues related to weather modification.

TABLE OF CONTENTS

LIST OF FIGURES

LIST OF TABLES

ACRONYMS AND ABBREVIATIONS

ACP	Aerosol-Cloud-Precipitation
AIC	Akaike information criterion
AN	Above-Normal
AOD	Aerosol Optical Depth
ARW	Advanced Research Weather Research and Forecasting Model
AVHRR	Advanced Very High-Resolution Radiometer
BMJ	Betts-Miller-Janjic
BN	Below Normal
CALIPSO	Cloud-Aerosol Lidar and Infrared Pathfinder Satellite Observation
CAPE	convective available potential energy
CCN	Cloud Condensation Nuclei
CDNC	Cloud Droplet Number Concentration
CERES	Clouds and Earth’s Radiant Energy System
COD	Cloud Optical Depth
CoV	Coefficient of Variation
CP	Convective parameterization
CR-WRF	Cloud Resolving- Weather Research and Forecasting Model
CSI	Critical Success Index
CTP	Cloud Top Pressure
CWC	Cloud Water Content

DCC	Deep Convective Cloud
DJF	December –January –February
DMA	Differential Mobility Analyzer
D-W	Durbin-Watson
EA	East Africa
EALLJ	East Africa Low-Level Jet
EFA	Empirical Factor Analysis
ENSO	El Nino Southern Oscillation
EOF	Empirical Orthogonal Function
FAR	False Alarm Ratio
FMF	Fine Mode Fraction
FNL	NCEP Final
GCCN	Giant CCN
GFS	Global Forecast System
GHA	Greater Horn of Africa
GHACOF	Greater Horn of Africa Climate Outlook Forum
GR	GRell scheme
GRIB	GRIdded Binary
HSS	Heidke Skill Score
HYSPLIT	Hybrid Single-Particle Lagrangian Integrated Trajectory
IN	Ice Nuclei

INDOEX	Indian Ocean region during the Indian Ocean Experiment
IOD	Indian Ocean Dipole
IPCC	Intergovernmental Panel on Climate Change
ISCCP	International Satellite Cloud Climatology Project
ITCZ	Inter-Tropical Convergence Zone
JJA	June–July–August
KF	Kain-Fritsch
LES	Large Eddy Simulations
LSMs	Land-Surface Models
LW	Long-Wave
LWP	Liquid Water Path
MAM	March-April-May
MATLAB	MATrix LABoratory
MCS	Mesoscale Convective Systems
MJO	Madden-Julian Oscillation
MLR	Multiple Linear Regression
MM5	Fifth-Generation Penn State/NCAR Mesoscale Model
MODIS	Moderate Resolution Imaging Spectroradiometer
NCAR	National Center for Atmospheric Research
NCEP	National Centers for Environmental Prediction
NE	North-Eastern

NMM	Non-Hydrostatic Mesoscale Model
NN	Near-Normal
NOAA	National Oceanic and Atmospheric Administration
NW	North West
NW	North-Western
NWP	Numerical Weather Prediction
OLR	Outgoing Longwave Radiation
PA	Parallel Analysis
PBL	Planetary Boundary Layer
PCA	Principal Component Analysis
PCs	Principal Components
POD	Probability Of Detection
PR	Precipitation Radar
QBO	Quasi-Biennial Oscillation
QQ	Quantile-Quantile
QR	Quantile Regression
REOF	Rotated Empirical Orthogonal Function
RPC	Rotated Principal Component
RPCA	Rotated Principle Component Analysis
RRTM	Rapid Radiative Transfer Model
SE	South East

SOND	September-October-November-December
SPOB	Specific Objective
SSE	Sum of Squared Errors
SST	Sea Surface Temperatures
SW	South-Western
TKE	Turbulent Kinetic Energy
TMI	TRMM Microwave Imager
TRMM	Tropical Rainfall Measuring Mission
VIFs	Variable Inflation Factors
VIRS	Visible Infrared Scanner
WRF	Weather Research and Forecasting Model
2D	2-Dimensional
3D	3-Dimensional

CHAPTER ONE

1 INTRODUCTION

1.1 Background of the Study

Precipitation that includes rain, snow, and hail is the primary mechanism for transporting water from the atmosphere back to the Earth's surface. Precipitation significantly influences the quality of human life through the availability of fresh water (Levin and Cotton, 2009). It is also a fundamental physical process that links aspects of climate, weather, and global hydrological cycle. However, it displays the largest variability in both spatiotemporal distribution and magnitudes (Gitau *et al.,* 2013). Responses to the rainfall shift are already being observed in many terrestrial water sources (Bates *et al.,* 2008). These could be considered as possible indicators of future water stress linked to climate variability (Majone *et al.*, 2012).

Clouds play a crucial role in the dynamic and thermodynamics of the atmosphere. Thick clouds or deep convective clouds dominate the tropical atmosphere and account for 60% of the observed precipitation (Schumacher and Houze, 2003). The response of clouds due to changes in the ambient aerosol differs depending on the cloud type or aerosol regime (Seifert *et al.*, 2011). The interaction between aerosol particles and clouds involve processes on multiple scales (Solomon *et al.,* 2007). They range from nanometres (nucleation of liquid and solid particles) to several micrometres (growth of droplets) and even kilometres (dynamics of cloud systems and the hydrological cycle). Cloud droplets grow into raindrops by coalescence, which will take longer and lead to a delay in precipitation formation when starting from small droplets (Rosenfeld, 2008; Noppel and Beheng, 2009).

Studies such as Rosenfeld *et al.* (2008), Huang *et al.* (2009a) and Intergovernmental Panel on Climate Change (IPCC 2013) indicate the dominance of anthropogenic aerosols over the land area. These aerosols affect Cloud composition, hydrological cycle, and atmospheric circulation systems as well as cloud dynamics feedbacks on multiple scales (Solomon *et al.,* 2007). Worth noting, aerosols are of particular importance in some of the heaviest precipitation-producing events such as deep convective storms (Rosenfeld, 2000).

Weather modification or Cloud seeding involves the emission of substances into the air to serve as Cloud Condensation Nuclei (CCN). The CCN may lead to changes in the amount and type of precipitation or the dynamics of clouds. In EA, weather modification studies dominated the early 1960s and beginning of the 1980s (Alusa, 1976; Dye and Breed, 1979; Summers *et al.,* 1979). However, the success of weather modification was limited by inadequate understanding of key processes in Aerosol-Cloud-Precipitation (ACP) interactions.

The inadequacy of environmental water supplies makes the potential for enhancing the sources, storage, and recycling of freshwater inevitable. Improved availability of fresh water sources will ensure that at least 30% of the average annual flow of a stream, ecological health and related ecosystems are to be maintained (Jury and Vaux, 2007).

1.2 Statement of the Problem

Water resources are subjected to considerable hydrological and climatic variability over space and time (Kundzewicz *et al.,* 2007). Intergovernmental Panel on Climate Change (IPCC) fifth assessment report (IPCC, 2014) indicate that projected climate change will exacerbate the already water-stressed catchments. In many global water sources, observed responses to rainfall shift linked to climate variability are considered as possible indicators of future water stress (IPCC, 2007). In EA, inadequate water supplies will have both direct and indirect adverse impacts on sustainable development in areas such as health, agriculture, energy, communication and transport. Although precipitation enhancement is one of the possible measures to improve on the available fresh water, there exist a gap in knowledge on suitable and potential areas for cloud seeding. Further, the inadequate understanding of ACP interactions limits the success of weather modification aimed at improving fresh water sources, storage and recycling.

1.3 Objectives of the Study

This study aimed at modelling the effects of aerosols on clouds and precipitation for weather modification in EA.

Specific objectives used to achieve the broad objective are:

1. Determine the spatial-temporal variability of aerosols, clouds and precipitation in EA.

2. Determine the correlation between aerosols, clouds and precipitation in EA.

3. Evaluate the efficiency of Weather Research and Forecasting model in simulating deep convective cloud system in EA.

4. Simulate effects of cloud seeding on precipitation modification Deep Convective Cloud (DCC) system in EA

1.4 Hypotheses of Study

Changes in the size and concentration of aerosols acting as CCN will lead to changes in the rate of growth of cloud droplet and thus modify precipitation.

1.4.1 Assumptions

The underlying assumptions in this study include

1. All cloud droplets must form on pre-existing aerosol particles that act as CCN.

2. Increased aerosols change the composition of clouds (i.e. the size distribution of cloud droplets) and thus determines to a large extent the precipitation forming processes.

1.5 Justification for the Study

In EA, most countries are dependent on rainfall as a source of fresh water. The high precipitation variability in both time and space is expected to exacerbate the existing water stress in the region. Even with the use of conventional mitigation measures to combat water shortage and support the efficiency of water management schemes, the water demand will still surpass the available water resources. The inadequacy of environmental water supplies will make the potential for enhancing the sources, storage, and recycling of freshwater inevitable. Therefore, precipitation enhancement through weather modification is one of the possible means to improve water supply and alleviate the existing water stress (Rosenfeld *et al.*, 2005). Precipitation enhancement will ensure that at least 30% of the average annual flow of a stream, ecological health and related ecosystems are to be maintained (Jury and Vaux, 2007). However, the success of weather modification depends on adequate understanding of ACP interactions. For example, aerosols in the atmosphere can act as CCN to modify cloud microphysical processes. The potential modification may result in change the intensity, location, and type of precipitation (Tao *et al.,* 2012; Fan *et al.,* 2013). Therefore, modelling the effects of aerosols on clouds and precipitation provides insights into key ACP processes.

1.6 Conceptual Framework

Rainfall, the ultimate source of freshwater, is a function of a combination of several factors. These factors include air temperature, wind patterns, moisture content in the atmosphere and presence of cloud condensation nuclei such as dust particles. Condensation of atmospheric moisture to form cloud droplets originates from vapour evaporated mainly from oceans, seas, rivers, soils, plants and other continental water bodies. Cloud droplets may grow by collision - coalescence processes. Cloud droplets of varied sizes may fall at different speeds and collide with each other coalescing into a larger droplet. This process continues until cloud droplet is large enough to overcome the updraft speed within the cloud and fall as rain at about 20 -30 µm. Additionally, there exist factors that can deplete the liquid water from eventually becoming rain on the ground. These include evaporation of the droplets or the freezing of small droplets into small ice crystals that are unable to fall as precipitation through a process known as cloud glaciation. Thus, the amount of water vapour that enters a cloud never all falls to the ground as rain. However, once the droplets reach approximately more than 1mm in diameter, their terminal velocity is large enough for them to fall from the cloud as rain. To enhance collision and coalescence processes and thus rain formation, additional particles of larger sizes increases conversion of more cloud water to rainfall. Efficient collision and coalescence rain formation process result in more rainfall on the ground.

Figure 1-1 shows the approach adopted to model effects of aerosols on clouds and precipitation. Aerosols, clouds and precipitation climatology provides insights into ACP interactions and thus suitability and potential of both inadvertent and advertent weather modification activity. Validation of cloud-resolving model aims to evaluate the efficiency of the model in simulating identified convective systems. Weather Research and Forecasting Model (WRF) was utilized to assess the potential of weather modification through cloud seeding. Detailed review on weather modification and related studies are provided in Chapter two.

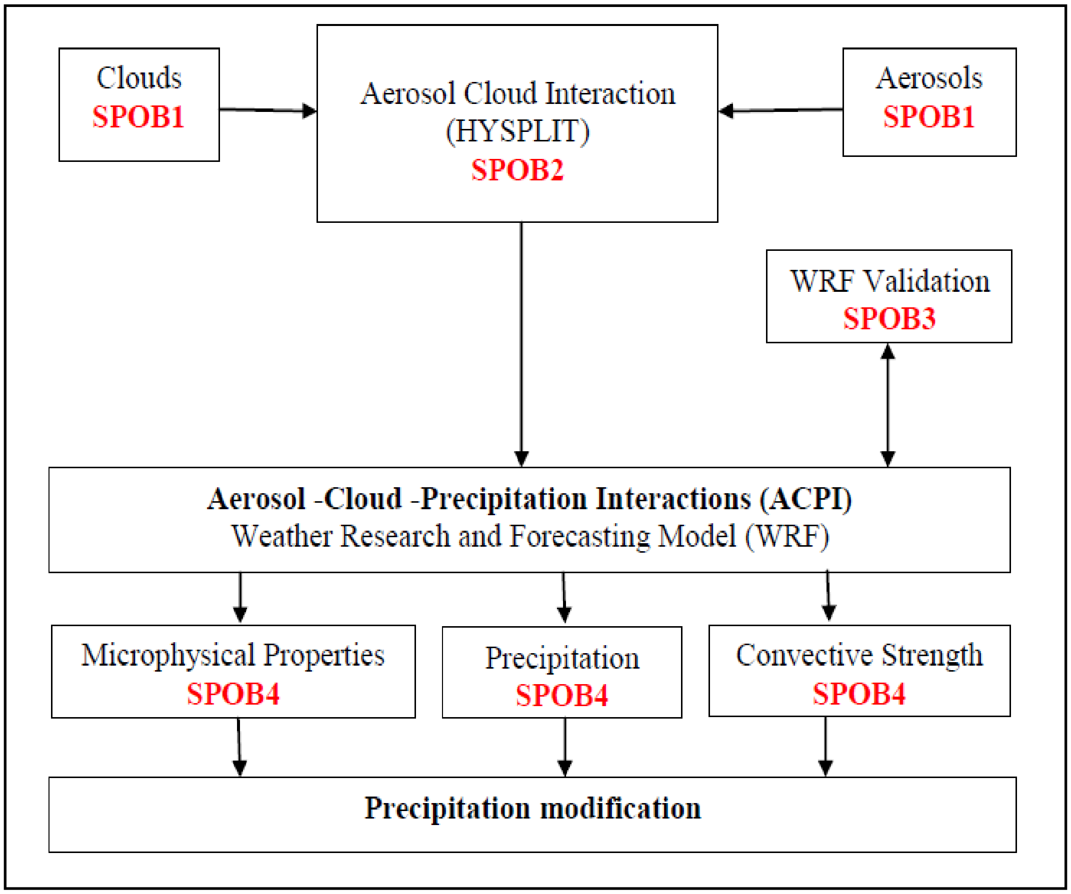

Figure 1-1: Conceptual framework of the study. Specific objective (SPOB)1, SPOB2, SPOB3, and SPOB4 stand for specific objectives one (1), two (2), three (3), and four (4) respectively.

1.7 The area of study

The study domain covered countries within EA namely Burundi, Kenya, Rwanda, Tanzania and Uganda. The location of the study domain is within the latitudes 6^{o}N and 12^{o}S and longitudes 28^{o}E and 45^{o}E. Figure 1.2 shows the topography of EA region. EA has a great diversity of topographic features. These include the Eastern and Western highlands that run North-South (NS), parallel to the Great Rift Valley. On the highlands are snow-capped mountains; Mt Kilimanjaro and Mt Kenya whose attitudes are about 5892 Metres (m) and 5202m above sea level respectively. Other mountain features include Mt Elgon (4321m) on the Kenya/Uganda boundary, Ruwenzori Mountain in Western Uganda, Mt Meru in North-Eastern (NE) Tanzania and Kipengere ranges in South-Western (SW) Tanzania. The Eastern and Western highlands make up the Eastern and Western escarpments of the Great Rift Valley respectively. To the North of these highlands is the Ethiopian Highlands with a low-level valley region between these highlands called the Turkana channel.

Empirical and theoretical studies have shown that topography plays a leading role in the formation of local perturbations, in the creation of vertical components of wind speeds. It promotes the formation and development of clouds, precipitation and thunderstorms (Indeje *et al.*, 2001; Oettli and Camberlin, 2005). The study region has large inland water bodies in the form of deep vault lakes along the Great Rift Valley. These include Lakes Turkana, Baringo, Kyoga, Naivasha, Eyasi, Manyara and Tanganyika among many others. Lake Victoria is at the centre and shared by the three countries. Lake Victoria is not only the largest freshwater lake in Africa but also second in the world. It has an area of about 68,000km^2. It generates strong mesoscale circulation. The temporal and spatial variability of rainfall in EA at different time scales are due to complex topographical features and existence of large water bodies (Oettli and Camberlin, 2005).

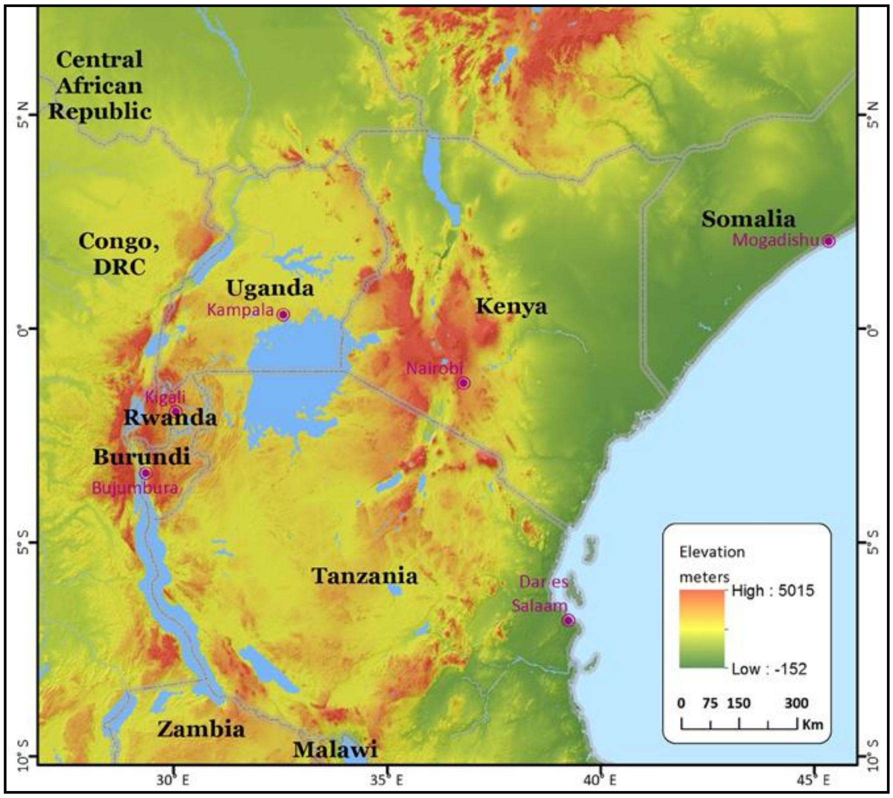

Figure 1-2: A topography map of East Africa region (Himeidan and Kweka, 2012)

CHAPTER TWO

2 LITERATURE REVIEW

This section sought to review previous studies on aerosols, clouds and precipitation.

2.1 Weather Modification

Cloud seeding is the emission of substances into the atmosphere to act as Ice Nuclei (IN), or CCN (Noppel and Beheng, 2009). These substances have potential to change the dynamics of a cloud, type and amount of precipitation. In most cases, cloud seeding involves intentional emission of substances into the atmosphere to enhance precipitation or to suppress hail. However, emissions from industry, traffic, biomass-burning and other anthropogenic activities also change IN and CCN condition leading to similar modification of clouds and precipitation. Two broad categories of cloud seeding include hygroscopic seeding that involves the effects of CCN conditions only and glaciogenic seeding that involves the effects of IN only. This study focuses on hygroscopic seeding to enhancing precipitation in convective clouds.

Noppel and Beheng (2009) indicated that high number concentrations of CCN (aerosol particles) results in large numbers of cloud droplets. As they compete for the available water vapour, the mean size of the nucleated drops will be smaller than for lower CCN concentrations. The focus of cloud seeding is to enhance precipitation efficiency in treated (seeded) clouds compared to natural (unseeded) clouds (DeFelice *et al.,* 2013). According to reviews by Bruintjes (1999) and Silverman (2003), hygroscopic seeding is aimed at conversion of cloud water to precipitation i.e. accelerating autoconversion process. Therefore, a seeded cloud or cloud system is made up of potentially enhanced dynamic effects or microphysical effects, which increase the amount of precipitation.

Numerous observations in the atmosphere and the laboratory have shown that cloud water droplets can remain unfrozen at temperatures well below freezing (Orville *et al.,* 2004). According to Noppel and Beheng (2009), small aerosol particles in high number concentrations will produce small cloud droplets with a narrow size distribution. Small aerosol particles will lead to a delay in precipitation formation and often to a decrease in rain amount. On the contrary, large hygroscopic particles may result in large cloud droplets with a wider spectrum. These may accelerate and enhance the formation of rain. Pruppacher and Klett (1997) noted that an increase in aerosol load led to an increase in cloud droplet number concentration. In the fixed liquid water content, it resulted in a decrease of the average cloud droplet size. It is on this basis that the current study aims to model the effects of varying aerosol concentration on observed precipitation.

Pristine tropical cloud with low CCN concentrations rain out too quickly to mature into long-lived clouds (Rosenfeld, 2008). However, heavily polluted clouds evaporate much of their water before precipitation can occur. In case of orographic precipitation, its distribution will strongly depend on the composition and size of the background aerosols (Muehlbauer and Lohmann, 2009). Lack of sufficient CCN or efficient IN results to slow precipitation development. Therefore, a higher fraction of the precipitation moved by the winds to the lee side of the mountain. Therefore, seeding could increase the efficiency of precipitation formation on the upwind side of the mountain.

Slowing of the autoconversion rate by large concentrations of CCN can leave much of the cloud droplets airborne (Rosenfeld *et al.,* 2008). These occur when strong updrafts thrust them above the homogeneous ice nucleation level of ~ –38°C, where they freeze into small ice particles that have no effective mechanism to coagulate and fall as precipitation. Rosenfeld and Woodley (2000) observed this phenomenon by aircraft. It was also simulated for convective storms in West Texas and U.S. high plains (Khain *et al.,* 2000; Cui *et al.,* 2006). Repetition of the same simulation (Khain *et al.,* 2000) with reduced CCN concentrations resulted in a substantial increase in calculated rainfall amount. According to Cotton and Pielke (1995), the success of a cloud seeding window applied to clouds that were relatively cold-based, continental and had Cloud Top Temperature (CTT) in the range -10^{o}C to -25^{o}C. To identify suitable conditions, the seeding window in the range -10^{o}C to -25^{o}C was considered as optimal in this study.

Sub-micrometer CCN aerosols decrease precipitation from shallow clouds (Rosenfeld *et al.,* 2008; Andreae *et al.,* 2004) and invigorated DCCs with warm (> ~15°C) cloud base (Koren *et al.,* 2005; Lin *et al.,* 2006; Bell *et al.,* 2008). However, the impact on the overall rainfall amount was not easily detectable (Schultz *et al.,* 2007; Bell and Rosenfeld, 2008). Adding giant CCN to polluted clouds accelerates the autoconversion by nucleating larger droplets(Teller and Levin, 2006). The large droplets rapidly grow into precipitation particles by collecting the other smaller cloud droplets. However, the autoconversion rate is not restored to that of pristine clouds. Sharon *et al.* (2006) confirmed strong connections between precipitation, cloud morphology, and aerosol loading, with precipitating portions of marine clouds nearly devoid of aerosols. Further, it suggested a strong positive feedback where precipitation removes aerosol, leading to a more efficient formation of precipitation. The existing feedback is thought to shift closed-cellular to open cellular convection, in sub-regions that are non-raining and, raining respectively (Stevens and Savic–Jovcic 2008; Wang and Feingold 2009a). In this study, the strong connection between precipitation, cloud morphology and aerosol loading forms the basis of investigation to understanding the complex ACP interactions.

In EA, weather modifications studies aimed at suppressing hail formation dominated the period between early 1960s to beginning of the 1980s. Over Kericho tea estates, cumulus clouds were classified as continental (Dye and Breed, 1979). These suggest that the ice phase may be the predominant precipitation formation mechanism in these clouds. Schnell and Vali (1976) observed that size distribution of aerosols produced from the tea litter over Kericho areas were similar to natural aerosols associated with thunderstorms. Moreover, they maintained appreciable IN activity at aerosol mass loadings observed in natural atmospheres. Assessment of Colorado cumulus clouds suggested that surface aerosol and nucleus measurements are representative of the inflow air at cloud base (Rogers and Vali, 1978). In the hail suppression project (Henderson, 1975), annual rainfall amounts were statistically compared using target-control relationships developed from data obtained during the historical period prior to the start of this hail suppression program. The results of this analysis indicated a surprising 12% average annual increase in rainfall within the protected area, statistically significant at the 0.10 level. Therefore, the reported success in hail suppression indicates existing potential of enhancing precipitation through cloud seeding in EA.

In West African Monsoon region, large-scale precipitation reduction has been associated with a high aerosol load (Huang *et al.,* 2009a, 2009b). Along the Gulf of Guinea coast, observed aerosol-related rainfall reductions in different types of precipitation (convective, stratiform, and shallow) peaked in the cold boreal season. Therefore, it did not follow the seasonal migration of the monsoon rain-band inland and peaking in summer when monsoon rainfall was strongest.

Further, both dust and smoke lead to precipitation reductions with dust-related reduction dominating the Gulf of Guinea while the smoke-related reduction dominated both the western Sahel and the Gulf. Moreover, aerosol-related precipitation changes were sensitive to rain rate with largest changes in precipitation observed only at weak to moderate rain rates and not at very high rain rates. This study adopts use of aerosol scenarios ranging from low to extreme concentration to understand the complex ACP interactions.

Remote sensing of seeding signature from space provided near-real-time feedback to the targeting efficacy of the cloud seeding (Rosenfeld *et al.,* 2005). Glaciated seeded tracks in super-cooled layer clouds were observed to spread slowly for more than an hour after seeding and reached a width of less than 15km (Rosenfeld, 2007). Over the Qilian Mountains of the Tibetan Plateau, cloud optical thickness, efficient radius and liquid water content were retrieved from MODIS Terra and Aqua satellites channels 0.65µm and 2.1µm (Zhang *et al.,* 2006). The information provided valuable information on the water resource usage and suitability of weather modification program in West China.

Satellite-derived vertical profiles of the cloud droplet effective radius were noted to increase as the depth of the cloud increased (Rosenfeld and Lensky, 1998; Freud *et al.,* 2005). However, in continental clouds with higher cloud droplet concentrations, the growth of the particles was slower than in the maritime ones who have lower droplet concentrations. Similarly, this study utilized available remotely sensed atmospheric parameters based on satellites such as Moderate Resolution Imaging Spectroradiometer (MODIS) and Tropical Rainfall Measuring Mission (TRMM) as proxy for monitoring presence of seedable conditions in EA.

2.2 Aerosols Transport and Dispersion

Aerosol is a collective name for suspended particulate matter. They act as nuclei upon which cloud droplets form. Aerosols are tiny liquid, solid, or mixed phase particulates suspended in the air, ranging in size from 0.001µm to 100µm (Slinn 1975). Aerosol variation in terms of its size distribution and composition in the atmosphere depends on a complex combination of processes. These processes involve primary and secondary sources, transport, dispersion, cloud processing and removal by precipitation (Levin and Cotton, 2009). Smaller droplets are also less suitable to collide and coalesce and thus inhibiting precipitation with a potential increase in cloud lifetime (Koren and Feingold, 2011; Tao *et al.*, 2012).

According to Hudson (2007), the size of CCN reflects the hygroscopicity (solubility) of atmospheric particles. Therefore, measurement of critical supersaturation (a function of particle size and chemistry) of a narrow size range of an aerosol can be utilized to determine the size of CCN. It is obtained by passing the aerosol through a differential mobility analyzer (DMA) and then to a CCN spectrometer (Hudson and Da, 1996; Hudson, 2007). By adjusting the DMA voltage, it is possible to select various different narrow sizes. Therefore, isolating the effects of chemistry (particle composition) CCN activation. Depending on their water solubility, particles with similar sizes can have different critical supersaturation.

Dusek *et al.* (2006) have shown that it is possible to deduce particles critical supersaturation from small variations in particle solubility. Rosenfeld (2006) notes that this relationship could be quite useful from the perspective of remote sensing from space. The data on a global scale from instruments such as MODIS, which can detect coarse and fine aerosol and optical depth, could be used to estimate effective radius. Unfortunately, the calculated cloud drop nuclei concentrations also have high error bars associated with them, and due to the requirements for the method of estimation, could only be retrieved overwater. Identification of aerosol composition is more costly and involves more instrumentation than the identification of CCN. Capabilities of new satellite missions such as the Cloud-Aerosol Lidar and Infrared Pathfinder Satellite Observation (CALIPSO) platform may help to decrease error regarding these measurements.

The susceptibility of Cloud Droplet Number Concentration (CDNC) to changes in the aerosol is very variable, depending on the number of aerosol particles and the updraft velocity. Reutter *et al.* (2009) distinguished three different regimes of the susceptibility of CDNC to varying aerosol concentrations, based on simulations with a parcel model. In the first regime, the fraction of activated particles was high with the available particle number limiting CDNC independent of the updraft velocity. In the second regime, CDNC dominated the updraft velocity since the fraction of activated particles, and the super-saturation are low. In the third intermediate regime, CDNC was sensitive to both, aerosol, and updraft velocity. Effects of aerosols on the temperature profile and its role as CCN influences the hydrologic cycle, through changes in precipitation, cloud cover and cloud properties (Kaufman *et al.*, 2002). Existing uncertainties in quantifying aerosol feedbacks points to aerosol's multitude of shapes and forms that range from urban pollution to desert dust. Further, aerosol concentrations vary strongly over space and time.

To accurately study aerosol distribution and composition, continuous observations from networks of ground-based instruments, satellites, and dedicated field experiments will be inevitable. Kaufman *et al.* (2002) indicated that changes in their composition and increases in aerosol concentration, driven by population growth and industrialization may adversely affect the Earth's climate and water supply. Dust aerosols can modify cloud properties such as the size of cloud droplets and number concentration and (Liu *et al.,* 2003; Huang *et al.,* 2006). Changes in cloud properties have the potential to modify both cloud lifetime and cloud albedo. Further, aerosol absorption at solar wavelengths may result in increased diabatic heating in the atmosphere and enhance cloud formation and evaporation (Koren *et al.,* 2004).

A complex interplay between different aerosol effects and feedbacks has been observed for clouds in smoky conditions over the Amazon (Koren *et al.*, 2008). It showed that radiative (semi-direct) aerosol effects on the clouds dominated the high aerosol conditions while microphysical (indirect) aerosol effects dominated the low aerosol conditions. Aerosol particles could also modify atmospheric radiative fluxes and interact with clouds (Bell *et al.,* 2008). African aerosol loading is strongly controlled by the monsoon (De Graaf *et al.,* 2010). Its enormous amounts have significant effects in the global to regional climate change through rainfall feedbacks and aerosol-cloud interactions. Existing uncertainties in quantifying the anthropogenic contribution to climate change involves to effects of aerosol on clouds and precipitation (Koren and Wang, 2008).

Gupta *et al.* (2008) showed that satellite data had tremendous potential for mapping the distribution and properties of aerosols. Alam *et al.* (2011) showed that aerosol concentrations in Africa and Asia had continually increased in virtually all urbanized and industrialized regions. In EA, coated organic and hygroscopic aerosols may readily swell when the humidity reaches 80% (Christy *et al.* 2009). Moreover, aerosol forcing is still yet to be known. However, model studies in Los Angeles (high concentration of thermally active aerosols than EA, aerosols accounted for an enhanced nocturnal down-welling radiation of 13 Wm^{-2} (Jacobson 1997). In India (similar to EA), estimated daily mean of down-welling radiation enhancement from aerosols ranged from 6.5 to 8.2 Wm^{-2} (Panicker *et al.,* 2008).

During the June–July–August (JJA) and December –January –February (DJF) season, variability in Aerosol Optical Depth (AOD) revealed maximum AOD values (Ngaina and Mutai, 2014). Further, aerosols reaching EA were transported from either Arabian and Indian sub-continent or western parts of the Indian Ocean. Aerosol data retrieved from MODIS overestimated the aerosol loading in EA with Arabian, India and western Indian Ocean identified as an important source of aerosols (Ngaina *et al.,* 2014). In Kenya, absorbing or non-absorbing aerosols dominate in the formation of rainfall with aerosols variability coinciding with patterns of the prevailing wind (Muthama, 2004). Further, Muthama (2004) showed that relationship in aerosol indices on average lead rainfall by about two months.

Gatebe *et al.* (1999) developed air transport climatology for Kenya at synoptic scale. During January and March, the sources of transported air to Kenya were North-Western (NW) Indian Ocean and Saharan region whereas, during May and November, the air was transported from southwest Indian Ocean. In the upper troposphere, Atlantic westerly transport occurred during January, March, and November. Equatorial easterly dominated airflow away from Kenya to the Atlantic Ocean during January, March, and November while to the Arabian Peninsula, recurved easterly dominated. Saudi Arabia and Atlantic Ocean formed the main channel for airflow off the African continent. In May, air is mainly transported from South-Western (SW) Indian Ocean and exited to the Atlantic Ocean.

In most active regions of aerosol emission, mixtures of combustion produced particles with desert dust aerosol occur seasonally (Eck *et al.,* 2010). For example, the Sudanian zones of northern Africa and the Sahelian experience very high loadings of desert dust from sources in the Sahel and Sahara for most of the year. During the months of November-March, biomass burning aerosols from several fires occurring in the Sudanian and Sahel zones mix in various concentrations with dust particles. Mixed coarse and fine aerosols not only affect large continental regions but are also seasonally advected over significant areas of ocean. Aerosols are either well mixed within a single layer(s) or layers of different particle types occurring at different altitudes (Johnson *et al.,* 2008).

Over the Indian Ocean, very limited number of wet deposition studies based on air mass trajectories exist (Kulshrestha and Kumar, 2014). A study by Granat *et al.* (2002) reported on rainwater chemistry in Indian Ocean region during the Indian Ocean Experiment (INDOEX) campaign held in January–March 1999. Krishnamurti *et al.* (1998) reported on the possibility of long-range transport of dust from Arabian Desert to the central Indian Ocean region with a transit time of 2-3 days. Li and Ramanathan (2002) studied the long-range transport of dust from the Greater Horn of Africa (GHA) over the Arabian Sea and mid-tropospheric transport of dust from the Arabian Peninsula. The study indicated that transport of these dust affected the summer monsoons and resulted in higher aerosol loadings in the south of the equator. Further, the study by Li and Ramanathan (2002) attributed the increase in AODs over equatorial Indian Ocean to long range transports of emissions from Indonesia forest fires in 1997.

Numerous studies indicated higher pollution in the north of the equator in Indian Ocean (Granat *et al.*, 2002; Kulshrestha and Kumar, 2014) and attributed to the location of most of the emission sources. In the Southern Indian Ocean, a relatively pristine atmosphere dominates due to negligible human perturbations. Scavenging of various aerosols and gaseous pollutants can modify the clouds in south of Intertropical Convergence Zone (ITCZ) which can further affect monsoon process (Kulshrestha and Kumar, 2014).

These studies on aerosol transport and dispersion forms the basis for identification of sources and sinks of aerosols. It also enables characterisation of the different composition of aerosol available in the atmosphere and thus correct attribution of the observed effects on precipitation. Understanding the transport and dispersion of air pollutants provides information on the choice of seeding material, type and location. Therefore, ensuring that optimum precipitation is achieved in the targeted area.

2.3 Cloud Formation and Distribution

Cloud particles are composed mostly of the visible aggregate of minute particles water or ice in the free air (Muthama, 2003). At sufficient sizes, cloud particles become falling hydrometeors and categorized as raindrops, drizzle drops, graupel, hailstones and snow crystals. Moisture and cloudiness distribution influences precipitation (IPCC, 2013). Therefore, in the atmosphere, clouds are a visible manifestation of physical processes taking place. Factors that determine the appearance of clouds include growth of precipitation within it and stability of the atmosphere in which it forms. Dispersion of clouds occurs through either fall out as precipitation or evaporation (Muthama, 2003).

Deep convection occurs on vertical scales that encompass most of the troposphere. All Mesoscale Convective Systems (MCS) can be considered to be deeply convective, as they exist over the entire vertical span of the troposphere. They are often horizontally cover hundreds of kilometers (Houze 1993) and are fuelled by moist convective processes. Updrafts within the convective cores are quite strong, on the order of several tens of ms^{-1}, and penetrate the freezing level. Uptake of water by aerosol or CCN, as described in the previous section, is just the first step in the journey of the aerosol and water in the case of deep convection. As water ascends and experiences changes of phase, water and energy are redistributed vertically.

Within the updraft, latent heat release occurs at low levels due to condensation of water vapour onto aerosol or CCN and occurs aloft due to freezing of droplets and ice. The net energy change due to microphysical processes in the updraft region above cloud base of a deep convective system. Therefore, it would gain diabatic heating (Houze 1989). As the system matures, a cloud shield typically develops, and stratiform precipitation falls within a broad area of weaker vertical motion. Within the stratiform region, the net energy change due to microphysical processes is more of a balance between heating by vapour deposition aloft and cooling by melting and evaporation at lower levels. Though this theory applies to MCS, it can be extended to squall lines (Houze 2004), which are a related sub-classification of MCSs. Studies of MCS (and squall line) organization and structure are important for determining the redistribution of energy and moisture within the storm environment, as well as how these processes affect surrounding environment (Houze 2004).

Within deep convection, updraft cores accelerate air parcels quickly, and as they ascend, the parcels experience reductions in pressure (Kaufeld, 2010). The parcels adiabatically expand to compensate for the lowering pressure and work is done by the parcel, which requires energy. The source of energy for this process is the kinetic energy, represented by the temperature of the parcel itself. Significant additional energy for parcel ascent comes from the latent heat of condensation upon CCN. The importance of accurately representing aerosols becomes clearer here: for a given water vapour content and updraft, increased aerosol or CCN presence will result in increased droplet concentration, but decreased droplet size. If the temperature remains above the freezing point of water, the convective process is termed a “warm-rain” process. In warm rain processes, aerosol activation, droplet growth, and collision coalescence are considered to be the primary mechanisms that lead to the formation of rain, and precipitation.

In most cases of deep convection, even within the tropics, updrafts ascend higher, and the temperature of the parcel will continue to decrease. At subfreezing temperatures, the energy required to allow the parcel to continue to expand can come at the expense of another phase change of the water in the parcel. With the changeover of droplets to ice particles, a rapid boost of energy helps accelerate the parcel upward even more (Zipser, 2003). The gain in elevated Convective Available Potential Energy (CAPE) due to this release of latent heat is estimated to add as much as 1000 Jkg^{-1}. Therefore, it results in an increase in updraft invigoration by approximately 20%. Such areas include Amazon with the typical climate of the equatorial belt had sea surface-based CAPE values of 1000 –1500 Jkg^{-1} (Williams *et al.,* 2002; Khain *et al.,* 2005, Khain *et al.,* 2008).

Andreae *et al.* (2004) report that storms strengthened with the polluted air produced large hail and latent heat release higher in the atmosphere than storms under a cleaner air mass. Rosenfeld (2008) presented a synthesis of many of the recent observational and modelling studies and attempts to make conclusions regarding the influence of aerosol on deep convective systems. Recognised theories include Zipser (2003) of enhanced invigoration and secondary (outflow-based) updraft invigoration as a characteristic of high aerosol concentration deep convective cases. Higher cloud water mixing ratios present in instances of high aerosol concentrations are argued to lead to enhanced cooling by evaporation within downdrafts. Through the enhanced cooling and downward momentum, these more strengthened downdrafts can spawn secondary updrafts as they push ambient air upward, leading to more precipitation (Rosenfeld 2008).

Aerosol effects are highly dependent upon the environmental conditions in which they exist, as factors such as the presence of moisture, temperature, and wind velocities dictate the rates of conversion. Because of these inherent complexities, it is incredibly difficult to separate the microphysical and radiative effects using observational datasets. Therefore, models are an appropriate tool to use to disentangle and quantify contributing factors. Tropical warm rain processes are important in the modulation of clouds and rain types and organization of tropical convection (Lau *et al.,* 2005). Studies by Short and Nakamura (2000) showed that shallow convection accounted for more than 20% of the total rain from the Tropics. Further, approximately 28% of the rainfall was accounted by warm rain from mid-level Cumulus Congestus during the Tropical Ocean Global Atmosphere Couple Ocean–Atmosphere Research Experiment (Johnson *et al.,* 1999). It pointed to the importance of a mid-tropospheric inversion layer formed by the melting of ice phase precipitation falling from above, in limiting the growth of deep convection. Wu (2003) inferred from theoretical calculations that mid- to low-level condensation processes would contribute to 20% of the latent heating in the Tropics and thus maintain the observed moist static stability profile.

In Optically thick clouds, cloud albedo associated with the decrease in droplet size are expected to increase (Nakajima *et al.,* 2001). On the contrary, there is an unexpected decrease of cloud albedo with decreasing droplet size in optically thinner clouds. Over continents, the higher shortwave albedo in clouds with same liquid water content and vertical extent are observed compared to oceans (Theodore *et al.,* 2003). Therefore, suppressed cloud reflectivity are associated with water bodies.

Distribution of orographic precipitation strongly depend on the composition and size of the background aerosols which serve CCN (Muehlbauer and Lohmann (2009). They also influence the microphysical properties of clouds (Peng *et al.,* 2002). The shift in the precipitation distribution was expected to affect the hydrological cycle on the local scale (Givati and Rosenfeld 2005; Jirak and Cotton, 2006). The rate of latent heat release and processes of precipitation formation are affected by microphysical processes in the formative and growth, and interaction of drops and ice particles (Khain *et al.,* 2000).

DCCs play a significant role in the hydrological and radiative balance of the atmosphere. It constitutes an upward branch of the Hadley cell and provide a conduit for transport of moisture, energy, momentum, chemical species and aerosols from the Boundary Layer to the Upper Troposphere or Lower Stratosphere Processes. In DCC, aerosols in the lower part of the cloud suppress warm rain and allows lifting of the greater amount of Liquid Water Content by updrafts above the freezing level. Therefore, additional latent heat is released to energize the clouds (Andreae *et al.,* 2004; Koren *et al.*, 2005; Rosenfeld *et al.*, 2008). High-resolution cloud resolving models (Morrison and Grabowski, 2007) can resolve the deep-convective and mesoscale motion.

The short lifetime of cloud particles in the sub-saturated air creates relatively fine-scale variations and sharp cloud edges in cloud properties, which is less typical of aerosol layers (IPCC, 2013). Therefore, it slows down the rate of cloud droplet coalescence into raindrops (i.e. autoconversion). According to Rosenfeld *et al.* (2008), delaying the formation of rain is sufficient to cause invigoration of cloud dynamics even if the increase in aerosols does not decrease the total rainfall amount. Condensed water can form ice precipitation particles if it does not rain early and thus release the latent heat of freezing aloft (Rosenfeld, 2006; Koren *et al.*, 2005).

Cloud droplets coalesce into raindrops that rain out from the pristine clouds (Tao *et al.,* 2007). Precipitation of smaller droplet in polluted air occurs supercooled levels. For the same amount of precipitation in the more polluted atmosphere, reabsorbed heat at lower levels by melting ice and additional release of freezing results in greater upward heat transport (Rosenfeld *et al.*, 2008). Inevitably, consumption of more instability for the same amount of rainfall lead to the invigoration of the convective clouds and additional rainfall (Tao *et al.*, 2007). These occur despite the slower conversion of cloud droplets to raindrops.

Clouds have a significant role in climate predictability (Bony *et al.*, 2006). They cool the climate system by long wave radiation at approximately the same temperature as the surface and reflect shortwave radiation back to space. The interaction of clouds and prevailing systems at multiple scales result in rainfall formation. Clouds depend on both aerosol properties and local meteorological conditions. There exist challenges in decoupling the effects of aerosols from changes in other environmental conditions on clouds (Lehahn *et al.,* 2011). However, it attributed stronger surface wind to enhanced marine coarse particles formation and thus less stable conditions. In a study of shallow cumulus clouds, Nuijens *et al.* (2009) linked precipitation and wind speed. They attributed it to boundary layer humidity while acknowledging the possible effect of sea salt aerosols (Nuijens *et al*., 2009).

The response of clouds to climate forcing mechanisms varies. The primary sources of uncertainty in both equilibrium and transient climate responses could be explained by inter-model differences (Dufresne and Bony, 2008). Confidence in climate projections necessitate the detailed analysis of cloud processes are accounted for despite unanimous positive feedback observed from models (Randall *et al.,* 2007).

The modelling of clouds is one of the weakest links in the general circulation modelling efforts and thus representations of cloud processes in climate models drive much of the uncertainty surrounding prediction (IPCC, 2007). Significant efforts to study clouds and their interactions with aerosols exist in the past (Koren and Feingold, 2011). It includes intensive field campaigns, remote sensing and modelling (Van Zanten *et al.,* 2005; Matsui *et al.,* 2006; Feingold *et al.,* 2010). To account for the contribution of aerosols acting as CCN, accurate representation of aerosol properties is necessary. These include mass concentration, particle size and size-dependent composition, optical properties, and the ability to serve as nuclei of cloud particles is inevitable. These provided insights into potential weather modification and thus effective and efficient cloud seeding aimed at enhancing or suppressing rainfall.

Yin *et al.* (2000) examined the diurnal cycle of convective activity and cloudiness over Lake Victoria using infrared satellite data. The results indicated that geographically distinct patterns of convection occurred. Maximum activity occurred over the north-western quadrant of the lake and tended to occur during the night time. Although the similar trend in the southwest, convection was relatively infrequent. In the eastern quadrants, convective activity is somewhat weaker than in the northwest but considerably stronger than in the surrounding catchment. A significant relationship between satellite-derived reflectivity and ground-based cloud cover has observed by Muthama *et al.* (2008). Moreover, Muthama *et al.* (2008) recommended the use of that satellite-derived reflectivity as a proxy for observed cloud cover over areas lacking ground-based cloud observations. Consequently, models can be designed to estimate the in-situ cloud observations.

A review by Tazalika (2003) noted that continuous observations of different meteorological phenomena using Outgoing Long Wave Radiation (OLR) has existed since 1974. The measurements provide invaluable information in the study of both ocean and land. OLR is the energy measured in the form of thermal radiation leaving the top of earth's atmosphere. Continuous measurement of OLR greatly bridged an existing gap in conventional meteorological observations over large remote oceanic and land areas.

Over the tropics, Arkin et al. *(*1989) related OLR variations to changes in the distribution of precipitation and cloudiness due to its high and stable surface temperature. Further, CTT largely modulates OLR. In the tropics, CTT largely modulates OLR with areas of intense convection represented by low OLR values while cloud-free locations appear as areas of high OLR. Therefore, high (low) OLR values indicate less(greater) cloudiness that implies decreased (increased) depth of cumulus convection. According to Lyons (1990), interpreting OLR signature requires much caution due to the fact in some instances, high clouds may be a result of convective clouds. However, this study notes that despite the numerous advantages provided by OLR measurements, the current resolution of 2.5×2.5 may limit analysis at finer grid scales.

2.4 Rainfall Variability and Change

Precipitation significantly influences the quality of human life through the availability of fresh water (Levin and Cotton, 2009). Therefore, precipitation is one of the fundamental physical process that links aspects of climate, weather, and global hydrological cycle. Over EA, a study by Gitau *et al*. (2013) showed that precipitation displayed the largest variability in both spatiotemporal distribution and magnitudes. Further, IPCC assessment (IPCC, 2007) notes that changes in precipitation regimes and frequency of extreme hydrologic events, such as floods, droughts, severe storms, Monsoon fluctuations and hurricanes have a high potential impact on climate. Responses to the rainfall shift are already being observed in many terrestrial water sources (Bates *et al.,* 2008). These could be considered as possible indicators of future water stress linked to climate variability (Majone *et al.,* 2012).

A variety of physical processes influences rainfall in EA (Rosell and Holmer, 2007; Hession and Moore, 2011). In EA, frequent episodes of both excessive (Webster *et al*. 1999; Latif *et al*. 1999) and deficient rainfall (Hastenrath *et al*. 2007) are reported. In particular, the frequency of anomalously strong rainfall causing floods has increased. Mean MAM and OND precipitation increases are simulated almost everywhere in East Africa with semi-arid areas in northern Kenya, the western parts, which include Rwanda and Burundi projecting an increased precipitation by more than 10% (Shongwe *et al*., 2010). However, studies by Williams and Funk (2011), Funk *et al.* (2008) and Lyon and DeWitt (2012) showed that rainfall between March and May/June indicated a decreasing over EA.

Several studies have confirmed the presence of the Quasi-Biennial Oscillation (QBO) in various atmospheric parameters. Some variables that have exhibited QBO include temperature, ozone, Indian Monsoon and Africa rainfall (Indeje and Semazzi, 2000). During the March-April-May (MAM) rainfall season, about 36% of rainfall variability was associated to QBO in the lower equatorial stratospheric zonal winds. Furthermore, the relative role of QBO and rainfall over Eastern Africa is stronger in the time-lag sense than the simultaneous relationship. Many studies have investigated the relationship between East African rainfall and El Nino Southern Oscillation (ENSO).

The Indian Ocean Sea Surface Temperatures (SST) anomalies also impact significantly on regional atmospheric circulation and rainfall anomalies that extend into Eastern and Southern Africa (Saji *et al.*, 1999; Owiti *et al.*, 2008). Analysis of the evolutional phases of Indian Ocean Dipole (IOD) index by Owiti *et al.* (2008) indicated significant SST anomalies began to appear in April. After that, attained a maximum peak around October/November and started decaying in January. Most cycles do not extend beyond one year. As such, the significant association between the IOD and Eastern Africa regional rainfall is stronger during OND rainfall season.

Several studies show that ENSO is the most dominant mode of interannual climate variability in EA (Schreck and Semazzi, 2004). Studies by Semazzi and Indeje (1999) and Schreck and Semazzi (2004) examined the coupled variability between African continental rainfall and ENSO events. Warming over the western Indian Ocean during the ENSO events is associated with high moisture fluxes over the marine boundary layer (Trenberth, 1997). The increased tropospheric moisture related to the warm El Niño events is advected into EA by the relatively strong easterly wind flow during the wet seasons. The advected moisture supports enhanced convection and orographic precipitation through latent heat release thus sustaining wet conditions over EA. The Madden-Julian Oscillation (MJO) plays an important role in climate variability and has a significant influence on medium-to-extended ranges of weather forecasting in the tropics (Pohl and Camberlin, 2006). Proximity to the ocean, varied topography and existence of large inland lakes induces vigorous mesoscale circulations with a strong diurnal cycle in several parts of the East Africa region.

The Inter-Tropical Convergence Zone (ITCZ) is a narrow zone into which low-level tropical equator-ward moving air masses from both hemispheres converge (Okoola, 1999). Over EA, ITCZ is an important synoptic-scale system that controls seasonal rainfall (Asnani, 2005). The location of the ITCZ together with its overall horizontal and vertical structures largely depends on the intensity of the north-easterly and south-easterly winds that are in turn driven by the subtropical anticyclones.

The East Africa Low-Level Jet (EALLJ) stream occurs near the coast of East Africa. This jet stream is one of the major well-recognized cross-equatorial flows. The location of the jet core is between 1 and 1.6 km above the mean sea level (Indeje *et al.,* 2001). According to Indeje *et al.* (2001), the jet stream induces strong currents and upwelling over the western equatorial Indian Ocean. The EALLJ plays an integral role in the seasonal development of the Somali Current, an intense ocean current that flows northward only during the southwest monsoon. The jet builds during the months of April and May, becomes more pronounced in June to August and decays in September and October, during which the flow reverses to NE monsoons. Its horizontal divergence and vertical wind shear lead to dry conditions over East Africa.

In areas of high terrain, TRMM’s algorithms have been noted not perform optimally. For example, a study by Hong *et al*. (2007) indicated that the presence of relatively warmer cloud temperatures in mountainous regions resulted in missed light precipitation events by the passive infrared retrievals. This could be attributed to cloud temperatures being deemed as too warm for the precipitation to occur by the satellite's algorithms. Misrepresentation of precipitation events could lead to underestimation of total rainfall (Bitew and Gebremichael, 2010). Even in heavy rain events in mountainous regions, the warmer cloud temperatures implies less ice aloft and thus underestimation of total rainfall by the passive microwave sensors (Dinku *et al*. 2010). Bare and ice-covered mountain tops have been interpreted as rain-producing clouds in passive microwave algorithms, leading to overestimation (Hirpa *et al*. 2010).

Using TRMM precipitation radar at high elevations in the Himalayas, Barros *et al*. (2006) noted difficulties in detecting precipitation. However, Dinku *et al*. (2007) evaluated how different satellite products perform over complex topography in the tropics based on data from the Ethiopian highlands. At a monthly time scale, TRMM 3B43 performed very well with a bias less than 10% and an RMS of about 25%. Considering the complex topography of Ethiopian highlands, the results were considered as very good and consistent with results for West Africa. Therefore, this study notes that despite advance developments in satellite-based data sources, estimation of the rainfall over areas with complex terrain continue to experience challenges due to the instruments algorithms (Hirpa *et al*., 2010). Rosenfeld *et al.* (2014) indicate that improved observational tests are essential for validating the results of simulations and ensuring that modelling developments are on the right track.

The study notes that precipitation remains highly variable in both space and time in EA. Since most countries in EA remain rainfall dependent, the high spatial and temporal variability in precipitation greatly impacts key socio-economic development such as agriculture, tourism energy and transport. Therefore, affecting the quality of life that significantly depends on available fresh water.

2.5 Aerosols, Clouds and deep convection

A few meteorological models have incorporated aerosols and aerosol chemistry. Several studies such as Dusek *et al.* (2006), Seifert and Beheng (2006) and Van den Heever *et al.* (2006) represent aerosols as CCN. These is due to computational cost and diversity of aerosols. Therefore, aerosol effects on precipitation have been indirectly studied by using CCN or CCN droplet spectra as a starting point, instead of aerosol themselves. This intermediate step is essential for gaining confidence in linking of these two as of-yet-separate components of the atmosphere: atmospheric chemistry and meteorology. Worth noting, not all aerosol are CCN, and not all CCN are aerosols.

Banta and Hanson (1987) were the forerunners of examining the influence of aerosols on convection within the modern meteorological model. They realized the importance of adequately capturing the process of collision/coalescence in cloud microphysics, represented as a statistical autoconversion rate. The choice of a proper autoconversion method allows for a more accurate representation of the size and number of raindrops, and, therefore, the evolution of the thermodynamic environment. Banta and Hanson (1987) bypassed explicit representation of aerosol or CCN by varying In-cloud droplet concentrations from representative maritime to continental numbers in a thermodynamic environment that produced a thunderstorm. They used a 2-Dimensional (2D) cloud model of Tripoli and Cotton (1986) which included ice microphysics and a Manton and Cotton (1977) autoconversion scheme sensitive to a threshold cloud droplet number. Results showed suppressed warm rain process with increased droplet concentrations. Primarily produced variables through cold processes such as the collision of ice crystal, ice aggregation, and vapour deposition included graupel and other ice particles. Decreased droplet concentrations yielded a lower cloud base and graupel formed mainly by freezing of raindrops.

A study by Khain and Sednev (1999) found that lower aerosol concentrations are much more conducive to rain formation, and precipitation occurs in the vicinity of the development of the cloud. Higher aerosol concentrations were found to delay the formation of rain, and thus lifting more water mass above the freezing level. In the simulations, precipitation was diminished and tended to fall further downwind (as a function of ambient wind speed). Changes in chemical composition were observed to alter the concentration of activated droplets and resulted in precipitation differences of 25-30%.

Khain *et al.* (2001) used their model to show that high mixing ratios of liquid water at temperatures of up to -38°C can occur due to higher concentrations of CCN within convective environments. The number of CCN can influence significant environmental factors such as the height of the glaciation level. Therefore, the emphasis of these modelling studies had been deciphering microphysical differences due to CCN concentrations and types. However, it was becoming clear that the simultaneous effects on dynamics of convective systems was just as important, and the tools they had developed were suitable for such investigations.

Van den Heever *et al.* (2006) tested the effects of aerosol size distribution of precipitation in deep convective storms by altering the CCN, giant CCN (GCCN), and IN concentrations independently. Typical concentrations for clean cases were in the range of 300 cm^{-3} for CCN (diameters of 1 μm or less), 0.5 cm^{-3} for GCCN (diameters of 1-50 μm), and 0.1 m^{-3} for IN. Typical concentrations for polluted cases were in the range of 1000 cm^{-3} for CCN, 500 cm^{-3} for GCCN, and 15 m^{-3} for IN. The boundary layer displayed the highest concentrations except for the case of IN, for which the highest concentrations were at ~3 km. The effects of varying CCN on dynamical and microphysical properties of the simulated thunderstorms in Florida were the most pronounced. Updraft velocities in the developing stages of the storms consistently increased with increased CCN concentrations while surface precipitation decreased due to inhibition of the warm rain process and enhanced upward transport of liquid compared to the clean case. During the mature and dissipating stages of the storms, higher concentrations of GCCN and IN were observed. They had more influence on updraft velocities.

Lee *et al.* (2008) noted that secondary convection induced by downdrafts could not be simulated accurately using a two-dimensional model compared to a three-dimensional model. However, using the same thermodynamic environment, a comparison of 3-Dimensional (3D) simulation (Phillips and Donner, 2006) and a 2D simulation (Lee *et al.*, 2008) indicated similar results concerning precipitation. Both cases of increased aerosol led to increases in precipitation despite differences in model microphysics and resolution. Therefore, processes leading to enhanced precipitation in cases of increased aerosol can be represented by models with less sophisticated, bulk microphysics and 2D simulations.

Khain *et al.* (2008) attempted to classify different types of aerosol effects on surface precipitation. Their classification schematic incorporates wind shear, humidity, and aerosol effects, the combinations of which lead to either a net loss or gain in the condensate. Also, it should be noted that their scheme is appropriate only for convective systems reaching at least 4 km and include ice and mixed-phase precipitation. This schematic, while highly simplified, addresses the issues core to the influence of aerosol on deep convective precipitation and provides a sound system of orientation for the past, current, and future studies. Ekman *et al.* (2007) systematically varied concentrations and vertical profiles of CCN and IN from 250 cm^{-3} to 3000 cm^{-3}. The domain was 2 km horizontal resolution and vertical resolution of 400 m. The responses of the model to increasing CCN concentrations were all non-monotonic with respect to average updraft velocity, precipitation rates, and ice formation. The model showed similar sensitivities to the range of IN tested. This study emphasizes the importance of performing systematic, stepwise tests with several increments of aerosol concentrations, rather than the tendency other modelling studies have shown to represent more limited testing scenarios of clean or polluted conditions.

In Lee *et al.* (2008), two idealized experiments, representing high and low aerosol concentration profiles, were carried out using the Advance Research WRF (ARW). The goal of the study was to replicate experiments such as Van den Heever *et al.* (2006) and Lynn *et al.* (2005a, 2005b). The double moment bulk microphysics scheme of Phillips and Donner (2007) was used, and limited chemistry with several types of particles (sulfate, sea salt, dust, organics, and black carbon). Only hygroscopic aerosol such as sulfate and sea salt were allowed to function as CCN while the hydrophobic aerosol types were assumed to act only as IN. By analyzing microphysical terms of the precipitation budget, and examining dynamical terms associated with near-surface convergence, this study helped clarify processes that lead to increased precipitation in cases of increased aerosol. They found that higher values of CAPE and wind shear resulted in more precipitation for scenarios with high aerosol concentrations. Notably, warm rain onset delayed with increased aerosol concentrations.

Proposed causality for aerosol-cloud-precipitation interactions included the Twomey effect (Twomey, 1977), Albrecht effect (Albrecht, 1989) and Drizzle-entrainment effect (Lu and Seinfeld, 2005; Wood, 2007). Others include Sedimentation -entrainment effect (Bretherton *et al.,* 2007; Hill *et al.*, 2009) and Evaporation-entrainment effect (Hill *et al.*, 2008). In the Twomey effect which assumes constant Liquid Water Path (LWP), aerosol number concentration increase results to smaller, more numerous droplets and thus higher albedo (Twomey, 1977; Chen *et al.*, 2011). The Albrecht effect (drizzling cloud) assumes an increase in aerosol number concentration leading to a smaller, more numerous droplets, reduced collision-coalescence. Therefore, it leads to less precipitation whereas a rise in LWP results to higher albedo (Albrecht, 1989; Chen *et al.,* 2011). Drizzle-entrainment effects (drizzling cloud) leads to increase in aerosol number concentration with smaller, more numerous droplets, reduced collision-coalescence and less precipitation (Chen *et al.,* 2011). It also results in reduced below-cloud evaporative cooling and in-cloud latent heat release with higher Turbulent Kinetic Energy (TKE) and stronger entrainment. Further, LWP decreases with lower albedo (e.g. Lu and Seinfeld, 2005; Wood, 2007). In sedimentation-entrainment effect (non-drizzling cloud), an increase in aerosol number concentration results to smaller, more numerous droplets. It also results in reduced in-cloud sedimentation with a rise of cloud water and evaporation in entrainment regions. It occurs with stronger entrainment, LWP decrease and lower albedo (Ackerman *et al.*, 2004; Bretherton *et al.,* 2007; Hill *et al.,* 2009). Evaporation-entrainment effect (non-drizzling cloud) increase in aerosol number concentration results to smaller, more numerous droplets with more efficient evaporation. Further, it displays higher TKE, stronger entrainment, LWP decrease and lower albedo (Xue and Feingold, 2006; Hill *et al.,* 2008; Chen *et al.,* 2011).

Cumulus Parameterization is the representation of precipitation process in Numerical Weather Prediction (NWP) models. Widely used Convective parameterization (CP) schemes in high-resolution models are Anthes-Kuo (Anthes, 1977), Betts-Miller and Betts-Miller-Janjic (BMJ) (Betts and Miller, 1986; Janjic, 1994). Others include Grell scheme (GR) (Grell, 1993; Grell *et al.,* 1994) and the Kain-Fritsch cumulus scheme (KF) (Kain and Fritsch, 1993). Various studies (Wang and Seaman, 1997; Gallus, 1999; Alapaty *et al.,* 1994a, 1994b) are available demonstrating the performance of CP schemes with mesoscale models over different regions. Alapaty *et al.* (1994a, 1994b) carried out a comparative study on the simulation of orographic and monsoon rainfall over the Indian region with a limited area model using KF and Kuo schemes. They came to the conclusion that Kuo scheme performs well over the Indian region during the monsoon season. Vaidya (2006) studied the performance of two convective parameterization schemes KF and BMJ over the Indian region using Atmospheric Regional Prediction System model. Rainfall prediction skill is subjectively assessed based on the amount and spatial distribution. The study showed that out of four cases, BMJ scheme produced better results in three cases while KF scheme performed better in only one case. Ratnam and Cox (2006) tested GR and KF cumulus schemes using Fifth-Generation Penn State/NCAR Mesoscale Model (MM5) model for the simulations of the monsoon depression. They found that both the schemes are capable to simulate the large-scale features of monsoon depressions, but failed to capture the correct location of depressions at 24 hours and 48 hours forecast.GR scheme tends to overestimate the rainfall. KF scheme could simulate the distribution of precipitation, but the location of maximum rainfall was different. These studies conclude that the performance of the

NWP models is highly dependent on initial inputs, model resolution and physics options, especially cumulus parameterizations scheme.

Enhanced amounts of cloud water and rain intensities later in the life cycle of the cloud leads to a delay of early rain causes. These are affirmed by modelling studies to predict invigoration through increased aerosol loads (Tao *et al.*, 2007). Notably, studies by Rosenfeld *et al.* (2008) and Phillips *et al.* (2007) details the role played by ice melting below the 0°C isotherm level. The enhanced evaporative cooling of the added cloud water, mainly in the downdrafts, provides part of the invigoration by the mechanism of enhanced cold pools near the surface that push the ambient air upward. The heating above and greater cooling below results in increased upward heat transport for the same amount of precipitation at the surface. For the same amount of rainfall, more CAPE would be consumed and converted to an equally greater amount of released Kinetic energy. Therefore, the resulting invigorating convection leads to greater convective overturning and more precipitation (Rosenfeld, 2006).

2.6 Modelling Framework

2.6.1 Description of Weather Research and Forecasting Model

To understand the interaction of aerosol particles and the atmosphere at a particular scale, treatment of the relevant chemical, physical, and aerosol dynamical processes are inevitable (Bangert *et al.*, 2011). The current study utilises WRF Model. WRF is a NWP mesoscale modelling system (Skamarock *et al.*, 2008) developed for both atmospheric research needs and operational forecast. WRF implemented dynamical cores include the Non-Hydrostatic Mesoscale Model (NMM) and the ARW (Chen *et al.*, 2011). NMM was primarily designed for weather forecasting purposes while ARW was created to be suitable for a broad range of applications at varying the time and spatial scales. This study utilized the ARW model.

Several studies (Moeng *et al.*, 2007; Wang and Feingold, 2009a, 2009b; Wang *et al.*, 2009a) have used the WRF model for Large Eddy Simulations (LES) experiments. They found the results were in good agreement with observations and other LES studies (Wang *et al.*, 2009b: Ackerman *et al.*, 2009). Most model variables and derived quantities were found to lie within the corresponding ensemble range in Ackerman *et al.* (2009). The derived quantities included total water mixing ratio, liquid water potential temperature, LWP, buoyancy flux, total water flux, TKE, and cloud fraction. However, the variance of vertical velocity and below cloud rain rate for the case they considered were underestimated by WRF LES. Appendix 11 outlines the ARW Modelling System Program Components.

2.6.1.1 Microphysical Processes

Microphysics in the WRF model handles the cloud microphysical processes that drive the cloud particle formation, growth and dissipation. It handles explicitly resolved water vapour, clouds and precipitation processes. The available options mostly differ in the number of phase changes of water and the number of interactions between clouds and precipitation particles (Stensrud, 2007).

The microphysical processes include sedimentation, drop collisional breakup, condensation-evaporation, aerosol activation, and collision-coalescence. Aerosol size distribution assumes a single mode lognormal size distribution. Aerosol activation (or cloud droplet activation) occurs when the ambient supersaturation exceeds the critical supersaturation (Sc) for the given particle size. The composition dependence of the solution water activity was represented by a hygroscopicity parameter (κ). The hygroscopicity parameter indicates the relationship between cloud condensation nuclei activity and dry particle diameter (Petters and Kreidenweis, 2007);

$$S_C(D_d) = \frac{D^3{}_d - D^3{}_a}{D^3{}_d - D^3{}_d(1-\kappa)} \exp\left(\frac{4\sigma_{\frac{s}{a}} M_w}{RT\rho_W D_d}\right) - 1 \qquad 2.1$$

Where D_a is the aerosol dry diameter, D_d is droplet diameter while M_w is the molecular weight of water. The density of water is represented by ρ_w the surface tension of the solution/air interface by $\sigma_{\frac{s}{a}}$. The microphysical used in the study assumes aerosols to be ammonium sulfate. The hygroscopicity parameter (κ) has a constant value of 0.615 as detailed by Petters and Kreidenweis (2007). Worth noting, aerosol number concentration are held constant. Computed activated CDNC at each time is the difference between the pre-existing droplet number and the particle number at the diagnosed supersaturation. These are consistent with several previous studies (Lu and Seinfeld, 2005; Lu and Seinfeld, 2006; Sandu *et al.*, 2008). Diffusional growth and evaporation of water drops are described following the vapour diffusion equation

(Pruppacher and Klett, 1997). The terminal velocity of water drops are calculated based on the Best and Bond number approach (Pruppacher and Klett, 1997). In computing the kernel function, efficiencies of collision-coalescence between drops are derived from Hall (1980) data. Information on the collisional breakup of water drops used are detailed in Feingold *et al.* (1988). Local wind speed and difference in specific humidity/potential temperature following the Monin-Obukhov scheme are used to compute sensible heat fluxes and surface latent. Prognosis of TKE utilized a 3-D turbulence scheme with 1.5-order TKE closure (Deardorff, 1980). Calculation of Longwave radiative fluxes used the Rapid Radiative Transfer Model (RRTM) (Mlawer *et al.*, 1997) with 16 LongWave (LW) bands. Simulation of the cloud-top radiative cooling and heating rates utilized the correlated-k method. To ensure that shortwave absorption, solar flux and scattering in clear air, and reflection and absorption in cloud layers, shortwave radiation is represented using the Dudhia scheme (Dudhia, 1989).

2.6.1.2 Radiation Scheme

The radiation scheme represents both the atmospheric heating due to radiative flux divergence and the surface radiation for the ground heat budget. Parameterization of radiation processes at sub-grid scales for both longwave and shortwave used National Center for Atmospheric Research (NCAR) Community Atmosphere Model (Collins *et al.*, 2004). It is recommended for regional climate simulations because it has an ozone distribution that varies during the simulation according to monthly zonal-mean climatological data. The scheme also interacts with resolved clouds and cloud fractions. Furthermore, it handles optical properties of several aerosol types and trace gases.

2.6.1.3 Cumulus Scheme

The cumulus schemes represent the effects of convective and shallow clouds within a grid cell. They describe the vertical fluxes due to unresolved updrafts and downdrafts as well as the compensating motion outside the clouds. The cumulus schemes also provide the convective component of rainfall caused by convective eddies that are not captured by the model. There is an evident need for developing convection adequately in both time and space because it is a critical factor in describing rainfall. Therefore, a suitable cumulus scheme is of major importance since extreme precipitation events in this region are directly affected by an accurate description of convective processes. Furthermore, convection is also determinant predicting large-scale atmospheric circulations correctly, because it redistributes heat and moisture, affects radiation and overturns the atmosphere (deep convection)

2.6.1.4 Planetary Boundary Layer

The land surface fluxes and the turbulence that occurs in the Planetary Boundary Layer (PBL) are crucial factors in the evolution of the atmosphere because their impact might propagate to the whole atmospheric column. Besides, they usually provide the conditions for certain sensible phenomena to occur, such as the deep convection. An appropriate description of the turbulence permits to distribute heat, moist and momentum all over the atmosphere, not only in the PBL. Since the surface influences the PBL and considering that the variety of surfaces on the Earth is huge, resolving the turbulence adequately in a broad range of conditions is undoubtedly a challenge.

An important problem in the description of the PBL is that of the closure associated with non-linear characteristics of turbulence. Namely the number of unknowns in the set of equations for turbulent flow remains always larger than the number of equations. Consequently, the complete description of the turbulence requires an infinite set of equations (Stull, 1988). Truncation solves the problems of turbulence closure, selecting some equations and calculate the remaining unknowns by semi-empirical relations in terms of the known variables. Depending on the number of terms retained, the order of the approximation is different. The first way of classifying the parameterizations of the PBL involves the order. Therefore, the 1st order closure means that there are equations for the state variables (u, v, w, T, q) –or the first moments. Second-order Closure implies that there are equations for the state variables and their covariance terms. However, parameterization of the triple correlation terms are done. Besides, there are also non-integer schemes, such as the half-order or the one-and-a-half-order closure. When the unknown terms are parameterized according to local parameters, that is, at the same level or neighbour levels, then the scheme is local. Parameters dependent, on the whole, vertical profile in the PBL are used to incorporate the contribution of the large-scale eddies to the total flux. The scheme is called non-local. Non-local schemes tend to perform better, reproducing more accurately the structure and the depth of the PBL as well as the wind profiles within it. However, local schemes tend to produce less mixing than non-local schemes and thus might be more suitable for stable conditions such as the night time. Some schemes switch between non-local and local approaches depending upon the stability of the PBL.

2.6.1.5 Land Surface Scheme

The land-surface models (LSMs) handle the initialization of the state of the ground and account for the surface forcing in the atmosphere. They provide the fluxes that determine the lower boundary condition for PBL schemes by describing the ground temperature, the soil moisture and temperature profiles, the canopy effects and the snow cover. The use of an appropriate sophisticated model that updates these variables is crucial from a climate point of view.

2.6.1.6 Bulk Microphysical Schemes

An important role played by cloud microphysical processes is through latent heating due to condensation. Further, it has direct influences on the cold pool strength due to rainfall evaporation. Therefore, a principal source of uncertainty in convection are microphysical parameterizations. It is also crucial to determine the uncertainty associated with the cloud microphysics parameterization. Evaluating the cloud microphysical schemes is not only of practical significance but also helpful for guiding the future improvement of cloud microphysics parameterizations.

Several studies have addressed the sensitivity of cloud microphysics in predicting convective storms and precipitation (Reisner *et al.,* 1998; Gilmore *et al.,* 2004; Liu and Moncrieff, 2007). Liu and Moncrieff (2007) evaluated the sensitivity of explicit simulations of coherent rainfall patterns to several bulk microphysical schemes using multi-day cloud-system-resolving simulations at 3 km grid spacing. They compared four microphysical parameterization schemes. They found that upper-level condensate and cloudiness, upper-level radiative cooling/heating and rainfall spectrum were the most sensitive. Moreover, the areal coverage and domain-mean rainfall rate displayed moderate sensitivity. In EA, studies related to modelling of clouds and thunderstorms are scarce.

2.6.1.7 Representation of the Aerosol Size Distribution

Evaluating both indirect and direct forcing of aerosols in model simulations in the representation of the aerosol size distribution is essential (Li *et al.*, 2008). Sectional and Modal approaches are the two methods used in atmospheric models to represent the aerosol size distribution. In the Modal approach, analytical functions (usually lognormal distribution) representing various modes of the particle population approximate the particle size distribution. In the sectional approach, a discrete number of size sections approximate the particle size distribution. Different Modal formulations simulate the number, mass and surface area for each mode. They also predict the mean diameter and standard deviation (three moments) or simulate the number and mass and hold standard deviation fixed (two-moment). According to Li *et al.* (2008), the sectional approach represents more accurately the aerosol size distributions than the Modal approaches (two-moment or three-moment). However, memory constraints and computational burden more efficient choice to represent the aerosol size distributions corresponds to the modal approach (two-moment or three-moment).

For the three moment modal approach, the aerosol size distribution is represented as a log-normal size distribution;

$$\mathrm{n}(\ln \mathrm{D}) = \frac{\mathrm{N}}{\sqrt{2\pi}\ln \sigma_{\mathrm{g}}} \exp\left[-\frac{1}{2}\left(\frac{\ln \mathrm{D} - \ln \mathrm{D_g}}{\ln \mathrm{D_g}}\right)^2\right] \qquad 2.2$$

Where, N, D, σ_g Dg is the aerosol number concentration, aerosol diameter, geometric mean diameter and geometric standard deviation of the distribution. Conservation equations for aerosols considered in the Cloud Resolving-WRF (CR-WRF) model are detailed in Li *et al.* (2008). Aerosol spectrum ranged from 0.002 mm to 2.5mm and divided into 92 sections for the CCN nucleation. Based on Kohler theory, the critical radius of dry aerosols is calculated using water supersaturation predicted from the CR-WRF model (Pruppacher and Klett, 1997). Activating aerosols results in the calculation of the mass of water condensing on CCN is calculated under the equilibrium assumption (Kohler equation) if the radius (r_a) of dry aerosols is less than 0.03mm. If the radius is greater than 0.03mm, the mass of water condensing on these CCN at zero supersaturation is calculated as;

$$m_w = K\frac{4}{3}\pi {r_a}^2\rho_w \qquad 2.3$$

According to Khain *et al.* (2000), 3<K<8. Li *et al.* (2008) indicated that when droplets with a high number concentration are competing for available water vapour, a substantial reduction in supersaturation occurs within the cloud. When the cloud water mass of the total nucleated particles is equal to the available water vapour, the nucleation process is terminated to avoid the fact that the air becomes sub saturated after nucleation.

2.6.1.8 Air Mass Trajectory Modelling

Lagrangian and Eulerian are the two primary approaches used to describe airflow (Thomson and Wilson, 2012; Kulshrestha and Kumar, 2014). The Eulerian approach computes atmospheric concentration by integrating pollutant fluxes at every grid interface resulting from advection and diffusion (Escudero *et al.*, 2006). However, the Lagrangian approach computes atmospheric concentrations by summing the contribution of each pollutant puff advected past the grid cell based on its trajectory.

Most of chemistry models use the Eulerian approach as this is a useful tool to explain the various chemical and physical processes. In the Eulerian model, chemical reactions are calculated based on the concentration of a pollutant diluted over the entire grid scale. Most of transport and dispersion models use Lagrangian approach due to limitations in the Eulerian model such as representation of convective transport (Davis *et al.*, 1997; Seibert, 2004). Compared to Eulerian approach, the Lagrangian approach has minimum numerical diffusion (Seibert, 2004). Airmass trajectory is calculated to show the pathway of an infinitesimally air parcel through a centerline of an advected airmass having vertical and horizontal dispersion. Backward air trajectory involves tracing of the pathway followed by an air parcel upwind from the selected coordinates. Further, calculation of best possible pathway to be followed downwind from the selected coordinates in due course of time is called forward trajectory. The calculation of backward air trajectory using Lagrangian approach is easier and computationally cheap as it excludes the influence of upwind on the receptor site (Kulshrestha and Kumar, 2014).

Several studies utilized Hybrid Single-Particle Lagrangian Integrated Trajectory Model (HYSPLIT) model in air mass trajectories analysis. The studies include Hui *et al.* (2008), Reddy *et al.* (2010), Begum *et al.* (2011), Saadat *et al.* (2013) and Budhavant *et al.* (2014). The HYSPLIT is also used to compute dispersion and disposition simulations. In this study, Air parcel trajectories are mainly computed by HYSPLIT. Draxler and Hess (1998) provides a detailed description of the HYSPLIT model.

CHAPTER THREE

3 MATERIALS AND METHODS

This chapter presents data types, sources and methodology used in the study. Figure 3.1 gives the summary of the station utilized in the study. The stations comprised of all synoptic stations in EA.

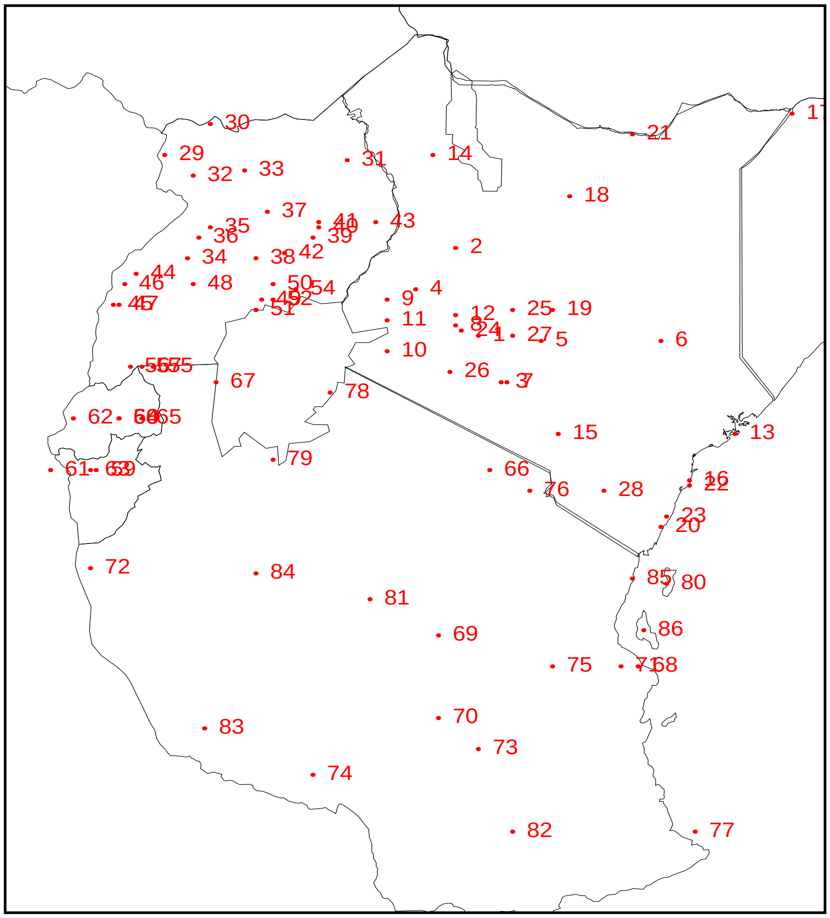

Figure 3-1: Locations and stations used in the study

Appendix 1 presents a detailed description of locations of the stations.

3.1 Data

In this study, different daily datasets were obtained and used as detailed in the subsequent sections. The datasets comprised of aerosols, clouds and precipitation. The satellite-derived parameters covered the period between 2001 and 2012.

3.1.1 Precipitation Data

Quality assured gridded TRMM 3B42 (daily) product with a $0.25^{o}\times0.25^{o}$ spatial resolution (Fisher 2004) extending from -10^{o} S to 7^{o} N latitude was used. The dataset covered the period between 2001 and 2012. The primary goal of the TRMM is to determine the four-dimensional distribution of precipitation in the tropics (Simpson *et al.,* 1988). The TRMM satellite is a low-altitude, low-inclination polar orbit. It is a non-sun synchronous orbit provides potential documentation of the diurnal cycle of rainfall. Generation of 3B42 estimates involves four main stages. First, it involves calibration and combination of microwave precipitation estimates. Secondly, it involves the creation of infrared precipitation estimates using the calibrated microwave precipitation. Thirdly, the combination of microwave and IR estimates. The final stage involves rescaling to monthly data. According to Huffman *et al.* (2007), each precipitation field is best interpreted as the precipitation rate effective at the nominal observation time.

The three sensors of precipitation on the TRMM satellite are shown in Table 3.1 (Kummerow *et al.,* 1998). They include Precipitation Radar (PR), a multi-channel passive TRMM Microwave Imager (TMI) and a Visible Infrared Scanner (VIRS). Other sensors include Clouds and Earth's Radiant Energy System (CERES), and a Lightning Imaging Sensor. The PR is an active microwave sensor that provides specific height information on a precipitating system. The TMI is a passive microwave sensor (Giovannettone and Barros, 2009) that measures the integrated absorption, emission and scattering along the sensor view path and is essentially limited to column amounts. They are complementary in that the observations from the PR are used to tune the TMI retrieval assumptions for more accurate rain estimates over the TMI's swath that is 3.5 times wider that of the PR. The VIRS provides the additional information of cloud-top temperatures and structure. The VIRS also acts as a link between the long time series of visible and IR observations available from geostationary platforms and the brief but more viable precipitation measurements of the TRMM microwave sensors.

Table 3-1: TRMM satellite instrument specifications

Parameter	PR	VIRS	TMI	CERES	LIS
Frequency/wavelength	13.8GHz	0.6-12 µm	10.65-85.5 GHz	0.3-50 µm	0.78 µm
Resolution (km)	4.3 (nadir)	2.1 (nadir)	5-63	10	4 (nadir)
Swath width (km)	215	720	759	Whole globe	550

3.1.2 Aerosol Data

In the study, all available satellite-derived aerosol data from MODIS atmosphere utilized spanned the period 2001-2012. Quality assured level-3 daily data on aerosol distribution include AOD at 0.55 nanometres and Fine Mode Fraction (FMF). These datasets are at a spatial resolution of $1^0 \times 1^0$ and obtained from MODIS Collection 5.1 (C051) data.

AOD is a proxy of the integrated columnar aerosols load measurements (IPCC, 2013). MODIS orbits at an altitude of 700 km in a sun-synchronous polar orbit and onboard Terra and Aqua. It detects aerosols over the entire globe on a daily basis with a broad swath of about 2330 km (Remer *et al.,* 2006). For aerosol retrieval over ocean and land, MODIS makes use of different algorithms as the surface reflectance is different from ocean and land (Kaufman *et al.,* 1997; Tanre *et al.,* 1997). The optimal combination of MODIS observations from both Terra and Aqua ensures attainment of maximal spatial coverage and better daily representation. MODIS Terra equatorial crossing time is 10:30 local time while MODIS Aqua equatorial crossing time is 13:30 local time. The mean value of observations from the two satellites used are in a $1^0 \times 1^0$ grid (Aloysius *et al.,* 2008; Prijith *et al.,* 2012). They are taken if data from both the satellites are available or by keeping the value from one of the satellites if the data from the other is missing. Therefore, enables attaining almost complete global coverage on a daily basis.

3.1.3 Clouds Data

In the study, clouds were evaluated based on CTT, Cloud Top Pressure (CTP) and Cloud Optical Depth (COD). Cloud variability was also determined using CAPE at the surface and Outgoing Longwave Radiation. Quality assured MODIS level-3 daily data on clouds was obtained from MODIS Collection 5.1 (C051) data. It included CTT, CTP and COD at a spatial resolution of

$1^0 \times 1^0$ Vertical velocity (Omega), and CAPE was sourced from NCEP/NCAR reanalysis (Kalnay *et al.,* 1996). CAPE is the amount of buoyant energy available to speed up a parcel vertically and lift it to the level of free convection. Daily CAPE data utilized the 20th Century Reanalysis data from NOAA (NOAA/ERSL PSD) (Compo *et al.,* 2011) was used. The ensemble mean fields on a $2^o \times 2°$ global latitude-longitude grid were used.

OLR data from the Advanced Very High-Resolution Radiometer (AVHRR) instrument aboard the National Oceanic and Atmospheric Administration (NOAA) polar orbiting spacecraft was used. These data are available as twice-daily observations from satellites in the form of pentad means, pentad anomalies and monthly means of a $2.5^0 \times 2.5^0$ latitude/longitude grid. In this study, daily OLR data that covered the period of 2000-2012 was used. OLR data has been used as a proxy for cumulus convection/cloud variability over convectively active regions of the tropics by Prasad *et al.* (2000) and many others. Low (high) values of OLR indicate greater (less) cloudiness and hence increased (decreased) depth of cumulus convection. Interpreting OLR as convection or rainfall requires much caution. Thick, high clouds can produce an identical OLR signature to convective clouds while substantially different rainfall can occur between the two types of clouds (Lyons, 1990). OLR data from NCAR archives, with gaps then filled with temporal and spatial interpolation (Liebmann and Smith, 1996).

3.1.4 Initial and Boundary Conditions

The initial and boundary condition utilized NCEP Final (FNL) operational global Analysis (Yu *et al.,* 2013). NCEP FNL are on $1^0 \times 1^0$ grids prepared operationally every six hours (NCEP/NWS/NOAA, 2000). The NCEP FNLs comes from the same model that NCEP uses in the Global Forecast System (GFS). However, the FNLs lag by at least an hour after GFS is initialized so that more observational data could be used. NCEP FNL analyzes are available on the surface, at 26 mandatory levels from 10 millibars to 1000 Millibars, in the surface boundary layer and at some sigma layers and tropopause. Parameters include u- and v- winds, temperature, soil values, sea level pressure, surface pressure and sea surface temperature. Others included geopotential height, relative humidity, ice cover, vorticity, vertical motion, and ozone.

3.2 Methodology of the Study

This subsection describes techniques used to achieve the specific objectives of the study.

3.2.1 Spatial and Temporal Variability of Aerosols, Clouds, and Precipitation

Spatial-temporal variability of aerosols, clouds, and precipitation involved regionalization of the study area into homogeneous zones based Principal Component Analysis (PCA), time series analysis based on trend and seasonality and Hovmoller analysis.

3.2.1.1 Time Series Analysis

In this study, the trend and seasonality components of the time series were determined.

3.2.1.1.1 Trend Analysis

The trend component of the time series was determined using Mann-Kendall rank statistic to detect abrupt changes in the satellite-derived estimates of cloud, aerosols and precipitation in EA. The test has been found to be most appropriate for analysis of series that show a significant trend, to locate the period with the trend (Sneyers, 1990). The Mann-Kendall rank statistic is considered the most appropriate for analysis of climatic changes in climatological time series for the detection of a climatic discontinuity (Sneyers, 1990; Chrysoulakis *et al.,* 2002). The test uses the ranks y^i of all the terms, x^i in a series under analysis when arranged in increasing order of magnitude. For each element y^i, the number n^i of element y^i preceding it $(i>j)$ is calculated such that $y^i > y^j$. Equation 3.1 gives the test statistic.

$$t_i = \sum_i n_i \qquad 3.1$$

Moreover, its distribution function under the null hypothesis is asymptotically normal, with mean (Equation 3.2) and variance (Equation 3.3);

$$E(t_i) = \frac{n(n-1)}{4} \qquad 3.2$$

$$Var(t_i) = \frac{n(n-1)(2n+5)}{72} \tag{3.3}$$

For large values of $u(t^i)$;

$$u(t_i) = \frac{[n(t_i) - E(t_i)]}{\sqrt{Var(t_i)}} \tag{3.4}$$

In these conditions, a probability α^1 is determined using a standard normal distribution table such that;

$$\alpha_1 = \mathrm{P}(|\mathrm{u}| > |\mathrm{u}(t_i)|)\frac{[n(t_i) - E(t_i)]}{\sqrt{Var(t_i)}} \tag{3.5}$$

Rejecting or accepting the null hypothesis at α level depends on whether $\alpha^1 > \alpha^0$ or $\alpha^1 < \alpha^0$. Absolute values of $u\ (t^i)$ higher than 1.96 indicate an increasing or decreasing trend. In case of a significant trend (α=0.05) in the series, the start of the phenomena is located through sequential analysis. The number n^i of y^i terms for each y^i term such that $y^i > y^j$ with $i<j$, gives a check on the first calculation, given $n^i = y^i$ -1-n *so* that;

$$i^{'} = (N+1) - 1 \tag{3.6}$$

The total number of observations is given as N. Therefore, the values of $u'(t)$ for the reversed series can be calculated similarly, to $u(t)$. Curves that overlap several times indicate the absence of a trend. In this study the significance level (α) considered is 0.05 i.e. at 95% confidence interval.

3.2.1.1.2 Seasonality Analysis

Coefficient of Variation (CoV) indicate temporal variability of daily precipitation, clouds, and aerosols. The CoV is a statistical measure of the dispersion of the data in a series around the mean and computed as shown in equation 3.7.

$$\text{Coeffcient of Variation, CoV} = \frac{\sqrt{\frac{1}{N}\sum_{i=1}^{N}(x_i - \overline{\mathrm{x}})^2}}{\overline{\mathrm{x}}} \tag{3.7}$$

where N is the sample size, x_i is the selected variable and $\overline{\text{X}}$ is the mean.

3.2.1.2 Principal Component Analysis

PCA is useful for compressing geophysical data both in space and time, as well as separating noise from meaningful data. Studies e.g. Ledesma and Valero-Mora (2007) and Gitau *et al.* (2013) indicate the importance of retaining the optimum number Principal Components (PCs). Under-extraction and over-extraction have consequences that adversely impact the Empirical Factor Analysis (EFA) efficiency and meaning. Under-extraction can lead to the loss of relevant information and a substantial distortion in the solution; for example, in the variables loading. On the contrary, over-extraction can result in factors with few substantial loading, which can be difficult to interpret or replicate (Gitau *et al.*, 2013). PCA is an orthogonal linear transformation that converts the data to a new coordinate system. It involves the transformation of variables into a linear combination of orthogonal (perpendicular) common components with decreasing variation. PCA produces a visual representation of the relative positions of the data in a space/time of reduced dimensions, thus indicating spatial and temporal relationships among the variables. A series of axes provides the location of each of the data points which represents separate uncorrelated information. The output is a covariance/correlation matrix denoting the transformation coefficients (eigenvectors) listed in decreasing order of variation. The total variance accounted for by each component is the Eigenvalue. Closely related, inversely related alternatively, unrelated regions are assessed by plotting contour or vector maps. Determination of each mode by its associated Eigenvalue is then used to calculate the variance attributable to that mode. Let P be an $m \ x \ n$ matrix of daily data, where m is the number of days and n is the number of stations. This matrix can be decomposed into linear functions of m temporal and n spatial vectors so that the observation P_{ij} on day i at station j is

$$P_{ij} = \sum_{k=i}^{n} a_{ik} e_{ik} \Leftrightarrow P = ae \qquad 3.8$$

Where a_{ik} the element for day *i* in the kth is time vector and e_{ik} is the element for station *j* in the kth space vector.

The strength of the analysis is that often a large part of the spatial variability of the original data can be reproduced using only a few of the space vectors. The time vector may be seen as a time series of weights, giving more or less weight to a particular space vector (spatial pattern) each day. The weighted spatial patterns were superimposed recreated the original daily spatial pattern.

The inhomogeneous terrains in EA justified the use of correlation matrix to compute the space vectors as opposed to covariance matrix (Svensson, 1999). Since the daily rainfall, clouds, and aerosols distribution at each station was skewed, the daily data had to be transformed. Two approaches to the transformation that can be used are the square root and logarithm transformations. This study utilized square-root transformation as it works well over EA (Camberlin and Okoola, 2003). Stephenson *et al.* (1999) indicated that square root transformation is the optimal variance stabilizing transformation for a Poisson process and thus is beneficial in stabilizing the variance of sporadic rainfall time series.

The square-root transformed data (P_{ij}) were standardized by subtracting the mean ($\bar{P}_j$) of the time series for each station. It is then divided by the standard deviation (σ_j) so that the new standardized dataset (A_{ij}) is;

$$A_{ij} = \frac{P_{ij} - \bar{P}_j}{\sigma_j} \qquad 3.9$$

The symmetric *n x n* correlation matrix C (i.e. column-wise for the matrix A) is given by;

$$c = \frac{A' A}{(m-1)} \qquad 3.10$$

The eigenvectors are the space vectors, and the corresponding eigenvalues are measures of the explained variance accounted for by each eigenvector. Decomposition of the correlation matrix into eigenvectors e, and associated eigenvalues λ (Svensson, 1999) uses Equation 3.11 while the eigenvectors are obtained by solving Equation 3.12.

$$(C - \lambda I)e = 0 \qquad 3.11$$

$$|C - \lambda I| = 0 \qquad 3.12$$

Spatial orthogonality and temporal uncorrelation of the PCs impose limits on the physical interpretability of loading patterns (Hannachi *et al.*, 2007). The difficulties associated with interpreting PCAs have led to the development of more tools to overcome this problem. The linear transformation of PCs, based on rotation is one such tool that have been introduced and yielded the concept of Rotated Principle Component Analysis (RPCA) as discussed by Richman (1986). The main purposes of RPCA are to alleviate the strong constraints of PCA. These include orthogonality/uncorrelation of outputs and domain dependence of spatial patterns (Dommenget and Latif, 2002), obtain simple structures, and ease of the interpretation of the obtained patterns.

Rotation of the Empirical Orthogonal Function (EOF) patterns can systematically alter the structures of EOFs. Based on a study by Hansen *et al.* (2008), rotation of EOF has the effect of redistributing the variance within the eigenvectors. Therefore, it removes the ambiguities while conserving the variance extracted by the selected subset of non-rotated eigenvectors (Indeje, 2000). The Rotated Empirical Orthogonal Function (REOF) patterns can be made simple by constraining the rotation to maximize a simplicity criterion

Given a $p \ x \ m$ matrix, U_m= (u1, u2, u3 ...., u_m) of the leading m PCA loadings. The rotation is achieved by seeking an m x m rotation matrix R to construct the REOFs K according to;

$$K = U_m \beta \qquad 3.13$$

Where β is either R or $(R^{T)-1}$ depending on the type of rotation desired. The simplicity criterion for choosing the rotation matrix for maximization problem is expressed by equation 3.14 over a specified subset or class of $m \ x \ m$ square rotation matrices R.

$$\max f \ (U_m \beta) \qquad 3.14$$

Various rotation criteria exist (Richman, 1986) and mainly classified into two families (Jennrich, 2002). It includes an orthogonal in which the rotation matrix is chosen to be orthogonal, and β=R; and oblique in which the rotation matrix is selected to be non-orthogonal and β=$(R^{T)-1}$. In this study, the varimax orthogonal rotation is used as opposed to the Quartimax oblique rotation because rotated PCA yield components that are easier to interpret physically (Gitau *et al.,* 2013). Moreover, by normalizing the spatial eigenvectors to unity, Varimax rotation produces uncorrelated components that satisfy the assumptions of cluster analysis (Phillips and Denning, 2007).

Parallel Analysis (PA) based on Monte Carlo simulations was used to determine the number of the principal components to be retained and rotated (O'Connor, 2000). Parallel analysis is used to simulate a statistical model under the assumption that a given null hypothesis Ho is true (von Storch and Zwiers, 1999). Various studies indicate that PA is an appropriate method to determine the number of factors (Ledesma and Valero-Mora, 2007) as it shows the least sensitivity and variability of different factors.

For this matrix, PCA is computed, and the eigenvalues stored. This procedure was repeated 500 times. All the eigenvalues are ranked and compared at the 95th percentile (95% confidence threshold). As long as the i^{th} eigenvalue from the actual data is greater than the i^{th} eigenvalue from the random data, the components are retained. If the random data eigenvalue is close to the observed eigenvalue, a larger number of replications were run to obtain a more reliable solution. PA was implemented through a MATrix LABoratory (MATLAB) script as shown in Appendix 2

REOF and simple correlation analyzes were used to delineate the homogeneous rainfall sub-regions in East Africa using the quality controlled daily gauge rainfall. The approach utilized in this analysis is similar to the one employed by Indeje (2000). Stations with significant correlation coefficient identified were correlated to each Rotated Principal Component (RPC) time series obtained from REOF analysis. Delineation of a homogeneous sub-region was accomplished by identifying the stations with the largest correlation with the RPC time series associated with the eigenvector of the daily dataset in a season. Maximum factor loadings after rotation that is the correlation coefficients between the variables and factors were used to determine the relation of selected variables (aerosols, clouds, and precipitation).

3.2.1.3 Hovmoller Analysis

Composite analyses are used to assess non-linear relationships especially where simple linear correlation method cannot be applied (Okoola, 1999; Omeny *et al.,* 2008). Composites are useful at indicating common features, trends, and patterns in various variables. This method reduces the number of maps and figures associated with individual cases. Composite analysis enables one to average extreme events with similar characteristics. However, it is a subjective approach and results should not be generalized. It involves identification and averaging of one or more categories of fields of a variable selected according to their association with the main conditions.

Longitude-time (Hovmoller) plots are useful in identifying zonal moving meteorological systems underlying meteorological parameters. It enables inferences of convection and used in the analysis to identify the propagation of intraseasonal convection lies while Latitude –time plots are useful in identifying meridional moving meteorological systems. Composites based on time – longitude sections of OLR was used to examine the evolution and propagation characteristics of clouds variability. The low OLR value ($\leq$ 240Wm^{-2}) was used to indicate areas of active convective periods over the study region.

3.2.2 Relationship between Aerosols, Clouds, and Precipitation

The relationship between aerosols, clouds, and precipitation over EA was investigated using HYSPLIT and Multiple Linear Regression (MLR) analysis. Investigating of weather modification potential in EA involved identification of rainfall season and convective cloud system by use of cloud properties and GHA consensus climate outlook. The pentad calendar was utilized as detailed in Appendix 3.

3.2.2.1 Multiple Linear Regression Analysis

Determination of combined effect of aerosols and clouds on precipitation utilized MLR analysis. The MLR analysis provides insight into how well a set of variables can predict a particular outcome i.e. to determine which variable in a set of variables is the best predictor of an outcome. The MLR first-order models are given as;

$$Y_i = \beta_0 + \beta_1 x_{1i} + \beta_2 x_{3i} + \beta_3 x_{3i} + \cdots + \beta_k x_{ki} + \varepsilon_i \qquad 3.15$$

where, Y_i , β_k and β_0 represent the value of the response variable in the ith observation, the slope parameter associated with the kth variable and the intercept parameter. Moreover, ε_i and x_{ki} represent a random error term with mean $E(\varepsilon_i) = 0$ and variance $\sigma^2\{\varepsilon_i\} = \sigma^2$ with the error terms being independent and identically distributed, and the kth independent variable associated with the ith observation respectively. In MLR, the least squares method is used to find a function that fits a given data. The least squares method minimizes the Sum of the *n* Squared Errors (SSE) of the observed value (y) and the predicted values on the fitted line ($\hat{y}_i$).

$$\sum_{i=1}^{n} (y_i - \hat{y}_i)^2 \qquad 3.16$$

In this study, satellite-derived rainfall estimates are considered as independent variables while aerosols and clouds are the dependent variables. The data included AOD, FMF and CTT at a spatial resolution of $1^{o}\times1^{o}$ while OLR dataset used was at a spatial resolution of $2.5^{o}\times2.5^{o}$. Variables used in MLR were re-gridded to $0.25^{o}\times0.25^{o}$ resolution for comparison purposes. Variable collinearity was detected using Variable Inflation Factors (VIFs) which measure the impact of collinearity on the standard errors of the estimate. Collinear variables offer the same information about the predictand. The square root of VIF shows the inflation of standard error by the other variables in the model. Collinearity was addressed by re-specifying the model i.e. dropping one or more collinear variables. Calculation of VIF is for each independent variable is computed as follows:

$$(VIF_k) = \left(1 - {R_k}^2\right)^{-1} \qquad 3.17$$

In the model, when VIF_k is regressed on the remaining $p-2$ predictors, ${R_k}^2$ represent the coefficient of multiple determination. According to Kutner *et al.* (2004), lower VIF values indicate desirable results since VIF greater than 10 (high levels of multicollinearity) can inflate estimates from least squares. Stepwise variable selection was adopted and involved a combination of both the backward and forward strategies until no changes occur. Model selection utilized Akaike information criterion (AIC). The AIC measures the relative quality of a statistical model, for a given set of data with tradeoffs between the complexity and goodness of fit of the model. The important AIC statistic is calculated as follows:

$$AIC = n\ln\left(\frac{SSE}{n}\right) + 2p \qquad 3.18$$

where, *p* and *n represent* the number of independent variables and observations. AIC aims to balance model complexity and accuracy by finding the minimum value (Akaike 1974). The study utilized AIC with a correction for finite sample sizes i.e. with a greater penalty for extra parameters. The preference arose from the fact that at small sample sizes, it tends to select less complex models. Durbin-Watson (D-W) test statistic was used to assess model independence i.e. the hypothesis of uncorrelated errors based on differences between consecutive residuals. It lies between 0 and 4 and values around 2 indicate independence. Small/large test statistics indicates positive/negative autocorrelation. Model‘s residual normality was checked visually using histograms and/or Quantile-Quantile (QQ) plots. The QQ plots were computed based on Quantile Regression (QR) model (Koenker, 2005),

$$Q_{yi}\langle\tau|x\rangle = \beta_0 + \beta_i x_i + {F_u}^{-1}(\tau) \qquad 3.19$$

where, Q_{yi} is the conditional value of the response variable given τ in the ith trial, is the β_0 intercept, β_i is a parameter, τ denotes the quantile (e.g., τ=0.5 for the median), x_i is the value of the independent parameters in the ith trial, F_u is the common distribution function (e.g.,normal, Weibull, and lognormal.) of the error given τ, $E\left({F_u}^{-1}(\tau)\right) = 0$, for $i = 1, \dots, n$. For example, $\mathrm{F}^{-1}(0.5)$ is the median or the 0.5 quantiles.

For normality, histograms should be symmetrical (bell-shaped) whereas QQ plots should follow a straight line (Koenker, 2005). Wilk-Shapiro test was used to check whether the residuals come from a normal distribution. Small/large p-values signal strong evidence against/for normality. The model's goodness of fit utilized the coefficient of determination, R^2.

3.2.2.2 HYbrid Single-Particle Lagrangian Integrated Trajectory Analysis

Backward trajectories of air parcels passing through the centers of 20 sub-domains were computed using HYSPLIT model. Meteorology data for trajectory calculation utilized NCAR/NCEP global reanalysis data. In the HYSPLIT model, the AOD values are divided logarithmically into 20 bins and regressed against the average of their corresponding precipitation anomalies.

In this study, the model calculation method used is a hybrid between the Lagrangian approach and the Eulerian approach. The Lagrangian approach uses a moving frame of reference as the air parcel moves from their initial location. The Eulerian approach uses a fixed three-dimensional grid as a frame of reference. Calculation of pollutant trajectory was on a fixed grid based archived meteorological data from National Weather Service's National Centers for Environmental Prediction (NCEP). It is archived four times a day at 00, 06, 12, and 18 UTC. NCEP post-processing of the GDAS converts data from the spectral coefficient form to 1 degree latitude-longitude (360×181) grids. It also converts data from sigma levels to mandatory pressure levels. HYSPLIT Model output is in GRIdded Binary (GRIB) format.

The model computed the puff or advection of a particle from the average of the three-dimensional velocity vectors at the initial position, P(t) and first-guess position, P'(t+Δt). Linear interpolation of velocity vectors in both space and time is used. Equation 3.20 gives the first guess position.

$$P'(t+\Delta t) = P(t) + V(P, t)\,\Delta t \qquad 3.20$$

The final position is

$$P(t+\Delta t) = P(t) + 0.5V(P, t) + V(P', t+\Delta t)\,\Delta t. \qquad 3.21$$

During the simulation, the integration time step (Δt) can vary. Advection distance per time-step should be less than the grid spacing in all computation. Trajectory analysis uses integration method (Kreyszig 1968). Greater precision cannot be achieved using higher order integration methods due to the linear interpolation of data from the grid to the integration point. If the trajectories exit the meteorological data grid, they are usually terminated. However, advection continues along the surface if trajectories intersect the ground.

For back trajectory analysis, the one (1), two (2) and three (3) day back trajectories starting with 1500 or 3000 m heights was calculated. These typical heights have been justified in the preliminary CALIPSO results in Huang *et al.* (2009b). Starting points was identified at the centre of 20 sub-grids within the tropical East Africa domain and used to conduct back trajectory analysis from each centre. For each sub-grid on each calendar day, precipitation anomalies were marched with the upwind aerosol at the endpoints of the 1-day, 2-day and 3-day back trajectories. Section 2.6.1.8 discusses other details of HYSPLIT model.

3.2.2.3 Identification of Weather Modification Conditions

Investigation of potential weather modification in EA required identification of rainfall season and convective cloud system.

3.2.2.3.1 Identification of Suitable Season for Weather Modification

MAM and OND constitutes an important rainfall season over EA. Further, the OND and MAM rainfall seasons are directly linked to the movement of ITCZ Southward and Northward

(Nicholson, 1996). Mwangi *et al.* (2014) indicated that GHA experienced two major droughts in the last decade (2008–2009 and 2010–2011) resulting in humanitarian crises.

3.2.2.3.1.1 Greater Horn of Africa Consensus Forecast Analysis

The consensus forecast (map showing the probability of rainfall) developed at the GHA Climate Outlook Forum (GHACOF) consensus forecast was used to identify suitable season for precipitation enhancement. The numbers for each zone in the GHACOF map show the likelihood of rainfall in each of the three categories (Patt *et al.*, 2007; Mwangi *et al.* 2014). The three categories comprise of Above-Normal (AN), Near-Normal (NN) and Below-Normal (BN). The process used to develop the consensus forecast used in GHACOF are detailed in Mwangi *et al.* (2014). . It should be noted that the regional GHA consensus map during the climate outlook forum are usually issued for MAM, June-July-August (JJA), September-October-Novemeber-December (SOND) and December-January-February (DJF). Therefore, the major rainfall seasons (MAM and OND) for 2009, 2010, 2011 and 2012 are utilized in the study

3.2.2.3.1.2 Verification of Seasonal Forecast

The study assessed the quality of GHA consensus forecast using the contingency table (Wilks, 2006; Skripnikova, 2013). According to Wilks (2006), the contingency table is based on the joint distribution of the observations and forecast. The Table 3-2 shows a 3×3 the contingency table used in the study. The entries are observed and forecast precipitation.

Table 3-2: A 3×3 contingency table for the verification of consensus forecast

	Forecast				
Observed		BN	NN	AN	M-Totals
	BN	a	b	c	a+b+c
	NN	d	e	f	d+e+f
	AN	g	h	i	g+h+i
	M-Totals	a+d+g	b+e+h	c+f+i	n=a+b+c+d+e+f+g+h+i

The letters a-i in the contingency table shows the correspondence, or relationship, between the observed and forecast pairs and their absolute marginal totals. The letters *a*, *e* and *i* are the hits, while *b*, *d*, and *g* represents the misses. The letters *c*, *f* and *h* represents the false alarms. The contingency table verification scores include False Alarm Ratio (FAR), Hit Rate and Critical Success Index (CSI) (Betschart and Hering, 2012; Skripnikova, 2013). Other include Heidke Skill Score (HSS) and Bias (B).

i. Hit Rate

The Hit rate or Probability of Detection (POD) corresponds to the ratio of the forecast (hit) to the total number of observations on the ground. The Hit rate is given by equation 3.22;

$$\mathrm{H} = \frac{\mathrm{hits}}{\mathrm{hits} + \mathrm{misses}} \qquad 3.22$$

A high POD means an accurate forecasted precipitation observed on the ground. On the contrary, a low Hit rate indicates that the forecast does not capture the observed.

ii. False Alarm Ratio

The FAR is a corresponds to detections that turn out to be wrong or without any truth (false alarms) i.e.

$$\mathrm{FAR} = \frac{\mathrm{false\ \ alarms}}{\mathrm{hits} + \mathrm{false\ \ alarms}} \qquad 3.23$$

A high FAR values indicate that the consensus forecast do not correspond to the observed. Worth noting, lack of ground truth data results in distortion of the output as high FAR could imply that the forecast are not correct (Wilks, 2006).

iii. Critical Success Index

CSI is a useful index utilized when the forecasted event occurs less frequently than the non-occurrence (Wilks, 2006). It is a simple index used to characterise the accuracy of the forecast. The CSI corresponds to the number of the correct forecasts (hit) divided by the total number of cases/events observed (hit, false alarms, missed). The CSI is given by equation 3.24.

$$\mathrm{CSI} = \frac{\mathrm{hits} + \mathrm{correct\ \ negatives}}{\mathrm{Total}} \qquad 3.24$$

The CSI ranges between 0 and 1 with 1 being the best score and 0 the worst score.

iv. Bias

Bias (B) measures the relationship between the average forecast and the mean observation (Wilks, 2006). It corresponds to the ratio of the positive forecast to the positive observations as defined in equation 3.25.

$$B = \frac{\text{hits} + \text{false alarms}}{\text{hits} + \text{misses}} \qquad 3.25$$

A Bias of 1 means that the forecast is unbiased and that the event was detected the same number of times it was observed. Notably, Bias does only give overall information based on the dataset. A Bias value greater than 1 indicates more forecast cases than observations i.e. overestimation. Conversely, Bias values less than 1 indicates less forecast than observations i.e. underestimation of observed precipitation.

v. Heidke Skill Score

Heidke Skill Score indicates the proportion correct achieved by a random forecast that are statistically independent of the observations (Wilks, 2006). The HSS has the following form:

$$\text{HSS} = \frac{2(aei - ceg)}{(a+d+g)(b+e+h)(c+f+i) - (a+b+c)(d+e+f)(g+h+i)} \qquad 3.26$$

An HSS value of 1, 0 and -1 indicates a perfect forecast, forecast equal to the observed and a forecast worse than the observations respectively.

3.2.2.3.2 Identification of Deep Convective Clouds

Identification of DCCs followed International Satellite Cloud Climatology Project (ISCCP) cloud classification criteria based on COD and CTP (Figure 3.2).

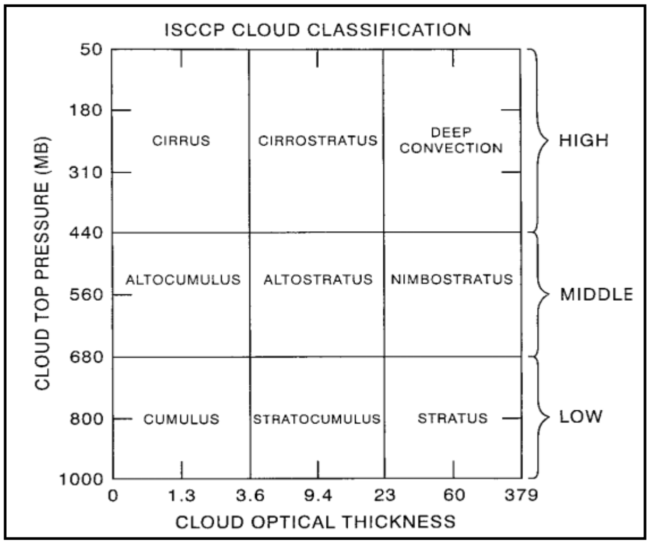

Figure 3-2: New cloud-type definitions used in the ISCCP D-series datasets for daytime (Rossow and Schiffer, 1999).

Liquid and ice types can result from low and middle cloud types while all high clouds are ice. Night time cloud types are low, middle, and high, as indicated on the right (Rossow and Schiffer, 1999). Based on Rossow and Schiffer (1999) classification criteria, CTP values of greater than 440 MB and COD values of greater than 23 were identified as deep convection. Daily CAPE at the surface was used to evaluated the stability of the atmosphere. The updraft depends on the CAPE environment. Therefore, positive values ranged between 1-1500 J/kg while large values ranged between 1500 J/kg to 2500 J/kg. Extreme CAPE values were above 2500. According to Rossow and Schiffer (1999), CAPE increases (especially above 2500 J/kg) results in a rise in the hail potential. Large hail requires large CAPE values. Intense updraft produces intense downdraft. Notably, the intense updraft condenses out a large amount of moisture. Large and extreme CAPE will produce storms with abundant lightning.

3.2.3 Evaluation of WRF Microphysics to Simulations of Deep Convective Cloud System

The WRF model is used to simulate features associated with DCCs. In this study, it was aimed at examining the effectiveness of Morrison double moment bulk microphysics (Appendix 4) in the cloud-resolving model in simulating convective cloud system.

Bulk Microphysics enables the prediction of two moments (i.e. both number concentration and mixing ratio). It is the most robust treatment of the particle size distributions and key in computing cloud/precipitation evolution and microphysical process rates. Morrison double moment microphysics scheme (Morrison *et al.*, 2009) is a double moment mixed-phase cloud microphysics parameterization scheme predicting mixing ratio and number concentration of the 6-class water substance variables.

Prognostic variables comprise number concentrations and mixing ratios of rain, cloud ice, snow and graupel or hail and mixing ratios of water vapour and cloud droplets. The gamma distribution explains the cloud droplet size distribution and the other remaining hydrometeor particles are assumed to follow the Marshell–Palmer size distribution (i.e. inverse exponential distribution) (Morrison *et al.*, 2005). As the scheme does not explicitly predict CCN concentration, aerosols concentration and characteristics can be prescribed (Morrison *et al.*, 2009). Droplet activation occurs as a function of the grid and sub-grid scale vertical velocity.

For model simulations, configuration with two nested domains of 25 km and 10 km grid spacing defined on a Mercator projection for all the selected cases was used. The WRF model utilized a standard set up. The study adopted Tao *et al.* (2007) and Morrison (2012) subgrid-scale (TKE) 1.5 turbulence closure. BMJ Cumulus parameterization scheme (Rajeevan *et al.,* 2010) was used while periodic boundary conditions applied to the horizontal boundary. Radiation utilized the RRTM long-wave scheme. The RRTM long-wave scheme is a spectral band radiative transfer model using the Dudhia (1989) shortwave scheme and correlated K-method (Mlawer *et al.*, 1997). For the land surface process, RUC Land Surface Model scheme was used (Ek *et al.*, 2003).

WRF model initialization and boundary conditions utilized NCEP FNL data. The model was initialized for three simulations at 1200 UTC on 20, 23 and 25 May 2012 and integrated for 36 hours each. Integration time step was set to 60s. Low-level convergence in these simulations takes some time to spin up from the large-scale circulation due to lack of storm data in the initial conditions. Therefore, the models are not reliable for at least the first 6 hours (Wilson *et al.*, 1998). For analyzing surface observed features of DCCs, simulated results from Morrison Two-Moment Scheme was compared to TRMM satellite derived daily rainfall..

3.2.4 Effects of Cloud Seeding on Precipitation Enhancement

In this study, numerical simulation of effects of cloud seeding on precipitation enhancement was based on MAM 2012 season. Simulation based on Morrison scheme was designed to investigate aerosol effects by changing the initial value of the CCN number concentration.

For model simulations, basic set up as described in section 3.2.3 are used. The grid in both directions comprised 120 points with ~3 km grid spacing defined on a Mercator projection was used. The number of vertical layers was 40. Cloud-resolving utilized explicit convection in the 3 km grid spacing (innermost domain). The model was initialized at 1200 UTC on 20th , 22nd and 24th May 2012 and integrated for 36 hours. Integration time step was set to 60s.

Effects of initial aerosol concentrations on the DCCs was evaluated based on microphysical properties, precipitation, and convective strength by varying the number and mass of aerosols. The study defined the cumulus cloud core as the area with the absolute vertical wind speed greater than 1 ms^{-1}. Moreover, the area has a total condensed water mixing ratio greater than 0.01 gkg^{-1} and absolute vertical wind speed greater than 1 ms^{-1} (Li *et al.* (2008). These effects reflected in the changes in the number concentrations of CCN and CDNC. Initiation of simulations utilized five different initial CCN scenarios of 100, 500, 1000, 2000 and 3000 cm^{-3} and CDNC of 200, 400, 800, 1600 and 2000 cm^{-3}. The Table 3-3 shows a summary of aerosol scenario adopted in the study.

Table 3-3: Summary of aerosol scenarios adopted in the study

Parameters	Quantity (cm^{-3})	Scenario	Remark
CDNC	200	CDNC200	Low
	800	CDNC800	Intermediate
	2000	CDNC2000	High
CCN	100	CCN100	Low
	1000	CCN1000	Intermediate
	3000	CCN3000	High

3.3 Limitation for the Study

In this study, analysis are based MAM and OND season that are considered as significant in EA. Inadequate observed datasets necessitated the use of satellite-derived estimates of aerosols, clouds and precipitation. The satellite datasets used spanned the period 2001 and 2012. The limited length of available satellite data (12 years) constrained robust analysis of time series components (trend and seasonality). The retrieved satellite-based datasets had different spatial resolutions necessitating use of re-gridding techniques to enhance their comparability.

CHAPTER FOUR

4 RESULTS AND DISCUSSION

This chapter presents results and discussion of spatial-temporal variability and relationship of aerosols, clouds and precipitation. It also presents a detailed evaluation of the efficiency of the cloud-resolving model in simulating precipitation and numerical simulation study on the effects of aerosols on clouds and precipitation modification.

4.1 Spatial and Temporal Variability of Aerosols, Clouds and Precipitation

Spatial and temporal variability of aerosols, clouds and precipitation were mainly determined using PCA and time series (trend and seasonality) analysis. Determination of trend and seasonality utilized Mann-Kendall rank statistic and CoV respectively. Determination of zonal and meridional movement of features associated with aerosols, clouds and rainfall over time was achieved through Hovmoller analysis.

4.1.1 Time Series Analysis

The time series analysis included both trend and seasonality.

4.1.1.1 Trend Analysis

The Figure 4-1 to Figure 4-5 presents the trend of aerosols, clouds and precipitation determined by Mann-Kendall statistic. Appendix 5 provides detailed Mann-Kendall rank statistics analysis.

In Figure 4-1 (a), AOD showed significant trend ($\alpha=0.05$) during MAM in Northern Tanzania towards Mt. Kilimanjaro. It extended Central areas of Kenya over Eastern Mt. Kenya, Eastern Uganda along Lake Victoria and Northern Uganda. However, OND season (Figure 4-1 b) indicated a significant trend ($\alpha=0.05$) over SW Tanzania, Northern Kenya around Marsabit and Eastern Uganda (around Lake Victoria), Northern Uganda and Coastal Tanzania.

During MAM, Western EA indicated a significant trend ($\alpha=0.05$) of FMF. These areas included Rwanda, Burundi, Western Uganda, parts of Tanzania (Figure 4-2 a) and Kenya (NE, Central and Eastern) (Figure 4-2 a). During OND season, significant trend ($\alpha=0.05$) in FMF were observed over Northern EA region and western Tanzania (Figure 4-2 b).

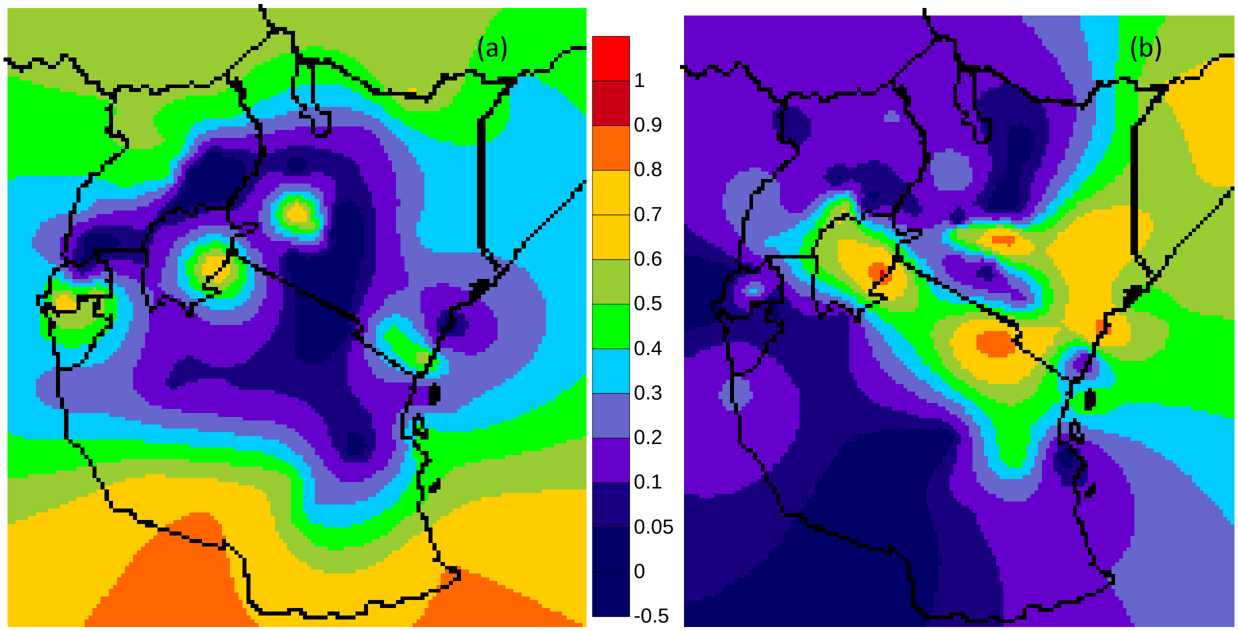

Figure 4-1: Trend of AOD during a) MAM and b) OND over EA (2001-2012)

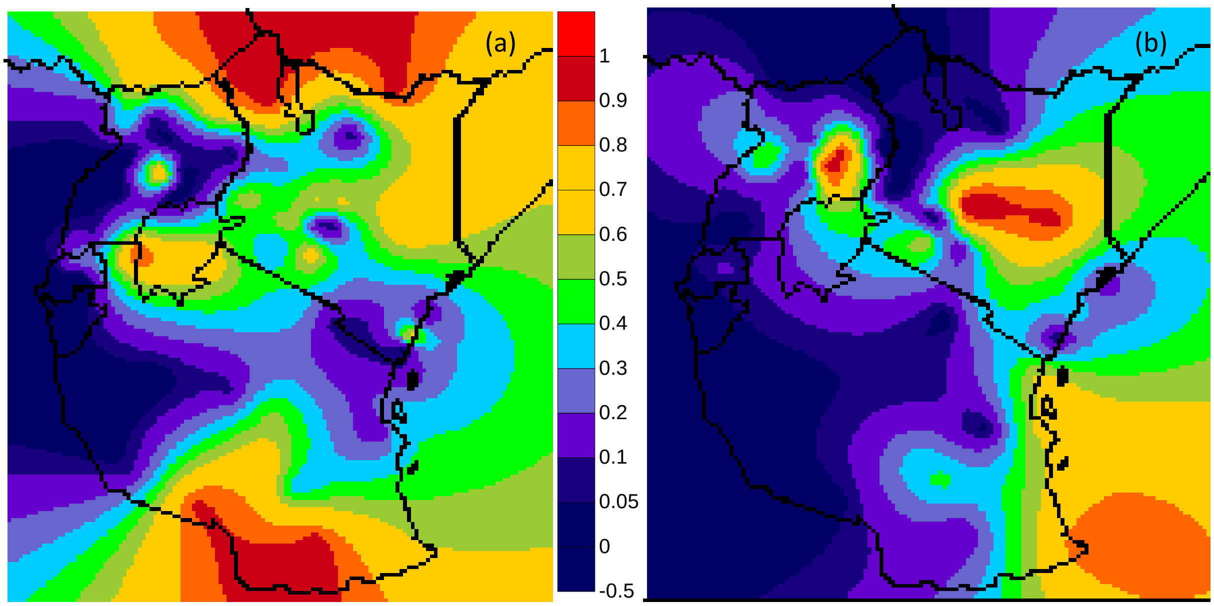

Figure 4-2: Trend of FMF during a) MAM and b) OND over EA (2001-2012)

During MAM season, a significant trend (α=0.05) of CTT was noted in Kenya over South, West and Northern regions with Uganda being in Central and Western Uganda (Figure 4-3 a). At 95% significant level, a trend existed during OND season over central parts of Kenya, Northern Uganda, and Southern Tanzania (Figure 4-3 b). The EA region indicated a significant trend (α=0.05) in OLR except NE Kenya during MAM (Figure 4-4 a), and Northern Kenya, Uganda, and southern Tanzania during OND season (Figure 4-4 b). The coarse resolution of OLR data used at a resolution of 2.5^{o} x 2.5^{o} explained the uniformly distributed values in EA.

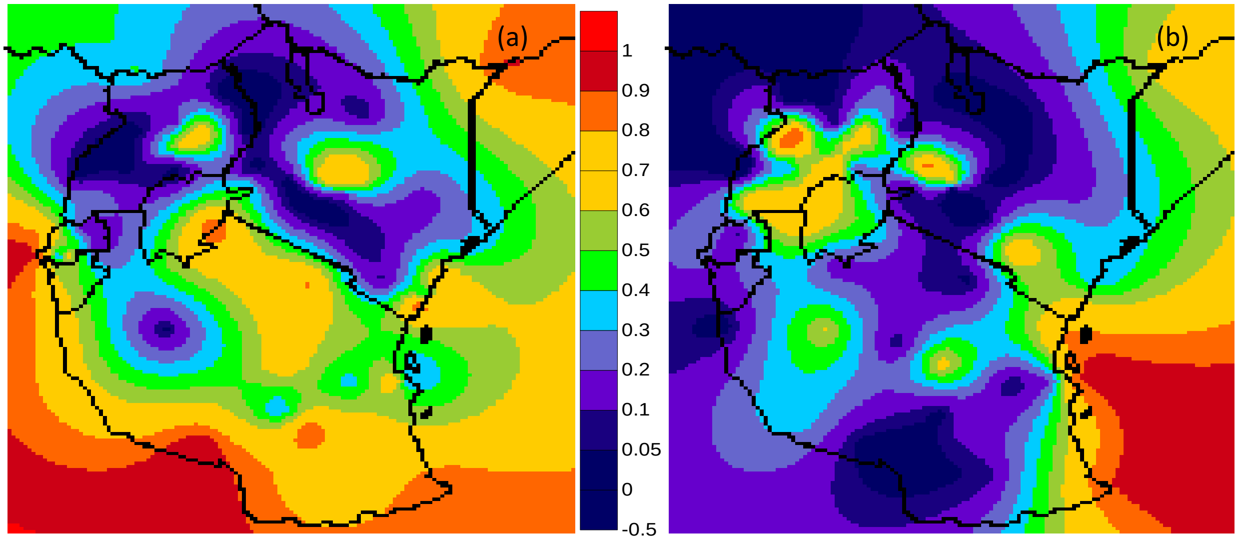

Figure 4-3: Trend of CTT during a) MAM and b) OND over EA (2001-2012)

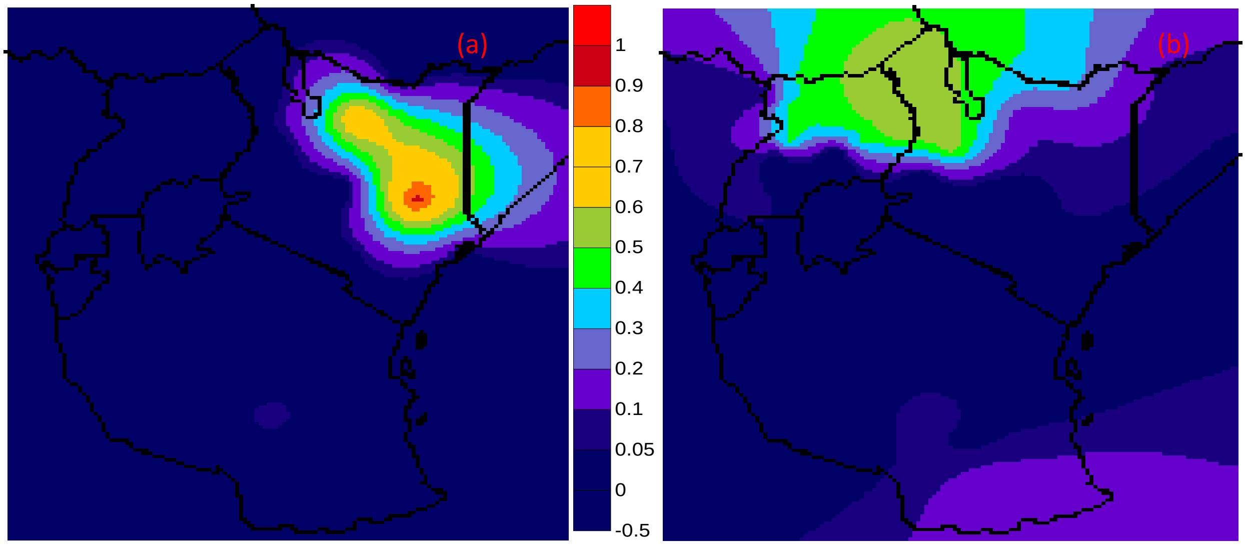

Figure 4-4:Trend of OLR during a) MAM and b) OND over EA (2001-2012)

Daily TRMM rainfall showed a significant positive trend (α=0.05) in rainfall over several areas in EA during MAM (Figure 4-5 a) and OND (Figure 4-5 b). The areas included coastal (Mombasa), SW Kenya, Lake Victoria basin (Kakamega), Coastal Tanzania (Dar es Salaam) and

South-western Indian Ocean. During OND, the areas included the Coast of EA, Rwanda and Burundi with few continental areas of Western Tanzania, Kakamega, Kitale, Marsabit, Nyeri Kigoma and Morogoro. The results of this study is affirmed by Shongwe *et al*. (2010) which noted increased frequency of anomalously strong rainfall causing floods during both MAM and OND almost everywhere in EA.

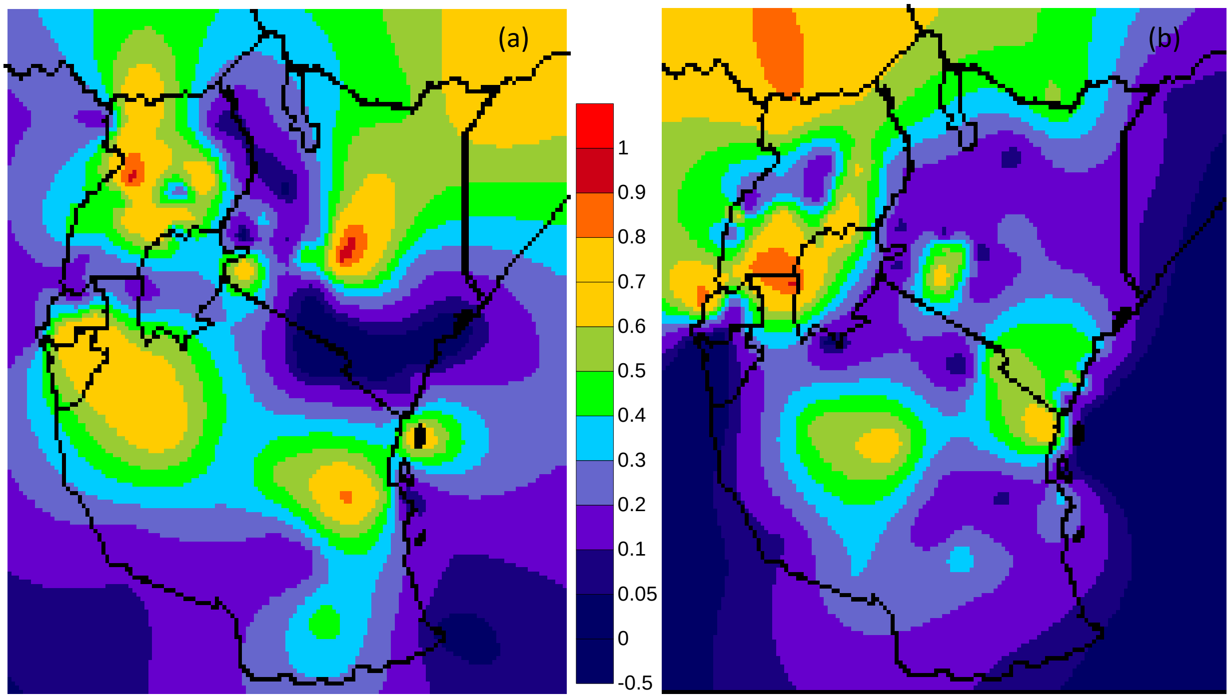

Figure 4-5: Trend of TRMM during a) MAM and b) OND over EA (2001-2012)

4.1.1.2 Seasonal Mean Analysis

Seasonality of aerosol, clouds and precipitation was based on the daily Mean and CoV.

4.1.1.2.1 Diurnal Mean

The Figure 4-6 to Figure 4-9 presents results of diurnal mean variation aerosols, clouds, and precipitation.

In Figure 4-6 (a), the average spatial pattern of mean AOD showed a higher distribution of coarse aerosols of up to 0.34. The areas included Northern Kenya, and Western parts of EA region over Rwanda, Burundi, and parts of Uganda. Lower mean AOD values of 0.1 over

Western, NE, and Central Kenya indicated clear and unpolluted skies. In many areas of EA, the study assumes that the mean AOD values of less than 0.22 during both MAM (Figure 4-6 a) and OND (Figure 4-6 b) maybe as a result of the rainout and washout precipitation processes that led to a reduction in the concentration of aerosols acting as CCN. Muthama (2003) indicated that dispersion of clouds occurs through either fall out as precipitation or evaporation. Further, it has been suggested that there exist a strong positive feedback where precipitation removes aerosol, leading to a more efficient formation of precipitation (Sharon *et al*., 2006; Stevens and Savic–Jovcic 2008; Wang and Feingold 2009a). The Southern Tanzania recorded smaller AOD values (less than 0.16) while Northern and Western EA recorded higher mean aerosol due to dust brought from the Northern hemisphere especially from Sahara Desert. Other studies e.g. Eck *et al.* (2010), Krishnamurti *et al*. (1998) and Li and Ramanathan (2002) indicated that the NH was an active source region. The locations included Sudanian zones of Northern Africa and the Sahel, Arabian Desert, Arabian Sea, Arabian Peninsula and India subcontinent.

The distribution of AOD explains the enhanced rainfall especially over Western, Central and NE Kenya, and Southern Tanzania as they act as CCN during rainfall formation processes.

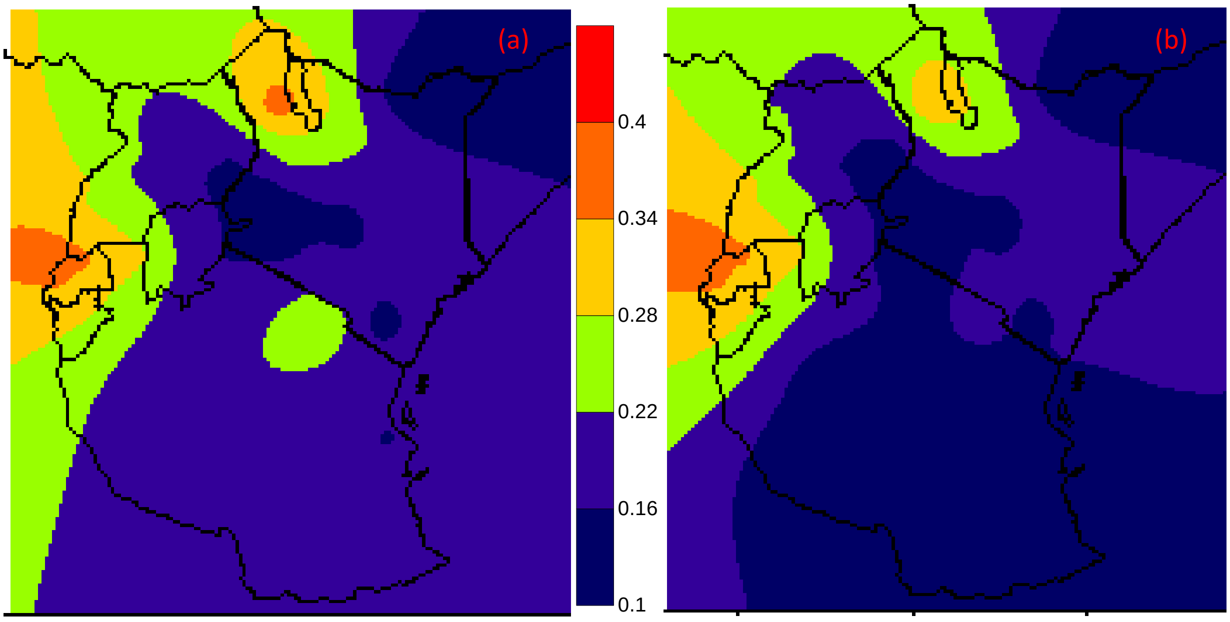

Figure 4-6: Spatial pattern of the mean aerosol based on AOD for a) MAM and b) OND (2001-2012)

During both MAM (Figure 4-7 a) and OND (Figure 4-7 b) season, lower AOD values of less than 0.2 are observed over Northern Kenya and parts of Southern Tanzania. Further, SW Uganda, Rwanda, Southern Tanzania and coastal Kenya (Mombasa) indicated high FMF values. FMF dominated Central and Northern Kenya during MAM. The pattern progressed northwards towards NE Kenya, an indication that FMF aerosols were less affected during the rainfall season. Therefore, reduction of FMF aerosols could be attributed to natural processes such as deposition through gravity as they could not act as CCN during rainfall formation. According to Eck *et al.* (2010), the combination of combustion sources such as vehicle emission, biomass burning of wood fuel and industrial emissions result in the production of fine mode aerosols.

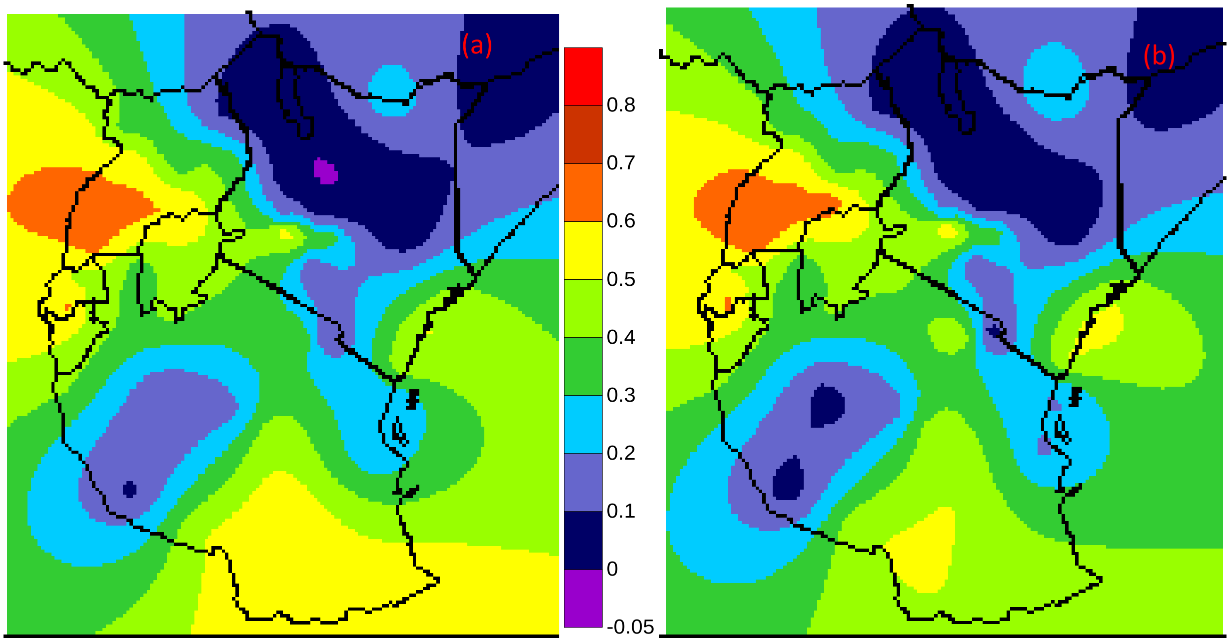

Figure 4-7: Spatial pattern of the mean aerosol based on FMF for a) MAM and b) OND (2001-2012).

During MAM season, spatial patterns of mean CTT indicated that temperatures were higher over the Eastern EA with a decreasing temperature gradient westward (Figure 4-8 a). This CTT pattern was noted to shift Northwards during OND season (Figure 4-8 b). Orville *et al*. (2004) observed that cloud water droplets can remain unfrozen at temperatures well below freezing in the atmosphere and the laboratory have shown that. According to Cotton and Pielke (1995), cloud seeding window depended on clouds with relatively cold-based, continental and CTT ranging between -10 and -25^{o}C. Therefore, this study indicates that stations located over Eastern and Western EA region with mean temperatures greater than -10°C were unsuitable for cloud seeding activities. However, areas located over central EA region and mainly adjacent to the Rift Valley and coastal Tanzania were noted as suitable locations with optimal temperatures for cloud seeding.

During MAM season, mean daily precipitation was high in over central Kenya, Lake Victoria Basin and coastal Tanzania with values of more than 4.5mm (Figure 4-9 a). Compared to rainfall during OND season (Figure 4-9 b), mean rainfall received during MAM season was higher than OND season. Mutai and Ward (2000) linked the wet spells in EA to synoptic disturbances that migrate eastwards into EA region in association with westerly near-surface wind anomalies.

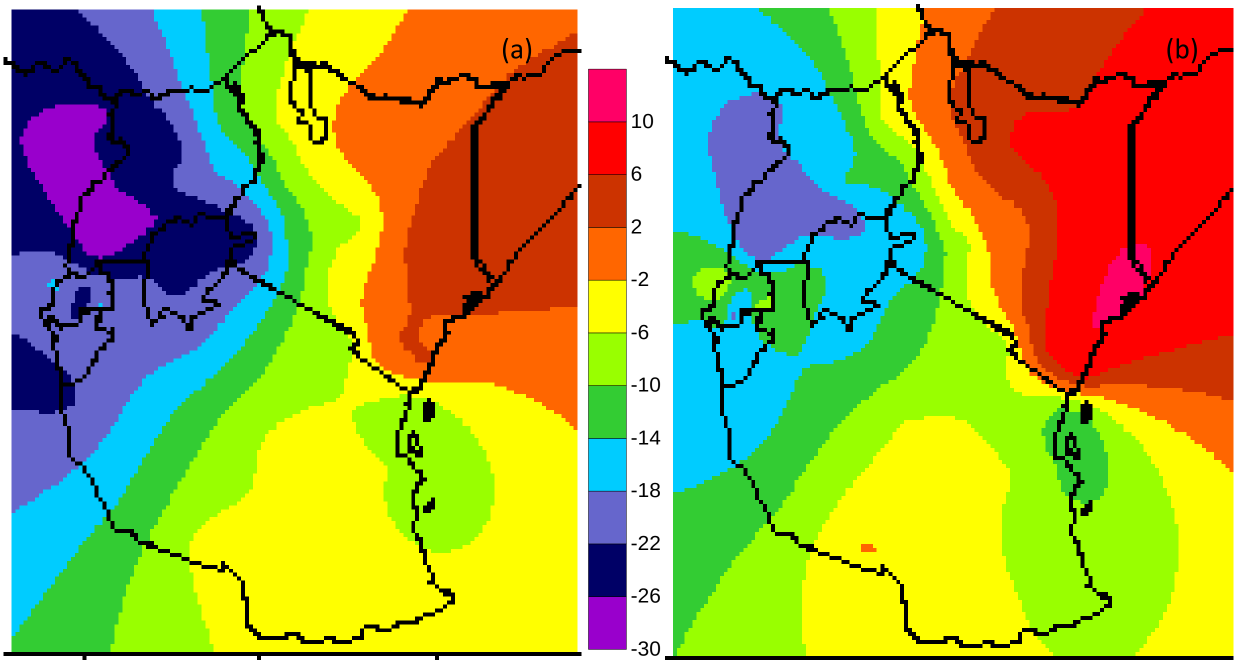

Figure 4-8: Spatial pattern of the mean clouds based on CTT for a) MAM and b) OND (2001-2012)

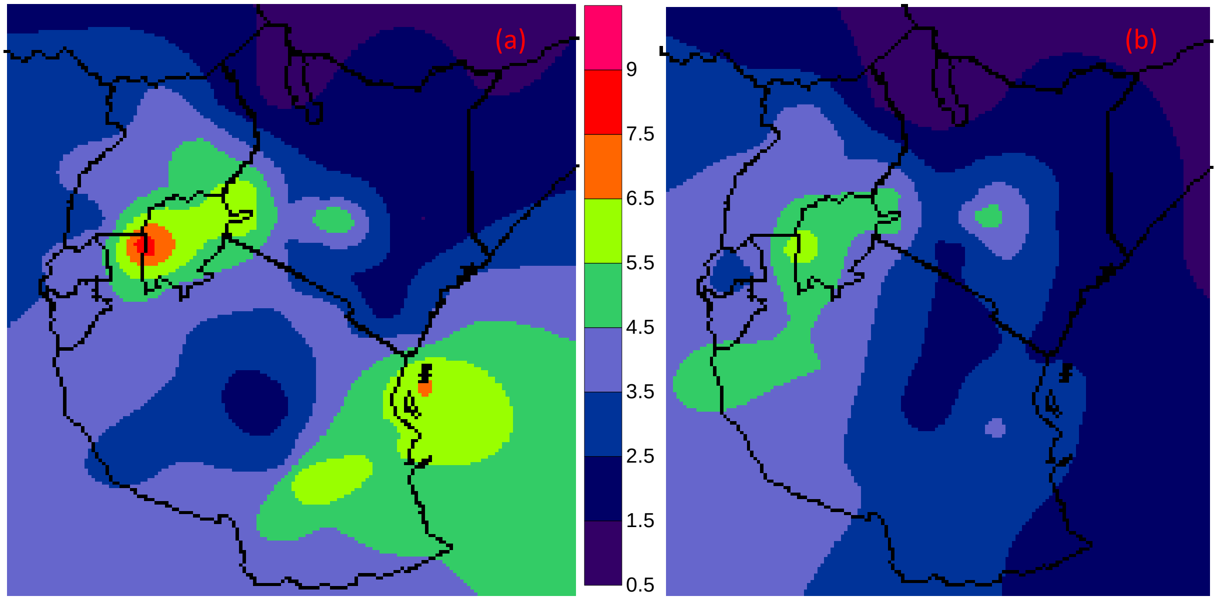

Figure 4-9: Spatial pattern of daily precipitation based on TRMM (3B42) for a) MAM and b) OND (2001-2012)

4.1.1.2.2 Seasonal Variation

The Figure 4-10 to Figure 4-14 presents the analysis based on the CoV for aerosol, clouds and precipitation.

During MAM season, AOD underwent highest diurnal variability over western parts of Kenya, Eastern Uganda, Northern Uganda, central Tanzania and the coast of Tanzania (Figure 4-10 a). The CoV values were above 0.7. During OND season, regions adjacent to rift valley from Southern Tanzania towards Kenya and Northern Uganda had the highest variability in AOD values of 0.6 (Figure 4-10 b). During MAM season, Northern Kenya showed highest FMF variability especially over Lodwar with CoV values greater than 4.8 (Figure 4-11 a). Over the Eastern and NE areas of Kenya, CoV values were of greater than 2.6 (Figure 4-11 b). However, higher variability of FMF over Lodwar was not significant since mean values over Lodwar was low with FMF values of less than 0.1 (as shown in Figure 4-11). In general, FMF varied highly during MAM compared to OND.

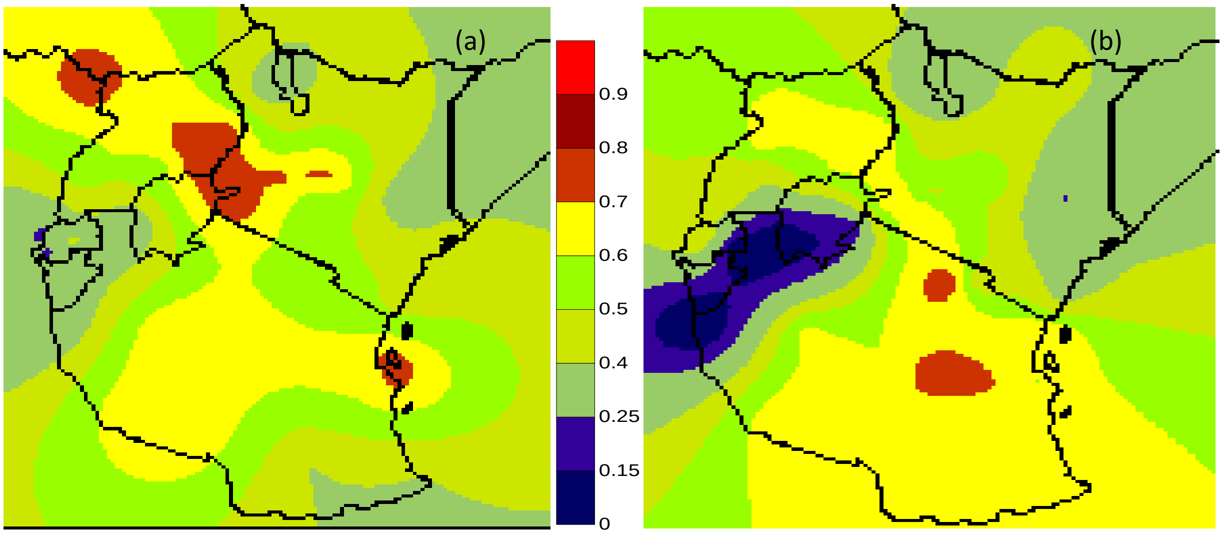

Figure 4-10: Coefficient of Variation based on AOD for a) MAM and b) OND (2001-2012)

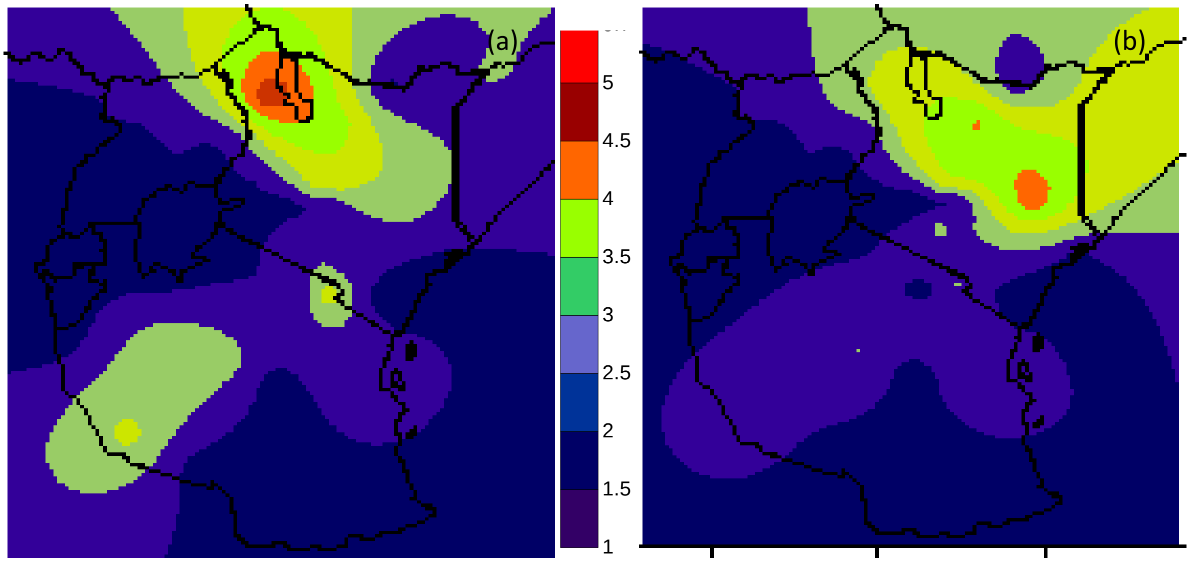

Figure 4-11: Coefficient of Variation based on FMF for a) MAM and b) OND (2001-2012).

The CoV for CTT was noted to be higher over north-western parts of Kenya and Uganda with MAM season (Figure 4-12 a) indicating higher variability of CTT than OND season (Figure 4-12 b). OLR variability was noted to be higher in SW Tanzania and NW Uganda during MAM season (Figure 4-13 a). Comparative analysis indicated that OLR was greater in MAM than OND (Figure 4-13 b). In EA (part of the tropics) Arkin *et al.* (1989) showed that CTT largely modulated OLR with areas of intense convection represented by low OLR values while cloud-free locations appear as areas of high OLR. Although continuous measurement of OLR has greatly bridged an existing gap in conventional meteorological observations over large remote oceanic and land areas (Tazalika, 2003), interpreting OLR signature requires much caution since there are instances whereby high clouds may be a result of convective clouds. According to Lyons (1990). The discrepancy may be resolved through improving the resolution of the current OLR data.

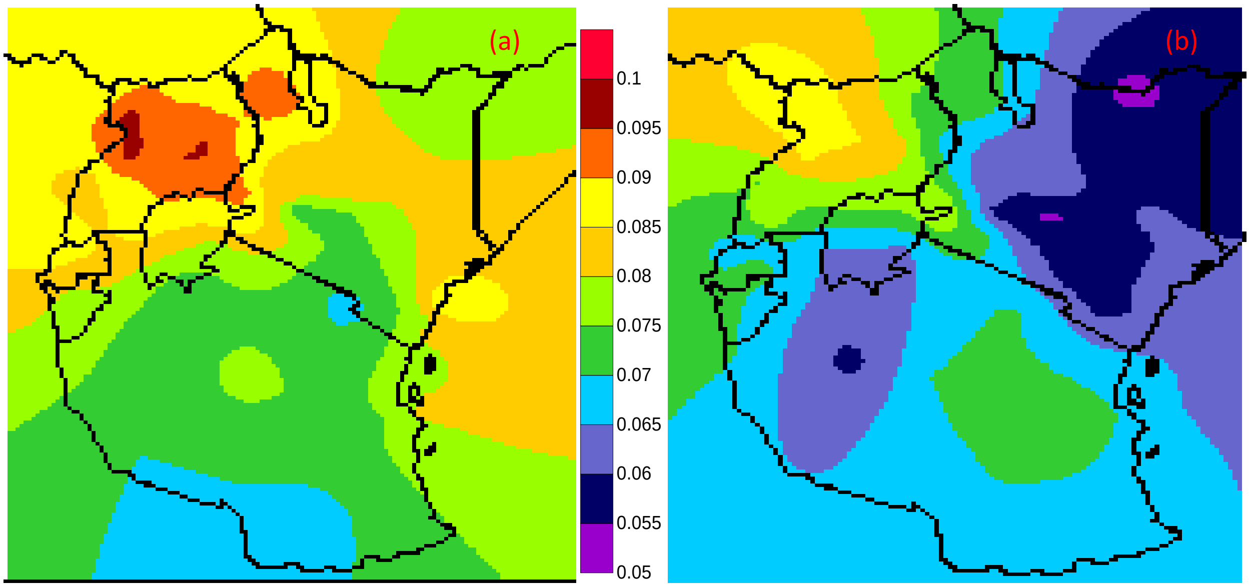

Figure 4-12: Coefficient of Variation based on CTT for a) MAM and b) OND (2001-2012)

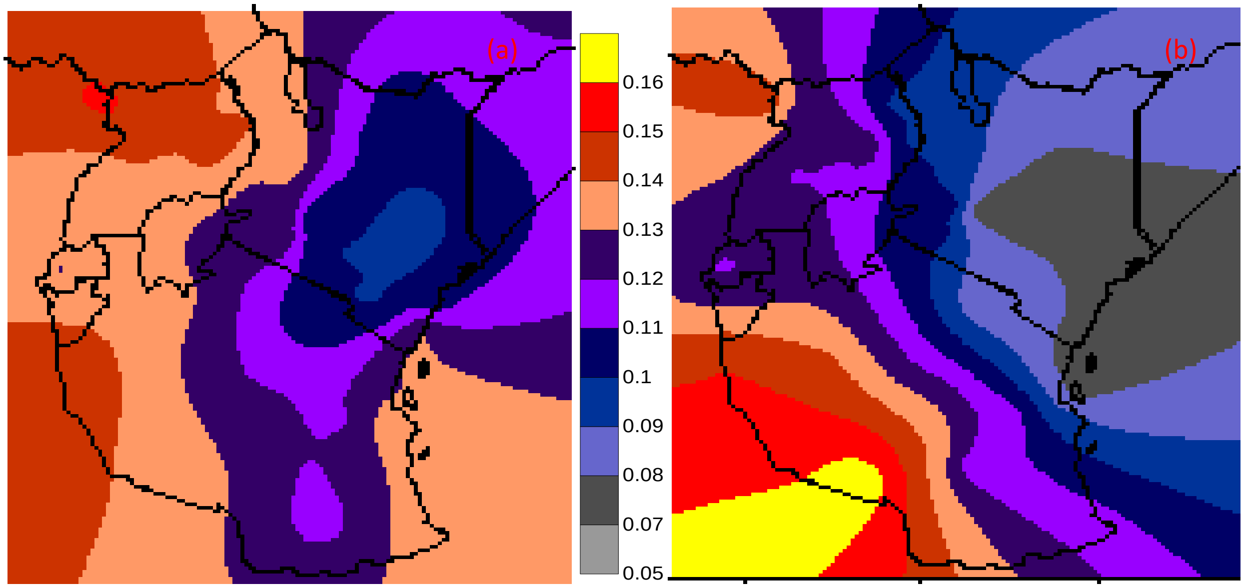

Figure 4-13: Coefficient of Variation based on OLR for a) MAM and b) OND (2001-2012)

Satellite-derived rainfall estimates from TRMM indicated highest variability over northern and NW parts of Kenya during both MAM (Figure 4-14 a) and OND (Figure 4-14 b) season. The areas located in arid conditions in EA had highest rainfall variability. The high spatial and temporal variability of precipitation in EA affirms studies by Gitau *et al*. (2013) and the IPCC assessments (IPCC, 2007, IPCC, 2013). Effects of the high variability in precipitation are already being manifested in many terrestrial water sources (Bates *et al*., 2008; Majone *et al*., 2012; IPCC, 2014) and linked with climate (Kundzewicz *et al*., 2007). According to Levin and Cotton (2009), the observed variability is expected to affect availability of fresh water and thus the quality of human life. In EA, processes and systems that control rainfall include synoptic and mesoscale flows as well as their interaction (Mukabana and Pielke, 1996; Rosell and Holmer, 2007; Hession and Moore, 2011). Other processes include Indian Ocean SST (Saji *et al*., 1999; Owiti *et al*., 2008), IOD index (Owiti *et al*., 2008), ENSO (Schreck and Semazzi, 2004; Semazzi and Indeje, 1999; Schreck and Semazzi, 2004; Trenberth, 1997) and MJO (Pohl and Camberlin, 2006) and ITCZ (Okoola, 1999; Asnani, 2005)

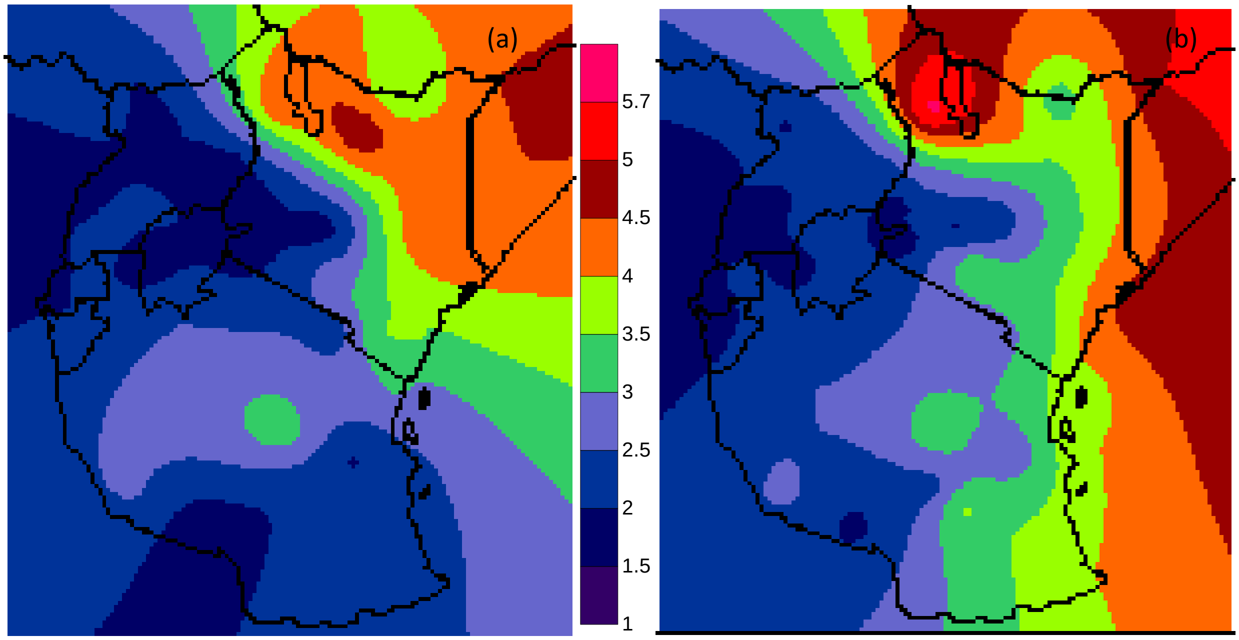

Figure 4-14: Coefficient of Variation based on TRMM (3B42) for a) MAM and b) OND season (2001-2012)

4.1.2 Principal Component Analysis

PCA was used to cluster the study region into homogeneous zones and evaluate the contribution of selected variables.

4.1.2.1 Identification of Homogeneous Zones

In this study, parallel analysis (Monte Carlo Simulation) was used to select significant PCs used to cluster satellite derived aerosols, cloud and precipitation in EA region into near homogeneous zones. The Table 4-1 presents results for the optimum number of the principal component retained based on aerosols, clouds and precipitation datasets. Detailed analysis to investigate the variability explained by the number of significant PCs retained for aerosols, clouds and precipitation is presented in Figures 4-15 to Figure 4-19. Appendix 6 shows detailed PCA of EA into near homogenous zones.

Table 4-1: Number of Significant PCs Retained for Aerosols, Clouds and Precipitation

Parameter	**Dataset**	**MAM season**	**OND season**
Aerosol	AOD	13	14
	FMF	20	18
Clouds	CTT	11	10
	OLR	9	10
Precipitation	TRMM	16	17

The PCA analysis yielded 13, 20, 11, 9 and 16 PCs during MAM for AOD, FMF, CTT, OLR and TRMM 3B42 respectively (Table 4.1). Similarly, PCA analysis yielded 14, 18, 10, 10 and 17 PCs during OND for AOD, FMF, CTT, OLR and TRMM 3B42 respectively (Table 4.1). The identified PCs were found to be significant at 95% confidence level based on Monte Carlo testing. Notably, OLR dataset had lower optimum significant PC and attributed to the course resolution (2.5^o x 2.5^o) of the datasets used. The number of significant PCs retained based on TRMM 3B42 for both MAM and OND were higher compared to other studies. For example, Gitau *et al.* (2013) found six PCs in both MAM and OND season using observed daily rainfall. The differences in retained PCs point to the different atmospheric dynamics responsible for the behaviour of climate during the various seasons of the year and spatial coherence arising from both inter-annual and intra-seasonal variability. Further, the use of seasonal and annual totals provides information on inter-annual variability only. However, Ininda (1995) showed that results from the monthly analysis were better during the prolonged rainfall due to high variability. Indeje (2000) classified the entire EA region into eight and nine near homogeneous zones based on the annual and seasonal observed rainfall respectively.

Based on AOD, Figure 4-15 shows that 13 and 14 significant PCs accounted for 67.5% and 67.8% of the total variability over the EA region during MAM and OND rainfall seasons respectively.

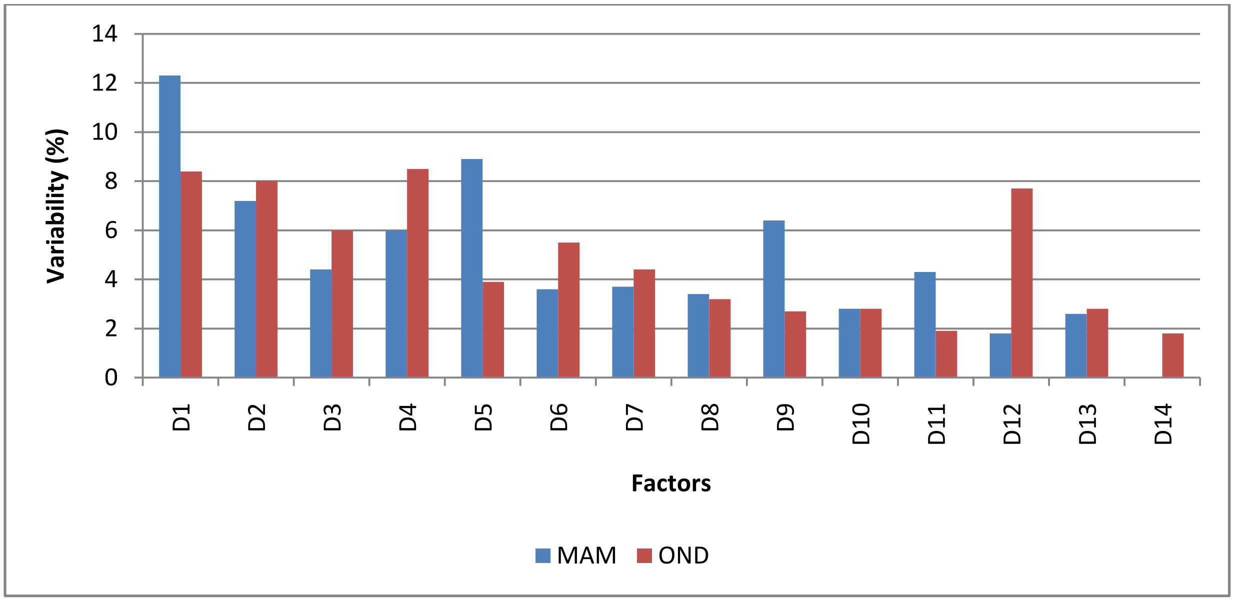

Figure 4-15: Percentage of explained variance based on AOD in EA (2001-2012)

Based on FMF, Figure 4-16 shows that 20 and 18 significant PCs accounted for 64.8% and 68.2% of the total variance over the EA region during MAM and OND rainfall seasons respectively.

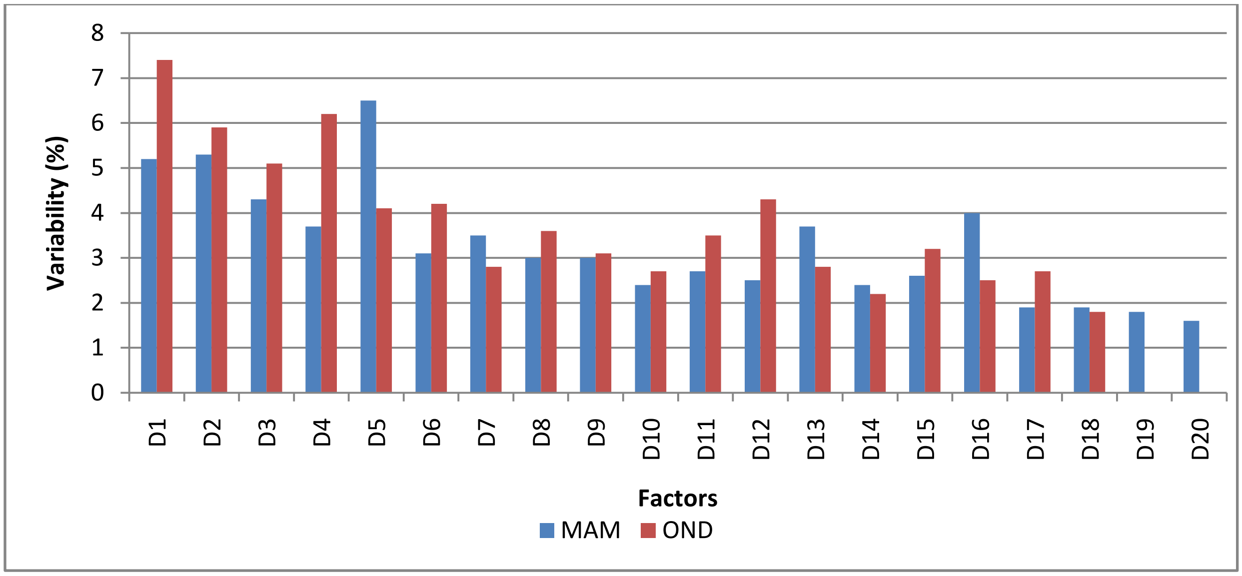

Figure 4-16: Percentage of explained variance based on FMF in EA (2001-2012)

Based on CTT, Figure 4-17 shows that eleven (11) and ten (10) significant PCs accounted for 76.7% and 73.2% of the total variance over the EA during MAM and OND respectively.

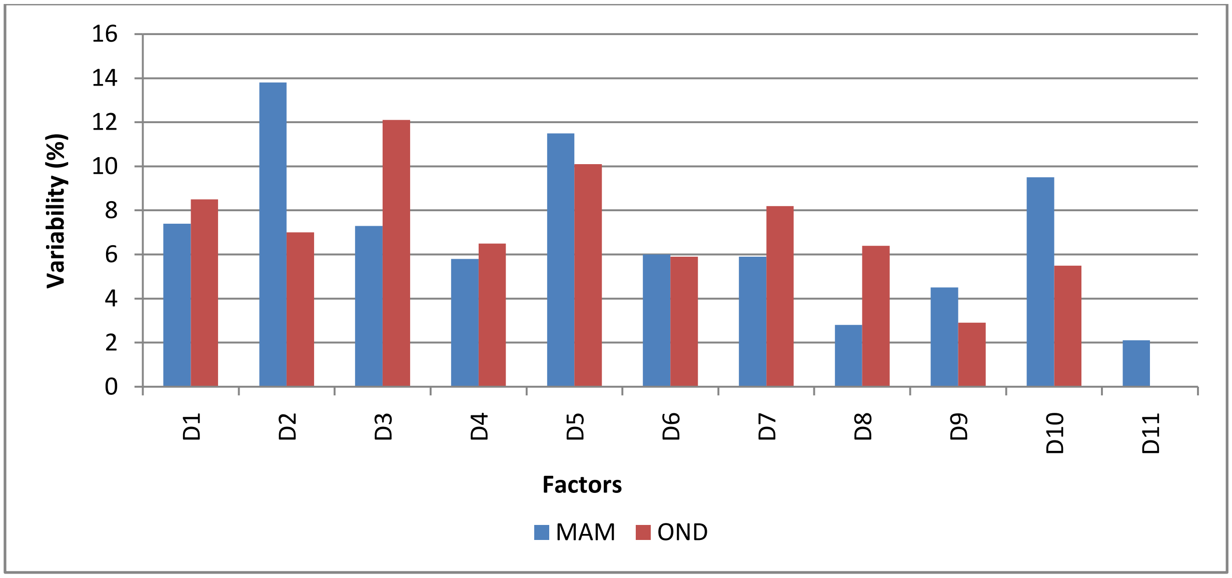

Figure 4-17: Percentage of explained variance based on CTT in EA (2001-2012)

Based on TRMM, Figure 4-18 shows that sixteen (16) and seventeen (17) significant PCs accounted for 57.3% and 57.1% of the total variance over the EA during MAM and OND respectively.

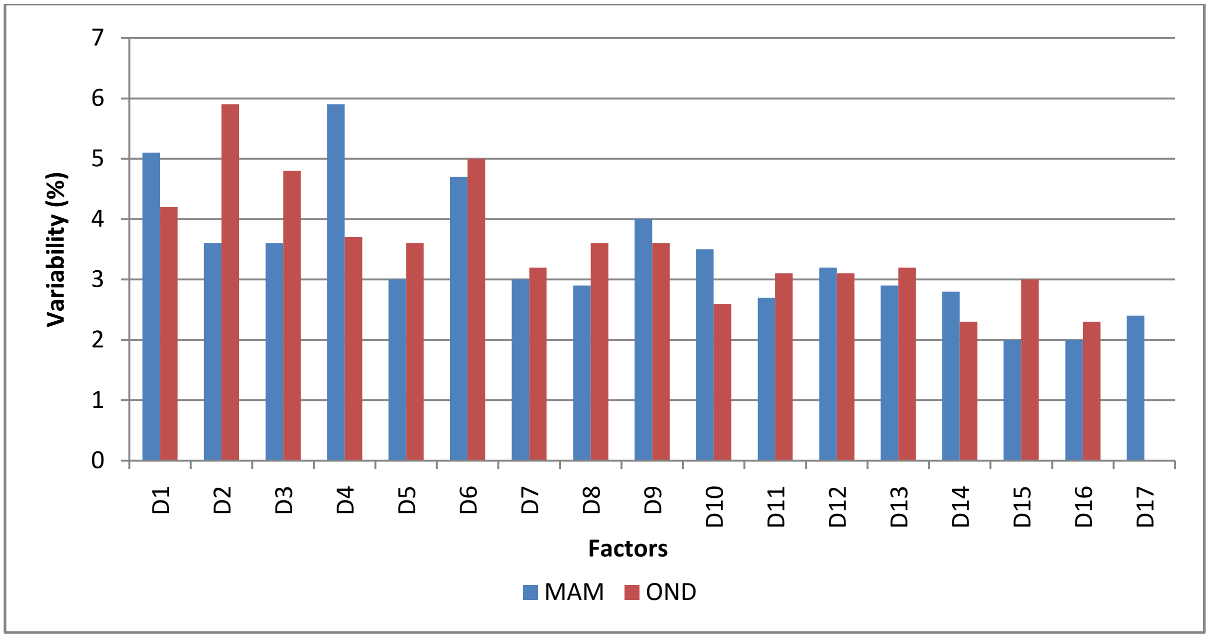

Figure 4-18: Percentage of explained variance based on TRMM in EA (2001-2012)

Based on OLR, Figure 4-19 shows that observed using the outgoing long wave radiation as nine (9) and ten (10) significant PCs were retained and accounted for 91.9% and 91.4% of the total variance in EA during MAM and OND respectively.

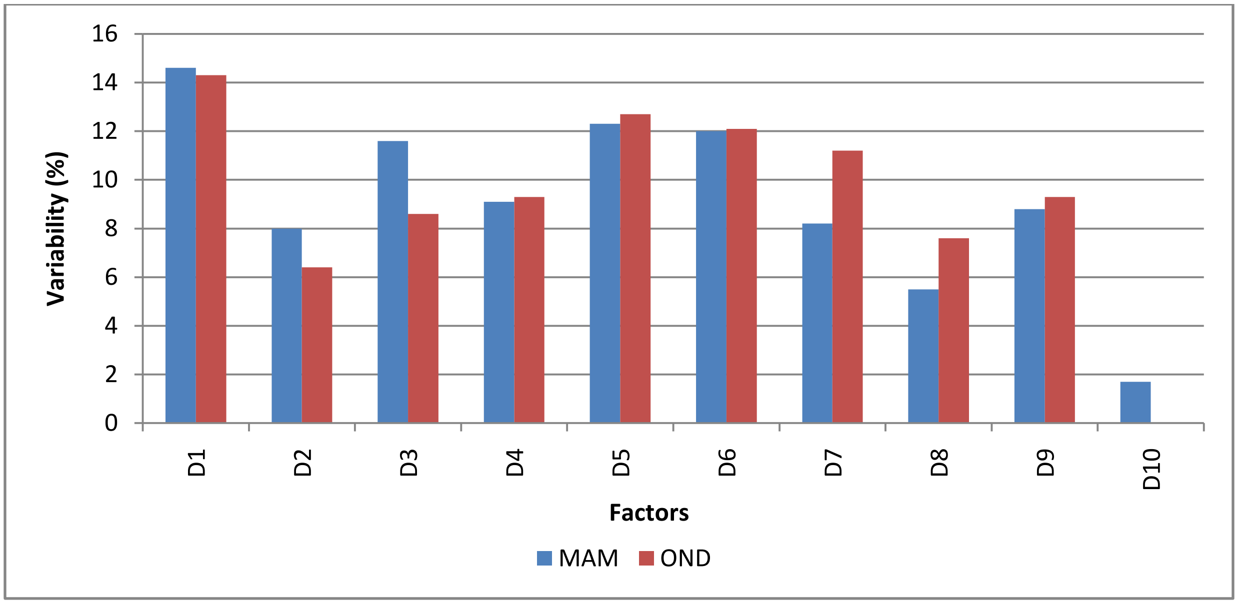

Figure 4-19: Percentage of explained variance based on OLR in EA (2001-2012)

4.1.2.2 Correlation Analysis

The Figure 20 to Figure 24 presents the maximum factor loadings after rotation. Appendix 7 and Appendix 8 provides detailed Scree parallel plots from the PCA analysis and regions with Strong Factor Loadings (>0.75) after Varimax rotation respectively.

AOD maximum factor loadings indicated a high concentration in Central Kenya, Coastal Kenya (Mombasa) and Tanzania (Dar es Salaam), Eastern Uganda (Lake Victoria), Western Uganda and Rwanda. AOD showed lower variability during MAM season (Figure 4-20 a) compared to OND season (Figure 4-20 b). Strong surface winds resulted to highest AOD values of >0.9 during OND. Prijith *et al.* (2013) associated it with the Asian summer monsoon during the June July August September which produces a large amount of sea salt aerosols leading to high aerosol production rate over the region. Over the land, the major contribution to global aerosol production comes from the regions extending from NW Africa to China known as global dust belt (Propsero *et al.*, 2002). Further, wind generation of marine aerosols contributed to aerosol production over the Ocean.

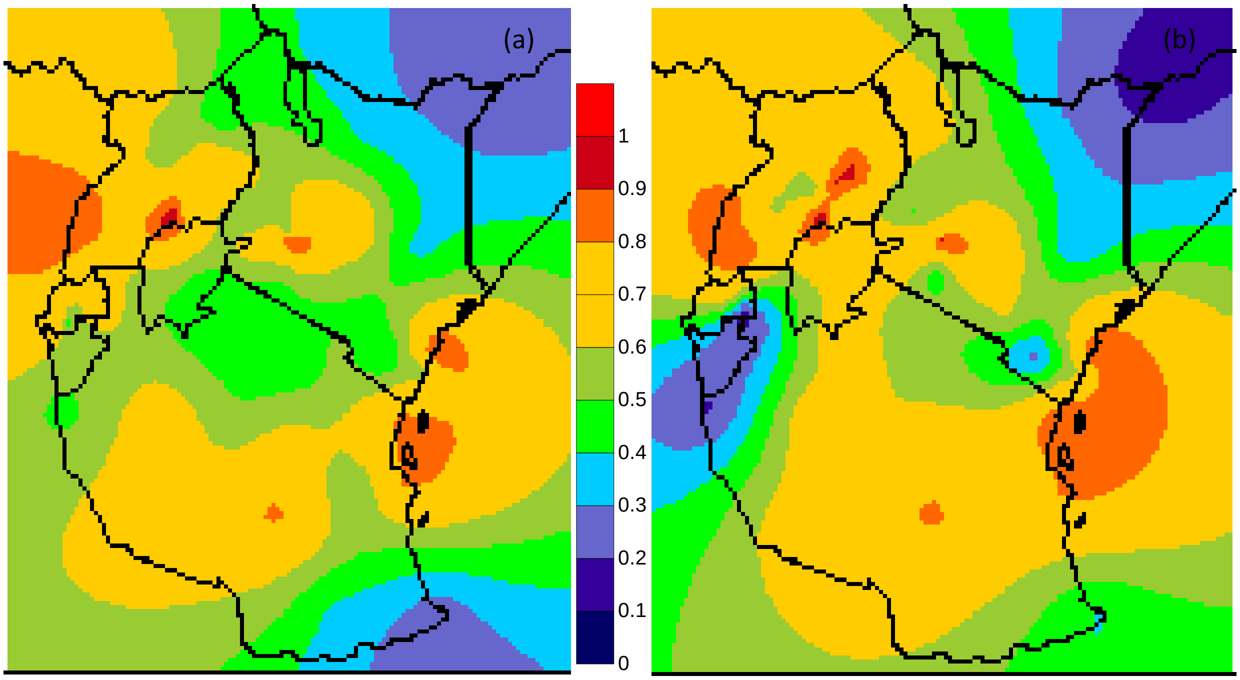

Figure 4-20: Spatial Pattern of AOD based on maximum factor loadings after Varimax rotation for a) MAM and b) OND

Spatial patterns of FMF based on maximum factor loadings showed similarities with AOD spatial distribution. Identified regions of high concentration included Central Kenya, Coastal Kenya (Mombasa) and Tanzania (Dar es Salaam), Eastern Uganda around Lake Victoria, Western parts of Uganda and Rwanda. FMF values showed highest variability during MAM season (Figure 4-21 a) compared to OND season (Figure 4-21 b). However, a study by Tosca *et al.* (2013) indicates persistent low -biases of AOD and AERONET values compared to observations in EA region from MODIS data. Studies by De Graaf *et al.* (2010) and Stein *et al.* (2003) noted that central-east Africa experiences low (high) aerosol loading during wet (dry) periods. Further, SE Africa shows alternating high and low residues with high values mainly local biomass burning aerosols during the local dry season. The local burning aerosol are usually absent during the local wet season and in phase with the desert dust production to the north of ITCZ (eastern Sahara).

Spatial analysis of clouds based on CTT values showed highest variability over Central Tanzania, Coastal regions of Mombasa and Zanzibar, Central parts of Kenya and Uganda. The western parts of Uganda and Rwanda with seasonal variability noted to be highest during OND (Figure 4-22 a) compared to MAM (Figure 4-22 b) period.

Spatial analysis of clouds based on OLR values showed highest variability over Northern Uganda, Rwanda and Eastern Parts of Mt. Kilimanjaro. Seasonal variability was high during OND (Figure 4-23 a) compared to MAM (Figure 4-23 b). Spatial analysis of satellite derived rainfall showed high variability during both MAM (Figure 4-24 a) and OND (Figure 4-24 b). Several pockets of high factor loading based on satellite data and attributed to observed high rainfall variability in the EA region due to complex mechanism and processes responsible for rainfall formation.

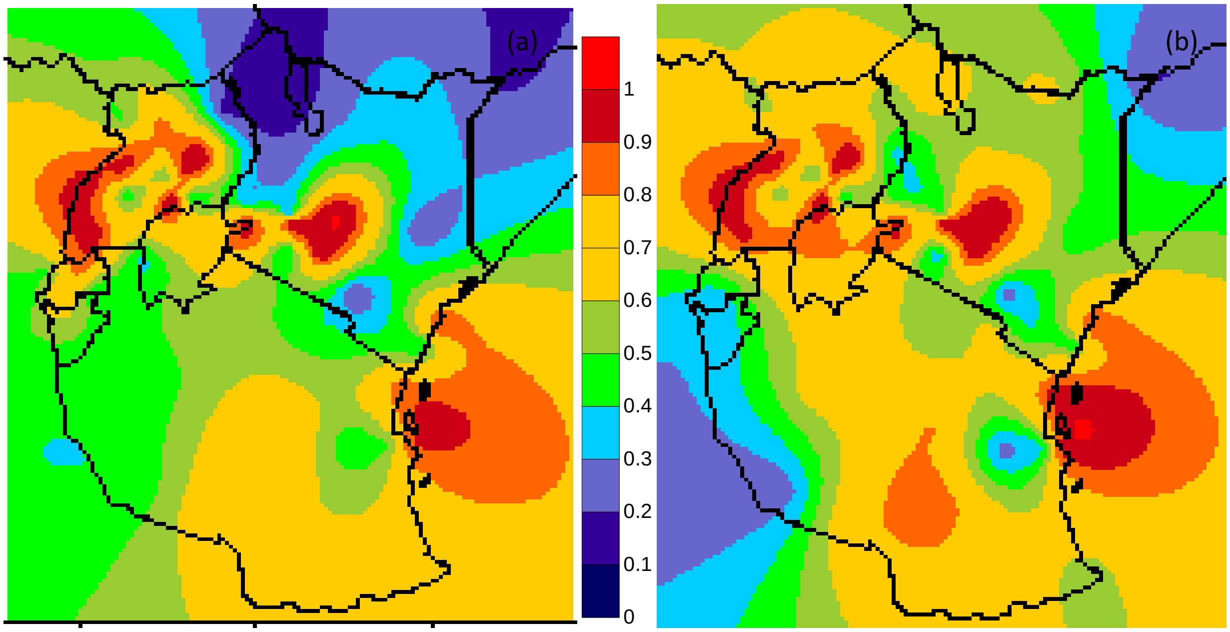

Figure 4-21: Spatial Pattern of FMF based on maximum factor loadings after Varimax rotation for a) MAM and b) OND

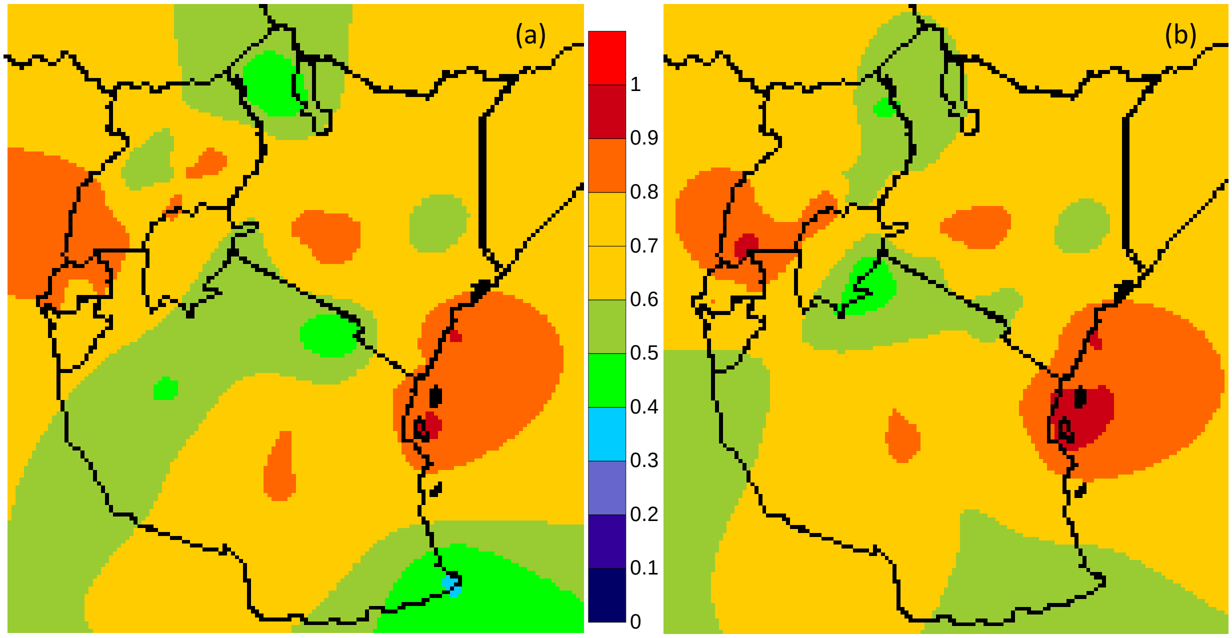

Figure 4-22: Spatial Pattern of CTT based on maximum factor loadings after Varimax rotation for a) MAM and b) OND

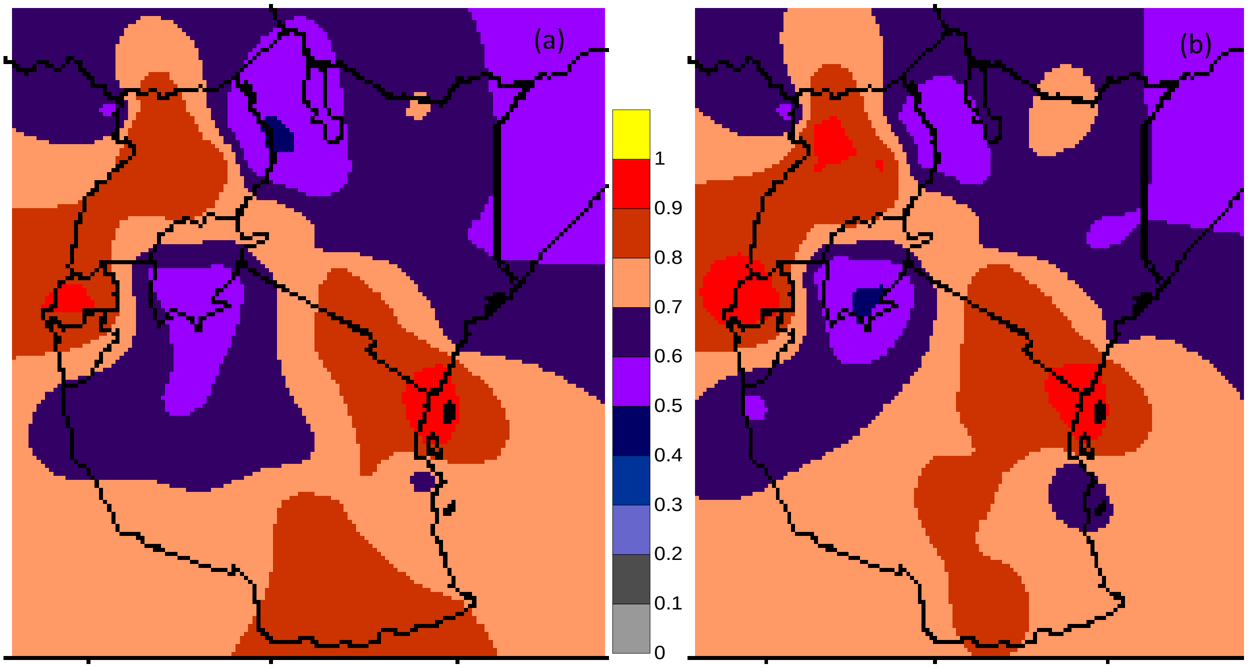

Figure 4-23: Spatial Pattern of OLR based on maximum factor loadings after Varimax rotation for a) MAM and b) OND season

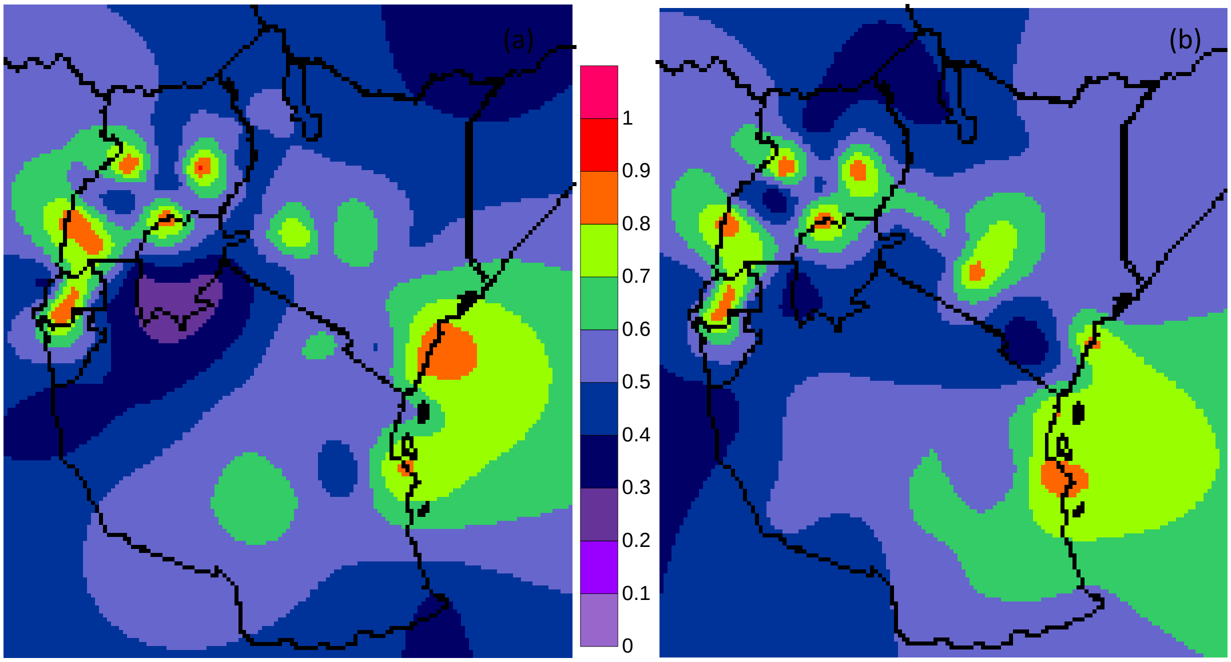

Figure 4-24: Spatial Pattern of TRMM (3B42) based on maximum factor loadings after Varimax rotation for a) MAM and b) OND season.

4.1.3 Hovmoller Analysis

Identification of zonal and meridional moving atmospheric systems utilized Latitude/longitude - time plots. The Figures 4-25 to 4-26, 4-27 to 4.29 and 4-30 to 4-33 presents results for clouds, aerosols and rainfall. The Figure 4-25 show the meridional pattern of CTT with higher CTT values over the SH of up to 300K compared to NH (Figure 4-25 a). An intra-seasonal analysis indicates that highest CTT values between June and September (Figure 4-25 b). Notably, EA region recorded an average CTT of 250K. The zonal distribution shows that CTT increased from west to east towards the Indian Ocean (Figure 4.26 a) with intra-seasonal variation showing highest CTT values during October, November December (Figure 4-26 b). In overall, CTT values are noted to undergo large variation both zonally and meridionally in EA.

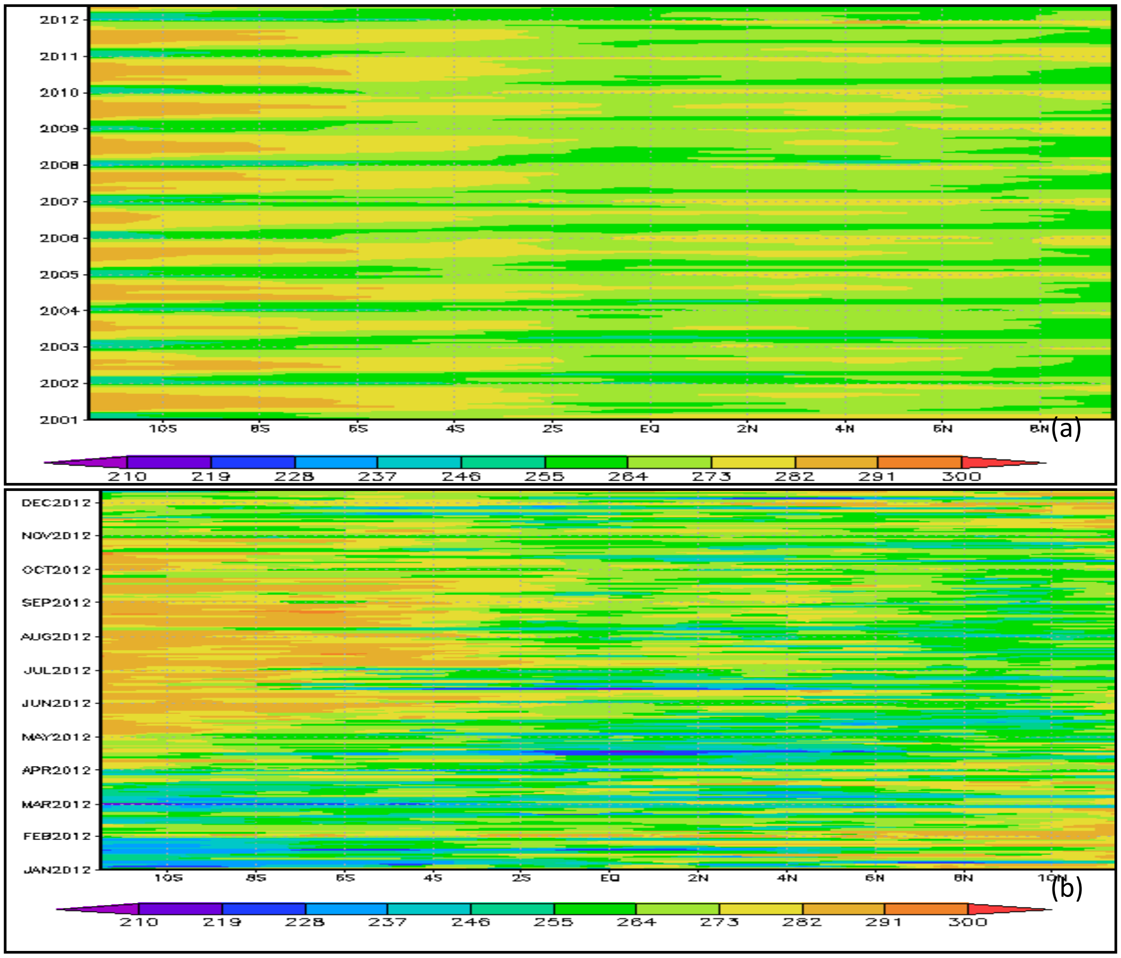

Figure 4-25: Latitude –Time Hovmoller diagram of Cloud Top Temperature (kelvin) for a) 2001 to 2012) and b) January to December 2012 over EA

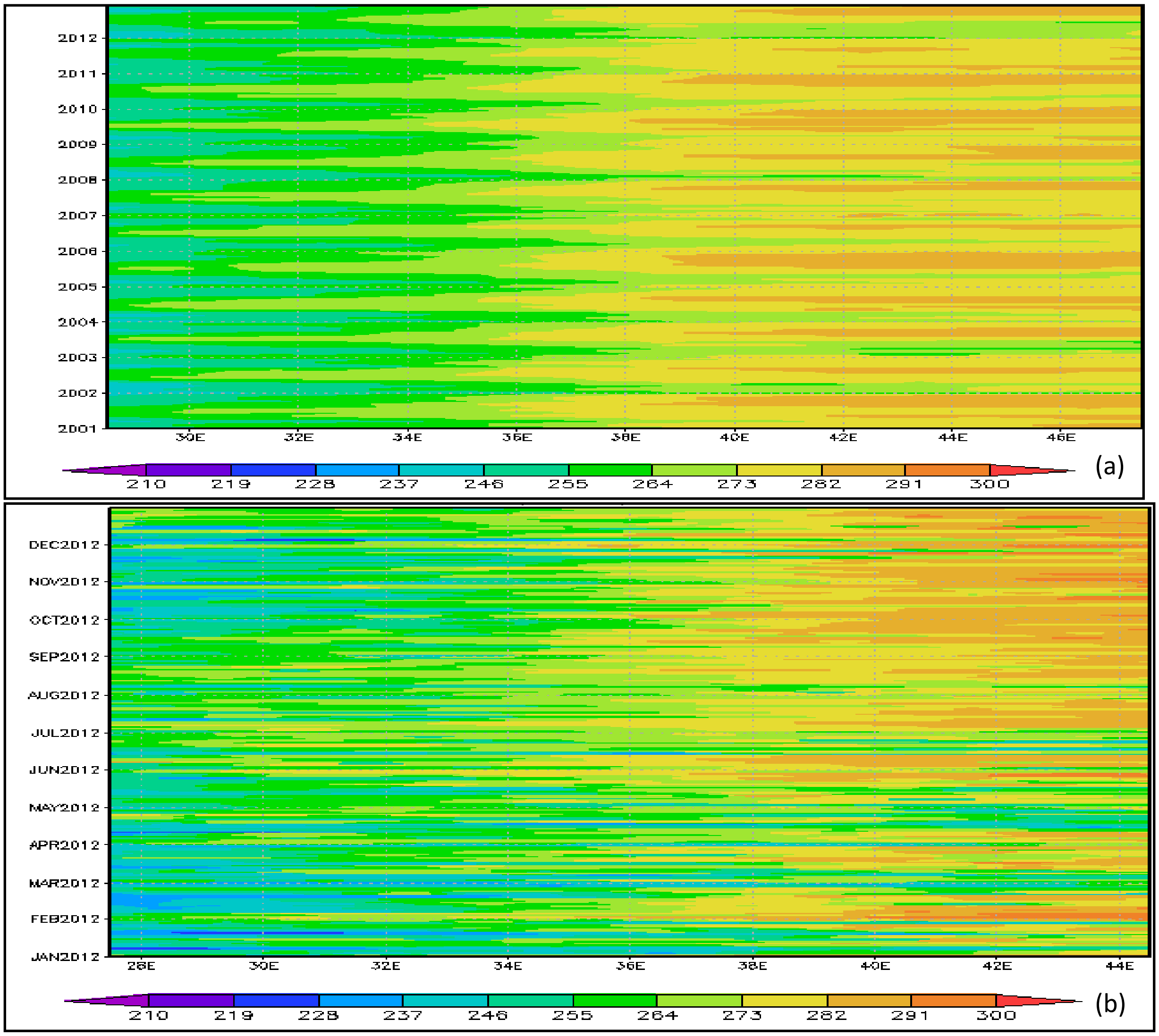

Figure 4-26: Longitude –Time Hovmoller diagram of cloud top temperature (kelvin) for a) 2001 to 2012) and b) January to December 2012 over EA

The Figure 4-27 (a) indicates that the Northern part of the EA experiences an influx of higher amounts of AOD due to the transport of dust aerosols particles by the North-Easterly winds. Seasonal analysis based on January to December 2012 time series (Figure 4-27 b) showed that low amount of AOD were observed in the southern hemisphere between March and June over latitude 12^{o}S and 4^{o}S. Along the equator, the amount of AOD increased. Similarly, AOD increased over latitude 8^{o}N and 10^{o}N during June –July –August period.

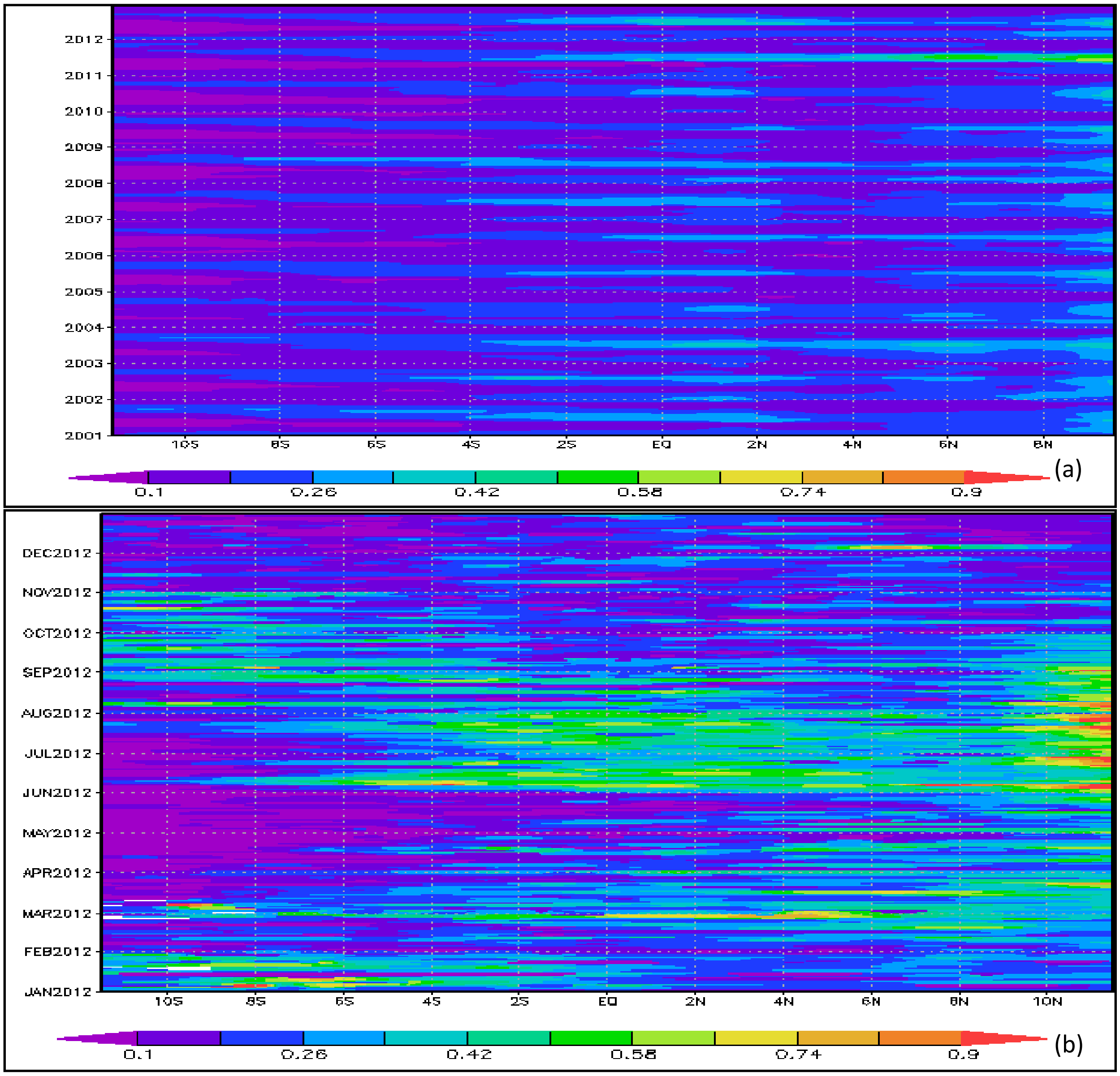

Figure 4-27: Latitude –Time Hovmoller diagram of Aerosol Optical Depth at 550nm(Unitless) for a) 2001 to 2012) and b) January to December 2012 over EA

Longitude time analysis (Figure 4-28 a) showed that the western parts of the EA experienced higher amounts of AOD as compared to the east in the same region. Higher AOD values were due to the influence of westerly winds throughout the year. Seasonal analysis based on January to December 2012 time series (Figure 4-28 b) showed enhanced amounts of AOD during the MAM. During OND, higher values dominated the western parts of EA.

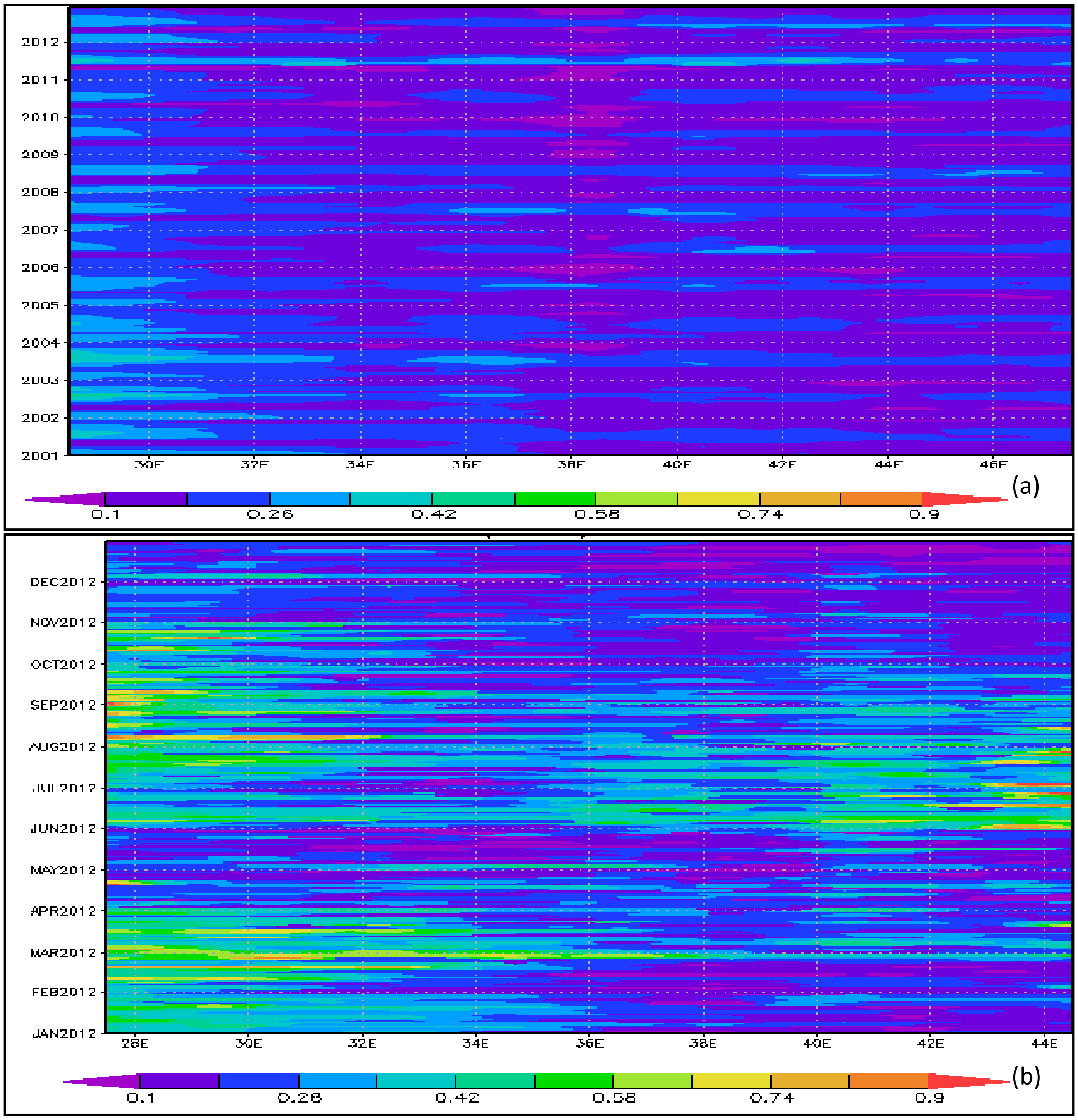

Figure 4-28: Longitude –Time Hovmoller diagram of Aerosol Optical Depth at 550nm (Unitless) for a) 2001 to 2012) and b) January to December 2012 over EA

The Figure 4-29 (a) showed higher amounts of FMF in the Southern Hemisphere (SH) compared to the Northern hemisphere. Notably, higher amounts of FMF (Figure 4-29 b) were noted during the October to December period. The enhanced distribution of FMF was attributed to aerosols particles associated with biomass burning in the SH transported into Equatorial Africa during the period by the south easterly winds (Williams *et al.*, 2010).

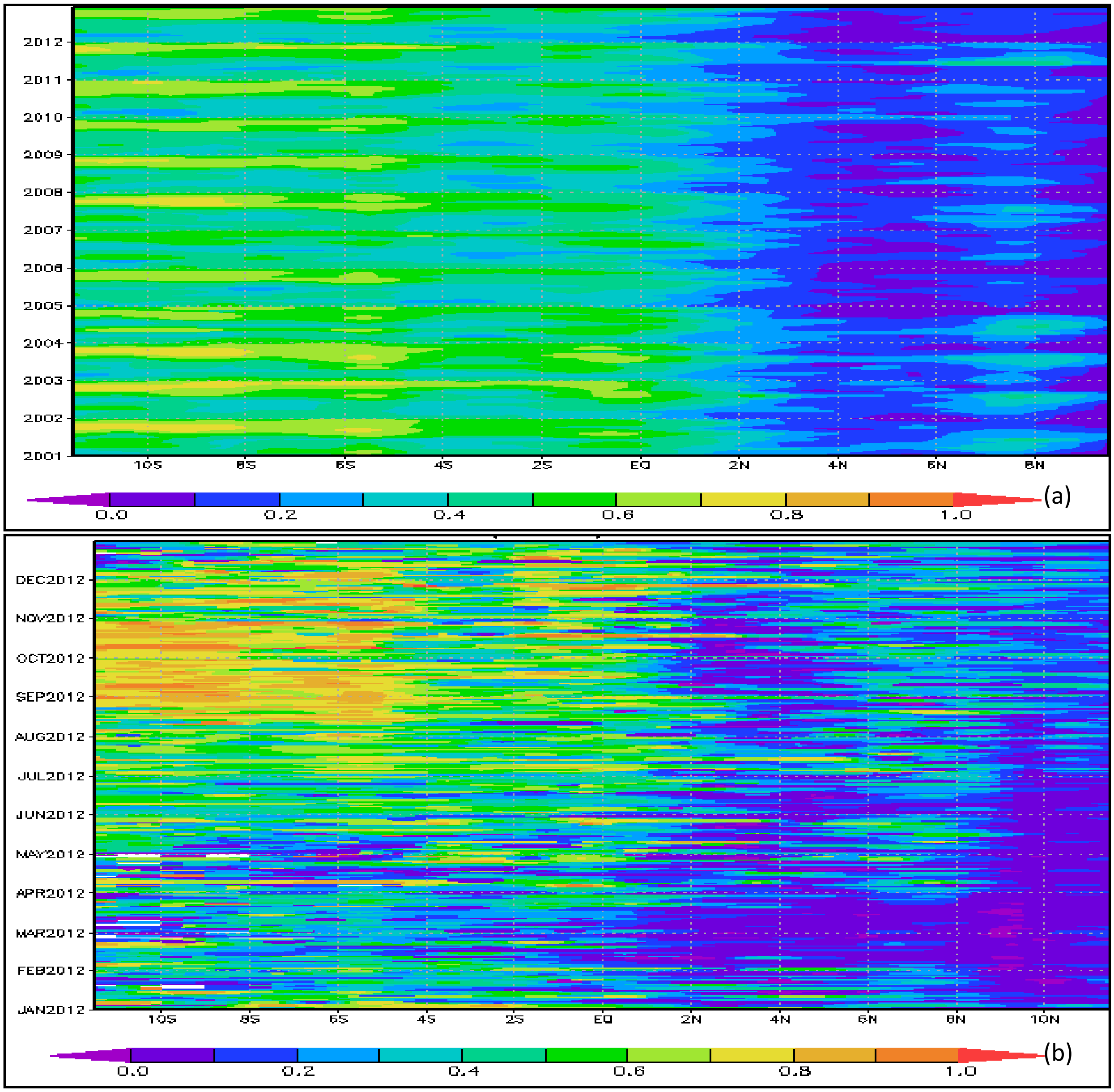

Figure 4-29: Latitude–Time Hovmoller diagram of Aerosol FMF for a) 2001 to 2012) and b) January to December 2012 over EA

A longitudinal –time analysis (Figure 4-30 a) showed higher amounts of FMF in the Eastern (38^{o}E to 46^{o}E) and Western (28^{o}E to 34^{o}E) parts of the EA. Notably, the central region of the EA was noted to have lower values of FMF. Further analysis based on the seasonal distribution of FMF values (Figure 4-30 b) indicated that higher FMF values were experienced in the western EA between June to November with peaks in September.

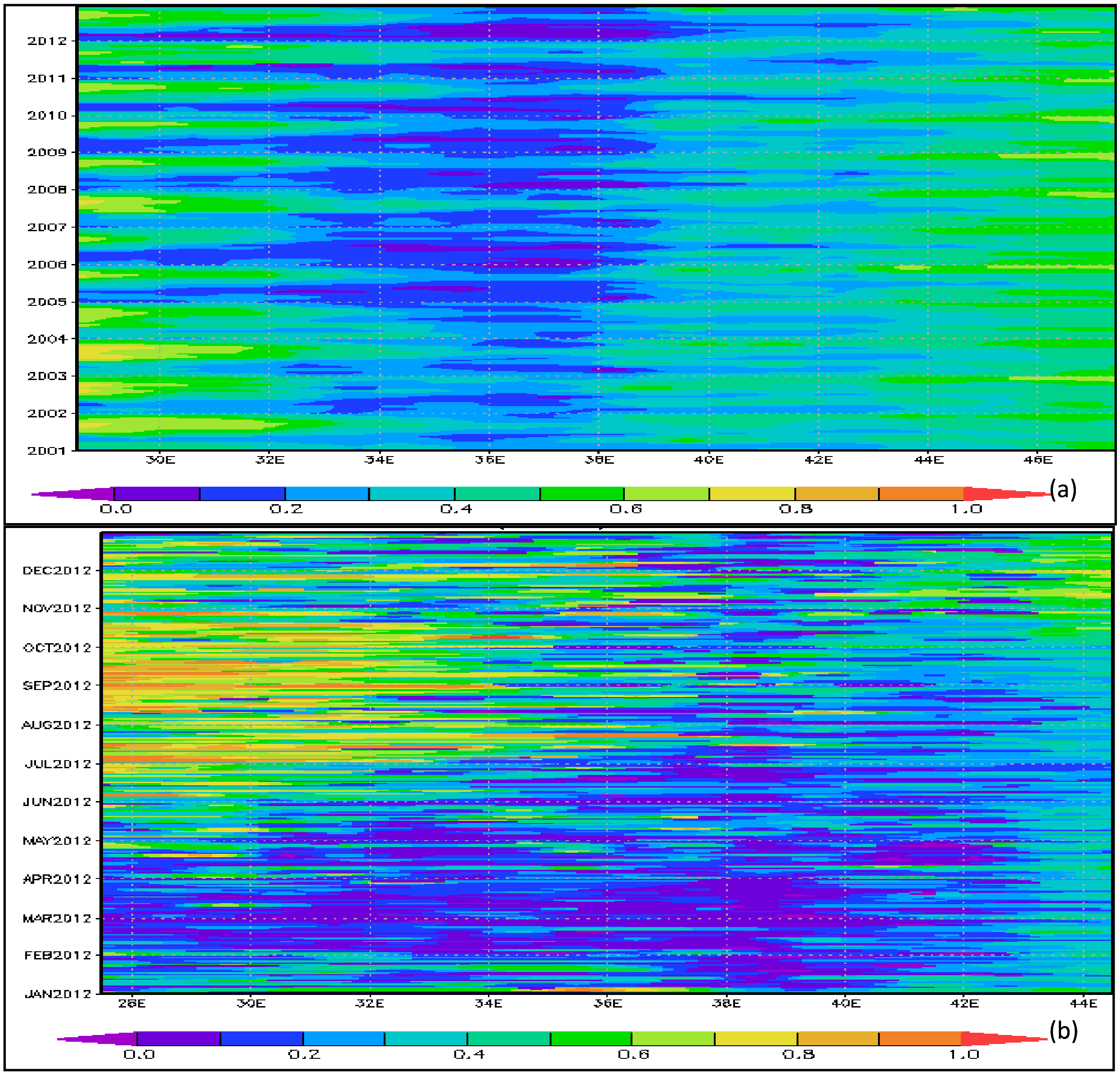

Figure 4-30: Longitude –Time Hovmoller diagram of Aerosol FMF for a) 2001 to 2012) and b) January to December 2012 over EA

In the Figure 4-31 (a), the latitude time Hovmoller diagram showed that southern parts of EA experienced higher amounts of accumulated monthly precipitation compared to the Northern Hemisphere. A further analysis based on the longitude time diagram (Figure 4-40 (b) showed higher amounts of accumulated precipitation over the Western EA compared to Eastern EA MAM. During OND, higher amounts of accumulated precipitation dominated Southern parts of EA. Increased precipitation dominated the equatorial EA.

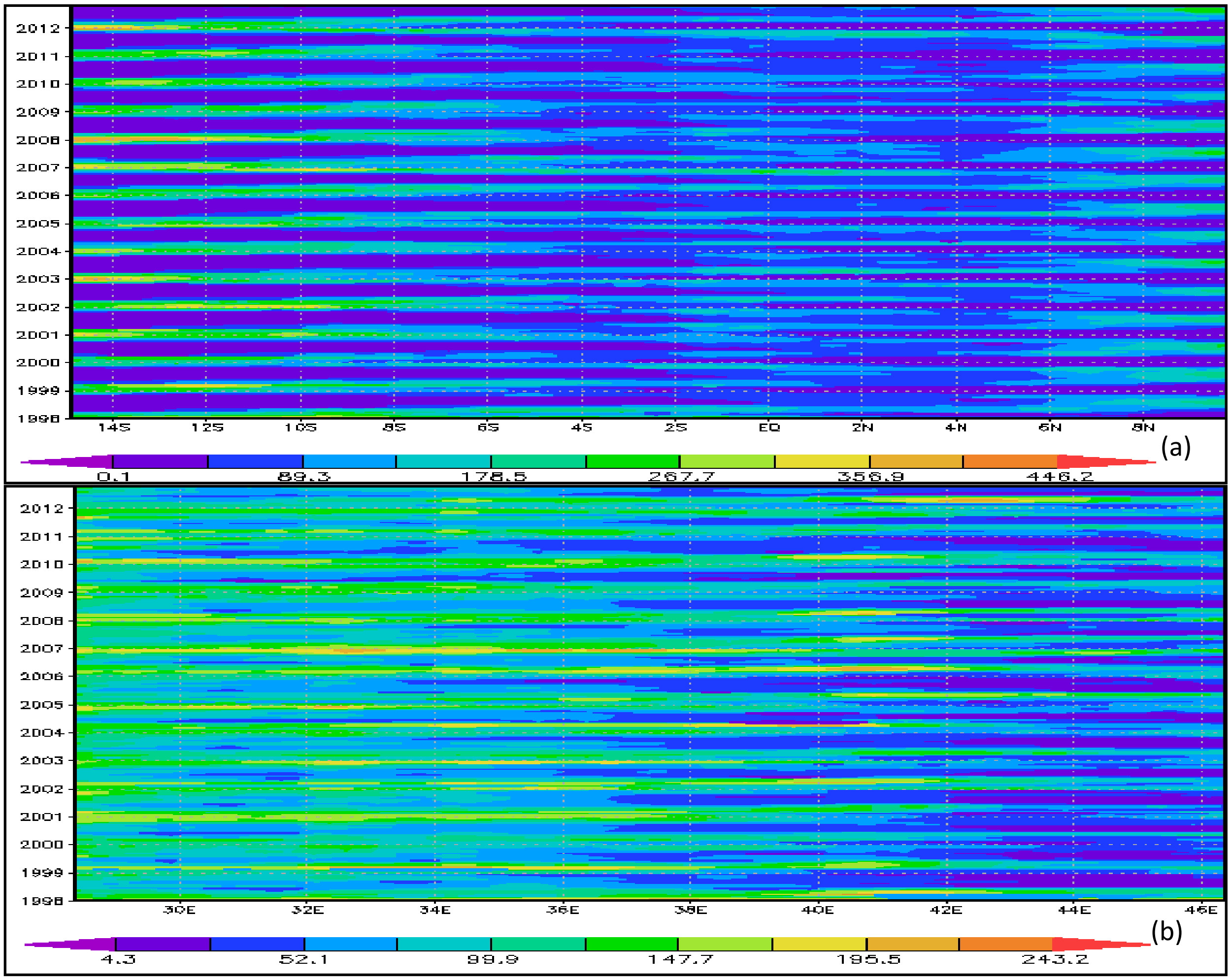

Figure 4-31: Hovmoller diagrams of a) Latitude–Time b) Longitude–Time accumulated monthly precipitation for 1998-2012 over EA

Seasonal analysis (Figure 4-32 a) showed that enhanced precipitation along the equator during the MAM season. Accumulated precipitation followed a skewed distribution along the equator with the southern EA receiving enhanced precipitation at the start of MAM period and increasing towards the Northern parts of EA. The study attributed the observed phenomena to the movement of ITCZ in the region which is associated area active convective activities due to its low pressure resulting in enhanced convergence. The longitude time diagram of accumulated monthly precipitation (Figure 4-32 b) showed less significant features in the region. Furthermore, distinct meridional gradient of accumulated precipitation indicates that it is possible to forecast locations of surface convection and thus effectively target seeding materials to modify the weather.

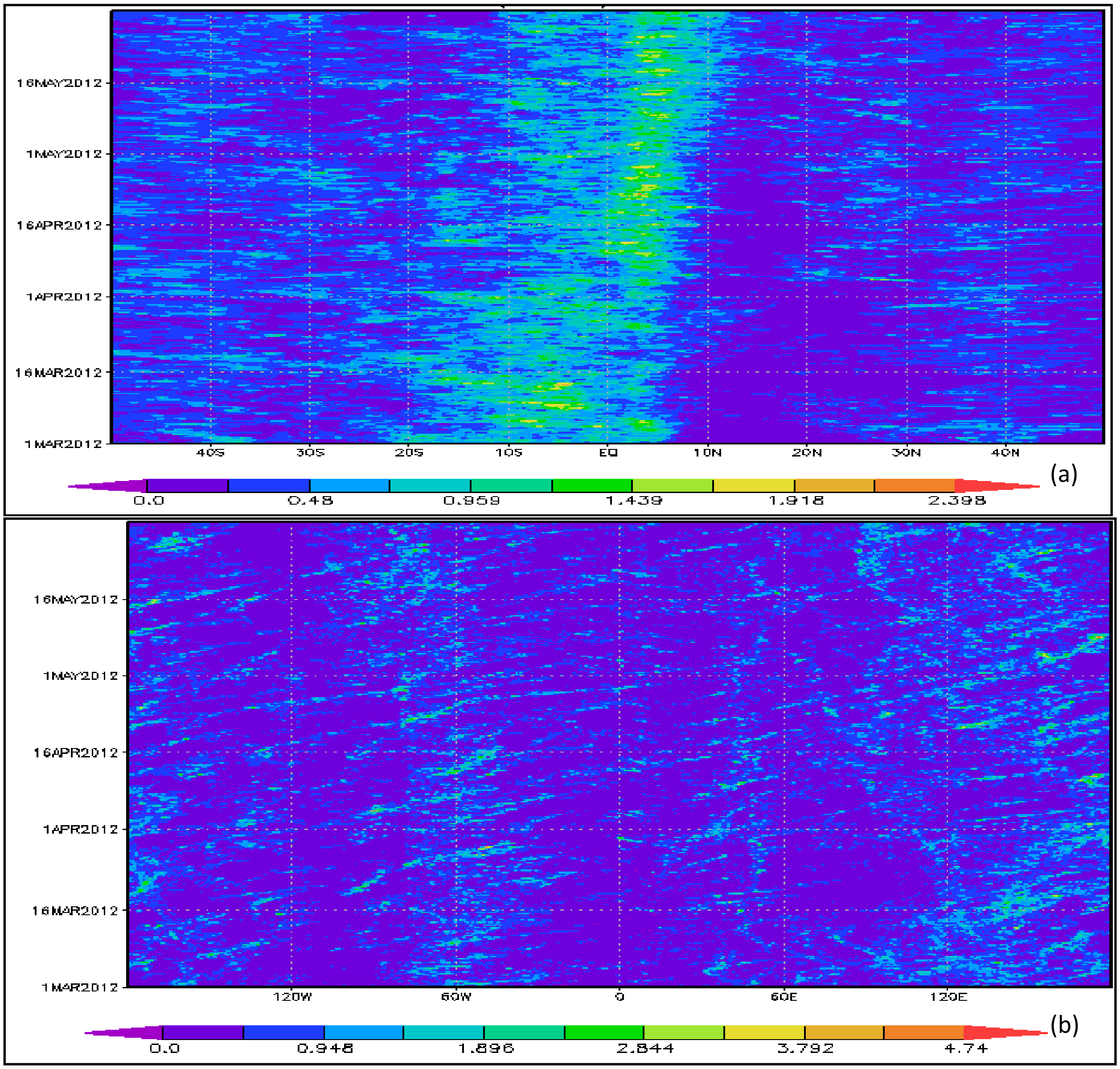

Figure 4-32: Hovmoller diagrams of a) Latitude –Time b) Longitude –Time accumulated monthly precipitation for January to December 2012 for MAM over EA

During OND season, both latitude -time (Figure 4-33 a) and (Figure 4-33, b) showed limited variability of accumulated precipitation in the EA region. Notably, both meridional and zonal movements of moisture and other rainfall formation variables did not have distinct patterns and thus not well organized above the surface.

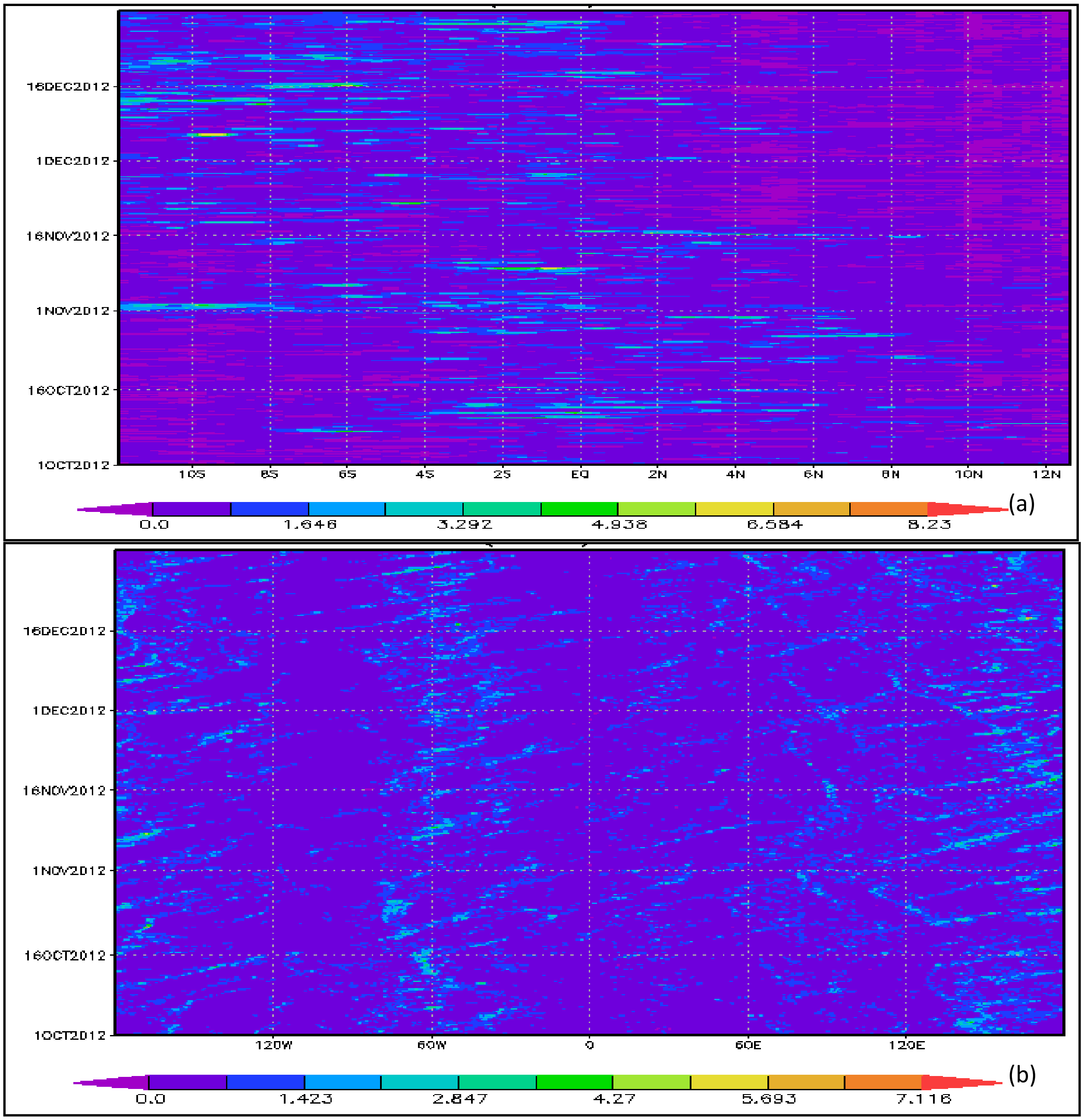

Figure 4-33: Hovmoller diagrams of a) Latitude –Time b) Longitude –Time accumulated monthly precipitation (mm) for January to December 2012 for OND over EA.

4.2 Relationship Between Aerosols, Clouds and Precipitation Processes over EA

This subsection presents results based on MLR, HYSPLIT and cloud characteristic analysis. The study used RRAI to validate the GHACOF maps.

4.2.1 Multivariate Regression Analysis

Multivariate regression analysis for both MAM and OND seasons was carried based on variables with higher factor loading after Varimax rotation. The Table 4-2 and Table 4-3 presents results for MAM and OND season.

In Table 4-2 and Table 4-3, autocorrelation analysis showed that all aerosol and cloud variables with strong factor loading in the region had positive relationship with rainfall. The only exceptions were in Kigali, Entebbe and Soroti during MAM season and Kasese and Tanga during OND season. Durbin-Watson test (D-W) indicated that these variables were independent with values distributed around 2 for both MAM and OND season. Histograms of model residual were symmetrical in shape over selected regions during both OND and MAM season in the MLR and thus indicated normality in the model residuals. The QQ plots affirmed the results based on histograms for the selected stations that followed a straight line (Appendix 10). Wilk-Shapiro test showed strong evidence against normality an indication that did not come from a normal distribution for both MAM and OND season. The percentage of data points that could be fitted based on R^2 ranged between 8% and 23% during MAM season and between 7% and 21% during OND season.

Rainfall regression model developed for MAM and OND identified optimal combination and number of variables. Detailed analysis is provided in Appendix 9 (a, b). During MAM, optimal stations (number of variables) selected in the developed model included Entebbe (10), Nakuru (11), Zanzibar (11) and Kasese (12). Others included Kigali (12), Malindi (14), Masindi (14), Mombasa (9) and Soroti. Clouds (CTT and OLR) indicated a negative contribution in the developed rainfall model as shown by negative coefficient values at selected stations. However, the negative coefficient values had small influence and thus less significant contribution attributed to low coefficient values all centred about zero. During OND, optimal stations (number of variables) selected in the developed model included Embu (15), Malindi (15), Entebbe (14) and Dagoretti (12). Others included Kasese (12), Mbarara (11), Tanga (10), Dar es Salaam (8), Kigali (8), Soroti (8) and Masindi (7). Clouds (CTT and OLR) and aerosols (AOD and FMF) had a similar influence on the model developed for OND season compared to MAM season. However, AOD and FMR had significant contribution to rainfall with absolute coefficient values of up to 11 over selected locations. A study by Muthama (2004) indicated that aerosol indices on average lead rainfall by about two months. However, CTT and OLR had less significant influence indicated by small coefficient values centred about zero. Studies on the relationship between precipitation and aerosol e.g. Andreae *et al.* (2004) and Rosenfeld (2008) showed that strengthening of storms with polluted air produced large hail and latent heat release higher in the atmosphere than storms under a cleaner air mass. Through the enhanced cooling and downward momentum, these more strengthened downdrafts can spawn secondary updrafts as they push ambient air upward, leading to more precipitation (Rosenfeld 2008).

Table 4-2: Multivariate Regression Analysis for MAM

Station	Auto - correlation	Durbin-Watson (D-W)	P value	Wilk Shapiro (W-S)	P value	R^2
Entebbe	-0.04	2.09	0.15	0.69	<2.2e-16	0.13
Kasese	0.03	1.93	0.26	0.73	<2.2e-16	0.08
Kigali	-0.05	2.03	0.65	0.65	<2.2e-16	0.1
Malindi	0.11	1.77	0.01	0.58	<2.2e-16	0.19
Masindi	0.03	1.95	0.34	0.71	<2.2e-16	0.13
Mombasa	0.28	1.45	0	0.52	<2.2e-16	0.16
Nakuru	0.07	1.85	0.01	0.8	<2.2e-16	0.21
Soroti	-0.02	2.03	0.62	0.77	<2.2e-16	0.17
Zanzibar	0.08	1.83	0.01	0.68	<2.2e-16	0.23

Table 4-3: Multivariate Regression Analysis for OND

Station	Auto - correlation	Durbin-Watson (D-W)	P value	Wilk Shapiro (W-S)	P value	R^2
Dagoretti	0.17	1.65	0	0.57	<2.2e-16	0.15
Dar es Salaam	0.14	1.71	0	0.56	<2.2e-16	0.2
Embu	0.18	1.65	0	0.74	<2.2e-16	0.21
Entebbe	0.08	1.98	0.6	0.66	<2.2e-16	0.12
Kasese	-0.02	2.03	0.59	0.74	<2.2e-16	0.07
Kigali	0.04	1.93	0.18	0.7	<2.2e-16	0.1
Malindi	0.06	1.89	0.07	0.53	<2.2e-16	0.14
Masindi	0.03	1.94	0.28	0.68	<2.2e-16	0.16
Mbarara	0.03	1.95	0.27	0.73	<2.2e-16	0.12
Soroti	0.15	1.7	0	0.69	<2.2e-16	0.19
Tanga	-0.04	2.08	0.14	0.56	<2.2e-16	0.16

4.2.2 HYbrid Single-Particle Lagrangian Integrated Trajectory Analysis

Backward trajectory analysis was done using the HYSPLIT model. A five-day backward trajectory analysis was utilized to identify the sources of atmospheric aerosols at 500, 1000 and 1500 Metres Above Ground Level (MAGL). Selected locations with high factor loading (>0.75) based on TRMM satellite-derived rainfall estimates were utilized. The trajectories were computed for the start, mid and end of the season for both MAM and OND season (Figure 4-34 and Figure 4-35).

At the beginning of MAM (pentad 13), backward trajectories identified the continental source regions as the Arabian deserts and India subcontinent at all levels. The selected continental stations included Entebbe, Kasese and Masindi (Figure 4-33 a); Soroti and Nakuru (Figure 4-34 b) and Kigali (Figure 4-34 c). Locations of maritime source regions were in Sub-western Indian Ocean. The selected sink stations included Malindi (Figure 4-34 b), Mombasa and Zanzibar (Figure 4-34 c). At the middle of the MAM season (pentad 21), source regions for all stations were in SW Indian Ocean except Entebbe at 1500 MAGL and Kigali at 1000MAGL. The sink stations included Kasese, Masindi (Figure 4-34 d); Soroti, Nakuru and Malindi (Figure 4-34 e)

Mombasa and Zanzibar (Figure 4-34 f). At the end of the MAM (pentad 30), all the source regions for all stations (Figure 4-34 c, f, i) at all levels were located in the SW Indian Ocean.

At the start of OND season (pentad 62), source regions for selected locations were in SW Indian Ocean for 500, 1000 and 1500 MAGL (Figure 4-34 a, b, c). These patterns continue towards mid-season (Figure 4-35 d, e, f) with source regions moving closer to the coastal areas. However, at the end of the season (Figure 4-35 g, h, i), the regions of origin were all located in the Arabian and Siberian Plateau and thus continental in Nature. Johnson *et al. (*2008) noted that aerosols are either well mixed within a single layer(s) or layers of different particle types occurring at different altitudes.

OND trajectory analysis all agreed well with other studies such as Gatebe *et al.* (1999) and Ngaina *et al.* (2014). These studies indicated that sources regions for locations in EA are mainly in SW Indian Ocean characterized by the oceanic nature or Arabian regions characterized by their continental character. In EA active regions of aerosol emission and mixtures of combustion produced particles with desert dust aerosol occurring seasonally include Sudanian zones of Northern Africa and the Sahel (Eck *et al.*, 2010). Other regions identified by previous studies include the Indian Ocean (Granat *et al.*, 2002; Kulshrestha and Kumar, 2014), Arabian Desert (Krishnamurti *et al.*, 1998), Arabian Sea, Arabian Peninsula and the Indonesia forest fires that occured in 1997 (Li and Ramanathan, 2002).

Generally, at different levels, transported particles in the atmosphere show varied source regions. Aerosol particles undergo vertical mixing inland of EA. Further, several high mountains (>2000m) are situated near the Great Rift Valley area in EA. They include Mount Kilimanjaro, Mount Kenya, and Mount Rwenzori. These mountains block the eastward transport of the Sahel smoke as well as dust from the Bodele Depression (Washington and Todd, 2005). Therefore, these mixed aerosols accounted for increased rainfall over locations with high factor loading based on TRMM rainfall.

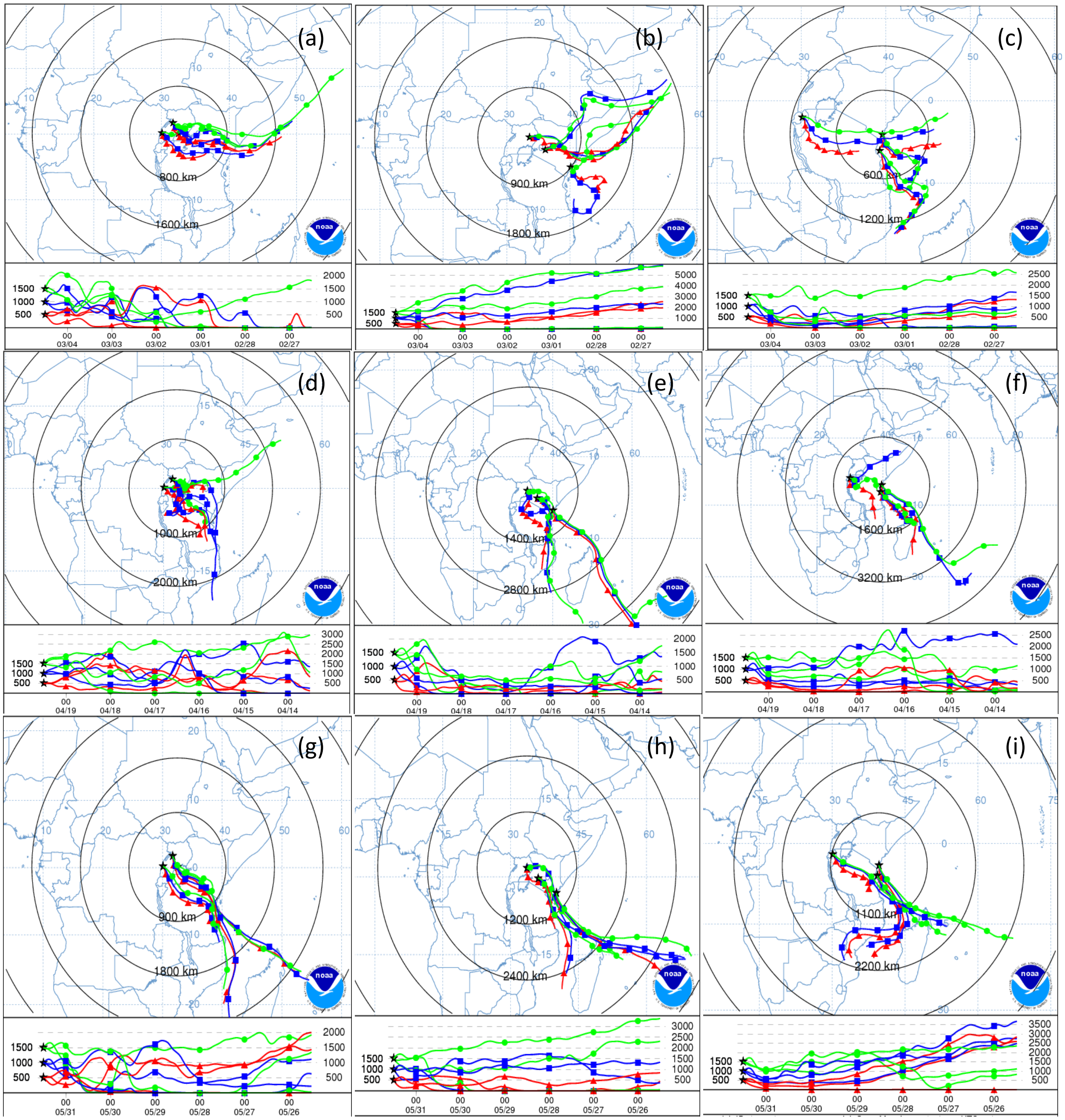

Figure 4-34: HYSPLIT back trajectory during start (a, b, c), mid (d, e, f) and end (g, h, i) of MAM.

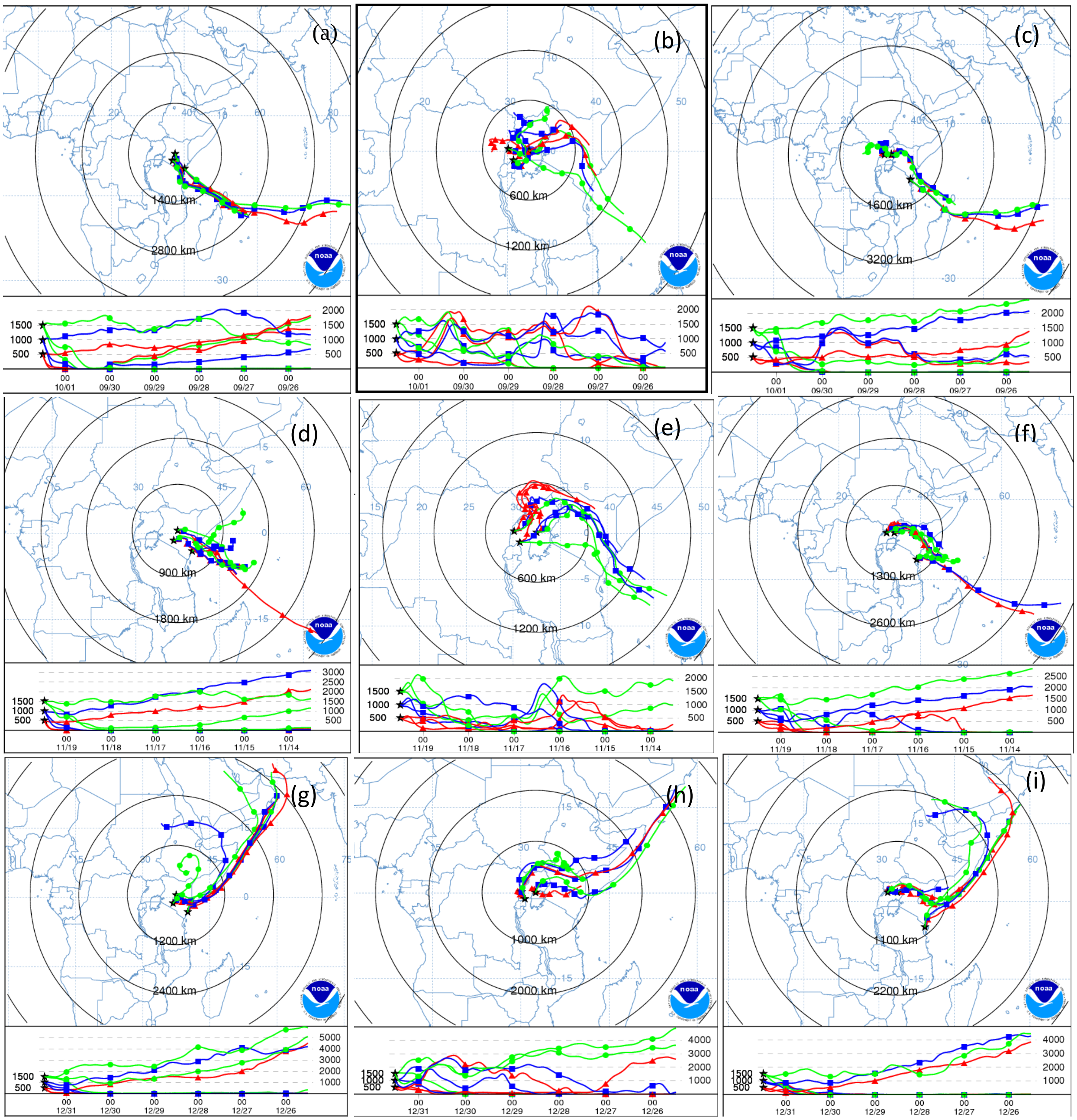

Figure 4-35: HYSPLIT back trajectory during start (a, b, c), mid (d, e f) and end (g, h, i) of OND.

4.2.3 Identification of Suitable Weather Modification Conditions

The GHA climate outlook and analysis of CAPE and cloud characteristics was used to identify weather modification conditions.

4.2.3.1 Greater Horn of Africa Consensus Forecast Analysis

The Figure 4-36 and Figure 4-37 shows the GHA consensus outlook for the MAM and OND season for the period 2009 to 2012.

In the Figure 4-36 (a), regional consensus forecast for the MAM 2012 rainfall (ICPAC, 2012 a) indicated a likelihood of NN to BN rainfall over GHA. The SW Tanzania, SW Ethiopia, South Sudan and SW Sudan showed a likelihood of NN to AN rainfall. Regional consensus forecast for MAM 2011 rainfall (ICPAC, 2011 a) indicated a probability of NN to AN rainfall over Western and Southern GHA (Figure 4-36 b). However, Eastern GHA showed likelihood NN to BN rainfall. The regional consensus forecast for MAM 2010 rainfall (ICPAC, 2010 a) indicated likelihood NN towards BN rainfall over GHA (Figure 4-36 c). Further, SW and NE parts of GHA showed the probability of NN to AN rainfall. Regional consensus forecast for MAM 2009 rainfall (ICPAC, 2012 a) showed the likelihood of BN rainfall over Eastern GHA with an increased probability of AN rainfall over Western and Southern GHA.

Regional consensus forecast for the SOND 2012 (ICPAC, 2012 b) indicated likelihood of AN to NN over GHA (Figure 4-37 a). The regional consensus forecast for SOND 2011 (ICPAC, 2011 b) indicated probability of AN to NN rainfall over Eastern equatorial parts of GHA. The areas covered Southern Somalia; coastal, eastern and central Kenya as well as NE Tanzania (Figure 4-37 b). Areas that showed likelihood of NN to AN rainfall and included parts of Tanzania; Northern Burundi; Rwanda; southern and central Uganda and Western Kenya. Others included South Sudan; western, central and northern Ethiopia; Djibouti; extreme South East (SE) Eritrea and extreme NW Somalia. Northern Somalia; Eastern and Southern Ethiopia; North West (NW) Kenya; northern Uganda; south-western Rwanda; southern Burundi and western Tanzania have increased the likelihood of NN to BN rainfall. Dry conditions are indicated over Sudan; much of Eritrea and extreme Northern Ethiopia.

The Figure 4-37 (c) shows that regional consensus forecast for SOND 2010 rainfall indicated likelihood of NN to AN rainfall over the western and northern GHA. These areas covered

Uganda, Western Kenya, southern and central Sudan, western Ethiopia, Eritrea, Lake Victoria Basin of Tanzania, Rwanda and much of Burundi. The GHACOF map indicated a likelihood of BN to NN rainfall over the eastern GHA covering Southern and SE Ethiopia, the East of Kenya, Somalia, and much of Tanzania (ICPAC, 2010 b). The regional consensus forecast for the SOND 2009 season (ICPAC, 2009 b) indicated likelihood of AN rainfall over the equatorial eastern and western GHA (Figure 4-37 d). Most of the central areas indicated increased probability of NN to AN rainfall. The Southern regions of the sub-region have increased the likelihood of receiving BN precipitation.

Regional consensus forecast for MAM 2012 for various zones in EA (part and parcel of the GHA) indicated a likelihood of NN to BN rainfall over much of the GHA. There exist evidence of frequent episodes of both excessive (Webster *et al*. 1999; Latif *et al*. 1999) and deficient rainfall (Hastenrath *et al*. 2007) in EA. Therefore, the MAM 2012 seasonal climate outlook would have necessitated precipitation enhancement as a means to increase available water resources. Moreover, Opijah *et al.* (2014) noted that MAM season is one of the two main rainfall seasons in the equatorial sector of the GHA. Therefore, the study identified MAM 2012 as representative of an NN to BN season in EA.

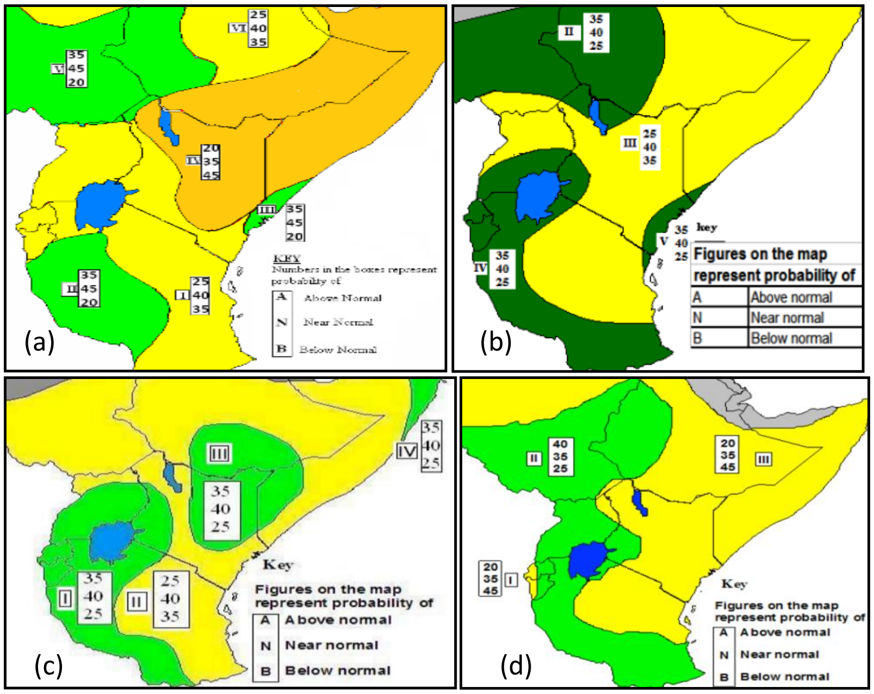

Figure 4-36: Greater Horn of Africa Consensus forecast for the March to May for a) 2012 b) 2011 c) 2010 and d) 2009 (Source ICPAC 2009-2012).

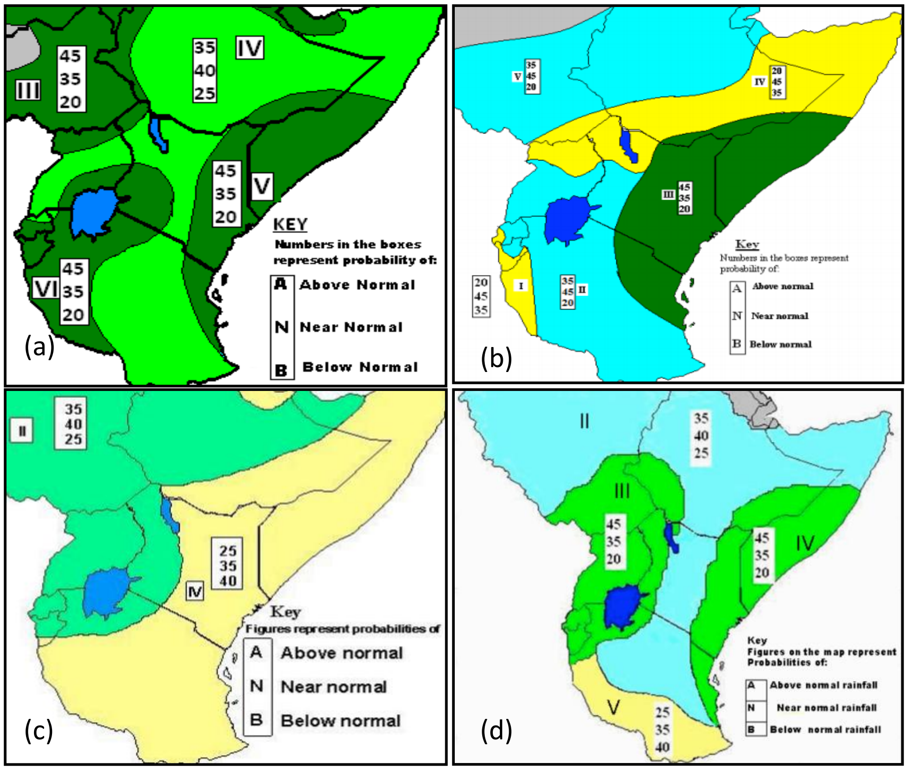

Figure 4-37: Greater Horn of Africa Consensus forecast for the September to December for a) 2012 b) 2011 c) 2010 and d) 2009 (Source ICPAC 2009-2012).

4.2.3.2 Verification of Seasonal Forecast

The Table 4-4 to 4-6 presents analysis of results from contingency table.

Table 4-4: Contingency Table for the observed and forecast precipitation during MAM

	Forecast				
Observed		BN	NN	AN	M-Totals
	BN	14	44	4	62
	NN	4	23	6	33
	AN	2	6	1	9
	M-Totals	20	73	11	104

Table 4-5: Contingency Table for the observed and forecast precipitation during SOND

	Forecast				
Observed		BN	NN	AN	M-Totals
	BN	0	13	13	26
	NN	4	17	23	44
	AN	13	8	13	34
	M-Totals	17	38	49	104

Table 4-6: Verification scores based on contingency table during MAM and SOND

	MAM			SOND		
	BN	NN	AN	BN	NN	AN
FAR (%)	30.0		90.9	100.0		73.5
Hit Rate (%)	22.6	69.7	11.1	0.0	38.6	38.2
BIAS	0.32	2.21	1.22	0.65	0.86	1.44
CSI	0.21	0.28	0.05	0.00	0.26	0.19
HSS	0.029			-0.094		

During MAM, the FAR was found to be 30% for BN compared to 90.9% for AN. On the contrary, during SOND, FAR was found to be 100% for BN compared to 73.5% for AN. The lower FAR indicates that the GHA consensus forecast corresponded well with the observed in the

BN category. The POD show a more accurate forecasted precipitation in the NN (69.7%) compared to BN (22.6%) and AN (11.1%) during MAM. Conversely, the POD showed that NN (38.6%) and AN (38.2%) were more accurate compared to BN (0.0%) category during SOND. During MAM, Bias values of 2..21 and 1.22 in the NN and AN categories indicated an overestimation of observed precipitation. However, the BN category had a Bias value of 0.32 and thus an underestimation of observed precipitation. Conversely, during the SOND, the BN and NN categories indicated underestimation of observed precipitation. The CSI values ranged between 5-28% and 0-26% during MAM and SOND. Therefore, indicating less reliability of GHA consensus forecast and attributed errors in the process used to develop them. Mwangi *et al.* (2014) noted that the development of consensus maps rely heavily on a plethora of information During MAM, HSS values of 0.029 indicated that consensus forecast was comparable to the observed. However, the during SOND, the negative HSS values indicated that consensus forecast was worse than the observations.

4.2.3.3 Identification of Deep Convective Clouds

4.2.3.3.1 Convective Available Potential Energy

The Figure 4-38 and Figure 4-39 presents results based on CAPE analysis.

In Figure 4-38, positive values of CAPE indicated the availability of energy for convection. Time latitude plots (Figure 4.38 a) shows that meridional transition in CAPE with higher values of up to 1100J/kg in the SH at the start of the MAM 2012 season. The movement in CAPE shifted northwards towards NH and intensified at the end of MAM season. Zonal transition in CAPE (Figure 4.38 b) showed higher values of up to 1000J/kg over Rwanda, Burundi and Western Tanzania at the start of the MAM season. Notably, the end of the MAM season indicated extreme CAPE values of up to 1800J/kg along the coast of EA. Therefore, potential for formation of deep convection. Several studies (Williams *et al.*, 2002; Khain *et al.*, 2005, Khain *et al.*, 2008) have shown increased updraft invigoration by approximately 20% with sea surface-based CAPE values of 1000–1500 Jkg^{-1}over Amazon which has a typical climate similar to the equatorial belt.

Time series analysis (Figure 4-39) of selected stations over Mt. Kenya catchment clustered as either in Location A (Nyahururu and Nakuru) or Location B (Nanyuki, Embu, Meru, Naivasha and Nyeri). They showed a similar temporal pattern of positive CAPE values with highest values in April towards May. Czaja and Blunt (2011) found that currents over the Western boundary such as Agulhas and their extensions into the open ocean that favour initiation and growth of deep convection. The study attributed the observed processes to the poleward advection of warm water in the western boundary currents that generate regions of strong atmosphere-ocean disequilibrium. Therefore, favouring heating and moistening at the base of the air column and leading to convective instability. Agulhas current (warm western boundary current) supports the highest air-sea fluxes in the world (Beal *et al.*, 2011; Rouault *et al.*, 2000; Rouault *et al.*, 1995).

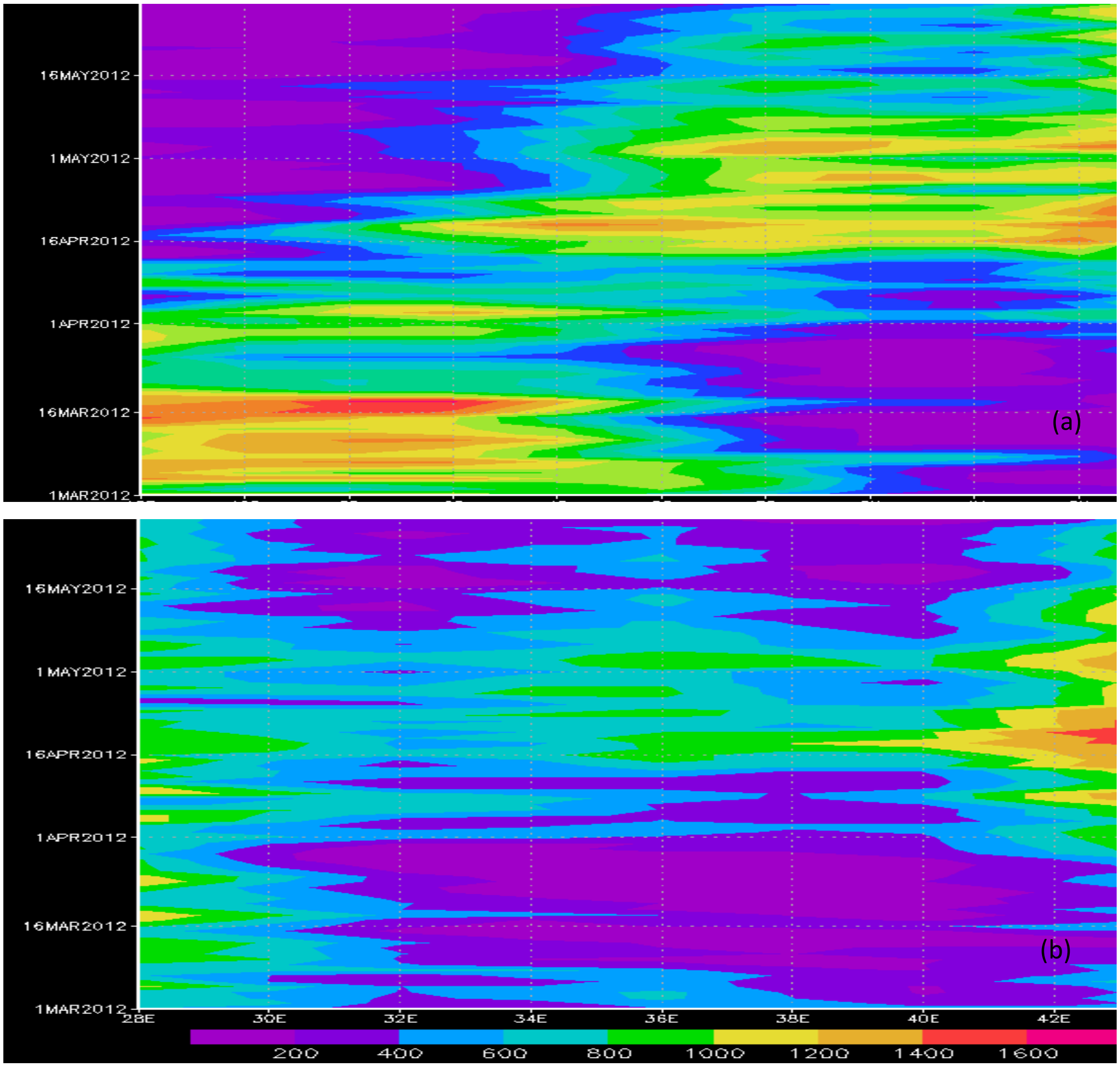

Figure 4-38: Hovmoller diagram a) time latitude b) time longitude of Convective Available Potential Energy for March April May 2012 period

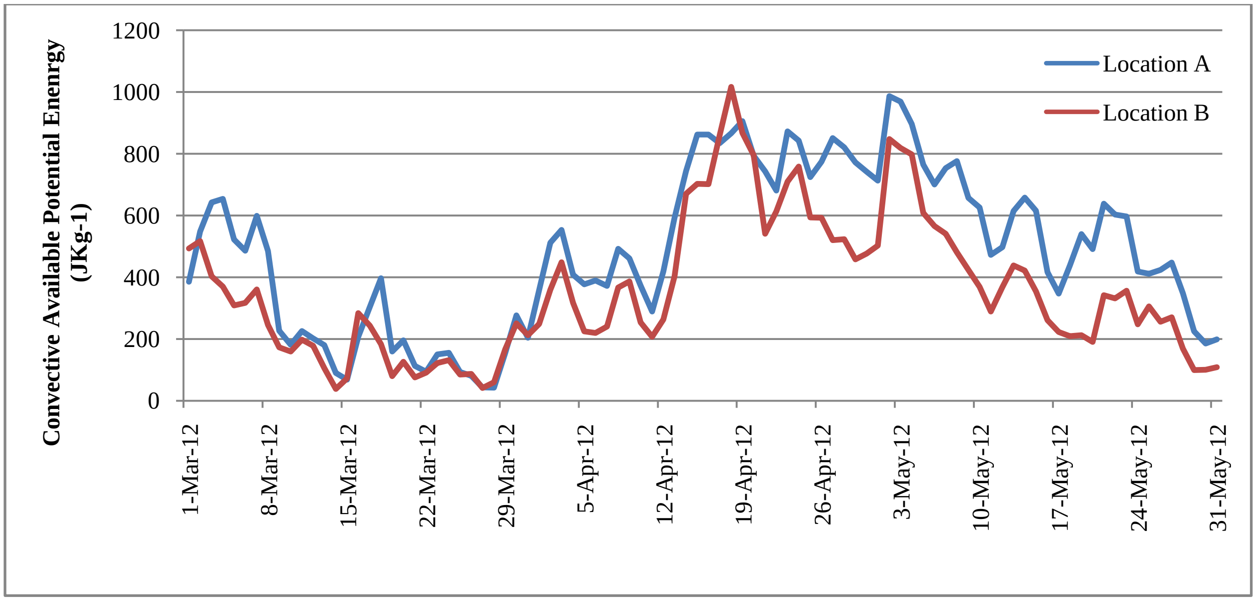

Figure 4-39: Daily Convective Available Potential Energy at the Surface over Mt. Kenya catchment during March April May 2012

4.2.3.3.2 Cloud Characteristics

The Figure 4-40 to Figure 4-43 presents results based on cloud characteristics analysis. Spatial variation of COD (Coloured) and CTP (Contour) in EA is shown in Figure 4-40 while Figure 4-41 to Figure 4-43 shows time series for COD and CTP over Mt. Kenya catchment.

The Figure 4-40 shows that COD for 2012 MAM season ranged between 0 and 50 with lower values of less than five off the coast of Kenya. Moreover, CTP values ranged between 300MB over western Lake Victoria to above 600MB on the eastern sides of EA over the coast of Kenya and Tanzania. The study attributes lower CTP values to the presence of the lake which provides a cooling effect. Notably Merchand *et al.* (2010) indicates that ISCCP uses the observed infrared brightness temperature to determine CTT, from which CTP is inferred using an atmospheric profile that relates temperature to pressure.

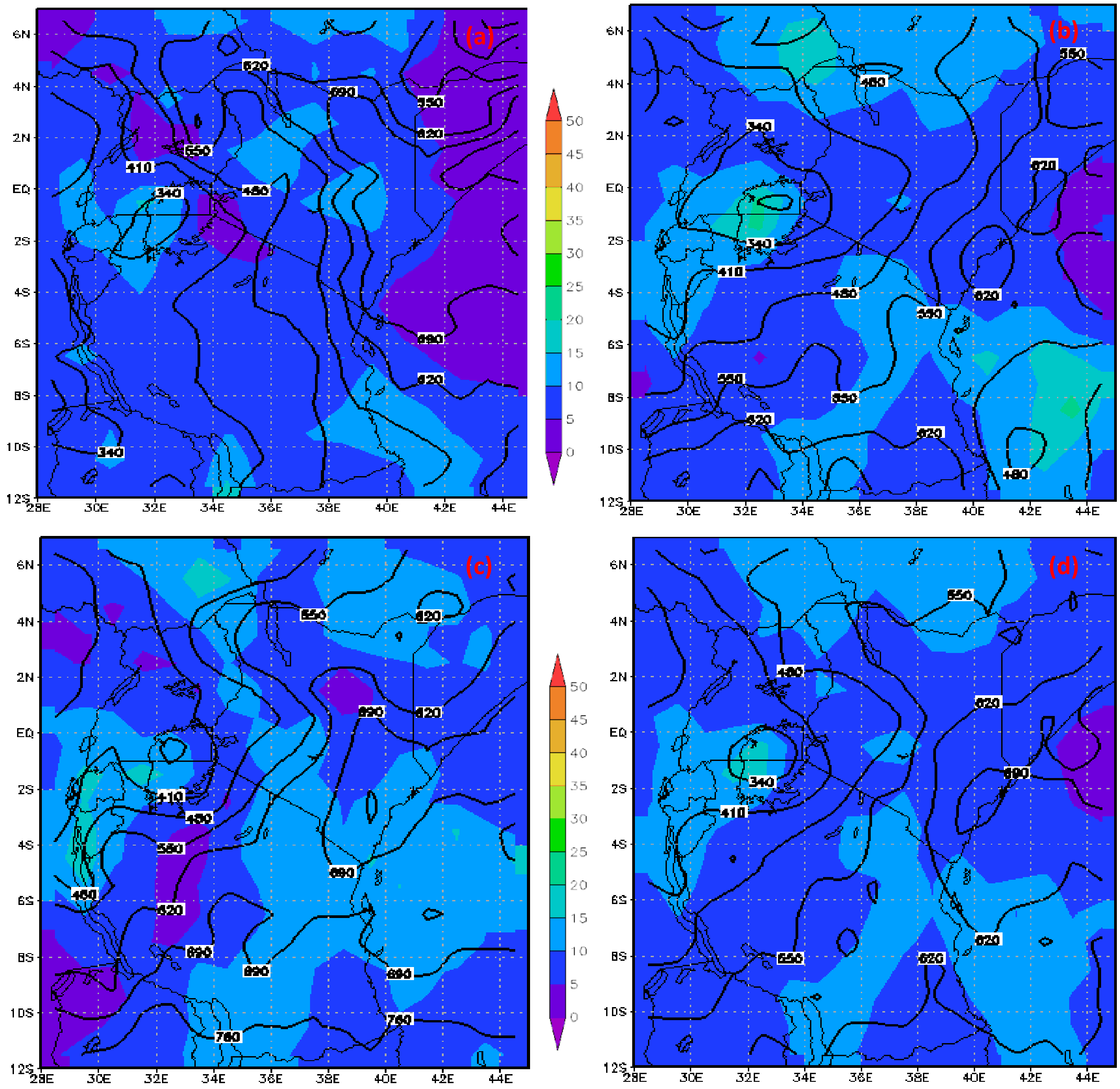

Figure 4-40:Spatial variation of Cloud Optical Depth (Colored) and Cloud Top Pressure (Contour) in EA for a) March b) April c) May and d) MAM 2012 period

In Figure 4-41, CTP and COD over selected stations around Mt. Kenya are highly varied with CTP ranging from 200MB to 900MB while COD ranged from 0 to 50. In Nyahururu, DCCs formed over pentad 13 (2nd March), pentad 19 (3rd April) and pentad 21 (12th April) (Figure 4-41 a). Others days in which DCCs formed included pentad 29 (21st, 23rd, 24th, 25th May) and pentad 24 (28th May). In Naivasha (Figure 4-41 b), DCCs formed on pentad 21 (12th April 2012).Empirical and theoretical studies have shown that orography plays a leading role in the formation of local perturbations, in the creation of vertical components of wind speeds and thus promoting the formation and development of clouds, precipitation and thunderstorms ().

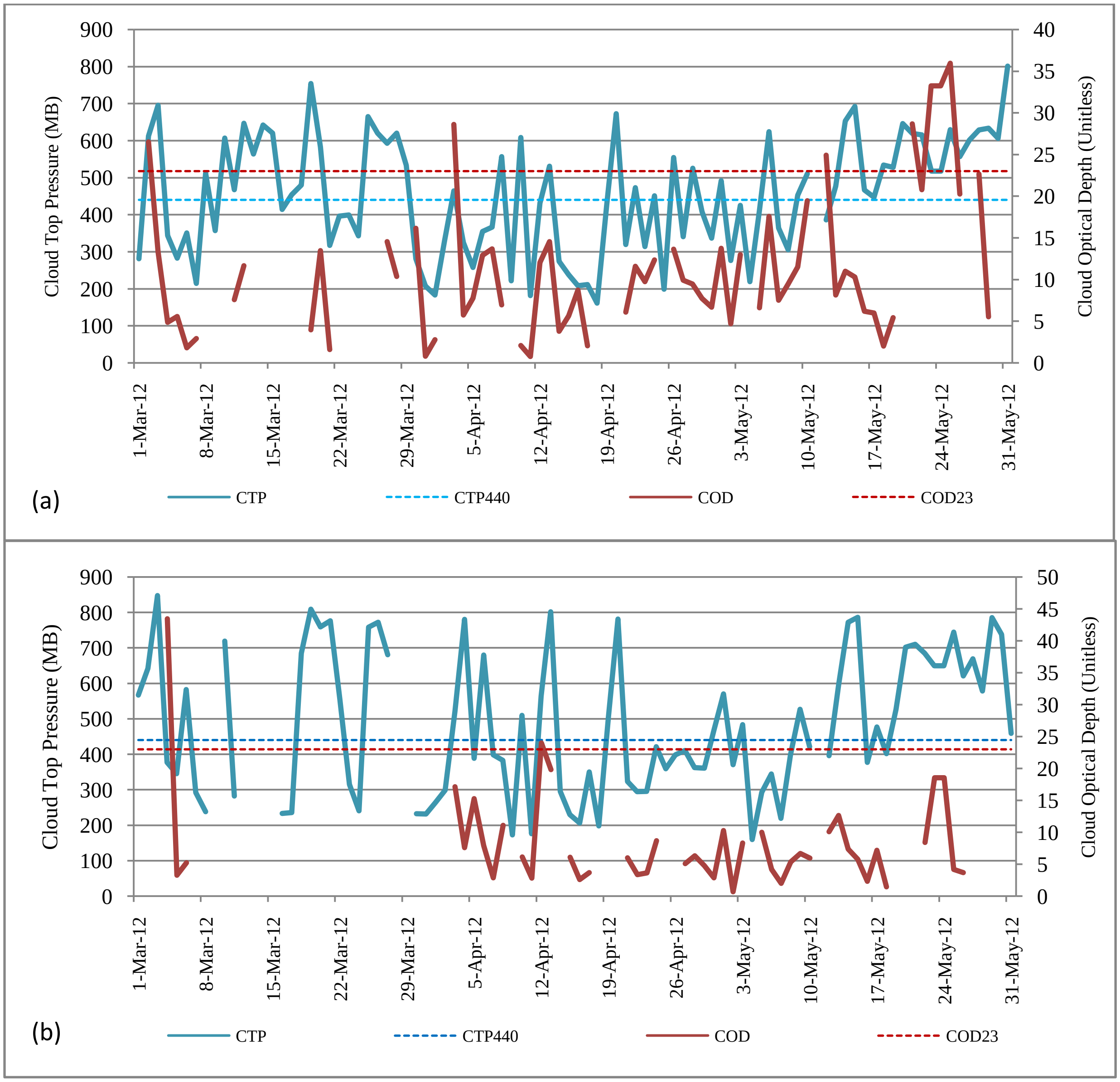

Figure 4-41: Time series of Cloud Top Pressure (CTP) and Cloud Optical Depth for a) Nyahururu b) Naivasha Stations

In Embu, DCCs formed on pentad 16 (20th March 2012), pentad 17 (25th March 2012) and pentad 19 (3rd and 5th April 2012) (Figure 4-42 a). Other days in which DCCs formed included pentad 29 (21st, 23rd, 24th and 25th May). In Meru, DCCs formed on pentad 16 (20th March) and pentad 29 (21st, 23rd and 24th May 2012) as shown in Figure 4-42 (b).

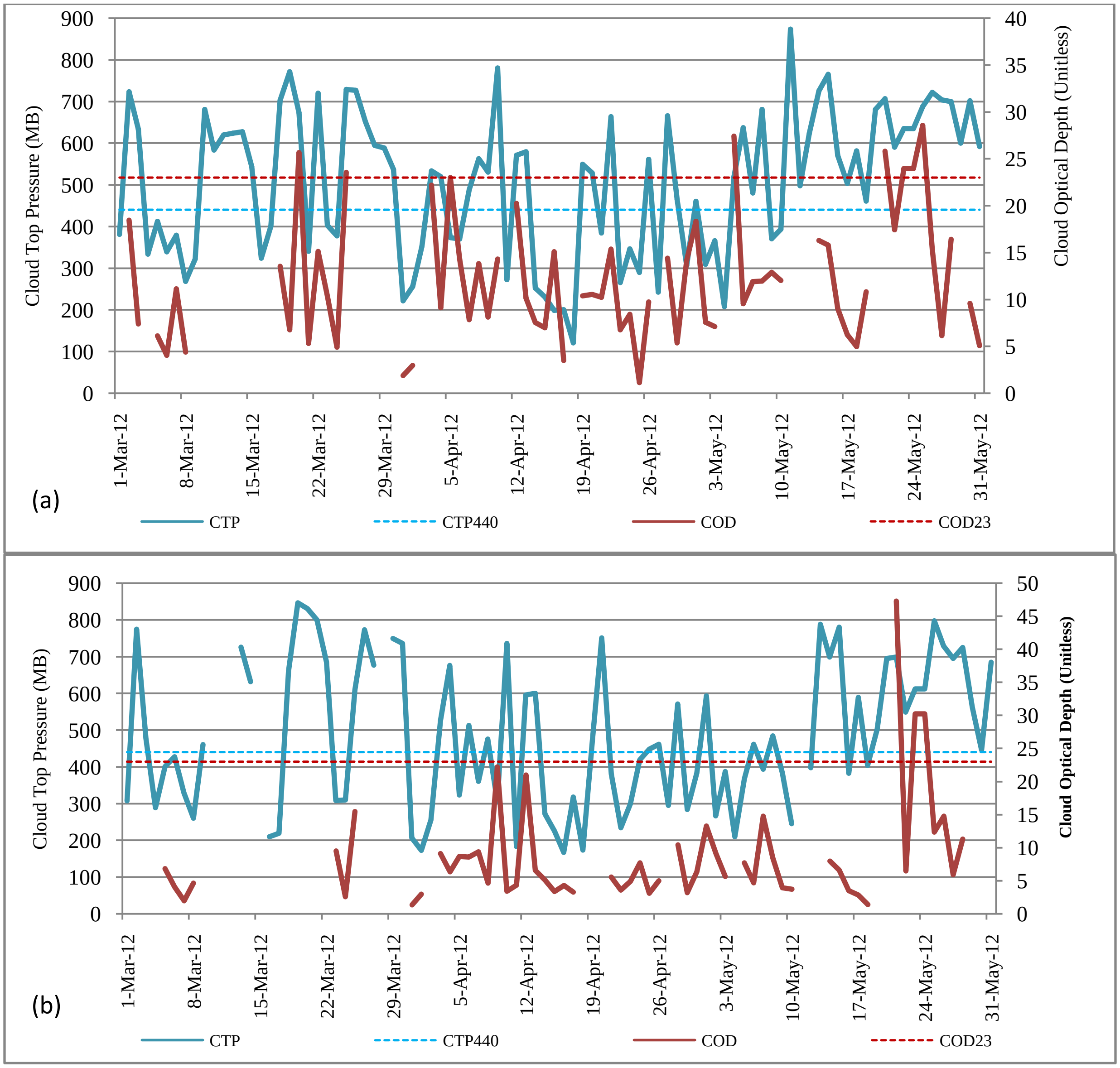

Figure 4-42: Time series of Cloud Top Pressure (CTP) and Cloud Optical Depth for a) Embu and b) Meru Stations

In Nakuru, DCCs formed on pentad 13 (2nd March), pentad 19 (3rd April) and pentad 27 (12th May) (Figure 4-43 a). Other days in which DCCs formed included pentad 29 (21st, 23rd, 24th and 25th May) as shown in Figure 4-43 (a). In Nanyuki, DCCs formed on pentad 16 (20th March), pentad 20 (9th April) and pentad 29 (21st, 23rd and 24th May 2012) (Figure 4.43, b).

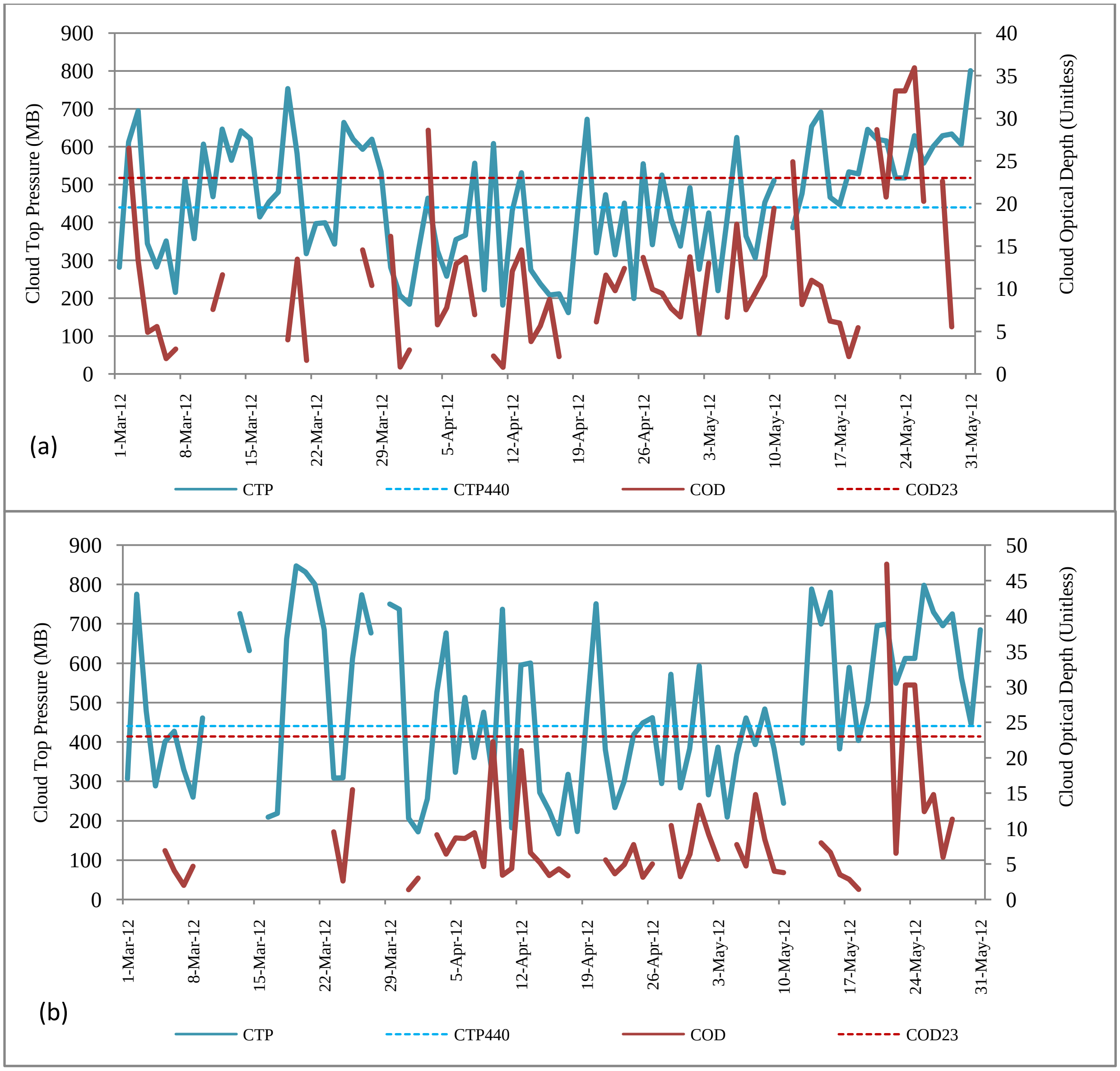

Figure 4-43: Time series of Cloud Top Pressure (CTP) and Cloud Optical Depth over (a) Nakuru and (b) Nanyuki station.

Times series of CTP and COD indicated two distinct patterns over Mt Kenya catchment. For MAM 2012 season, the formation of DCCs dominated pentad 29 (21^{st} to 25^{th} May 2012). Therefore, pentad 29 formed the basis for further analysis.

4.3 Evaluation of WRF Microphysics to Simulations of Deep Convective Cloud System

The study identified pentad 29 over Mt. Kenya catchment during MAM 2012 season as representative of weather modification conditions in EA. Therefore, the study aimed at evaluating the efficiency of WRF model to simulate the DCCs. Morrison bulk microphysics (Appendix 4) was assessed based on vertical velocity (updrafts and downdrafts profiles) and accumulated precipitation.

4.3.1 Simulation of Updrafts and Downdrafts

The Figure 4-44 to Figure 4-46 show observed, and model simulated updrafts and downdrafts profiles at the surface (1000 MB) and cloud base (700 MB) levels. In the three events considered in pentad 29, Morrison MP scheme simulated the initiation of downdraft Cores almost at the same time as observed. However, a difference of at least one (1) ms^{-1} was noted in the magnitude of simulated downdrafts and updrafts cores. The study attributed these differences to the resolution of the two datasets used in deriving the vertical velocity. Notably, observed data utilized NCEP reanalysed datasets that are at course resolution (~200 km) while WRF model output data are at a fine resolution (~ 10 km). Moreover, simulated updrafts were in the order of 2 ms^{-1} compared to observed updrafts which exceeding four (4) ms^{-1}. The finer resolution (~3 km) of WRF model output used resulted in the initiation of several updrafts and its associated downdrafts with strong downdrafts below the updraft cores. On the contrary, the NCEP reanalysis datasets indicated the presence of a single strong updraft core around 09:00 UTC. Lean *et al.* (2008) used the Met Office Unified Model and showed that in the case of explicit convection, the initiation of convection takes place more rapidly as the grid length is reduced. Studies e.g. Rosenfeld and Woodley (2000) and Rosenfeld *et al. (*2008) noted that strong updrafts may thrust large concentrations of CCN above the homogeneous ice nucleation level. Therefore, slowing the autoconversion rate due to freezing of particles into sizes that have no effective mechanism to coagulate and fall as precipitation.

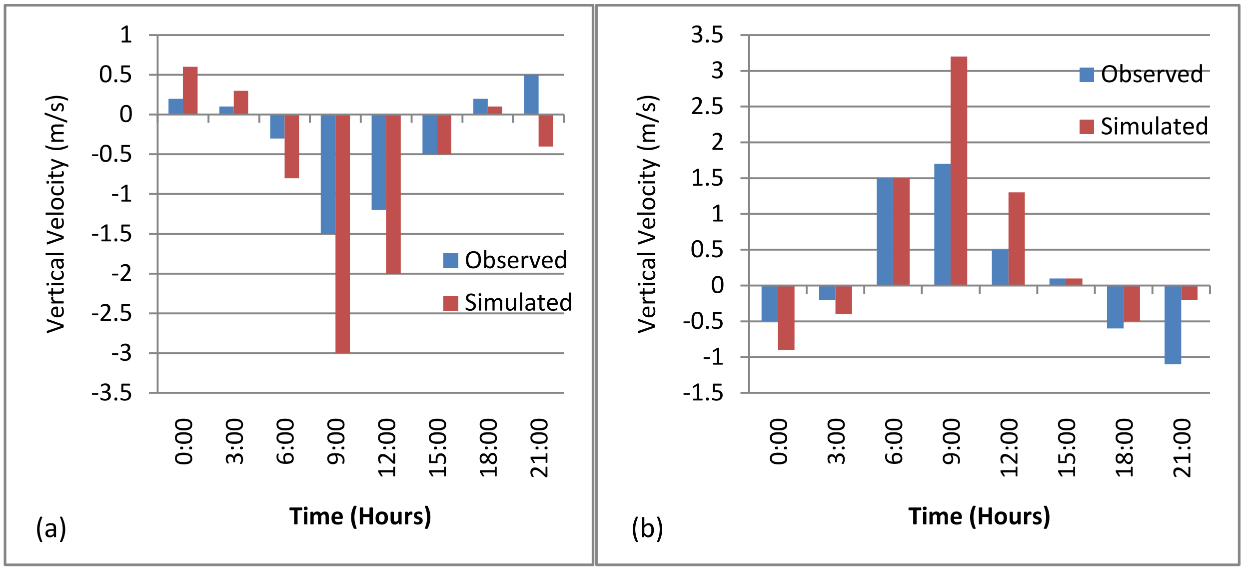

Figure 4-44: Vertical velocity (m/s) derived from observed and model simulation at a) 700 MB and b) 1000 MB over Mt. Kenya catchment (May 21, 2012).

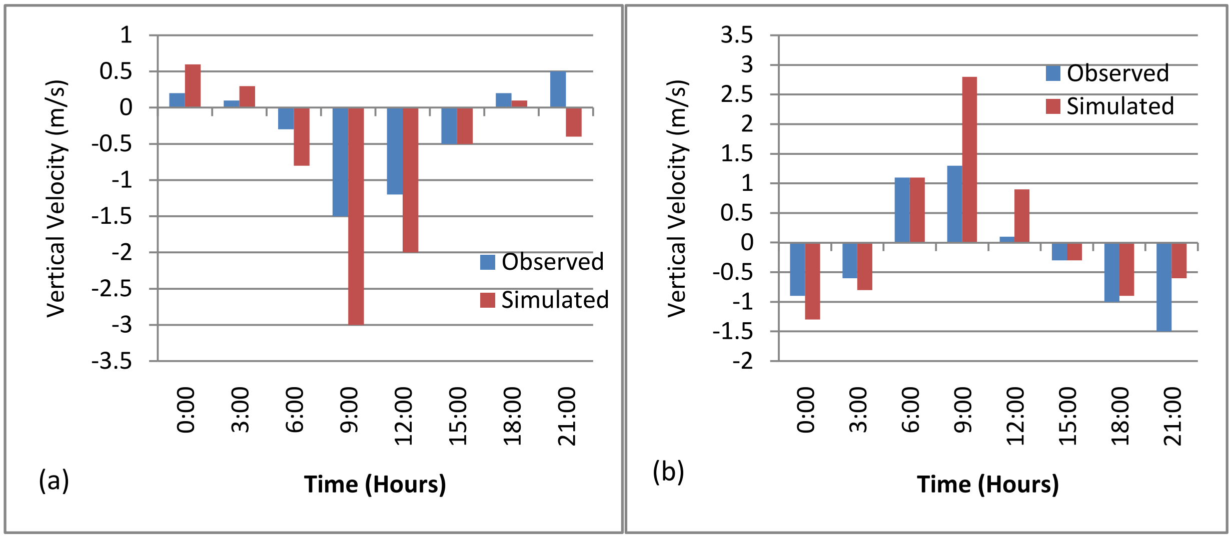

Figure 4-45: Vertical velocity (m/s) derived from observed and model simulation at a) 700 MB and b) 1000 MB over Mt. Kenya Catchment (May 23, 2012).

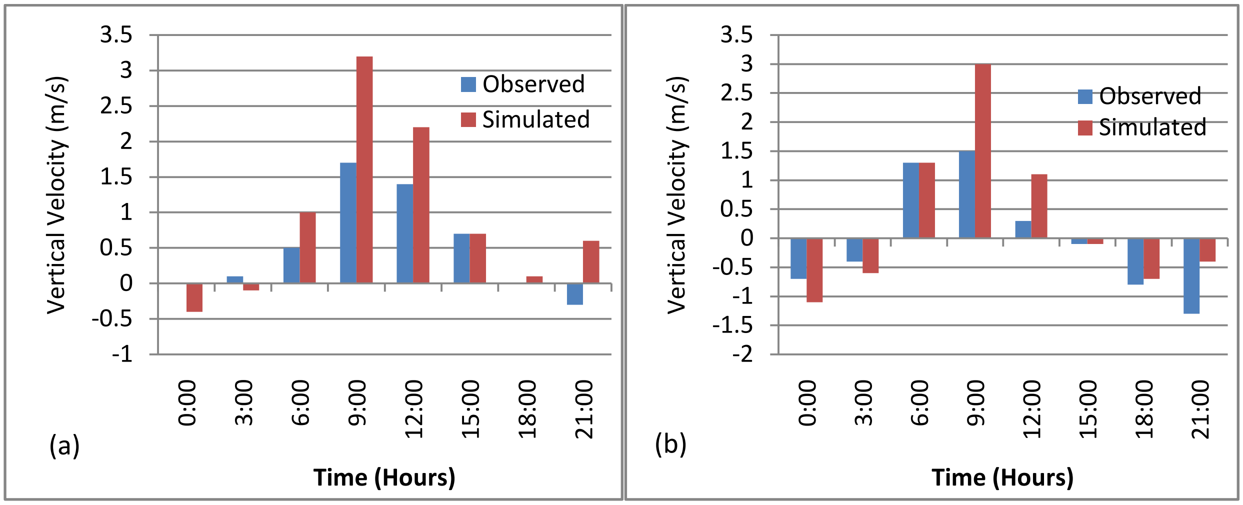

Figure 4-46: Vertical velocity (m/s) derived from observed and model simulation at a) 700 MB and b) 1000 MB over Mt. Kenya Catchment (May 25, 2012).

4.3.2 Precipitation

Simulated and observed accumulated rainfall associated with the DCCs event for 21st, 23rd and 25th May 2012 (pentad 29) is presented in Figure 4-47 to Figure 4-48. The study showed that WRF model simulated rainfall accumulated for 21st, 23rd and 25th May 2012 were comparable to observed. Jankov *et al.* (2005) found that the greatest variability in rainfall estimates from the WRF model originated from changes in the choice of the convective scheme. However, notable impacts were observed from changes in the microphysics and PBL schemes. Further, rainfall estimates slightly varied in different configurations while biases increased with time aggregation (Ruiz *et al.*, 2010). The study noted that finer spatial resolution used in WRF model compared to TRMM satellite explained the well representation of observed precipitation by the WRF model. Moreover, the use of explicit parameterization scheme ensured that DCCs were well represented. However, WRF model simulated precipitation overestimated the observed precipitation. Based on previous studies, the overestimation of observed precipitation maybe attributed to TRMM's algorithms that have been noted not perform optimally in areas of high terrain (Barros *et al.*, 2006; Hong *et al.*, 2007; Dinku *et al.*, 2007; Dinku *et al.*, 2008; Bitew and Gebremichael, 2010; Dinku *et al.*, 2010; Hirpa *et al.*, 2010; Rosenfeld *et al.*, 2014)

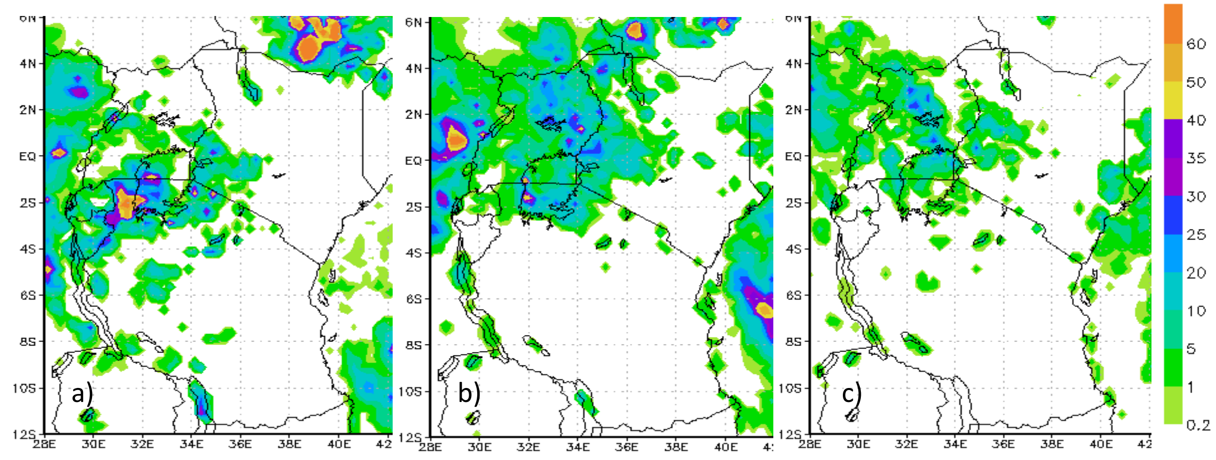

Figure 4-47: Simulated precipitation based on WRF model for 21st, 23rd and 25th May 2012.

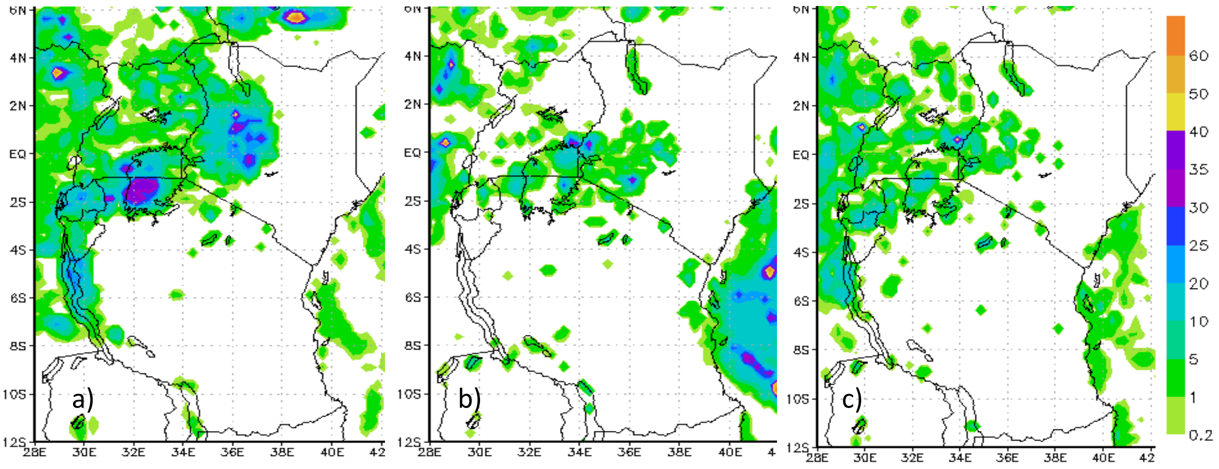

Figure 4-48: Observed precipitation based on observed (TRMM 3B42) for 21st, 23rd and 25th May 2012.

4.4 Effects of Cloud Seeding on Precipitation modification

Numerical simulation of effects of cloud seeding on precipitation modification was evaluated based on how it affected the microphysical properties and convective strength. The study also assesses how varying aerosol concentration influences precipitation.

4.4.1 Microphysical Properties

Figure 4-49 compares vertical profiles of mass concentrations (time-averaged and summed over the horizontal domain) of five hydrometeors under three aerosol scenarios. These scenarios included a low CCN of 100 cm^{-3}, an intermediate CCN of 1000 cm^{-3}, and a high CCN of 3000 cm^{-3}.

Within the cloud (Figure 4-49 a), the Maximum Cloud Water Content (CWC) was attained in the high CCN scenario case. In the low CCN scenario, CWC was lowest. Notably, the higher CCN concentration led to more condensation of water vapour on activated aerosols. Therefore resulting to a larger CWC. On the contrary, the highest or lowest rainwater content is achieved under the low or high CCN scenario (Figure 4-49). According to Li *et al.* (2008), observed phenomena was attributable to the delayed conversion of cloud droplets to raindrops due to the reduction of the mean effective radius of cloud droplets with increasing CCN. Further, Satellite-derived vertical profiles of the cloud droplet effective radius were noted to increase as the depth of the cloud increased (Rosenfeld and Lensky, 1998; Freud *et al.*, 2005). Glaciated seeded tracks in super-cooled layer clouds were observed to spread slowly for more than an hour after seeding and reached a width of less than 15 km (Rosenfeld, 2007).

At the freezing point, the condensation of water vapour occurs with negligible differences in the height of maximal CWC under the three aerosol scenarios. However, the heights of maximal CWC for the low aerosol scenario are lower than intermediate and high aerosol scenarios. Compared to intermediate CCN scenario, the study shows less precipitation reaching the ground in the low CCN scenario (Figure 4-49 b) since the raindrops and graupels are larger at higher CCN (Table 4-7). Increasing CCN concentrations results in delay initiation of precipitation with enhanced maximum updraft before rain formation (Table 4-7). Enhanced updrafts favour large sized precipitating particles and longer growth time and thus survive evaporation as they fall to a sub-saturated environment below the cloud base. Under the high CCN scenario, ice nucleation is hindered due to the formation of large concentrations of cloud droplets as a result of larger precipitation particles that are less concentrated (Li *et al.*, 2008; Noppel and Beheng, 2009). It should also be noted that several studies (Bruintjes, 1999; Silverman, 2003; DeFelice *et al.*, 2013) have indicated that seeded cloud or cloud system was made up of potentially enhanced dynamic effects or microphysical effects, which increase the amount of precipitation.

The Table 4-7 also shows that melting of graupels accounts for the largest size of raindrops in the high CCN scenario. Under the low CCN scenario, increased evaporation of precipitating particles with smaller sizes results in the greatest gradient in the rainwater profile below 3km (Figure 4-49 b). On the contrary, under the high CCN scenario, most precipitating particles reaching the surface due to their larger sizes are accounts for the small rainwater gradient profile below 3km. In the high CCN case, ice production is minimal because of inefficient ice nucleation. According to Pruppacher and Klett (1997), immersion freezing is dependent on the droplet size and is suppressed by the formation of large amounts of small droplets. Besides, anvil formation is hindered in the high CCN case because of a large mass loading of small droplets to decrease the buoyancy and less latent heat from droplet freezing. Hudson (2007) notes that the size of CCN reflects the hygroscopicity (solubility) of atmospheric particles.

The intermediate CCN case corresponds to the largest amounts of ice and snow (Figures 4-49 c and Figure 4-49 d) due to efficient ice nucleation and strongest convection strength. Therefore, through the process of aggregation, ice crystals are converted to snow efficiently. Compared to the high CCN scenario, the low CCN scenario is characterized by increased ice formation and less snow formation. Therefore, reflecting a less efficient conversion of ice to snow because of smaller ice crystals. The Figure 4-49 (e) shows that the largest graupel mass occurred under the low CCN scenario as a result of transportation of many raindrops and freezing in the cold cloud regime. However, the size of graupels is much smaller than those in the other two CCN cases (Table 4-7). On the contrary, inhibited ice nucleation results to reduced graupel produced in the high CCN scenario. However, once produced, the graupel particles are larger. In overall, the study indicated that the distribution of orographic precipitation strongly depends on the composition and size of the background aerosols which serve CCN as noted by Muehlbauer and Lohmann (2009).

Table 4-7: Time-averaged precipitable cloud properties under three aerosol conditions (Low, intermediate and high CCN concentrations)

Variable	Low	Intermediate	High
Time of Initial formation of rain (Minutes)	30	50	60
Maximum updraft before rain formation (m s^{-1})	2.6	4.6	5.9
Mean of effective radius of raindrop (µm)	300	500	600
Mean of effective radius of graupel (µm)	520	700	900

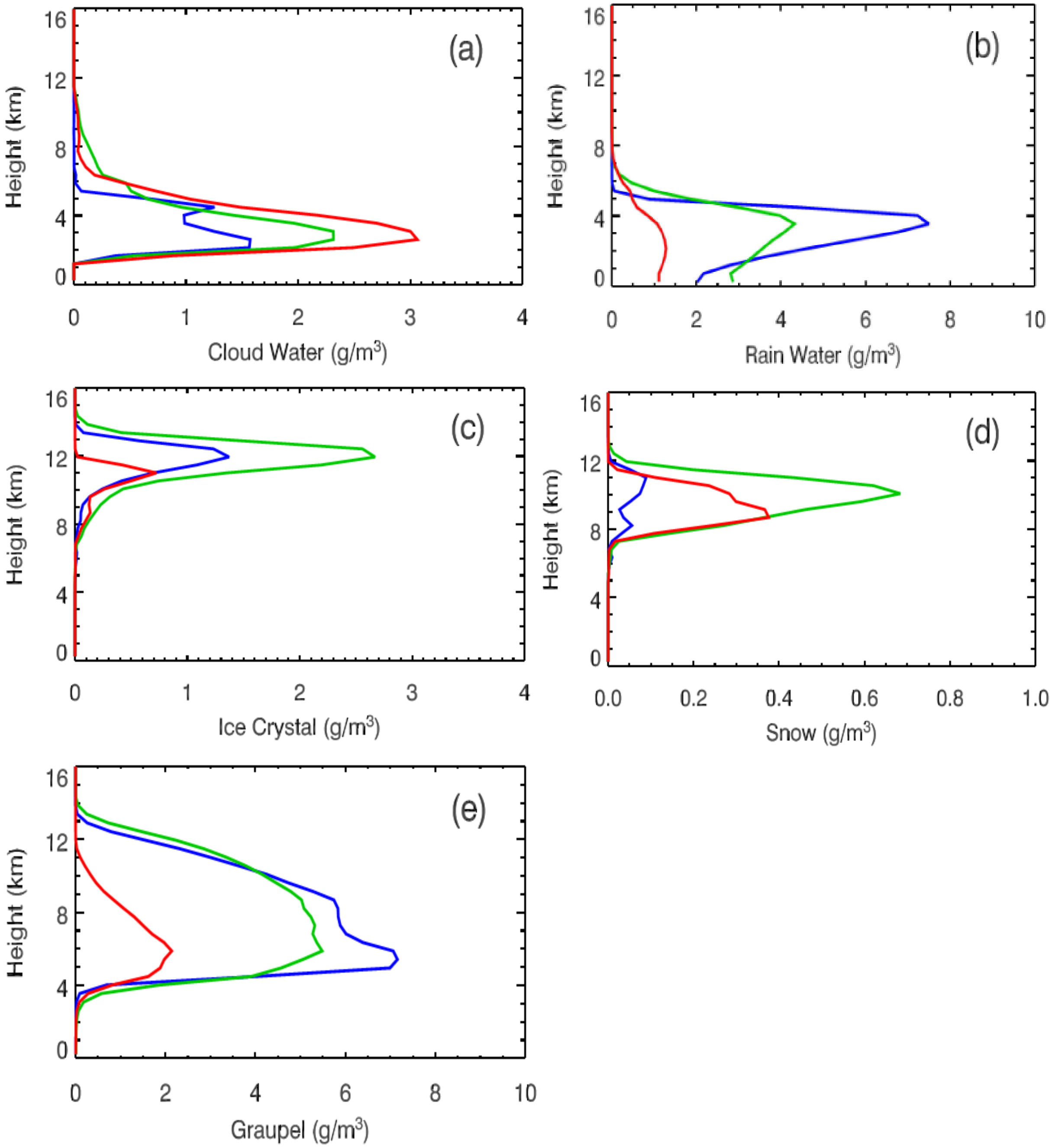

Figure 4-49: Vertical profiles of time-averaged masses of hydrometeors for (a) cloud water, (b) rainwater,(c) ice crystal, (d) snow, and (e) graupel

4.4.2 Precipitation

The Table 4-8 shows the dependence of precipitation on mean of the CDNC from 200 cm^{-3} to 3000 cm^{-3} and initial CCN from 100 cm^{-3} to 3000 cm^{-3}.

In general, the dependence of precipitation inside the model domain showed increasing CDNC with increasing CCN (Table 4-8). The increasing CDNC was consistent with more activation of aerosols to form cloud droplets with increasing CCN (Li *et al.,* 2008; Fan *et al.,* 2007). However, accumulated total precipitation exhibited a complex variation with both CDNC and CCN, showing a nonlinear relationship. When CCN is relatively small (CCN100 scenario), Total precipitation is not very sensitive to CCN and increases slightly by approximately 30% with CCN from 100 to 1000 cm^{-3}. Previous studies in EA over Kericho areas (Henderson, 1975; Schnell and Vali, 1976; Rogers and Vali, 1978) indicated average annual increase in rainfall upto 12% within the protected area, statistically significant at the 0.10 level attributed to aerosol. Likewise, when CDNC is relatively small, total precipitation is not very sensitive to CDNC but increases with increased concentration. According to Noppel and Beheng (2009), small aerosol particles in high number concentrations will produce small cloud droplets with a narrow size distribution. Similarly, Pruppacher and Klett (1997) noted that an increase in aerosol load led to an increase in cloud droplet number concentration. Aerosol sizes also influence the microphysical properties of clouds (Peng *et al.,* 2002) as aerosols in DCCs suppress warm rain and allows lifting of the greater amount of liquid water content by updrafts above the freezing level. Therefore, additional latent heat is released to energize the clouds (Andreae *et al.,* 2004; Koren *et al.,* 2005; Rosenfeld *et al.,* 2008).

Variation of CCN from 100 cm^{-3} to 3000 cm^{-3} resulted to significant increase in total precipitation from 2.1 mm to 2.6 mm and subsequent decreases in CCN concentration above 1000 cm^{-3}. According to Li *et al.* (2008), enhanced precipitation due to increasing aerosols under low CCN scenario is linked to suppression of conversion of cloud droplets to raindrops. Further, convective strength is enhanced resulting in more efficient mixed phase process and reduced efficiency in warm rain. Besides, the hydrometeors fall within a relatively wet environment that corresponds humid atmosphere. Therefore, accounts for the low loss of falling precipitating mass from high levels by evaporation and sublimation resulting in increased precipitation with an increase in aerosols (Khain *et al.,* 2005, Khain *et al.,* 2008; Huang *et al.,* 2009a, Huang *et al.,* 2009b). On the contrary, under extremely high CCN scenario, there is a significant decrease in total precipitation due to the minimal production of ice resulting from hindered anvil formation and inefficient ice nucleation. The varied response relates to less latent heat from droplet freezing and reduced buoyancy due to large mass loading of small droplets that inhibit sufficient growth of hydrometeors to survive evaporation. Studies indicate suppression of warm rain processes in convective clouds under the influence of heavy smoke (Rosenfeld, 1999) and clouds with CTT of about 10^{o}C in industrial and urban air pollution (Rosenfeld, 2000). Further, simulation of DCC under dry continental conditions showed decreased in precipitation with increasing aerosols from 100 to 1260 cm^{-3} (Khain *et al.*, 2005). Evaporation of drops and sublimation of ice when falling through the deep layer of dry air outside the cloud was attributable to reduced precipitating mass and thus decreased precipitation efficiency. Higher cloud water mixing ratios present in instances of high aerosol concentrations are argued to lead to enhanced cooling by evaporation within (Zipser, 2003).

Table 4-8: Accumulated precipitation as a function of Cloud Droplet Number Concentration (CDNC) and initial Cloud Condensation Nuclei (CCN) under different scenarios

	CDNC200	CDNC400	CDNC800	CDNC1600	CDNC2000
CCN100	2.1	2.5	2.9	3.4	1.8
CCN500	2.3	2.8	2.9	4.1	2.1
CCN1000	2.6	3.2	3.4	4.7	2.5
CCN2000	5.1	5.7	5.8	7.0	5.0
CCN3000	1.4	1.9	2.0	3.2	1.2

4.4.3 Convective Strength

The Figure 4-50 and Figure 4-51 presents results of the convective strength of the modelled cumulus measured by the mean downdraft and updraft in a core area.

The average of the cumulus core updraft increases from about 2.0 to 3.5 m s^{-1} when CCN is between 100 and 300 cm^{-3} but decreases when CCN is greater than 1000 cm^{-3} (Figure 4-50, blue). Efficient mixed phase processes are resulting in the release of extra latent heat due to droplet freezing contributed to increased core updrafts under CCN concentrations of less than 1000 cm^{-3}. These results are affirmed by Koren and Feingold (2011) and Tao *et al.* (2012) which noted that smaller droplets are less suitable to collide and coalesce and thus inhibit precipitation with a potential increase in cloud lifetime.

On the contrary, unlike precipitation, at CCN of 1000 cm^{-3}, the decrease in cumulus core draft to about 2.7 m s^{-1} corresponding to the latent heat released from droplet condensation. In contrast, the mean of the downdraft increases steadily with CCN (Figure 4-50, red). A study by Li *et al.* (2008) linked the rise in core downdraft to large mass loading of hydrometeors which resulted in decreased buoyancy. Moreover, Ntelekos *et al.* (2009) attributed stronger updrafts and downdraughts and more organized convection to elevated aerosol concentrations. Therefore, it either enhanced the growth of graupels leading to induced downdrafts locally with increasing CCN concentration or evaporation cooling of small droplets resulting to increased downdrafts and decreased updrafts. Similarly, the maximum updraft increased with increasing CCN until it reached 500 cm^{-3} (Figure 4-51, blue). The maximum updraft is less sensitive to changes in CCN when CCN concentration ranges between 500 and 1000 cm^{-3} whereas the maximum updraft reduces at CCN above 1000 cm^{-3}. The Figure 4-51 (red) shows that the maximum downdraft increases with increasing CCN concentration.

Studies e.g. Khain *et al.* (2000), Cui *et al. (*2006), Rosenfeld and Woodley (2000) and Rosenfeld *et al.* (2008) noted that reduced CCN concentrations resulted in a substantial increase in the convective strength of the clouds resulting to increased rainfall amount. Similarly, the results of this study affirms results by Koren and Feingold (2011) and Tao *et al.* (2012). Similarly, Reutter *et al.* (2009) indicated that activated particles was high with the available particle number limiting CDNC independent of the updraft velocity under high aerosol regime. Further, CDNC dominated the updraft velocity since the fraction of activated particles, and the super-saturation are low under low aerosol regime while CDNC was sensitive to both, aerosol, and updraft velocity under intermediate regime. Zipser (2003) noted that high aerosol concentration in DCCs enhanced invigoration and secondary (outflow-based) updraft invigoration.

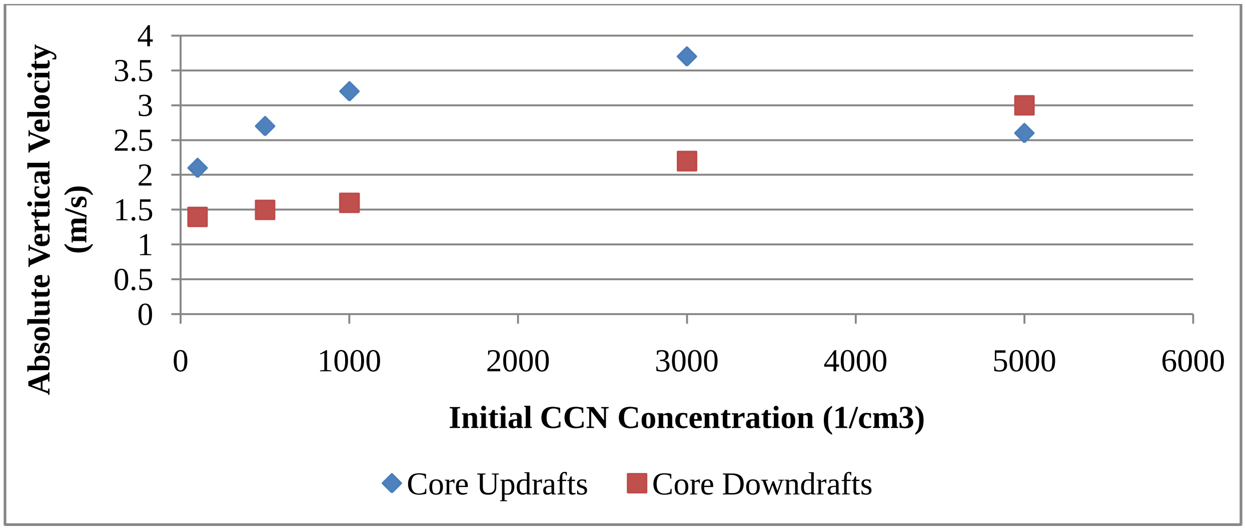

Figure 4-50: Simulated population means of updraft (blue) and downdraft (red) in the core area

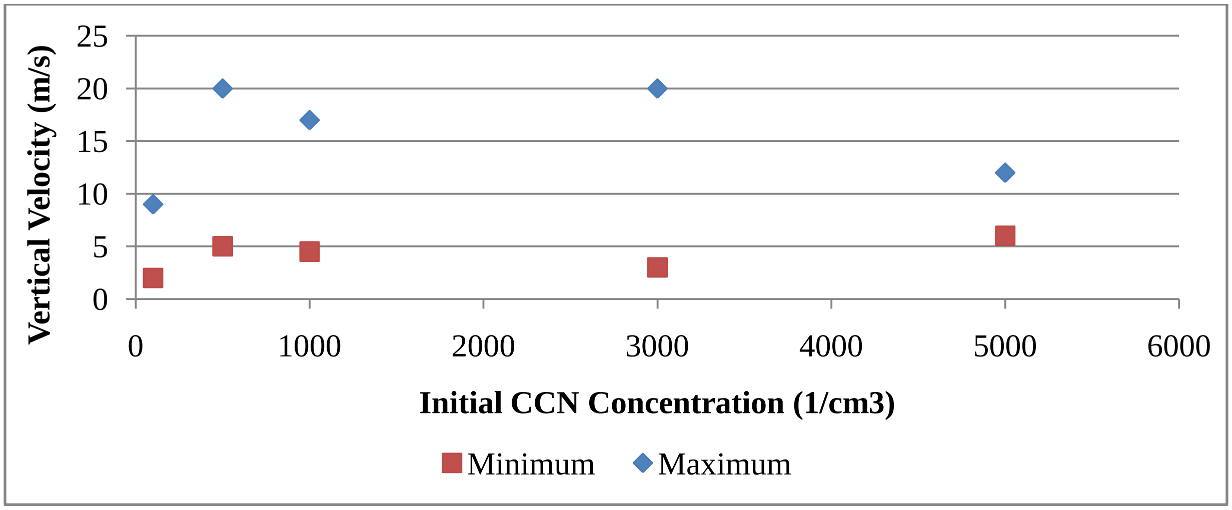

Figure 4-51: Simulated maximum (blue) and minimum (red) vertical velocity as a function of the initial CCN

CHAPTER FIVE

5 CONCLUSIONS AND RECOMMENDATIONS

This chapter presents conclusions and recommendation of the study.

5.1 Conclusion

The PCA analysis yielded 13, 20, 11, 9 and 16 PCs during MAM for AOD, FMF, CTT, OLR and TRMM 3B42 respectively. Similarly, PCA analysis yielded 14, 18, 10, 10 and 17 PCs during OND for AOD, FMF, CTT, OLR and TRMM 3B42 respectively. The identified PCs were found to be significant at 95% confidence (α=0.05) level based on Monte Carlo testing. Maximum factor loadings based on FMF showed similarities with AOD spatial distribution. Regions of high concentration identified included Central Kenya, Coastal Kenya (Mombasa), Coastal Tanzania (Dar es Salaam), Eastern Uganda around Lake Victoria, Western Uganda, and Rwanda. Notably, FMF values had the highest variability during MAM compared to OND. The CTT values showed the highest variability over Central Tanzania, Coastal Kenya, Zanzibar, Central Kenya, Uganda (Central and Western) and Rwanda. Seasonal variability was high during OND compared to MAM. OLR values showed highest variability over Northern Uganda, Rwanda and Eastern Parts of Mt. Kilimanjaro. Further, the study showed that OLR had highest seasonal variability during OND compared to MAM. Spatial analysis of satellite derived rainfall (3B42) showed high variability during both MAM and OND with several scattered areas of high rainfall distribution over the EA region attributed to complex mechanism and processes responsible for rainfall formation. Over Western, Central and NE Kenya and Southern Tanzania, variability in aerosols is linked to wash-out and rainout process during precipitation formation process. FMF were less affected by precipitation and dominated the Central and Northern Kenya and moved northwards towards NE Kenya during MAM. Longitude/Latitude -time plots in EA indicated the presence of both zonal and meridional moving atmospheric systems based on Clouds, Aerosols, and Rainfall.

During MAM, Clouds (CTT and OLR) were noted to have a negative contribution in the developed rainfall model as shown by negative coefficient values at selected stations. However, the negative coefficient values had small influence and thus less significant contribution attributed to low coefficient values all centred about zero. This pattern was similar during OND for clouds (CTT and OLR) and aerosols (AOD and FMF). All aerosol and cloud variables with strong factor loading in EA had a positive relationship with rainfall except in Kigali, Entebbe, and Soroti during MAM and Kasese and Tanga during OND. The D-W test indicated that these variables were independent with values around 2 for both MAM and OND. Histograms of model residual were symmetrical in shape over selected regions during both OND and MAM in the MLR and thus indicated normality in the model residuals. The QQ plots affirmed the results based on histograms for the selected stations that followed a straight line.

HYSPILT backward trajectory analysis indicated that at different levels above the ground, transported particles in the atmosphere had different origins. Aerosols particles underwent vertical mixing inland of EA. Further, several mountains as high as 2000m situated near the Great Rift Valley in EA not only block transport of Sahel smoke eastwards but also inhibit movement of dust. These mountains include Mt. Kenya, Kilimanjaro, and Ruwenzori. Inhibiting transport of smoke and dust results in mixing of aerosols and thus enhanced precipitation in areas with high precipitation factor loading.

The GHA consensus forecast maps showed that MAM rainfall season constitutes an important rainfall season over the equatorial parts of the GHA. The SOND season constitutes an important rainfall season over the equatorial and southern parts of GHA. Regional consensus forecast for MAM 2012 for various zones in EA region (part and parcel of the GHA) indicated a likelihood of NN to BN rainfall over much of the GHA. Therefore, the MAM 2012 seasonal climate outlook would have necessitated precipitation enhancement as a means to increase available water resources. The lower FAR indicates that the GHA consensus forecast corresponded well with the observed in the BN category. The POD shows a more accurate forecasted precipitation in the NN (69.7%) compared to BN (22.6%) and AN (11.1%) during MAM. Conversely, the POD showed that NN (38.6%) and AN (38.2%) were more accurate compared to BN (0.0%) category during SOND. During MAM, Bias values of 2.21 and 1.22 in the NN and AN categories indicated an overestimation of observed precipitation. However, the BN category had a Bias value of 0.32 and thus an underestimation of observed precipitation. Conversely, during the SOND, the BN and NN categories indicated underestimation of observed precipitation. The CSI values ranged between 5-28% and 0-26% during MAM and SOND. Therefore, indicating less reliability of GHA consensus forecast and attributed errors in the process used to develop them. During MAM, HSS values of 0.029 indicated that consensus forecast was comparable to the observed. However, the during SOND, the negative HSS values indicated that consensus forecast was worse than the observations.

Positive values of CAPE indicated the availability of energy for convection in EA. Time latitude plots showed that meridional transition in CAPE with higher values of up to 1100J/kg in the SH at the start of the MAM 2012 season. The movement in CAPE shifted northwards towards NH and intensified at the end of MAM season. Zonal transition in CAPE showed higher values of up to 1000J/kg over Rwanda, Burundi, and Western Tanzania at the start of the MAM 2012 season. Notably, the end of the MAM season indicated extreme CAPE values of up to 1800J/kg along the coast of EA. Therefore, potential for formation of deep convection. Similarly, the temporal pattern of positive CAPE values with highest values in April towards May indicated favourable conditions (heat and moisture) leading to convective instability. Times series of CTP and COD indicated two distinct patterns over Mt Kenya Region. For MAM 2012 season, the formation of DCCs dominated pentad 29 (21st to 25th May 2012). Stations located over Eastern and Western EA with mean temperatures greater than -10°C were unsuitable for cloud seeding activities. However, areas located over central EA region and mainly along the rift valley and coastal Tanzania were noted as suitable locations with optimal temperatures for cloud seeding.

Evaluation of the efficiency of WRF microphysics shows that Morrison scheme simulated the initiation of downdraft cumulus core almost at the same time as observed. The study used a finer resolution of WRF model output (innermost domain ~ 3 km with explicit convection). It resulted in the initiation of several updrafts and its associated downdrafts with strong downdrafts below the updraft cores compared to NCEP reanalysis datasets. Accumulated precipitation based on TRMM 3B42 and WRF model output for Mt. Kenya Region were also found to be comparable to the 24h simulation. However, instead of two nested domains, one single cloud resolving domain may be preferred to avoid the influence of convection parameterization in the outer domains.

The response of precipitation to the increase of aerosol concentration is non-monotonic. The study indicates that different meteorological and aerosols scenarios affect precipitation due to a complicated interaction between dynamics and cloud microphysics. Notably, the dependence of precipitation inside the model domain showed increasing CDNC with increasing CCN, which was consistent with more activation of aerosols to form cloud droplets with increasing CCN.

Increasing aerosols concentration from Maritime to continental backgrounds results in increased precipitation. Precipitation increased with increase in CDNC and CCN from maritime/clean to continental/polluted conditions and reduced/suppressed at highly polluted conditions (CDNC >1600 cm^{-3}, CCN >2000 cm^{-3}). However, under highly polluted aerosol scenarios, precipitation is considerably reduced or completely suppressed. Unlike precipitation, the core draft decreases in high CCN scenarios corresponding to the latent heat released from droplet condensation. In contrast, the mean of the downdraft increases steadily with CCN. The maximum downdraft increases with increasing CCN. Therefore, the response of precipitation to the increase of aerosol concentrations is non-monotonic due to a complicated interaction between dynamics and clouds microphysics. Similarly, the core updraft and maximal vertical velocity responses are comparable to precipitation.

The study indicates the possibility of enhancing precipitation in EA in locations with similar conditions to Mt. Kenya catchment. Therefore, this study forms part of the process towards design, development and implementation of weather modification programs to enhance available water resources in EA. Increasing the available fresh water through precipitation enhancement over major water towers in the region will augment existing stream flows. Therefore, ensure water is available downstream and thus spur sustainable development by alleviating the existing and projected water stress.

5.2 Recommendations for Further Study

Despite the significant progress made towards weather modification, many critical issues and challenges remain unresolved and require stronger scientific evidence and support.

Use of satellite-derived data as a proxy for ground-based measurements requires extensive validation. There is a need for continued improvement in the resolution of the datasets at both spatial and temporal scale. Increased monitoring network of ground-based measurements will enable availability of more datasets and thus improve on the validation exercise and thus more confidence.

In EA, the use of consensus forecast in predicting the seasonal weather limits assessment of weather modification efforts and thus need to develop and design of robust methodologies for use during seasonal consensus forecast. The complex mechanism involved in the aerosol-cloud-precipitation process in EA will necessitate detailed parameterization to enhance the utilization of these models not only in weather forecasting but also design and implementation of planned weather modification. Further, research into potential benefits and challenges of planned weather modification activities in EA.

References

Ackerman, A.S., Kirkpatrick, M.P., Stevens, D.E. and Toon, O.B., 2004. The impact of humidity above stratiform clouds on indirect aerosol climate forcing, *Nature*, **432**, 1014–1017.

Ackerman, A.S., van Zanten, M.C., Stevens, B., Savic-Jovcic, V., Bretherton, C.S., Chlond, A., Golaz, J.-C., Jiang, H., Khairoutdinov, M., Krueger, S.K., Lewellen, D.C., Lock, A., Moeng, C.-H., Nakamura, K., Petters, M.D., Snider, J.R., Weinbrecht, S. and Zulauf, M., 2009. Large-eddy simulations of a drizzling, stratocumulus-topped marine boundary layer, *Mon. Weather Rev.*, **137**, 1083–1110.

Akaike, H., 1974: Factor analysis and AIC. *Pschychometrika*. **52**:317-332.

Alam, K., Iqbal, M.J., Blaschke, T., Qureshi, S. and Khan, G., 2010. Monitoring the spatiotemporal variations in aerosols and aerosol-cloud interactions over Pakistan using MODIS data. *Advances in Space Research* **46**, 1162-1176.

Alapaty, K., Madala, R.V. and Raman, S., 1994a. Numerical simulation of orographic convective rainfall with Kuo and Betts-Miller cumulus parameterization schemes. *J. Meteor. Soc. Japan*, **72**, 123–137.

Alapaty, K., Raman, S., Madala, R.V. and Mohanty, U.C., 1994 b. Monsoon rainfall simulation with Kuo and Betts-Miller schemes. *Meteorol. Atmos. Phys.*, **53**, 33–49.

Albrecht, B.A., 1989. Aerosols, Cloud Microphysics, and Fractional Cloudiness, *Science*, **245** (4923), 1227–1230.

Aloysius, M., Mohan, M., Parameswaran, K., George, S.K. and Nair, P.R., 2008. Aerosol transport over the Gangetic basin during ISRO-GBP land campaign-II. *Ann. Geophys*. **26**, 431-440.

Alusa A.L., 1976. The occurrence and nature of hailstorms in Kericho, Kenya. *The second WMO Scientific Conference on Weather Modification, Boulder Colorado,* Preprints, WMO Geneva, 249-256.

Andreae, M.O., Rosenfeld D., Artaxo, P.A. Costa, Frank, A.G.P., Longo, K.M. and Silva-Dias, M.A.F., 2004. Smoking rain clouds over the Amazon. *Science*, **303**, 1337-1342.

Anthes, R. A. 1977. A cumulus parameterization scheme utilizing one-dimensional cloud model, *Mon. Weather Rev.,* **105**, 270–286.

Arkin. P.A. and Ardanuy, E., 1989. Estimating Climatic-scale precipitation from space. A Review. *J. Climate*, 2: 1229-1238.

Asnani, G.C., 2005. Tropical Meteorology, revised edition. Indian Institute of Tropical Meteorology, *Pune, India* **2**, 753pp.

Bangert, M., Kottmeier, C., Vogel, B. and Vogel, H., 2011. Regional scale effects of the aerosol cloud interaction simulated with an online coupled comprehensive chemistry model. *Atmos. Chem. Phys*, **11** (9), 4411–4423.

Banta, R. and Hanson, K.R., 1987. Sensitivity studies on the continentality of a numerically simulated cumulonimbus. J. *Clim. Appl. Met.,* **26**, 275-286.

Barros, A.P., Chiao, S. Lang, T.J. Burbank, D. and Putkonen J., 2006. From weather to climate—Seasonal and interannual variability of storms and implications for erosion process in the Himalaya. *Geological Society of America Special Paper,* **398**, Penrose Conference Series, Boulder, CO, 17–38.

Bates, B.C., Kundzewicz, Z.W., Wu, S. and Palutikof, J.P. (Eds.)., 2008. Climate Change and Water, IPCC Tech. Paper VI, IPCC Secretariat, Geneva.

Beal, L.M., De Ruijter, W.P.M., Biastoch, A. and Zahn, R., 2011. On the role of the Agulhas system in ocean circulation and climate. *Nature***, *472*** (7344), 429-436.

Begum, B.A., Biswas, S.K., Pandit, G.G., Saradhi, I.V., Waheed, S., Siddique, N., Seneviratne, M. C.S., Cohen, D.D., Markwitz, A. and Hopke, P.K., 2011: Long Range Transport of Soil Dust and Smoke Pollution in the South Asian Region. Atmos. Pollut. Res. 2: 151–157.

Bell, T.L, Rosenfeld, D., Kim, K.M., Yoo, J.M, Lee, M.I. and Hahnenberger, M., 2008. Midweek increase in U.S. summer rain and storm heights suggests air pollution invigorates rainstorms, *J. Geophys*. **113**, (D02) 209.

Bell, T.L., Rosenfeld, D. and Kim, K.-M. 2009: Weekly cycle of lightning: Evidence of storm invigoration by pollution. *Geophys. Res. Lett.,* **36**, L23805, doi:10.1029/2009GL040915.

Betschart, M. and Hering, A., 2012. Automatic Hail Detection at MeteoSwiss - Verification of the radar-based hail detection algorithms POH, MESHS and HAIL. Technical Report **238**, *Bundesamt fur Meteorologie und Klimatologie, MeteoSchweiz*.

Betts, A.K. and Miller, M. J. 1986: A new convective adjustment scheme part II: single column tests using GATE wave, BOMEX, ATEX and arctic air-mass data sets, *Q.J.R. Meteor. Soc.,* **12**, 693–709.

Bitew, M.M. and Gebremichael, M., 2010. Evaluation through independent measurements: Complex terrain and humid tropical region in Ethiopia. *Satellite Rainfall Applications for Surface Hydrology*, M. Gebremichael and F. Hossain, Eds., Springer-Verlag, 205–214.

Bony, S., Colman, R., Kattsov, V.M., Allan, R.P., Bretherton, C.S., Dufresne, J., Hall, A., Hallegatte, S., Holland, M.M., Ingram, W., Randall, D.A., Soden, B.J., Tselioudis, G. and Webb, M.J., 2006. How Well Do We Understand and Evaluate Climate Change Feedback Processes?. *J. Climate*, **19**, 3445–3482.

Bretherton, C.S., Blossey, P. N. and Uchida, J., 2007. Cloud droplet sedimentation, entrainment efficiency, and subtropical stratocumulus albedo. *Geophys. Res. Lett.,* **34**, L03813.

Bruintjes, R.T., 1999. A review of cloud seeding experiments to enhance precipitation and some new prospects, *Bull. Amer. Meteorol. Soc.*, **80**, 805– 820.

Budhavant K.B., Rao, P. S. P., Safai, P. D., Granat, L. and Rodhe, H., 2014. Chemical composition of the inorganic fraction of cloud-water at a high altitude station in West India. *Atmospheric Environment*, **88** 59–65.

Buizer, J. L., Foster, J., and Lund, D., 2000. Global impacts and regional actions: preparing for the 1997-98 El Nino. *Bulletin of the American Meteorological Society*, **81**, 2121-2139.

Camberlin, P. and Okoola, R.E., 2003. The onset and cessation of the “long rains” in eastern Africa and their interannual variability. *Theor. Appl. Climatol.*, **75**, 43 – 54.

Chen, Y.C., Xue L, Lebo., Z.J, Wang, H., Rasmussen, R.M, and Seinfeld, J.H., 2011. A comprehensive numerical study of aerosol –cloud –precipitation interactions in marine stratocumulus. *Atmos. Chem. Phys*, **11**, 9749–9769.

Christy, J.R., Norris, W.B. and McNider R.T., 2009. Surface temperature variations in East Africa and possible causes, *J. Clim.,* **22**, 3342–3356.

Chrysoulakis, N. and Cartalis, C., 2002. Improving the estimation of land surface temperature for the region of Greece: Adjustment of a split window algorithm to account for the distribution of precipitable water, *Int. J. Remote Sens.*, **23**, 871–880.

Collins, W.D., Rasch, P.J., Boville, B.A., Hack, J.J., McCaa, J.R. Williamson, D.L., Kiehl, J.T., and Briegleb B., 2004. Description of the NCAR Community Atmosphere Model (CAM 3.0), *Tech. Rep. NCAR TN–464+STR*, National Center for Atmospheric Research.

Compo, G.P., Whitaker, J.S., Sardeshmukh, P.D., Matsui, N., Allan, R.J., Yin, X., Gleason, B.E., Vose, R.S., Rutledge, G., Bessemoulin, P., Brönnimann, S., Brunet, M., Crouthamel, R.I., Grant, A.N., Groisman, P.Y., Jones, P.D., Kruk, M., Kruger, A.C., Marshall, G.J., Maugeri, M., Mok, H.Y., Nordli, O., Ross, T.F., Trigo, R.M., Wang, X.L., Woodruff, S.D. and Worley, S.J., 2011. The Twentieth Century Reanalysis Project. *Quarterly J. Roy. Meteorol. Soc.,* **137**, 1-28. DOI: 10.1002/qj.776.

Cotton, W.R, and Pielke, R.A., 1995. Human Impacts on Weather and Climate. *Cambridge University Press.*

Cui, Z., Carslaw, K.S., Yin Y. and Davies, S., 2006. A numerical study of aerosol effects on the dynamics and microphysics of a deep convective cloud in a continental environment. *J. Geophys. Res*. **111**, D05201. DOI: 10.1029/2005JD005981.

Czaja, A. and Blunt, N., 2011. A new mechanism for ocean–atmosphere coupling in midlatitudes, *Q. J. R. Meteorol. Soc.*, **137** (657), 1095-1101.

Davis, K.J., Lenschow, D.H., Oncley, S.P., Kiemle, C., Ehret, G., Giez, A. and J. Mann, 1997. Role of entrainment in surface-atmosphere interactions over the boreal forest, J. Geophys. Res., **102** (29) 219–29,230.

De Graaf M, Tilstra, L.G., Aben I. and Stammes P., 2010. Satellite observations of the seasonal cycles of absorbing aerosols in Africa related to the monsoon rainfall, 1995–2008. *Atmospheric Environment* **44** (10), 1274–1283.

Deardorff J.W., 1980. Stratocumulus-caped mixed layers derived from a three-dimensional model. *Boundary-Layer Meteorol* **18**:495–527.

DeFelice T.P., Golden J., Griffith D., Woodley W., Rosenfeld D., Breed D., Solak M, and Boe B, 2013. Extra Area Effects of Cloud Seeding - An Updated Assessment. Atmospheric Research. **135** (6), 193-203.

Dinku, T., Ceccato, P., Grover-Kopec, E., Lemma, M., Connor, S.J. and Ropelewski, C.F., 2007. Validation of satellite rainfall products over East Africa's complex topography, *International Journal of Remote Sensing*, **28** (7), 1503-1526.

Dinku, T., Chidzambwa, S., Ceccato, P., Connor S.J. and Ropelewski C.F., 2008. Validation of high-resolution satellite rainfall products over complex terrain, *International Journal of Remote Sensing*, **29:14**, 4097-4110.

Dinku, T., Connor, S.J. and Ceccato, P., 2010. Comparison of CMORPH and TRMM-3B42 over mountainous regions of Africa and South America. *Satellite Rainfall Applications for Surface Hydrology*, M. Gebremichael and F. Hossain, Eds., Springer-Verlag, 193–204

Dommenget, D. and Latif, M., 2002. A cautionary note on the interpretation of EOFs. *J. Climate*, **15**, 216-225.

Draxler, R. R. and Hess, G. D., 1998. An overview of the HYSPLIT_4 modelling system for trajectories, dispersion, and deposition, *Aust. Meteorol. Mag.*, 47, 295–308.

Dudhia, J., 1989. Numerical study of convection observed during the winter monsoon experiment using a mesoscale two-dimensional model. *J. Atmos. Sci.,* **46** (20), 3077-3107.

Dufresne, J.-L. and Bony, S., 2008. An assessment of the primary sources of spread of global warming estimates from coupled atmosphere-ocean models. *J. Clim.,* **21**, 5135–5144.

Dusek, U., Frank, G.P., Hildebrandt, L. Curtius, J. Schneider, J. Walter, S. Chand, D., Drewnick, F. Hings, S. Jung, D. Borrmann, S. and Andreae, M. O., 2006. Size matters more than chemistry for cloud-nucleating ability of aerosol particles. *Science*, **312**, 1375-1378.

Dye J.E and Breed D.W, 1979. The microstructure of clouds in the high-frequency hail area of Kenya. *J. Appl. Meteor.* **1** (18) 95-99.

Eck, T.F., Holben, B.N., Sinyuk, A., Pinker, R.T., Goloub, P., Chen, H., Chatenet, B., Li, Z., Singh, R.P., Tripathi, S.N., Reid, J.S., Giles, D.M., Dubovik, O., O’Neill, N.T., Smirnov, A., Wang, P. and Xia, X., 2010. Climatological aspects of the optical properties of fine/coarse mode aerosol mixtures, *J. Geophys. Res.*, 115, D19205.

Ek, M.B., Mitchell, K.E., Lin Y., Rogers, E., Grunmann, Koren, P.V., Gayno, G. and Tarpley, J.D., 2003. Implementation of Noah land surface model advances in the National Centers for Environmental Prediction operational mesoscale Eta model. *J. Geophys. Res.,* **108** (D22).

Ekman, A.M.L., Engström, A. and Wang, C., 2007. The effect of aerosol composition and concentration on the development and anvil properties of a continental deep convective cloud. *Q. J. R. Meteorol. Soc.,* **133**, 1439-1452.

Escudero, M., Stein, A., Draxler, R. R., Querol, X., Alastuey, A., Castillo, S. and Avila, A., 2006. Determination of the contribution of northern Africa dust source areas to PM10 concentrations over the central Iberian Peninsula using the Hybrid Single-Particle Lagrangian Integrated Trajectory model (HYSPLIT) model, *J. Geophys. Res.-Atmos.*, **111** (D6), D06210, doi:10.1029/2005JD006395, 2006.

Fan J., Ruby-Leung, L. DeMott, P.J., Comstock, J.M., Singh, B., Rosenfeld, D., Tomlinson, J.M., White, A., Prather, K., Minnis, P., Ayers, J.K., Min, Q., 2013. Aerosol Impacts on California Winter Clouds and Precipitation during CalWater 2011: Local Pollution versus Long-Range Transported Dust, *ACPD*, **13**, 19921–19970. doi:10.5194/acpd-13-19921-2013.

Fan, J, Zhang, R., Li, G., Tao, W.K. and Li, X., 2007. Simulations of cumulus clouds using a spectral microphysics cloud-resolving model. *J. Geophys. Res.–atmos.*, **112** (D4) 2341.

Feingold. G., Tzivion, S. and Levin, Z., 1988. The evolution of raindrop spectra: Part I. Stochastic collection and breakup. *J. Atmos. Sci.*, **45**, 3387-3399.

Feingold, G., Koren, I., Wang, H., Xue, H. and Brewer, W. A., 2010. Precipitation generated oscillations in open cellular cloud fields. *Nature*, **466**, 849–852.

Fisher, B.L., 2004. Climatological validation of TRMM TMI and PR monthly rain products over Oklahoma. *J. Appl. Meteor*, **43**, 519–535.

Freud, E. Rosenfeld, D., Andreae, M.O., Costa, A.A. and Artaxo, P., 2005. Robust relations between CCN and the vertical evolution of cloud drop size distribution in deep convective clouds, *ACPD*, **5** (5), 10,155–10, 195.

Funk, C., M.D. Dettinger, J.C. Michaelsen, J.P. Verdin, M.E. Brown, M. Barlow, and A. Hoell, 2008. Warming of the Indian Ocean threatens eastern and southern African food security but could be mitigated by agricultural development. *Proceedings of the National Academy of Sciences of the United States of America*, **105** (32), 11081-11086.

Gallus W.A.,1999. Eta simulation of three extreme precipitation events: sensitivity to resolution and convective parameterization, *Weather Forecast.*, **14**, 405–426.

Gatebe, C.K., Tyson, P.D. Annegarn, H., Piketh, S. and Helas, G., 1999. A seasonal air transport climatology for Kenya, *J. Geophys. Res.*, **104** (D12), 14237–14244.

Gilmore, M.S., Straka, S.M. and Rasmussen, E.N., 2004. Precipitation and evolution sensitivity in simulated deep convective storms: comparisons between liquid-only and simple ice and liquid phase microphysics, *Mon. Weather Rev*., **132**, 1897–1916.

Giovannettone, J.P. and Barros, A.P., 2009. Probing regional orographic controls of precipitation and cloudiness in the central Andes using satellite data. *J. Hydrometeor.,* **10**, 167–182.

Gitau, W., Ogallo, L.A., Camberlin, P. and Okoola, R.E., 2013. Spatial coherence and potential predictability assessment of intraseasonal statistics of wet and dry spells over equatorial Eastern Africa. *Int. J. Climatol*. **33** : 2690–2705.

Givati, A. and Rosenfeld, D., 2005. Separation between cloud-seeding and air-pollution effects. *J. Appl. Meteor*, **44**, 1298–1314.

Granat L., Norman, M., Leck, C., Kulshrestha, U.C. and Rodhe, H., 2002. Wet scavenging of sulfur compounds and other constituents during the Indian Ocean Experiment (INDOEX). *J. Geophys.* Res. - *Atmos*, **107** (19), 8025.

Grell, G.A., Dudhia, J. and Stauffer, D.R., 1994. A description of the fifth-generation Penn State-NCAR mesoscale model (MM5), *Tech. Note NCAR/TN- 23 398+STR*, 117 pp., Natl. Cent. Atmos. Res., Boulder, Colo.

Grell, G.A. 1993. Prognostic evaluation of assumptions used by cumulus parameterization, *Mon. Weather Rev.,* **121**, 764–787.

Gupta, P, Christopher, P.A., Wang, J., Gehring R., Lee, Y. and Kumar N., 2008. Satelliteremote sensing of particulate matter and air quality assessment over global cities. *Atmospheric Environment,* **40**, 5880-5892.

Hall, W.D., 1980. A detailed microphysical model within a twodimensional framework: Model description and preliminary results, *J. Atmos. Sci.,* **37**, 2486–2507.

Hansen, T.F., Pienaar, J. and Orzack S.H., 2008. A comparative method for studying adaptation to a randomly evolving environment. *Evolution* **62**:1965–1977.

Hastenrath, S., Polzin, D. and Mutai C., 2007. Diagnosing the 2005 drought in equatorial East Africa. J. Climate, **20**, 4628-4637.

Henderson T.J., 1975. The Kenya hail suppression program. *J. Weather Mod*, **7**, 192-199.

Hennessy, K.J., J.M. Gregory and J.F.B. Mitchell, 1997. Changes in daily precipitation under enhanced greenhouse conditions. *Clim. Dyn.*, **13**, 667-680.

Hession, S.L. and Moore, N., 2011. A spatial regression analysis of the influence of topography on monthly rainfall East Africa. *Int. J. Climatol.* **31**(10), 1440-1456.

Hill, A.A., Dobbie, S. and Yin, Y., 2008. The impact of aerosols on non-precipitating marine stratocumulus., *Q. J. Roy. Meteor. Soc.*, **134**, 1143–1154, doi:10.1002/qj.278.

Hill, A.A., Feingold, G. and Jiang, H., 2009. The influence of entrainment and mixing assumption on aerosol-cloud interactions in marine stratocumulus, *J. Atmos. Sci.*, **66**, 1450–1464, 2009.

Himeidan, Y.E. and Kweka E.J., 2012. Malaria in East African highlands during the past 30 years: impact of environmental changes. *Front Physiol*, **3**:1–11.

Hirpa, F.A., Mekonnen G. and Hopson T., 2010. Evaluation of High-Resolution Satellite Precipitation Products over Very Complex Terrain in Ethiopia. *J. Appl. Meteor. Climatol.*, **49**, 1044–1051.

Hong, Y., Gochis, D., Cheng, J.T., Hsu, K.L. Sorooshian, S., 2007. Evaluation of PERSIAN-NCCS rainfall measurement using the NAME Event Rain Gauge Network. *J. Hydrometeor*., 8, 469–482.

Houze, R.A., 1989. Observed structure of mesoscale convective systems and implications for large-scale heating. *Q. J. R. Meteorol. Soc.*, **115**, 425-461.

Houze, R.A., 1993. Cloud dynamics. *Academic Press*, Inc. 573 pp.

Houze, R.A., 2004. Mesoscale convective systems. *Rev. Geophys*, **42** (4), RG4003.

Huang, J., Lin, B., Minnis, P., Wang, T., Wang, X., Hu, Y., Yi, Y. and Ayers J.K., 2006. Satellite-based assessment of possible dust aerosols semi-direct effect on cloud water path over East Asia, *Geophys. Res. Lett.*, **33**, L19802, doi:10.1029/2006GL026561.

Huang, J., Zhang, C. and Prospero, J.M., 2009a. African aerosol and large-scale precipitation variability over West Africa. *Environ Res Lett,* 4 (1).

Huang, J., Adams, A., Wang, C. and Zhang, C., Fu, Q., Su, J., Tang, Q., Minnis, P., Hu, Y., Yi, Y. and Zhao, Q., 2009b. Taklimakan dust aerosol radiative heating derived from CALIPSO observations using the Fu-Liou radiation model with CERES constraints. *Atmos. Chem. Phys*, **9**, 4011–4021.

Hudson, J.G. and Da X., 1996. Volatility and size of cloud condensation nuclei, *J. Geophys. Res*.,101, 4435–4442.

Hudson, J. G., 2007. Variability of the relationship between particle size and cloud-nucleating ability, *Geophys. Res. Lett.,* 34, L08801, doi:10.1029/2006GL028850.

Huffman, G.J., Adler, R.F., Bolvin, D.T., Gu, G., Nelkin, E.J., Bowman, K.P., Hong, Y., Stocker, E.F. and Wolff, D.B., 2007. The TRMM Multi-satellite Precipitation Analysis: Quasi-Global, Multi-Year, Combined-Sensor Precipitation Estimates at Fine Scale. *J. Hydrometeor.,* **8**(1), 38-55.

Hui, W.J., Cook, B.I., Ravi, S., Fuentes, J.D. and D'Odorico, P., 2008. Dust–rainfall feedbacks in the West African Sahel. *Water Resources Res*.**44** W05202.

ICPAC., 2009a. Statement from the twenty third Greater Horn of Africa Climate Outlook Forum. *ICPAC*, Nairobi, Kenya.

ICPAC., 2009b. Statement from the twenty fourth Greater Horn of Africa Climate Outlook Forum. *ICPAC,* Nairobi, Kenya.

ICPAC., 2010a. Statement from the twenty fifth Greater Horn of Africa Climate Outlook Forum. *ICPAC*, Nairobi, Kenya.

ICPAC., 2010b. Statement from the twenty sixth Greater Horn of Africa Climate Outlook Forum. *ICPAC,* Nairobi, Kenya.

ICPAC., 2011a. Statement from the twenty sixth Greater Horn of Africa Climate Outlook Forum. *ICPAC,* Nairobi, Kenya.

ICPAC., 2011b. Statement from the twenty ninth Greater Horn of Africa Climate Outlook Forum. *ICPAC*, Nairobi, Kenya.

ICPAC., 2012a. Statement from the Thirtieth Greater Horn of Africa Climate Outlook Forum. *ICPAC*, Nairobi, Kenya.

ICPAC., 2012b. Statement from the Thirty two Greater Horn of Africa Climate Outlook Forum. *ICPAC*, Nairobi, Kenya.

Indeje, M. and Semazzi, F.H.M., 2000. Relationship between QBO in the lower equatorial stratospheric zonal winds and East African Seasonal Rainfall. *Meteorol. Atmos. Phys.*, **73**, 227 – 244.

Indeje, M., Semazzi, H.M. and Ogallo, L.J., 2000. ENSO signals in East African rainfall season. *Int. J. of Climatol,* **20**: 19-46.

Indeje, M., Semazzi, F.H.M., Xie, L. and Ogallo, L.J., 2001. Mechanistic model simulations of the East African Climate using NCAR Regional Climate Model: Influence of large scale orography on the Turkana Low-Level Jet. *J. Climate*, **14**, 2710 – 2724.

Ininda, J.M., 1995: Numerical simulation of the influence of sea surface temperature anomalies on the East African seasonal rainfall. *PhD thesis, Department of Meteorology, University of Nairobi*, Kenya.

IPCC., 2014. Climate Change 2014: Impacts, Adaptation, and Vulnerability. Part A: Global and Sectoral Aspects. Contribution of Working Group II to the Fifth Assessment Report of the Intergovernmental Panel on Climate Change [Field, C.B., V.R. Barros, D.J. Dokken, K.J. Mach, M.D. Mastrandrea, T.E. Bilir, M. Chatterjee, K.L. Ebi, Y.O. Estrada, R.C. Genova, B. Girma, E.S. Kissel, A.N. Levy, S. MacCracken, P.R. Mastrandrea, and L.L. White (eds.)]. *Cambridge University Press*, Cambridge, United Kingdom and New York, NY, USA, 1132 pp.

IPCC., 2013. Climate Change 2013: The Physical Science Basis. Contribution of Working Group I to the Fifth Assessment Report of the Intergovernmental Panel on Climate Change [Stocker, T.F., D. Qin, G.-K. Plattner, M. Tignor, S.K. Allen, J. Boschung, A. Nauels, Y.

Xia, V. Bex and P.M. Midgley (eds.)]. *Cambridge University Press,* Cambridge, United Kingdom and New York, NY, USA, 1535 pp, doi:10.1017/CBO9781107415324.

IPCC., 2007. Climate change 2007: The physical science basis. In Contribution of Working Group I to the Fourth Assessment Report of the Intergovernmental Panel on Climate Change, Solomon S, Qin D, Manning M, Chen Z, Marquis M, Averyt K. B, Tignor M, Miller H.L, Eds, *Cambridge University Press*: Cambridge, New York.

Jacobson, M.Z., 1997. Development and application of a new air pollution modeling system–Part III. Aerosol-phase simulations. *Atmos. Environ*., 31, 587-608.

Janjic, Z.I., 1994. The step-mountain eta coordinate model. Further developments of the convection, viscous sublayer and turbulence closure schemes, *Mon. Weather Rev.,* **122**, 927–945.

Jennrich, R. I. 2001: A simple general procedure for orthogonal rotation. *Psychometrika*, **66**, 289-306.

Jankov, I., Gallus, W. A., Segal, M., Shaw, B. and Koch S.E., 2005. The impact of different WRF model physical parameterizations and their interactions on warm season MCS rainfall, *Weather and Forecasting,* **20**, 1048–1060.

Jennrich, R.I., 2002. A simple general method for oblique rotation. *Psychometrika*, **67**,7-19.

Jirak, I.L. and Cotton, W.R., 2006. Effect of air pollution on precipitation along the front range of the Rocky Mountains. *J. Appl. Meteor*, **45**, 236–245.

Johnson, R.H., Rickenbach, T.M., Rutledge, S.A., Ciesielski, P.E. and Schubert, W.H., 1999. Trimodal characteristics of tropical convection, *J. Clim.,* **12** (8), 2397–2418.

Johnson, B.T., Osborne, S.R., Haywood, J.M. and Harrison, M.A.J., 2008. Aircraft measurements of biomass burning aerosol over West Africa during DABEX, *J. Geophys. Res*., **113**, D00C06, doi:10.1029/2007JD009451.

Jury, W.A. and Vaux, J., 2007. The emerging global water crisis: Managing scarcity and conflict between water and users. *Advances in Agro* **95**: 1 -76.

Kain, J.S. and Fritsch, J.M., 1993. Convective parameterization for mesoscale models: the Kain-Fritsch scheme. The representation of cumulus convection in numerical models, *Meteorol. Monogr*., **46**, Am. Meteor. Soc., 165–170.

Kalnay, E. and Jenne, R., 1996. The NCEP/NCAR 40-year reanalysis project, *Bull. Am. Meteorol Soc*, **77**, 437–471.

Kaufeld W.J., 2010. Toward assessing the effects of aerosols on deep convection: a numerical study using the WRF-chemistry model. *M.Sc Thesis, University of Illinois* at Urbana-Champaign.

Kaufman, Y.J., Tanre, D., Nakajima, T., Lenoble, J., Frouin, R., Grassl, H., 1997. Passive remote sensing of tropospheric aerosol and atmospheric correction for the aerosol effect. *Journal of Geophysical Research*, **102**, 16815–16830.

Kaufman, Y.J., Tanre, D., Boucher, O., 2002. A satellite view of aerosols in the climate system. *Nature*, **419**, 215e223.

Khain. A.D. and Sednev., 1999. Some effects of cloud-aerosolinteraction on cloud microphysics structure and precipitation: numerical experiments with a spectral microphysics cloud ensemble model. *Atmos. Res.* **52**, 195-220.

Khain, A.P, Ovtchinnikov, M., Pinsky, M., Pokrovsky, A. and Krugliak, H., 2000. Notes on the state-of-the-art numerical modeling of cloud microphysics, *Atmos. Res*, **55**, 159–224.

Khain, A., Rosenfeld, D. and Pokrovsky, A., 2001. Simulating convective clouds with sustained supercooled liquid water down to -37.5°C using a spectral microphysics model. *Geophys. Res.Lett.*, **28**, 3887-3890.

Khain, A., Rosenfeld, D. and Pokrovsky, A., 2005. Aerosol impact on the dynamics and microphysics of deep convective clouds. *Q. J. R. Meteorol. Soc.*, **131**, 2639-2663.

Khain, A.D., BenMoshe, N. and Pokrovsky, A., 2008. Factors determining the impact of aerosols on surface precipitation from clouds: An attempt at classification. *J. Atmos. Sci.*, **65**, 1721-1748.

Koenker, R., 2005. Quantile Regression. *Cambridge University Press*. New York, NY.

Koren, I. and Feingold, G., 2011. Aerosol–cloud–precipitation system as a predator-prey Problem. *PNAS,* **108** (30), 12227–12232.

Koren, I. and Wang C., 2008. Cloud–rain interactions: as complex as it gets. *Environ. Res. Lett.* 3 045018. doi:10.1088/1748-9326/3/4/045018.

Koren, I., Kaufman, Y., Remer, L. and Martins, J., 2004. Measurement of the effect of Amazon smoke on inhibition of cloud formation. *Science*, **303**, 1342–1345.

Koren, I., Kaufman, Y.J., Rosenfeld, D., Remer, L.A. and Rudich, Y., 2005. Aerosol invigoration and restructuring of Atlantic convective clouds, Geophys. Res. Lett., 32, L14828, doi:10.1029/2005gl023187.

Koren. I., Martins, J.V., Remer L.A. and Afargan H., 2008. Smoke invigoration versus inhibition of clouds over the Amazon. *Science,* **32, 1**946-960.

Kreyszig, E., 1968. Advanced engineering mathematics. 2nd Ed. *J. Wiley and Sons*, New York, 898 p.

Krishnamurti, T.N., Jha, B., Prospero, J., Jayaraman, A. and Ramanathan, V., 1998. Aerosol and pollutant transport and their impact on radiative forcing over the tropical Indian Ocean during the January-February 1996 pre-INDOEX cruise, Tellus, **50** (5) 521–542.

Kulshrestha U, and Kumar B., 2014. Airmass Trajectories and Long Range Transport of Pollutants: Review of Wet Deposition Scenario in South Asia, Advances in Meteorology, vol. 2014, Article ID 596041, doi:10.1155/2014/596041.

Kummerow, C., Barnes, W., Kozu, T., Shiue, J. and Simpson, J., 1998. The Tropical Rainfall Measuring Mission (TRMM) sensor package. *J. Atmos. Oceanic Technol.*, **15**, 809-817.

Kundzewicz, Z.W., Mata, L.J., Arnell, N., Doll, P., Kabat, P., Jimenez, B., Miller, K., Oki, T., Şen, Z. and Shiklomanov, I., 2007. Freshwater resources and their management. Climate Change 2007: Impacts, Adaptation and Vulnerability. Contribution of Working Group II to the Fourth Assessment Report of the Intergovernmental Panel on Climate Change (ed. by M. L. Parry, O. F. Canziani, J. P. Palutikof, P. J. van der Linden & C. E. Hanson), 173–210. *Cambridge University Press*, UK..

Kutner, M.H., Nachtsheim C. J. and Neter, J., 2004. Applied Linear Regression Models. 4th Ed. *McGraw-Hill Irwin*, Inc. Boston, MA.

Latif, M., Dommenget, D., Dima, M. and Grotzner A., 1999. The role of Indian Ocean sea surface temperature in forcing East African rainfall anomalies during December/January 1997/98. J. Climate, **12**, 3497-3504.

Lau, K.M., Wu, H.T., Sud, Y.C. and Walker, G.K., 2005. Effects of cloud microphysics on tropical atmospheric hydrologic processes and intraseasonal variability. *J. Clim.,* **18**, 4731–4751.

Lean, H.W., Clark, P.A., Dixon, M., Roberts, N.M., Fitch, A, Forbes, R. and Halliwell, C., 2008. Characteristics of high-resolution versions of the Met Office Unified Model for forecasting convection over the United Kingdom. *Mon. Wea. Rev*. **136**: 3408–3424.

Ledesma, R.D. and Valero-Mora, P.M., 2007. Determining the number of factors to retain in EFA: An easy-to-use computer program for carrying out Parallel Analysis. *Practical Assessment Research and Evaluation,* **12.**

Lee, S.S., Donner, L.J., Phillips, V.T.J. and Ming, Y., 2008. Examination of aerosol effects on precipitation in deep convective clouds during the 1997 ARM summer experiment. *Quart. J. Roy. Meteor. Soc.*, **134**, 1201-1220.

Lehahn, Y., Koren, I., Altaratz, O. and Kostinski A. B., 2011. Effect of coarse marine aerosols on stratocumulus clouds, *Geophys. Res. Lett*., 38, L20804, doi:10.1029/2011GL048504.

Levin, Z. and Cotton, W.R. *(*Eds.), 2009. Aerosol Pollution Impact on Precipitation: *A Scientific Review. Springer, Dordrecht*.

Li F. and Ramanathan, V., 2002. Winter to summer monsoon variation of aerosol optical depth over the tropical Indian Ocean, *J.Geophys. Res. D: Atmos*, **107** (16), 2–13.

Li, G., Wang, Y. and Zhang, R., 2008. Implementation of a two-moment bulk microphysics scheme to the WRF model to investigate aerosol-cloud interaction, *J. Geophys. Res.*,**113**, D15211, doi:10.1029/2007JD009361.

Liebmann, B. and Smith C., 1996. Description of a complete (interpolated) outgoing longwave radiation dataset, *Bull. Am. Meteorol. Soc*., **77**, 1275–1277.

Lin, J.C., Matsui, T., Pielke Sr R.A. and Kummerow, C., 2006. Effects of biomass-burning-derived aerosols on precipitation and clouds in the Amazon Basin: a satellite-based empirical study. *J. Geophys. Res*, **111**: D19204.

Liu, C. and Moncrieff, M.W., 2007. Sensitivity of cloud-resolving simulations of warm-season convection to cloud microphysics parameterizations, *Mon. Weather Rev.,* **135**, 2854–2868.

Liu, G., Shao, H., Coakley, J. A., Curry, J. A., Haggerty, J. A. and Tschudi, M. A., 2003. Retrieval of cloud droplet size from visible and microwave radiometric measurements during INDOEX: Implication to aerosols' indirect radiative effect, J. Geophys. Res., **108** (D1), 4006, doi:10.1029/2001JD001395.

Lu, M. and Seinfeld, J. H., 2005. Study of the aerosol indirect effect by large-eddy simulation of marine stratocumulus, *J. Atmos. Sci*., **62**, 3909–3932.

Lu, M. and Seinfeld, J.H., 2006. Effect of aerosol number concentration on cloud droplet dispersion: A large-eddy simulation study and implications for aerosol indirect forcing, *J. Geophys. Res.,* **111**, D02207, doi:10.1029/2005JD006419.

Lynn, B. H., Khain, A.P., Dudhia, J., Rosenfeld, D., Pokrovsky, A. and Seifert, A., 2005a. Spectral 51 (Bin) Microphysics Coupled with a Mesoscale Model (MM5). Part I: Model Description and First Results. *Mon.Weather Rev.,* **133**, 44-58.

Lynn, B. H., Khain, A.P., Dudhia, J., Rosenfeld, D., Pokrovsky, A. and Seifert, A., 2005b.

Spectral (Bin) Microphysics Coupled with a Mesoscale Model (MM5). Part II: Simulation of a CAPE rain event with a squall line. *Mon.Weather Rev.,* **133**, 59-71.

Lyon, B. and DeWitt, D.G., 2012. A recent and abrupt decline in the East African long rains. *Geophys. Res. Lett.,* **39** (2).

Lyons, S.W., 1990. Origins of convective variability over equatorial southern Africa during austrial summer. *Bull. Amer. Meteorol. Soc.,* **4**: 23-39.

Majone, B., Bovolo, C.I., Bellin, A., Blenkinsop, S. and Fowler, H.J., 2012. Modelling the impacts of future climate change on water resources for the Gállego river basin (Spain), *Water Resour. Res,* **48**, W01512.

Manton, M.J. and Cotton, W.R., 1977. Formulation of approximate equations for modeling moist deep convection on the mesoscale. *Dept. of Atmos. Sci. Paper* No. 266, Colo. State University Fort Collins, **80** (23), 62 pp.

Matsui, T, Masunaga, H., Kreidenweiss, S.M. Pielke Sr. RA., Tao, W-K., Chin, M., Kaufman, Y.J., 2006. Satellite-based assessment of marine low cloud variability associated with aerosol, atmospheric stability, and the diurnal cycle. *J.Geophys. Res.* **111**: D17204

Mlawer, E., Taubman, S., Brown, P., Iacono, M. and Clough. S., 1997. Radiative transfer for inhomogeneous atmospheres: RRTM, a validated correlated-k model for the longwave. *J. Geophys. Res*. **102** (14), 16663-16682.

Moeng, C.-H., Dudhia, J., Klemp, J.B. and Sullivan, P.P., 2007. Examining two-way grid nesting forlarge eddy simulation of the PBL using the WRF model, *Mon. Weather Rev.,* **135**, 2295–2311, doi:10.1175/MWR3406.1

Morrison, H. and Grabowski, W.W., 2007. Comparison of bulk and bin warm rain microphysics models using a kinematic framework. *J. Atmos. Sci.,* **64**, 2839-2861

Morrison, H., Curry, J.A. and Khvorostyanov, V.I., 2005. A new double-moment microphysics parameterization for application in cloud and climate models. Part I: Description. *J. Atmos. Sci.,* **62** (6), 1665-1677.

Morrison, H., Thompson, G. and Tatarskii, V., 2009. Impact of cloud microphysics on the development of trailing stratiform precipitation in a simulated squall line: Comparison of one and two-moment schemes, *Mon. Weather Rev.,* **137**, 991–1006.

Morrison, H., 2012. On the robustness of aerosol effects on an idealized supercell storm simulated with a cloud system-resolving model. *Atmos. Chem. Phys*. **12**, 7689–7705.

Muehlbauer, A. and Lohmann, U., 2009. Aerosol-cloud-precipitation interactions on mixed-phase orographic precipitation, *J. Atmos. Sci.,* **10** 1175.

Mukabana, J.R. and Pielke, R.A., 1996. Investigating the influence of synoptic-scale monsoonal winds and mesoscale circulations on diurnal weather patterns over Kenya using a mesoscale numerical model. *Mon. Wea. Rev.,* **124**, 224 – 243.

Muthama, N.J., 2003. Validation of satellite based rainfall estimates in the Greater Horn of Africa. *Proceedings of work shop on rainfall estimates, validation application, Nairobi, Kenya*, 10 -21 February 2003.

Muthama, N.J., 2004. Seasonal and intra-seasonal patterns of African tropical aerosols and their influence on Kenyan rainfall. *35th COSPAR Scientific Assembly. Held 18 - 25 July 2004, in Paris, France.,* p.1325.

Muthama, N.J., Kai, K.H. Ouma, G.O., Ng'ang'a J.K. and Opijah, F.J., 2008. Cloud Cover Estimation over Selected Locations in East Africa Using Satellite Derived Reflectivity Data. *J.Kenya Meteorol. Soc.,* **2**(2) 83–89.

Mwangi E., Wetterhall F., Dutra E., Di Giuseppe F. and Pappenberger F., 2014. Forecasting droughts in East Africa. *Hydrol. Earth Syst. Sci.* **18** 611–20.

Nakajima, T., Higurashi, A., Kawamoto, K. and Penner J.E., 2001. A possible correlation between satellite-derived cloud and aerosol microphysical parameters, Geophys. Res. Lett., **28**, 1171–1174.

National Centers for Environmental Prediction/National Weather Service/NOAA/U.S. Department of Commerce, 2000. NCEP FNL Operational Model Global Tropospheric

Analyses, continuing from July 1999, http://dx.doi.org/10.5065/D6M043C6, Research Data Archive at the National Center for Atmospheric Research, Computational and Information Systems Laboratory, Boulder, Colo. (Updated daily). Accessed 13 July 2014.

Nenes, A., Charlson, R.J., Facchini, M.C., Kulmala, M. and Laaksonen, A., 2002. Can chemical effects on cloud droplet number rival first indirect effect.*Geophys. Res.Lett.*, **29**, 29-21.

Ntelekos, A.A., Smith, J.A., Donner, L., Fast, J.D., Gustafson Jr, W.I., Chapman, E.G. and. Krajewski, W.F., 2009. The effects of aerosols on intense convective precipitation in the northeastern United States. *Q. J. R. Meteorol. Soc.*, **135**, 1367-1391.

Ngaina J.N., Mutai B.K., Ininda, J.M. and Muthama, J.N., 2014. Monitoring Spatio-Temporal Variability of Aerosol over Kenya. *Ethiopian Journal of Environmental Studies & Management* **7** (3): 244 – 252.

Nicholson, S. and Kim, J., 1997. The relationship of the El Niño–Southern Oscillation to African rainfall. *Int. J. Climatol.,* **17**, 117 – 135.

Nicholson, S.E., 1996. A review of climate dynamics and climate variability in Eastern Africa, in: The limnology, Climatology and Paleoclimatology of the East African Lakes, edited by: Johnson, T. C. and Odada, E. O., *Overseas Publishers Association, Amsterdam*, The Netherlands, 25–56.

Noppel, H., Beheng, K.D., 2009. Effects of intentional and inadvertent hygroscopic cloud seeding. In: Nagel WE, Resch MM (eds) High performance computing in science and engineering '08. *Springer, Berlin*. doi:10.1007/978-3-540-88303-6.

Nuijens, L., Stevens, B. and Siebesma A.P., 2009. The environment of precipitating shallow cumulus convection, *Journal of Atmospheric Science* **66**, 1962–1979.

O'Connor, B.P., 2000. SPSS and SAS programs for determining the number of components using parallel analysis and Velicer's MAP test. *Behavior Research Methods, Instruments, and Computers*, **32**,396-402.

Oettli, P. and Camberlin, P., 2005. Influence of topography on monthly rainfall distribution over

East Africa. *Climate Research*, **28**, 199 - 212.

Ogallo, L., 2008. Celebrating 10 years of COFs. *Presentation at the 21st Greater Horn of Africa Climate Outlook Forum, 27-29th February 2008*, Entebbe, Uganda.

Okoola, R.E., 1996. Space-time Characteristics of the ITCZ over equatorial Eastern Africa during anomalous rainfall years. *PhD thesis Department of Meteorology, University of Nairobi*, Kenya.

Okoola, R.E., 1999. Midtropospheric circulation patterns associated with extreme dry and wet episodes over equatorial Eastern Africa during the Northern Hemisphere spring. *J. Appl. Meteorol*. **38**, 1161 – 1169.

Okoola, R.E., Camberlin, P. and Ininda, J.M., 2008. Wet periods along the East Africa coast and the extreme wet spell event of October 1997. J. Kenya Meteor. Soc., **2**, 67–83.

Omeny, P.A., Ogallo, L., Okoola, R.E., Hendon, H. and Wheeler, M., 2008. East African Rainfall variability associated with Madden-Julian Oscillation. *J. Keny. Met. Soc*, **2**(2), 109 – 118.

Opijah, F.J., Mutemi, J.N. and Ogallo, L.A., 2014. Application of the EMS-WRF Model in Dekadal Rainfall Prediction over GHA Region. *Africa Journal of Physical Sciences* **1** (1) 18-24.

Orville, H.D., 1996. A review of cloud modelling in weather modification. *Bull Amer Meteor Soc* **77**: 1535–1555.

Owiti, Z.O., Ogallo L.A. and Mutemi, J., 2008. Linkages between the Indian Ocean Dipole and East African Seasonal Rainfall Anomalies. *J. Keny. Met. Soc*, **2**(1), 3 – 17.

Panicker, A.S., Pandithurai, G., Safai, P.D. and Kewat, S., 2008. Observations of enhanced aerosol longwave radiative forcing over an urban environment, *Geophys. Res. Lett.,* **35**, L04817, doi:10.1029/2007GL032879.

Patt, A.G., Ogallo, L. and Hellmuth, M., 2007. Learning from 10 years of climate outlook forums in Africa. *Science*, **318**, 49-50.

Peng, Y., Lohmann, U., Leaitch, R., Banic, C. and Couture, M., 2002. The cloud albedo-cloud droplet effective radius relationship for clean and polluted clouds from race and fire *J. Geophys. Res*,**107** 179-190.

Petters, M.D. and Kreidenweis, S.M., 2007. A single parameter representation of hygroscopic growth and cloud condensation nucleus activity, Atmos. Chem. Phys., **7**, 1961–1971, doi:10.5194/acp-7-1961-2007.

Phillips, I.D. and Denning, H., 2007. Winter daily precipitation variability over the South West peninsula of England. *Theoretical and Applied Climatology,* **87**: 103 – 122.

Phillips, V.T.J., Donner, L.J. and Garner, S., 2007. Nucleation processes in deep convection simulated by a cloud-system-resolving model with double-moment bulk microphysics. J.*Atmos. Sci.,* **64**, 738-761.

Phillips, V.T.J. and Donner, L.J., 2006. Cloud microphysics, radiation, and vertical velocities in two-and three-dimensional simulations of deep convection. *Q. J. R. Meteorol. Soc.,* **133**, 3011-3033.

Pohl, B. and Camberlin P., 2006. Influence of the Madden-Julian Oscillation on East African rainfall. Part I: intraseasonal variability and regional dependency. *Q J R Meteorol Soc.* **132**, 2521 –2539.

Prasad K.O., Bansod S.O. and Sabade S.S., 2000. Forecasting Indian summer Monsoon rainfall by outgoing longwave radiation over the Indian Ocean. *Inter. J.Clim*, **20**: 105-114.

Prijith, S.S., Aloysius, M., Mohan, M., Beegum, N. and Moorthy, K.K., 2012. Role of circulation parameters in long range aerosol transport: evidence from Winter ICARB. *J. Atmos. Sol. Terres. Phys.***77**, 144-151.

Prijith, S.S., Rajeev, K., Thampi, B.V., Nair, S.K. and Mohan, M., 2013. Multi-year observations of the spatial and vertical distribution of aerosols and the genesis of abnormal variations in aerosol loading over the Arabian Sea during Asian Summer

Monsoon Season. *J. Atmos. Solar-Terr. Phys*. **105** (106), 142-151.

Prospero, J.M., Ginoux P., Torres, O., Nicholson, S.E. and Gill, T.E., 2002. Environmental characterization of global sources of atmospheric soil dust identified with the NIMBUS 7 Total Ozone Mapping Spectrometer (TOMS) absorbing aerosol product, *Rev. Geophys.*, **40** (1), 1002, doi:10.1029/2000RG000095.

Pruppacher, H.R. and Klett, J.D., 1997. Microphysics of Clouds and Precipitation. *Journal of Boundary Layer Meteorology,* **86**, (1) 187-188.

Rajeevan, M., Kesarkar, A., Thampi, S.B., Rao, T. N., Radhakrishna, B. and Rajasekhar, M., 2010. Sensitivity of WRF cloud microphysics to simulations of a severe thunderstorm event over southeast India, *Ann. Geophys*., **28**, 603–619.

Randall, D., Khairoutdinov, M., Arakawa, A. and Grabowski, W., 2003. Breaking the cloud parameterization deadlock. *Bull. Am. Meteor. Soc.,* **84**, 1547–1564.

Ratnam, V. and Cox, E.A., 2006. Simulation of the monsoon depressions using MM5: sensitivity to cumulus parameterization schemes, *Meteorol. Atmos. Phys.,* **93**, 53–78.

Reddy, B.S.K., Kumar, K.R., Balakrishnaiah, G., Gopal, K.R., Reddy, R.R., Narasimhulu, K., Ahammed, Y.N., Reddy, L.S.S. and Lal, S., 2010. Observational Studies on the Variations in Surface Ozone Concentrations at Anantapur in Southern India. Atmos. Res. 98: 125–139.

Reisner, R., Rasmussen, R.M. and Bruintjes, R.T., 1998. Explicit forecasting of supercooled liquid water in winter storms using the MM5 mesoscale model. *Q. J. R. Meteorol. Soc.*, **124**, 1071-1107.

Remer, L.A., Tanre, D., Kaufman, Y.J., Levy, R.C., Mattoo, S., 2006. Algorithm for Remote Sensing of Tropospheric Aerosols from MODIS: Collection 005. NASA Goddard Space Flight Centre, Greenbelt, Md. *Algorithm Theoretical Basis Document.*

Reutter, P., Trentmann, S.H., Simmel, J., Rose, M., Gunthe, D., Wernli, S.S., Andreae, H. and Poschl, U., 2009. Aerosol and updraft-limited regimes of cloud droplet formation influence of particle number, size and hygroscopicity on the activation of cloud condensation nuclei, *Atmos. Chem. Phys*. **9**, 7067 -7080.

Richman, M.B., 1986. Rotation of principal components. *J. Climatology*, **6**, 293 – 335.

Rogers. D.C. and Vali. G., 1978. Summer climatology of aerosols and nuclei in the central high plains of the United States. Preprints, Conference on Cloud Physics and Atmospheric Electricity, Issaquah. Wash.. *AMS Boston*. Mass. 25-30.

Rosell, S. and Holmer, B., 2007. Rainfall change and its implications for Belg harvest in South Wollo, Ethiopia. Geografiska Annaler, Series A: *Physical Geography*, **89** A(4), 287-299.

Rosenfeld, D. and Lensky, I.M., 1998. Satellitebased insights into precipitation formation processes in continental and maritime convective clouds, *Bulletin of the American Meteorological Society*, **79** (11), 2457–2476.

Rosenfeld, D., 1999. TRMM observed first direct evidence of smoke from forest fires inhibiting rainfall, *Geophysical Research Letters,* **26** (20), 3105–3108.

Rosenfeld, D., 2000. Suppression of rain and snow by urban and industrial air pollution. *Science* **287**(5459):1793-1796.

Rosenfeld D. and Woodley, W. L., 2000. Deep Convective Clouds with Sustained Supercooled Liquid Water Down to -37.5°c. *Nature*, **405**, 440-442.

Rosenfeld, D., Yu, X. and Dai, J., 2005. Satellite retrieved microstructure of AgI seeding tracks in supercooled layer clouds.*Journal of Applied Meteorology*, **44**, 760-767.

Rosenfeld, D., 2006. Aerosols, Clouds, and Climate. *Science*, **312**, 1323-1324.

Rosenfeld, D., 2007. New insights to cloud seeding for enhancing precipitation and for hail suppression, J. Weather Modif., 39, 61–69.

Rosenfeld, D., Lohmann, U,. Raga, G., O'Dowd, C.D., Kulmala, M., Fuzz, S., Reissell, A. and Andrea, M.O., 2008. Flood or Drought: How Do Aerosols Affect Precipitation. *Science*, **321**, 5894 1309-1313.

Rosenfeld, D., Sherwood, S., Wood, R., Donner, L., 2014. Climate Effects of Aerosol-Cloud Interactions, *Science*, **343**, 379-380.

Rossow, W.B. and Schiffer, R.A., 1999. Advances in understanding clouds from ISCCP, Bull. *Amer. Meteorol. Soc.*, **80**, 2261–2287.

Rouault, M., Lee-Thorp, A.M., Ansorge, I. and Lutheharms, J.R.E., 1995. Agulhas Current Air-Sea Exchange Experiment,*S. Afr. J. Sci.*, **91**(10), 493.

Rouault, M., Lee-Thorp, A.M. and Lutjeharms, J.R.E., 2000. The Atmospheric Boundary Layer above the Agulhas Current during Along current Winds, *J. Phys. Oceanogr.*, **30** (1), 40-50.

Ruiz, J.J., Saulo, C. and Nogues-Paegle, J., 2010. WRF Model Sensitivity to Choice of Parameterization over South America: Validation against Surface Variables, Mon. Weather Rev., **138**, 3342–3355, doi:10.1175/2010MWR3358.1.

Saadat A.H.M., Rahman, M.M., Hasan, S. M. K. and Alam, A. T. M., 2013. Travelling and source point identification of some transboundary air pollutants by trajectory analysis in Sathkhira, Bangladesh, *Canadian Chemical Transactions*, **1** (1), 56–65.

Sandu, I., Brenguier, J., Geoffroy, O., Thouron, O. and Masson, V., 2008. Aerosol impacts on the diurnal cycle of marine stratocumulus, *J.Atmos. Sci.*, **65**, 2705–2718.

Schnell R.C. and Vali,G., 1976. Biogenic sources of ice nuclei, part I terrestrial and marine sources. *J. Amos. Sci.***33**, 1554-1564.

Schultz, D.M., Mikkonen, S., Laaksonen, A. and Richman, M.B. 2007. Weekly precipitation cycles? Lack of evidence fromUnited States surface stations, *Geophys. Res. Lett*, **34**, L22815,doi:10.1029/2007GL031889.

Schumacher, C. and Houze, R.A., 2003. Stratiform rain in the Tropics as seen by the TRMM precipitation radar, *Journal of Climate*, **16** (11), 1739–1756.

Schreck, C.J. and Semazzi, F.H.M., 2004. Variability of the recent climate of eastern Africa, *Int. J. Climatol.*, 24, 681–701.

Seibert P., 2004. Inverse modelling with a lagrangian particle dispersion model: application to point releases over limited time intervals in: air pollution modeling and its application, Journal of Applied Meteorology, vol. 14, pp. 381–389.

Seifert, A. and Beheng, K., 2006. A two-moment cloud microphysics parameterization for mixed-phase clouds. Part 2: Maritime vs. continental deep convective storms. *Meteorology and Atmospheric Physics*, **92**, 67-82.

Seifert, A., Kohler, C. and Beheng, K.D., 2011. Aerosol-cloud-precipitation effects over Germany as simulated by a convective-scale numerical weather prediction model. *Atmos. Chem. Phys*, **11** (7), 20203–20243.

Semazzi, F.H.M. and Indeje, M., 1999. Inter-seasonal variability of ENSO rainfall signal over Africa. *Journal of the African Meteorological Society* **4**: 81 – 94.

Sharon, T.M, Albrecht, B.A., Jonsson, H.H., Minnis, P., Khaiyer, M.M., Van Reken, T.M., Seinfeld, J. and Flagan, R., 2006. Aerosol and cloud microphysical characteristics of rifts and gradients in maritime stratocumulus clouds, *Journal of Atmospheric Science*, **63**, 983–997.

Shongwe, M.E., van Oldenborgh, G.J., van den Hurk, B.J.J.M. and van Aalst M.A., 2011. Projected changes in extreme precipitation in Africa under global warming, Part II: East Africa, *J. Clim*., **24**, 3718–3733.

Silverman, B.A., 2003. A critical assessment of hygroscopic seeding of convective clouds for rainfall enhancement. *Bull. Amer. Meteor. Soc.*, **84**, 1219-1230

Short, D. and Nakamura, K., 2000. TRMM radar observations of shallow precipitation over the tropical oceans, *J. Clim.*, **13**, 4107–4124.

Simpson, J., Adler, R.F. and North, G.R., 1988. Proposed tropical rainfall measuring mission (TRMM) satellite. *Bull. Amer. Met. Soc.*, **69**, 278-295.

Skamarock, W.C., Klemp, J. B., Dudhia, J., Gill, D.O., Barker, D.M., Duda, M., Huang, H., Wang, W. and Powers, J. G., 2008. A description of the advanced research WRF version

3. 53 *NCAR Tech. Note.*

Skripnikova H., 2013. Relationship between radar-derived hail kinetic energy and damage to insured buildings for severe hailstorms in Eastern Australia. *Atmospheric Research*, (81):215-235.

Slinn, W.G.N., 1975. Atmospheric aerosol particles in surface-level air. *Atmospheric Environment*, **9**, 763-764.

Sneyers, R., 1990. On the statistical analysis of series of observations, pp. 192. *Tech. Note 143*, *WMO No.* 415, Geneva.

Solomon, S., Qin D., Manning, M., Chen, Z., Marquis, M., Averyt, K., Tignor, M. and Miller, H. *(*Eds.), Climate Change 2007. The Physical Science Basis. Contribution of Working Group I to the Fourth Assessment Report of the Intergovernmental Panel on Climate Change, chap. 7.5.2, *Cambridge University Press*, Cambridge, United Kingdom and New York, USA.

Stein, D.C., Swap, R.J., Greco, S., Piketh, S.J., Macko, S.A., Doddridge, B.G., Elias, T. and Bruintjes, R.T., 2003. Haze layer characterization and associated meteorological controls along the eastern coastal region of southern Africa. *J. Geophys. Res*.**108**, D13.

Stensrud, D. J., 2007. Parameterization Schemes. *Cambridge University Press*, Cambridge, first edition.

Stephenson, D.B., Kumar, K.R., Doblas-Reyes, F.J., Royer, J.F., Chauvin, F.m and Pezzulli, S., 1999. Extreme daily rainfall events and their impacts on ensemble forecasts of the Indian monsoon. *Mon. Wea. Rev.*, **127**, 1954 – 1966.

Stevens, B. and Savic-Jovcic, V., 2008. The structure and mesoscale organization of precipitating stratocumulus, *J. Atmos. Sci*, **65**, 1587– 1605.

Stier J. H, Seinfeld, S, Kinne and Boucher O, 2007. Aerosol absorption and radiative forcing. *Atmos. Chem. Phys*, **7**(19):5237–5261.

Stull, R.B., 1988. An Introduction to Boundary Layer Meteorology. Atmospheric Sciences Library. *Kluwer Academic Publisher*, London.

Summers, P.W, Fankhauser, J.C, Morgan, G.M, Foote, G.B. and Modahl C.A., 1979. Results of a randomized hail suppression experiment in north East Colorado part VIII: the representative draw analysis. *J. Appl. Meteor*. **18**, 1618-1628.

Svensson, C., 1999. Empirical Orthogonal Function Analysis of daily rainfall in the upper reaches of the Huai River Basin, China. *Theor. Appl. Climatol.*, **62**, 147 – 161.

Tanre, D., Kaufman, Y.J., Herman, M. and Mattoo, S., 1997. Remote sensing of aerosol properties over oceans using the MODIS/EOS spectral radiances. *J. Geophys. Res.*, **102**, 16971–16988.

Tao, W.-K., Li, X., Khain, A., Matsui, T., Lang, S. and Simpson, J., 2007. Role of aerosol concentration on deep convective precipitation: Cloud-resolving simulations. *J. Geophys. Res.*, **112**, D24S18, doi:10.1029/2007JD008728.

Tao, W.-K., Chen, J.-P., Li, Z., Wang, C. and Zhang, C., 2012. Impact of aerosols on convective clouds and precipitation, *Rev. Geophys*., **50**, RG2001, doi:10.1029/2011RG000369.

Tazalilka L., 2003. Satellite derived rainfall over tropical Africa, its pattern, variability and calibration. *Master of Science thesis*, *Univ Zululand*, 150 pp

Teller A. and Levin Z., 2006. The effects of aerosols on precipitation and dimensions of subtropical clouds: a sensitivity study using a numerical cloud model, *Atmos. Chem. Phys*, **6**, 67–80.

Theodore L.A., Chalson, R.J., Winker, D.M., Ogren, J.A., Holmen K., 2003. Mesoscale variation of tropospheric aerosols. *J. Atmos. Sc.* **60**, No1, 119-136.

Thomson D.J. and Wilson J.D., 2012. History of Lagrangian Stochastic Models for Turbulent Dispersion, Langrangian Model of the Atmosphere, *Geographical Monograph Series* 200, American Geophhysical union.

Tosca, M.G., Randerson, J.T. and Zender, C.S., 2013. Global impact of smoke aerosols from landscape fires on climate and the Hadley circulation, Atmos. Chem. Phys., 13, 5227–5241, doi:10.5194/acp-13-5227-2013.

Trenberth, K. E., 1997. The definition of El Niño. Bull. Amer. Meter. Soc. 78, 2771 – 2777

Tripoli, G.J. and Cotton, W.R., 1986. An intense, quasi-steady thunderstorm over mountainous terrain. *J. Appl. Meteor.,* **43**, 894-912.

Twomey, S., 1977. The influence of pollution on the shortwave albedo of clouds, *Journal of the atmospheric sciences*, **34** (7), 1149–1152.

Vaidya, S.S., 2006. The performance of two convective parameterization schemes in a mesoscale model over the Indian region, Meteorol. Atmos. Phys., **2** ,175–190.

Van den Heever, S.C., Carrio, G.G., Cotton, W.R., DeMott, P.J. and Prenni, A.J., 2006. Impacts of nucleating aerosol on Florida storms. Part I: Mesoscale simulations. *J. Atmos. Sci*, **63** (7), 1752–1775.

Van Zanten, M.C, and Stevens, B., 2005. On the observed structure of heavily precipitating marine stratocumulus. *Journal of Atmospheric Sciences*, **62**: 4327-4342.

Von Storch, H. and Zwiers, F.W., 1999. Statistical Analysis in Climate Research. *Cambridge University Press*, Cambridge. 494 pp.

Wang, W. and Seaman, N.L., 1997. A comparison study of convective parameterization schemes in a mesoscale model, *Mon. Weather Rev.,* **125**, 252–278.

Wang, H., Skamarock, W.C. and Feingold, G., 2009a. Evaluation of scalar advection schemes in the advanced research WRF model using large-eddy simulations of aerosol-cloud interactions, *Mon. Weather Rev.,* **137**, 2547–2558, doi:10.1175/2009MWR2820.1.

Wang, H. and Feingold, G., 2009b. Modeling Mesoscale Cellular Structures and Drizzle in Marine Stratocumulus. Part I: Impact of Drizzle on the Formation and Evolution of Open Cells. *Journal of the Atmospheric Sciences*, **66** (11): 3237-3256.

Washington, R. and Todd, M.C., 2005. Atmospheric controls on mineral dust emission from the Bodélé Depression, Chad: Intraseasonal to interannual variability and the role of the Low *Level Jet, Geophys. Res. Lett.*, **32**, L17701.

Webster, P.J., Moore A.M., Loschnigg J.P. and Leben R.R., 1999. Coupled oceanatmosphere dynamics in the Indian Ocean during 1997-1998. *Nature*, **401**, 356-360.

Wilks, D. S., 2006. Statistical Methods in the Atmospheric Sciences. International Geophysics Series. Academic press, second edition.

Williams, E., Rosenfeld, D., Madden, N., Gerlach, J., Gears, N., Atkinson, L., Dunnemann, N., Frostrom, G., Antonio, M., Biazon, B., Camargo, R., Franca, H., Gomes, A., Lima, M., Machado, R., Manhaes, S., Nachtigall, L., Piva, H., Quintiliano, W., Machado, L. Artaxo, P., Roberts, G., Renno, N., Blakeslee, R., Bailey, J., Boccippio, D., Betts, A. Wolff, D., Roy, B., Halverson, J., Rickenbach, T., Fuentes, J. and Avelino, E., 2002. Contrasting convective regimes over the Amazon: Implications for cloud electrification. *J. Geophys. Res. –Atmos.*, **107**(D20), Art.No. 8082.

Williams, J.E., Scheele, M.P., van Velthoven, P.F.J., Thouret, V., Saunois, M., Reeves, C.E., and Cammas, J.-P., 2010. The influence of biomass burning and transport on tropospheric composition over the tropical Atlantic Ocean and Equatorial Africa during the West African monsoon in 2006, *Atmos. Chem. Phys.*, **10**, 9797–9817.

Williams, A.P. and C. Funk, 2011: A westward extension of the warm pool leads to a westward extension of the Walker circulation, drying eastern Africa. *Climate Dynamics*, **37** (11-12), 2417-2435.

Wilson, J.M., Crook, N.A., Mueller, C.K., Sun, J. and Dixon, M., 1998. Nowcasting thunderstorms: A status report, *B. Am. Meteorol. Soc.*, **79**, 2079–2099.

Wood R, 2007. Cancellation of aerosol indirect effects in marine stratocumulus through cloud thinning, *J. Atmos. Sci*, **64**, 2657–2669.

Wu, J., Del Genio, A.D., Yao, M.S. and Wolf, A.B , 2003. WRF and GISS SCM simulations of convective updraft properties during TWP-ICE, *J. Geophys. Res.,* 114, D04206.

Xue, H. and Feingold, G., 2006. Large-eddy simulations of trade wind cumuli: Investigation of aerosol indirect effects, *J. Atmos. Sci.*, **63**, 1605–1622.

Yin, X., Nicholson, S.E. and M.B.B., 2000. On the diurnal cycle of cloudiness over Lake Victoria and its influence on evaporation from the lake, *Hydrol. Sci. J.*, **45**, 407–424.

Zipser, E.J., 2003. Some views on “Hot Towers” after 50 years of tropical field programs and two years of TRMM data. *Meteor.Monogr.*, **29**, 49-58.

APPENDICES

Appendix 1: List of selected synoptic stations utilized in the study and their location

No.	Station	Lat	Lon	No.	Station	Lat	Lon	No.	Station	Lat	Lon	No.	Station	Lat	Lon
1	Nyahururu	-0.4	36.4	23	Mtwapa	-3.9	39.7	45	Kilembe	0.2	30	67	Bukoba	-1.3	31.8
2	Naivasha	1.3	36	24	Nakuru	-0.3	36.1	46	Rwimi	0.6	30.2	68	Dar es salaam	-6.8	39.2
3	Dagoretti	-1.3	36.8	25	Nanyuki	0.1	37	47	Kasese	0.2	30.1	69	Dodoma	-6.2	35.7
4	Eldoret	0.5	35.3	26	Narok	-1.1	35.9	48	Mubende	0.6	31.4	70	Iringa	-7.8	35.7
5	Embu	-0.5	37.5	27	Nyeri	-0.4	37	49	Makerere	0.3	32.6	71	Kibaha	-6.8	38.9
6	Garissa	-0.5	39.6	28	Voi	-3.4	38.6	50	Nakifuma	0.6	32.8	72	Kigoma	-4.9	29.6
7	JKIA	-1.3	36.9	29	Arua	3.1	30.9	51	Entebbe	0.1	32.5	73	Lupiro	-8.4	36.4
8	Kabarak	-0.2	36	30	Moyo	3.7	31.7	52	Kituza	0.3	32.8	74	Mbeya	-8.9	33.5
9	Kakamega	0.3	34.8	31	Kotido	3	34.1	53	Entebbe	0.1	32.5	75	Morogoro	-6.8	37.7
10	Kisii	-0.7	34.8	32	Wadelai	2.7	31.4	54	Jinja	0.5	33.2	76	Moshi	-3.4	37.3
11	Kisumu	-0.1	34.8	33	Gulu	2.8	32.3	55	Mbarara	-1	30.7	77	Mtwara	-10	40.2
12	Kitale	0	36	34	Pachwa	1.1	31.3	56	Rubale	-1	30.3	78	Musoma	-1.5	33.8
13	Lamu	-2.3	40.9	35	Masindi	1.7	31.7	57	Kikunda	-1	30.5	79	Mwanza	-2.8	32.8
14	Lodwar	3.1	35.6	36	Bulindi	1.5	31.5	58	Bujumbura	-2	30.1	80	Pemba	-5.2	39.7
15	Makindu	-2.3	37.8	37	Aduku	2	32.7	59	Rubona	-3	29.7	81	Manyoni	-5.5	34.5
16	Malindi	-3.2	40.1	38	Kakoge	1.1	32.5	60	Kigali	-2	30.1	82	Selous G.R	-10	37
17	Mandera	3.9	41.9	39	Serere	1.5	33.5	61	Kamembe	-3	28.9	83	Sumbawanga	-8	31.6
18	Marsabit	2.3	38	40	Soroti	1.7	33.6	62	Gisenyi	-2	29.3	84	Tambora	-5	32.5
19	Meru	0.1	37.7	41	Arapai	1.8	33.6	63	Gikongoro	-3	29.6	85	Tanga	-5.1	39.1
20	Mombasa	-4.1	39.6	42	Kiige	1.2	33	64	Ruhengeri	-2	30.1	86	Zanzibar	-6.1	39.3
21	Moyale	3.5	39.1	43	Namalu	1.8	34.6	65	Byumba	-2	30.5	*	*	*	*
22	Msabaha	-3.3	40.1	44	Kijura	0.8	30.4	66	Arusha	-3	36.6	*	*	*	*

Appendix 2: MATLAB script for Parallel Analysis (Monte Carlo Testing)

```
clear; tic;

% Parallel Analysis Program For Raw Data and Data Permutations.
%This program conducts parallel analyses on data files in which
%the rows of the data matrix are cases/individuals and the
%columns are variables; There can be no missing values;
%You must also specify:
%-- the # of parallel data sets for the analyses;
%-- the desired percentile of the distribution of random
%data eigenvalues;
%-- whether principal components analyses or principal axis/common
%factor analysis are to be conducted, and
%-- whether normally distributed random data generation or
%permutations of the raw data set are to be used in the
%parallel analyses;
%WARNING: Permutations of the raw data set are time consuming;
%Each parallel data set is based on column-wise random shufflings
%of the values in the raw data matrix using Castellan's (1992,
%BRMIC, 24, 72-77) algorithm; The distributions of the original
%raw variables are exactly preserved in the shuffled versions used
%in the parallel analyses; Permutations of the raw data set are
%thus highly accurate and most relevant, especially in cases where
%the raw data are not normally distributed or when they do not meet
%the assumption of multivariate normality (see Longman & Holden,
%1992, BRMIC, 24, 493, for a Fortran version); If you would
%like to go this route, it is perhaps best to (1) first run a
%normally distributed random data generation parallel analysis to
%familiarize yourself with the program and to get a ballpark
%reference point for the number of factors/components;
%(2) then run a permutations of the raw data parallel analysis
```

```
%using a small number of datasets (e.g., 10), just to see how long
%the program takes to run; then (3) run a permutations of the raw
%data parallel analysis using the number of parallel data sets that
%you would like use for your final analyses; 1000 datasets are
%usually sufficient, although more datasets should be used
%if there are close calls.
% The "load" command can be used to read a raw data file
% The raw data matrix must be named "raw"
%These next commands generate artificial raw data
%(50 cases) that can be used for a trial-run of
%the program, instead of using your own raw data;
%Just run this whole file; However, make sure to
%delete these commands before attempting to run your own data.
% Start of artificial data commands.
com = randn(3185,86);
load raw.txt
% End of artificial data commands.
ndatsets= 1000; % Enter the desired number of parallel data sets here
percent= 95; % Enter the desired percentile here
% Specify the desired kind of parellel analysis, where:
% 1 = principal components analysis
% 2 = principal axis / common factor analysis
kind = 1 ;
% Enter either
%1 for normally distributed random data generation parallel analysis, or
%2 for permutations of the raw data set (more time consuming).
randtype = 2 ;
%the next command can be used to set the state of the random # generator
randn('state',1953125)
% End of user specifications %%%%%%%%%%%%%%%
ncases,nvars = size(raw);
```

```
% principal components analysis & random normal data generation
if (kind == 1 & randtype == 1)
realeval = flipud(sort(eig(corrcoef(raw))));
for nds = 1:ndatsets; evals(:,nds) = eig(corrcoef(randn(ncases,nvars)));end
end
% principal components analysis & raw data permutation
if (kind == 1 & randtype == 2)
realeval = flipud(sort(eig(corrcoef(raw))));
for nds = 1:ndatsets;
x = raw;
for lupec = 1:nvars;
for luper = 1:(ncases -1);
k = fix( (ncases - luper + 1) * rand(1) + 1 )+ luper - 1;
d = x(luper,lupec);
x(luper,lupec) = x(k,lupec);
x(k,lupec) = d;end;end;
evals(:,nds) = eig(corrcoef(x));end;end
% PAF/common factor analysis & random normal data generation
if (kind == 2 & randtype == 1)
r = corrcoef(raw);
smc = 1 - (1 ./ diag(inv(r)));
for ii=1:size(r,1);r(ii,ii) = smc(ii,1);end;
realeval = flipud(sort(eig(r)));
for nds = 1:ndatsets;
r = corrcoef(randn(ncases,nvars));
smc = 1 - (1 ./ diag(inv(r)));
for ii=1:size(r,1);r(ii,ii) = smc(ii,1);end;
evals(:,nds) = eig(r);
end;end
% PAF/common factor analysis & raw data permutation
if (kind == 2 & randtype == 2)
```

```
r = corrcoef(raw);
smc = 1 - (1 ./ diag(inv(r)));
for ii=1:size(r,1);r(ii,ii) = smc(ii,1);end;
realeval = flipud(sort(eig(r)));
for nds = 1:ndatsets;
x = raw;
for lupec = 1:nvars;
for luper = 1:(ncases -1);
k = fix( (ncases - luper + 1) * rand(1) + 1 )+ luper - 1;
d = x(luper,lupec);
x(luper,lupec) = x(k,lupec);
x(k,lupec) = d;end;end;
r = corrcoef(x);
smc = 1 - (1 ./ diag(inv(r)));
for ii=1:size(r,1);r(ii,ii) = smc(ii,1);end;
evals(:,nds) = eig(r);
end;end
evals = flipud(sort(evals,1));
means = (mean(evals,2));% mean eigenvalues for each position.
evals = sort(evals,2);% sorting the eigenvalues for each position.
percentiles = (evals(:,round((percent*ndatsets)/100)));% percentiles.
format short
disp(' ');disp('PARALLEL ANALYSIS '); disp(' ')
if (kind == 1 & randtype == 1);
disp('Principal Components Analysis & Random Normal Data Generation' );disp(' ');end
if (kind == 1 & randtype == 2);
disp('Principal Components Analysis & Raw Data Permutation' );disp(' ');end
if (kind == 2 & randtype == 1);
disp('PAF/Common Factor Analysis & Random Normal Data Generation' );disp(' ');end
if (kind == 2 & randtype == 2);
disp('PAF/Common Factor Analysis & Raw Data Permutation' );disp(' ');end
```

```
disp('Variables= ' num2str(nvars) );
disp('Cases= ' num2str(ncases) );
disp('Datsets= ' num2str(ndatsets) );
disp('Percentile = ' num2str(percent) );disp(' ')
disp('Raw Data Eigenvalues, & Mean & Percentile Random Data Eigenvalues');disp(' ')
disp('RootRaw DataMeansPercentiles' )
disp((1:nvars).'realeval meanspercentiles);
if kind == 2;
disp('Warning: Parallel analyses of adjusted correlation matrices' );
disp('e.g., with SMCs on the diagonal, tend to indicate more factors' );
disp('than warranted (Buja, A., & Eyuboglu, N., 1992, Remarks on parallel' );
disp('analysis. Multivariate Behavioral Research, 27, 509-540).' );
disp('The eigenvalues for trivial, negligible factors in the real' );
disp('data commonly surpass corresponding random data eigenvalues' );
disp('for the same roots. The eigenvalues from parallel analyses' );
disp('can be used to determine the real data eigenvalues that are' );
disp('beyond chance, but additional procedures should then be used' );
disp('to trim trivial factors.' );disp(' ' );
disp('Principal components eigenvalues are often used to determine' );
disp('the number of common factors. This is the default in most' );
disp('statistical software packages, and it is the primary practice' );
disp('in the literature. It is also the method used by many factor' );
disp('analysis experts, including Cattell, who often examined' );
disp('principal components eigenvalues in his scree plots to determine' );
disp('the number of common factors. But others believe this common' );
disp('practice is wrong. Principal components eigenvalues are based' );
disp('on all of the variance in correlation matrices, including both' );
disp('the variance that is shared among variables and the variances' );
disp('that are unique to the variables. In contrast, principal' );
disp('axis eigenvalues are based solely on the shared variance' );
disp('among the variables. The two procedures are qualitatively' );
```

```
disp('different. Some therefore claim that the eigenvalues from one' );
disp('extraction method should not be used to determine' );
disp('the number of factors for the other extraction method.' );
disp('The issue remains neglected and unsettled.' );disp(' ');disp(' ');end
plot ( (1:nvars).',realeval meanspercentiles)
xlabel('Root'); ylabel('Eigenvalues'); title ('Real and Random-Data Eigenvalues for N-Roots:')
set(get(gca,'YLabel'),'Rotation',90.0) % for the rotation of the YLabel
set(gca,'XTick', 1:nvars)
set(gca,'FontName','Times', 'FontSize',16, 'fontweight', 'normal' );
legend('real data eigenvalues','mean random eigenvalues','percentile random eigenvalues',1); legend boxoff;
textobj = findobj('type', 'text'); set(textobj, 'fontunits', 'points');
set(textobj,'FontName','Times', 'fontsize', 16); set(textobj, 'fontweight', 'normal');
disp('time for this problem = ', num2str(toc) ); disp(' ')
```

Appendix 3: Pentad calendar

PENTAD NO.	MON	DATES	PENTA D NO.	MON	DATES	PENTAD NO.	MON	DATES
1	JAN	1 – 5	25	MAY	1 – 5	49	AUG-SEP	29 – 2
2	-	6 - 10	26	-	6 – 10	50	-	3 – 7
3	-	11– 15	27	-	11 – 15	51	-	8 – 12
4	-	16 - 20	28	-	16 – 20	52	-	13 – 17
5	-	21 – 25	29	-	21 – 25	53	-	18 – 22
6	-	26 – 30	30	-	26 – 30	54	-	23 – 27
7	JAN-FEB	31 – 4	31	MAY-JUN	31 – 4	55	SEP-OCT	28 – 2
8	-	5 – 9	32	-	5 – 9	56	-	3 – 7
9	-	10 – 14	33	-	10 – 14	57	-	8 – 12
10	-	15 – 19	34	-	15 – 19	58	-	13 – 17
11	-	20 – 24	35	-	20 – 24	59	-	18 – 22
12	FEB-MAR	25 – 1	36	-	25 – 29	60	-	23 – 27
13	-	2 – 6	37	JU-JUL	30 – 4	61	OCT-NOV	28 – 1
14	-	7 – 11	38	JUL	5 – 9	62	-	2 – 6
15	-	12 - 16	39	-	10 – 14	63	-	7 – 11
16	-	17 – 21	40	-	15 – 19	64	-	12 – 16
17	-	22 – 26	41	-	20 – 24	65	-	17 – 21
18	-	27 – 31	42	-	25 – 29	66	-	22 – 26
19	APR	1 – 5	43	JUL-AUG	30 – 3	67	NOV-DEC	27 – 1
20	-	6 – 10	44	AUG	4 – 8	68	-	2 – 6
21	-	11 – 15	45	-	9 – 13	69	-	7 – 11
22	-	16 – 20	46	-	14 – 18	70	-	12 – 16
23	-	21 – 25	47	-	19 – 23	71	-	17 – 21
24	-	26 – 30	48	-	24 – 28	72	-	22 – 26
						73	-	27 – 31

Courtesy of Okoola (1996)

Appendix 4: Sampled Module Containing the Morrison Two-Moment Microphysics Code

```
!WRF:MODEL_LAYER:PHYSICS
! THIS MODULE CONTAINS THE TWO-MOMENT MICROPHYSICS CODE DESCRIBED BY
!MORRISON ET AL. (2009, MWR)
! CHANGES FOR V3.2, RELATIVE TO MOST RECENT (BUG-FIX) CODE FOR V3.1
! 1) ADDED ACCELERATED MELTING OF GRAUPEL/SNOW DUE TO COLLISION WITH
RAIN, FOLLOWING LIN ET AL. (1983)
! 2) INCREASED MINIMUM LAMBDA FOR RAIN, AND ADDED RAIN DROP BREAKUP
FOLLOWING MODIFIED VERSION
!OF VERLINDE AND COTTON (1993)
! 3) CHANGE MINIMUM ALLOWED MIXING RATIOS IN DRY CONDITIONS (RH < 90%),
THIS IMPROVES RADAR REFLECTIIVITY
!IN LOW REFLECTIVITY REGIONS
! 4) BUG FIX TO MAXIMUM ALLOWED PARTICLE FALLSPEEDS AS A FUNCTION OF
AIR DENSITY
! 5) BUG FIX TO CALCULATION OF LIQUID WATER SATURATION VAPOR PRESSURE
(CHANGE IS VERY MINOR)
! 6) INCLUDE WRF CONSTANTS PER SUGGESTION OF JIMY
! bug fix, 5/12/10
! 7) bug fix for saturation vapor pressure in low pressure, to avoid division by zero
! 8) include 'EP2' WRF constant for saturation mixing ratio calculation, instead of hardwire constant
! CHANGES FOR V3.3
! 1) MODIFICATION FOR COUPLING WITH WRF-CHEM (PREDICTED DROPLET NUMBER
CONCENTRATION) AS AN OPTION
! 2) MODIFY FALLSPEED BELOW THE LOWEST LEVEL OF PRECIPITATION, WHICH
PREVENTS
!POTENTIAL FOR SPURIOUS ACCUMULATION OF PRECIPITATION DURING SUB-
STEPPING FOR SEDIMENTATION
! 3) BUG FIX TO LATENT HEAT RELEASE DUE TO COLLISIONS OF CLOUD ICE WITH
RAIN
! 4) CLEAN UP OF COMMENTS IN THE CODE
 ! additional minor bug fixes and small changes, 5/30/2011
! minor revisions by A. Ackerman April 2011:
! 1) replaced kinematic with dynamic viscosity
! 2) replaced scaling by air density for cloud droplet sedimentation
! with viscosity-dependent Stokes expression
! 3) use Ikawa and Saito (1991) air-density scaling for cloud ice
! 4) corrected typo in 2nd digit of ventilation constant F2R
! additional fixes:
! 5) TEMPERATURE FOR ACCELERATED MELTING DUE TO COLLIIONS OF SNOW AND
GRAUPEL
! WITH RAIN SHOULD USE CELSIUS, NOT KELVIN (BUG REPORTED BY K. VAN
WEVERBERG)
! 6) NPRACS IS NOT SUBTRACTED FROM SNOW NUMBER CONCENTRATION, SINCE
```

```
! DECREASE IN SNOW NUMBER IS ALREADY ACCOUNTED FOR BY NSMLTS
! 7) fix for switch for running w/o graupel/hail (cloud ice and snow only)
! hm bug fix 3/16/12
! 1) very minor change to limits on autoconversion source of rain number when cloud water is depleted
! WRFV3.5
! hm/A. Ackerman bug fix 11/08/12
! 1) for accelerated melting from collisions, should use rain mass collected by snow, not snow mass
! collected by rain
! 2) minor changes to some comments
! 3) reduction of maximum-allowed ice concentration from 10 cm-3 to 0.3
! cm-3. This was done to address the problem of excessive and persistent
! anvil cirrus produced by the scheme.
! CHANGES FOR WRFV3.5.1
! 1) added output for snow+cloud ice and graupel time step and accumulated
! surface precipitation
! 2) bug fix to option w/o graupel/hail (IGRAUP = 1), include PRACI, PGSACW,
! and PGRACS as sources for snow instead of graupel/hail, bug reported by
! Hailong Wang (PNNL)
! 3) very minor fix to immersion freezing rate formulation (negligible impact)
! 4) clarifications to code comments
! 5) minor change to shedding of rain, remove limit so that the number of
! collected drops can smaller than number of shed drops
! 6) change of specific heat of liquid water from 4218 to 4187 J/kg/K
!!!!!!!!!!!!!!!!!!!!!!!!!!!!!!!!!!!!!!!!!!!!!!!!!!!!!!!!!!!!!!!!!!!!!!!!!!!!!!!!!!!!!!!!!!!!!!!!!!!
! THIS SCHEME IS A BULK DOUBLE-MOMENT SCHEME THAT PREDICTS MIXING
! RATIOS AND NUMBER CONCENTRATIONS OF FIVE HYDROMETEOR SPECIES:
! CLOUD DROPLETS, CLOUD (SMALL) ICE, RAIN, SNOW, AND GRAUPEL.
MODULE MODULE_MP_MORR_TWO_MOMENT
 USEmodule_wrf_error
 USE module_utility, ONLY: WRFU_Clock, WRFU_Alarm ! GT
 USE module_domain, ONLY : HISTORY_ALARM, Is_alarm_tstep ! GT
 USE module_mp_radar
! USE WRF PHYSICS CONSTANTS
 use module_model_constants, ONLY: CP, G, R => r_d, RV => r_v, EP_2
! USE module_state_description
 IMPLICIT NONE
 REAL, PARAMETER :: PI = 3.1415926535897932384626434
 REAL, PARAMETER :: SQRTPI = 0.9189385332046727417803297
 PUBLIC :: MP_MORR_TWO_MOMENT
 PUBLIC :: POLYSVP
 PRIVATE :: GAMMA, DERF1
 PRIVATE :: PI, SQRTPI
 PRIVATE :: MORR_TWO_MOMENT_MICRO
!!!!!!!!!!!!!!!!!!!!!!!!!!!!!!!!!!!!!!!!!!!!!!!!!!!!!!!!!!!!!!!!!!!!!!!!!!!!!!!!!!
! SWITCHES FOR MICROPHYSICS SCHEME
```

```
! IACT = 1, USE POWER-LAW CCN SPECTRA, NCCN = CS^K
! IACT = 2, USE LOGNORMAL AEROSOL SIZE DIST TO DERIVE CCN SPECTRA
! IACT = 3, ACTIVATION CALCULATED IN MODULE_MIXACTIVATE

INTEGER, PRIVATE :: IACT
! INUM = 0, PREDICT DROPLET CONCENTRATION
! INUM = 1, ASSUME CONSTANT DROPLET CONCENTRATION
! !!!NOTE: PREDICTED DROPLET CONCENTRATION NOT AVAILABLE IN THIS VERSION
! CONTACT HUGH MORRISON (morrison@ucar.edu) FOR FURTHER INFORMATION

INTEGER, PRIVATE :: INUM

! FOR INUM = 1, SET CONSTANT DROPLET CONCENTRATION (CM-3)
REAL, PRIVATE ::NDCNST

! SWITCH FOR LIQUID-ONLY RUN
! ILIQ = 0, INCLUDE ICE
! ILIQ = 1, LIQUID ONLY, NO ICE

INTEGER, PRIVATE :: ILIQ

! SWITCH FOR ICE NUCLEATION
! INUC = 0, USE FORMULA FROM RASMUSSEN ET AL., 2002 (MID-LATITUDE)
!= 1, USE MPACE OBSERVATIONS

INTEGER, PRIVATE :: INUC

! IBASE = 1, NEGLECT DROPLET ACTIVATION AT LATERAL CLOUD EDGES DUE TO
!UNRESOLVED ENTRAINMENT AND MIXING, ACTIVATE
!AT CLOUD BASE OR IN REGION WITH LITTLE CLOUD WATER USING
!NON-EQULIBRIUM SUPERSATURATION,
!IN CLOUD INTERIOR ACTIVATE USING EQUILIBRIUM SUPERSATURATION
! IBASE = 2, ASSUME DROPLET ACTIVATION AT LATERAL CLOUD EDGES DUE TO
!UNRESOLVED ENTRAINMENT AND MIXING DOMINATES,
!ACTIVATE DROPLETS EVERYWHERE IN THE CLOUD USING NON-EQUILIBRIUM
!SUPERSATURATION, BASED ON THE
!LOCAL SUB-GRID AND/OR GRID-SCALE VERTICAL VELOCITY
!AT THE GRID POINT

! NOTE: ONLY USED FOR PREDICTED DROPLET CONCENTRATION (INUM = 0)

INTEGER, PRIVATE :: IBASE

! INCLUDE SUB-GRID VERTICAL VELOCITY IN DROPLET ACTIVATION
! ISUB = 0, INCLUDE SUB-GRID W (RECOMMENDED FOR LOWER RESOLUTION)
! ISUB = 1, EXCLUDE SUB-GRID W, ONLY USE GRID-SCALE W
```

```
INTEGER, PRIVATE :: ISUB
! SWITCH FOR GRAUPEL/NO GRAUPEL
! IGRAUP = 0, INCLUDE GRAUPEL
! IGRAUP = 1, NO GRAUPEL

INTEGER, PRIVATE :: IGRAUP

! HM ADDED NEW OPTION FOR HAIL
! SWITCH FOR HAIL/GRAUPEL
! IHAIL = 0, DENSE PRECIPITATING ICE IS GRAUPEL
! IHAIL = 1, DENSE PRECIPITATING GICE IS HAIL

INTEGER, PRIVATE :: IHAIL

! CLOUD MICROPHYSICS CONSTANTS

REAL, PRIVATE ::AI,AC,AS,AR,AG ! 'A' PARAMETER IN FALLSPEED-DIAM RELATIONSHIP
REAL, PRIVATE ::BI,BC,BS,BR,BG ! 'B' PARAMETER IN FALLSPEED-DIAM RELATIONSHIP
!REAL, PRIVATE ::R! GAS CONSTANT FOR AIR
!REAL, PRIVATE ::RV! GAS CONSTANT FOR WATER VAPOR
!REAL, PRIVATE ::CP! SPECIFIC HEAT AT CONSTANT PRESSURE FOR DRY AIR
REAL, PRIVATE ::RHOSU! STANDARD AIR DENSITY AT 850 MB
REAL, PRIVATE ::RHOW! DENSITY OF LIQUID WATER
REAL, PRIVATE ::RHOI! BULK DENSITY OF CLOUD ICE
REAL, PRIVATE ::RHOSN! BULK DENSITY OF SNOW
REAL, PRIVATE ::RHOG! BULK DENSITY OF GRAUPEL
REAL, PRIVATE ::AIMM! PARAMETER IN BIGG IMMERSION FREEZING
REAL, PRIVATE ::BIMM! PARAMETER IN BIGG IMMERSION FREEZING
REAL, PRIVATE ::ECR! COLLECTION EFFICIENCY BETWEEN DROPLETS/RAIN AND SNOW/RAIN
REAL, PRIVATE ::DCS! THRESHOLD SIZE FOR CLOUD ICE AUTOCONVERSION
REAL, PRIVATE ::MI0! INITIAL SIZE OF NUCLEATED CRYSTAL
REAL, PRIVATE ::MG0! MASS OF EMBRYO GRAUPEL
REAL, PRIVATE ::F1S! VENTILATION PARAMETER FOR SNOW
REAL, PRIVATE ::F2S! VENTILATION PARAMETER FOR SNOW
REAL, PRIVATE ::F1R! VENTILATION PARAMETER FOR RAIN
REAL, PRIVATE ::F2R! VENTILATION PARAMETER FOR RAIN
!REAL, PRIVATE ::G! GRAVITATIONAL ACCELERATION
REAL, PRIVATE ::QSMALL! SMALLEST ALLOWED HYDROMETEOR MIXING RATIO
REAL, PRIVATE ::CI,DI,CS,DS,CG,DG ! SIZE DISTRIBUTION PARAMETERS FOR CLOUD ICE, SNOW, GRAUPEL
REAL, PRIVATE ::EII! COLLECTION EFFICIENCY, ICE-ICE COLLISIONS
REAL, PRIVATE ::ECI! COLLECTION EFFICIENCY, ICE-DROPLET COLLISIONS
```

```
REAL, PRIVATE ::RIN! RADIUS OF CONTACT NUCLEI (M)
! hm, add for V3.2
REAL, PRIVATE ::CPW! SPECIFIC HEAT OF LIQUID WATER

! CCN SPECTRA FOR IACT = 1

REAL, PRIVATE ::C1! 'C' IN NCCN = CS^K (CM-3)
REAL, PRIVATE ::K1! 'K' IN NCCN = CS^K

! AEROSOL PARAMETERS FOR IACT = 2

REAL, PRIVATE ::MW! MOLECULAR WEIGHT WATER (KG/MOL)
REAL, PRIVATE ::OSM! OSMOTIC COEFFICIENT
REAL, PRIVATE ::VI! NUMBER OF ION DISSOCIATED IN SOLUTION
REAL, PRIVATE ::EPSM ! AEROSOL SOLUBLE FRACTION
REAL, PRIVATE ::RHOA ! AEROSOL BULK DENSITY (KG/M3)
REAL, PRIVATE ::MAP! MOLECULAR WEIGHT AEROSOL (KG/MOL)
REAL, PRIVATE ::MA! MOLECULAR WEIGHT OF 'AIR' (KG/MOL)
REAL, PRIVATE ::RR! UNIVERSAL GAS CONSTANT
REAL, PRIVATE ::BACT ! ACTIVATION PARAMETER
REAL, PRIVATE ::RM1! GEOMETRIC MEAN RADIUS, MODE 1 (M)
REAL, PRIVATE ::RM2! GEOMETRIC MEAN RADIUS, MODE 2 (M)
REAL, PRIVATE ::NANEW1 ! TOTAL AEROSOL CONCENTRATION, MODE 1 (M^-3)
REAL, PRIVATE ::NANEW2 ! TOTAL AEROSOL CONCENTRATION, MODE 2 (M^-3)
REAL, PRIVATE ::SIG1 ! STANDARD DEVIATION OF AEROSOL S.D., MODE 1
REAL, PRIVATE ::SIG2 ! STANDARD DEVIATION OF AEROSOL S.D., MODE 2
REAL, PRIVATE ::F11! CORRECTION FACTOR FOR ACTIVATION, MODE 1
REAL, PRIVATE ::F12! CORRECTION FACTOR FOR ACTIVATION, MODE 1
REAL, PRIVATE ::F21! CORRECTION FACTOR FOR ACTIVATION, MODE 2
REAL, PRIVATE ::F22! CORRECTION FACTOR FOR ACTIVATION, MODE 2
REAL, PRIVATE ::MMULT ! MASS OF SPLINTERED ICE PARTICLE
REAL,                                                    PRIVATE
::LAMMAXI,LAMMINI,LAMMAXR,LAMMINR,LAMMAXS,LAMMINS,LAMMAXG,LAMMI
NG

! CONSTANTS TO IMPROVE EFFICIENCY

REAL,                        PRIVATE                        ::
CONS1,CONS2,CONS3,CONS4,CONS5,CONS6,CONS7,CONS8,CONS9,CONS10
REAL,                        PRIVATE                        ::
CONS11,CONS12,CONS13,CONS14,CONS15,CONS16,CONS17,CONS18,CONS19,CONS20
REAL,                        PRIVATE                        ::
CONS21,CONS22,CONS23,CONS24,CONS25,CONS26,CONS27,CONS28,CONS29,CONS30
REAL,                        PRIVATE                        ::
CONS31,CONS32,CONS33,CONS34,CONS35,CONS36,CONS37,CONS38,CONS39,CONS40
REAL, PRIVATE :: CONS41
```

```
CONTAINS

!!!!!!!!!!!!!!!!!!!!!!!!!!!!!!!!!!!!!!!!!!!!!!!!!!!!!!!!!!!!!!!!!!!!!!!!!!!!!!!!
SUBROUTINE MORR_TWO_MOMENT_INIT
!!!!!!!!!!!!!!!!!!!!!!!!!!!!!!!!!!!!!!!!!!!!!!!!!!!!!!!!!!!!!!!!!!!!!!!!!!!!!!!!
! THIS SUBROUTINE INITIALIZES ALL PHYSICAL CONSTANTS AMND PARAMETERS
! NEEDED BY THE MICROPHYSICS SCHEME.
! NEEDS TO BE CALLED AT FIRST TIME STEP, PRIOR TO CALL TO MAIN MICROPHYSICS INTERFACE
!!!!!!!!!!!!!!!!!!!!!!!!!!!!!!!!!!!!!!!!!!!!!!!!!!!!!!!!!!!!!!!!!!!!!!!!!!!!!!!!

IMPLICIT NONE

integer n,i

!!!!!!!!!!!!!!!!!!!!!!!!!!!!!!!!!!!!!!!!!!!!!!!!!!!!!!!!!!!!!!!!!!!!!!!!!!!!!!!!!!!!!!!
!!!!!!!!!!!!!!!!!!!!!!!!!!!!!!!!!!!!!!!!!!!!!!!!!!!!!!!!!!!!!!!!!!!!!!!!!!!!!!!!!!!!!!!

! THE FOLLOWING PARAMETERS ARE USER-DEFINED SWITCHES AND NEED TO BE
! SET PRIOR TO CODE COMPILATION

! INUM IS AUTOMATICALLY SET TO 0 FOR WRF-CHEM BELOW,
! ALLOWING PREDICTION OF DROPLET CONCENTRATION
! THUS, THIS PARAMETER SHOULD NOT BE CHANGED HERE
! AND SHOULD BE LEFT TO 1

INUM = 1

! SET CONSTANT DROPLET CONCENTRATION (UNITS OF CM-3)
! IF NO COUPLING WITH WRF-CHEM

NDCNST = 250.

!!!!!!!!!!!!!!!!!!!!!!!!!!!!!!!!!!!!!!!!!!!!!!!!!!!!!!!!!!!!!!!!!!!!!!!!!!!!!!!!!
! NOTE, THE FOLLOWING OPTIONS RELATED TO DROPLET ACTIVATION
! (IACT, IBASE, ISUB) ARE NOT AVAILABLE IN CURRENT VERSION
! FOR WRF-CHEM, DROPLET ACTIVATION IS PERFORMED
! IN 'MIX_ACTIVATE', NOT IN MICROPHYSICS SCHEME


! IACT = 1, USE POWER-LAW CCN SPECTRA, NCCN = CS^K
! IACT = 2, USE LOGNORMAL AEROSOL SIZE DIST TO DERIVE CCN SPECTRA

IACT = 2
```

```
! IBASE = 1, NEGLECT DROPLET ACTIVATION AT LATERAL CLOUD EDGES DUE TO
!UNRESOLVED ENTRAINMENT AND MIXING, ACTIVATE
!AT CLOUD BASE OR IN REGION WITH LITTLE CLOUD WATER USING
!NON-EQULIBRIUM SUPERSATURATION ASSUMING NO INITIAL CLOUD WATER,
!IN CLOUD INTERIOR ACTIVATE USING EQUILIBRIUM SUPERSATURATION
! IBASE = 2, ASSUME DROPLET ACTIVATION AT LATERAL CLOUD EDGES DUE TO
!UNRESOLVED ENTRAINMENT AND MIXING DOMINATES,
!ACTIVATE DROPLETS EVERYWHERE IN THE CLOUD USING NON-EQUILIBRIUM
!SUPERSATURATION ASSUMING NO INITIAL CLOUD WATER, BASED ON THE
!LOCAL SUB-GRID AND/OR GRID-SCALE VERTICAL VELOCITY
!AT THE GRID POINT

! NOTE: ONLY USED FOR PREDICTED DROPLET CONCENTRATION (INUM = 0)

IBASE = 2

! INCLUDE SUB-GRID VERTICAL VELOCITY (standard deviation of w) IN DROPLET ACTIVATION
! ISUB = 0, INCLUDE SUB-GRID W (RECOMMENDED FOR LOWER RESOLUTION)
! currently, sub-grid w is constant of 0.5 m/s (not coupled with PBL/turbulence scheme)
! ISUB = 1, EXCLUDE SUB-GRID W, ONLY USE GRID-SCALE W

! NOTE: ONLY USED FOR PREDICTED DROPLET CONCENTRATION (INUM = 0)

ISUB = 0
!!!!!!!!!!!!!!!!!!!!!!!!!!!!!!!!!!!!!!!!!!!!!!!!!!!!!!!!!!!!!!!!!!!!!!!!!


! SWITCH FOR LIQUID-ONLY RUN
! ILIQ = 0, INCLUDE ICE
! ILIQ = 1, LIQUID ONLY, NO ICE

ILIQ = 0

! SWITCH FOR ICE NUCLEATION
! INUC = 0, USE FORMULA FROM RASMUSSEN ET AL., 2002 (MID-LATITUDE)
!= 1, USE MPACE OBSERVATIONS (ARCTIC ONLY)

INUC = 0

! SWITCH FOR GRAUPEL/HAIL NO GRAUPEL/HAIL
! IGRAUP = 0, INCLUDE GRAUPEL/HAIL
! IGRAUP = 1, NO GRAUPEL/HAIL

IGRAUP = 0
```

```
! HM ADDED 11/7/07
! SWITCH FOR HAIL/GRAUPEL
! IHAIL = 0, DENSE PRECIPITATING ICE IS GRAUPEL
! IHAIL = 1, DENSE PRECIPITATING ICE IS HAIL
! NOTE ---> RECOMMEND IHAIL = 1 FOR CONTINENTAL DEEP CONVECTION

IHAIL = 0

!!!!!!!!!!!!!!!!!!!!!!!!!!!!!!!!!!!!!!!!!!!!!!!!!!!!!!!!!!!!!!!!!!!!!!!!!!!!!!!!!!!!!!
!!!!!!!!!!!!!!!!!!!!!!!!!!!!!!!!!!!!!!!!!!!!!!!!!!!!!!!!!!!!!!!!!!!!!!!!!!!!!!!!!!!!!!
! SET PHYSICAL CONSTANTS

! FALLSPEED PARAMETERS (V=AD^B)
AI = 700.
AC = 3.E7
AS = 11.72
AR = 841.99667
BI = 1.
BC = 2.
BS = 0.41
BR = 0.8
IF (IHAIL.EQ.0) THEN
        AG = 19.3
        BG = 0.37
ELSE ! (MATSUN AND HUGGINS 1980)
AG = 114.5
BG = 0.5
END IF

! CONSTANTS AND PARAMETERS
!R = 287.15
!RV = 461.5
!CP = 1005.
RHOSU = 85000./(287.15*273.15)
RHOW = 997.
RHOI = 500.
RHOSN = 100.
IF (IHAIL.EQ.0) THEN
        RHOG = 400.
ELSE
RHOG = 900.
END IF
AIMM = 0.66
BIMM = 100.
ECR = 1.
```

```
DCS = 125.E-6
MI0 = 4./3.*PI*RHOI*(10.E-6)**3
          MG0 = 1.6E-10
F1S = 0.86
F2S = 0.28
F1R = 0.78
!F2R = 0.32
! fix 053011
F2R = 0.308
!G = 9.806
QSMALL = 1.E-14
EII = 0.1
ECI = 0.7
! HM, ADD FOR V3.2
! hm, 7/23/13
!CPW = 4218.
CPW = 4187.

! SIZE DISTRIBUTION PARAMETERS

CI = RHOI*PI/6.
DI = 3.
CS = RHOSN*PI/6.
DS = 3.
CG = RHOG*PI/6.
DG = 3.

! RADIUS OF CONTACT NUCLEI
RIN = 0.1E-6

MMULT = 4./3.*PI*RHOI*(5.E-6)**3

! SIZE LIMITS FOR LAMBDA

LAMMAXI = 1./1.E-6
LAMMINI = 1./(2.*DCS+100.E-6)
LAMMAXR = 1./20.E-6
!LAMMINR = 1./500.E-6
LAMMINR = 1./2800.E-6

LAMMAXS = 1./10.E-6
LAMMINS = 1./2000.E-6
LAMMAXG = 1./20.E-6
LAMMING = 1./2000.E-6

! CCN SPECTRA FOR IACT = 1
```

```
! MARITIME
! MODIFIED FROM RASMUSSEN ET AL., 2002
! NCCN = C*S^K, NCCN IS IN CM-3, S IS SUPERSATURATION RATIO IN %

K1 = 0.4
C1 = 100.

! CONTINENTAL

!K1 = 0.5
!C1 = 1000.

! AEROSOL ACTIVATION PARAMETERS FOR IACT = 2
! PARAMETERS CURRENTLY SET FOR AMMONIUM SULFATE

MW = 0.018
OSM = 1.
VI = 3.
EPSM = 0.7
RHOA = 1777.
MAP = 0.132
MA = 0.0284
RR = 8.3187
BACT = VI*OSM*EPSM*MW*RHOA/(MAP*RHOW)

! AEROSOL SIZE DISTRIBUTION PARAMETERS CURRENTLY SET FOR MPACE
! (see morrison et al., 2007, JGR)
! MODE 1

RM1 = 0.052E-6
SIG1 = 2.04
NANEW1 = 72.2E6
F11 = 0.5*EXP(2.5*(LOG(SIG1))**2)
F21 = 1.+0.25*LOG(SIG1)

! MODE 2

RM2 = 1.3E-6
SIG2 = 2.5
NANEW2 = 1.8E6
F12 = 0.5*EXP(2.5*(LOG(SIG2))**2)
F22 = 1.+0.25*LOG(SIG2)

! CONSTANTS FOR EFFICIENCY
```

```
CONS1=GAMMA(1.+DS)*CS
CONS2=GAMMA(1.+DG)*CG
CONS3=GAMMA(4.+BS)/6.
CONS4=GAMMA(4.+BR)/6.
CONS5=GAMMA(1.+BS)
CONS6=GAMMA(1.+BR)
CONS7=GAMMA(4.+BG)/6.
CONS8=GAMMA(1.+BG)
CONS9=GAMMA(5./2.+BR/2.)
CONS10=GAMMA(5./2.+BS/2.)
CONS11=GAMMA(5./2.+BG/2.)
CONS12=GAMMA(1.+DI)*CI
CONS13=GAMMA(BS+3.)*PI/4.*ECI
CONS14=GAMMA(BG+3.)*PI/4.*ECI
CONS15=-1108.*EII*PI**((1.-BS)/3.)*RHOSN**((-2.-BS)/3.)/(4.*720.)
CONS16=GAMMA(BI+3.)*PI/4.*ECI
CONS17=4.*2.*3.*RHOSU*PI*ECI*ECI*GAMMA(2.*BS+2.)/(8.*(RHOG-RHOSN))
CONS18=RHOSN*RHOSN
CONS19=RHOW*RHOW
CONS20=20.*PI*PI*RHOW*BIMM
CONS21=4./(DCS*RHOI)
CONS22=PI*RHOI*DCS**3/6.
CONS23=PI/4.*EII*GAMMA(BS+3.)
CONS24=PI/4.*ECR*GAMMA(BR+3.)
CONS25=PI*PI/24.*RHOW*ECR*GAMMA(BR+6.)
CONS26=PI/6.*RHOW
CONS27=GAMMA(1.+BI)
CONS28=GAMMA(4.+BI)/6.
CONS29=4./3.*PI*RHOW*(25.E-6)**3
CONS30=4./3.*PI*RHOW
CONS31=PI*PI*ECR*RHOSN
CONS32=PI/2.*ECR
CONS33=PI*PI*ECR*RHOG
CONS34=5./2.+BR/2.
CONS35=5./2.+BS/2.
CONS36=5./2.+BG/2.
CONS37=4.*PI*1.38E-23/(6.*PI*RIN)
CONS38=PI*PI/3.*RHOW
CONS39=PI*PI/36.*RHOW*BIMM
CONS40=PI/6.*BIMM
CONS41=PI*PI*ECR*RHOW

!+---+-----------------------------------------------------------------+

END MODULE module_mp_morr_two_moment
!+---+-----------------------------------------------------------------+
```

Appendix 5: Mann Kendall Rank Statistic based on computed P Values

No.	Stations	AOD		FMF		CTT		OLR		TRMM	
		MAM	OND	MAM	OND	MAM	OND	MAM	OND	MAM	OND
1	Nyahururu	0.54	0.59	0.58	0.03	0.02	0.03	< 0.01	0.02	0.58	0.68
2	Naivasha	< 0.01	0.32	0.26	0.11	0.28	0.20	< 0.01	0.57	0.01	0.14
3	Dagoretti	< 0.01	0.03	0.69	0.10	0.03	0.01	< 0.01	< 0.01	0.06	0.12
4	Eldoret	0.26	0.18	0.51	< 0.01	0.04	0.91	0.02	0.02	0.39	0.21
5	Embu	0.01	0.93	0.03	0.85	0.14	0.09	< 0.01	0.02	0.98	0.13
6	Garissa	0.36	0.80	0.78	0.95	0.14	0.17	0.97	0.07	0.29	0.16
7	JKIA	< 0.01	0.03	0.69	0.10	0.03	0.01	< 0.01	< 0.01	0.06	0.12
8	Kabarak	0.54	0.59	0.58	0.03	0.02	0.03	0.02	0.02	0.18	0.58
9	Kakamega	0.14	0.06	0.58	< 0.01	0.03	0.41	0.02	0.02	0.02	0.02
10	Kisii	0.14	0.20	0.42	0.37	0.42	0.04	0.02	0.02	0.82	0.04
11	Kisumu	0.14	0.20	0.42	0.37	0.42	0.04	0.02	0.02	0.01	0.18
12	Kitale	0.86	0.02	0.45	0.32	0.02	0.65	0.02	0.02	0.08	0.09
13	Lamu	0.21	0.44	0.39	0.13	0.32	0.35	< 0.01	< 0.01	0.01	0.16
14	Lodwar	0.34	0.12	0.93	0.09	0.04	0.04	< 0.01	0.57	0.20	0.39
15	Makindu	0.08	0.13	0.29	0.46	0.07	0.80	< 0.01	< 0.01	0.03	0.38
16	Malindi	0.01	0.90	0.06	0.37	0.78	0.29	< 0.01	< 0.01	0.01	0.48
17	Mandera	0.39	0.61	0.63	0.37	0.91	0.67	< 0.01	0.08	0.75	0.11
18	Marsabit	0.15	0.02	0.02	0.02	0.04	0.02	0.82	0.11	0.57	0.07
19	Meru	0.04	0.09	0.63	0.99	0.82	0.03	< 0.01	0.02	0.92	0.27
20	Mombasa	0.64	0.02	0.01	0.02	0.98	0.62	< 0.01	< 0.01	0.04	0.02
21	Moyale	0.61	0.15	0.93	0.28	0.36	0.21	< 0.01	0.35	0.45	0.53
22	Msabaha	0.01	0.90	0.06	0.37	0.78	0.29	< 0.01	< 0.01	0.04	0.01
23	Mtwapa	0.28	0.17	0.82	0.08	0.36	0.58	< 0.01	< 0.01	0.21	0.69
24	Nakuru	0.54	0.59	0.58	0.03	0.02	0.03	0.02	0.02	0.01	0.28
25	Nanyuki	0.04	0.09	0.63	0.99	0.82	0.03	< 0.01	0.02	0.26	0.12
26	Narok	0.02	0.11	0.25	0.65	0.11	0.06	0.02	0.02	0.13	0.73
27	Nyeri	0.01	0.93	0.03	0.85	0.14	0.09	< 0.01	0.02	0.41	0.04
28	Voi	0.46	0.65	0.10	0.38	0.07	0.53	< 0.01	< 0.01	0.01	0.49

29	Arua	0.49	0.09	0.13	0.27	0.27	0.12	0.04	0.03	0.12	0.66
30	Moyo	0.53	0.14	0.69	0.02	0.41	< 0.01	0.04	0.41	0.83	0.83
31	Kotido	0.46	0.21	0.74	0.08	0.01	0.25	< 0.01	0.57	0.03	0.52
32	Wadelai	0.53	0.04	0.43	0.21	0.16	< 0.01	0.04	0.41	0.76	0.61
33	Gulu	0.48	0.17	0.03	0.14	0.15	< 0.01	0.04	0.41	0.58	0.50
34	Pachwa	0.48	0.17	0.02	0.45	0.02	0.90	< 0.01	< 0.01	0.37	0.26
35	Masindi	0.48	0.17	0.02	0.45	0.02	0.90	0.04	0.41	0.93	0.29
36	Bulindi	0.48	0.17	0.02	0.45	0.02	0.90	0.04	0.41	0.93	0.29
37	Aduku	0.48	0.17	0.03	0.14	0.15	< 0.01	0.04	0.41	0.61	0.08
38	Kakoge	0.41	0.02	0.93	0.04	0.43	0.35	< 0.01	< 0.01	0.40	0.07
39	Serere	0.02	0.09	0.07	0.94	0.70	0.69	0.04	0.41	0.81	0.58
40	Soroti	0.02	0.09	0.07	0.94	0.70	0.69	0.04	0.41	0.81	0.58
41	Arapai	0.02	0.09	0.07	0.94	0.70	0.69	0.04	0.41	0.74	0.70
42	Kiige	0.02	0.09	0.07	0.94	0.70	0.69	< 0.01	< 0.01	0.12	0.55
43	Namalu	0.08	0.16	< 0.01	< 0.01	0.01	0.02	< 0.01	0.57	0.13	0.21
44	Kijura	0.34	0.28	< 0.01	0.10	0.03	0.01	< 0.01	0.08	0.39	0.04
45	Kilembe	0.34	0.28	< 0.01	0.10	0.03	0.01	< 0.01	0.08	0.45	0.17
46	Rwimi	0.34	0.28	< 0.01	0.10	0.03	0.01	< 0.01	0.08	0.46	0.83
47	Kasese	0.34	0.28	< 0.01	0.10	0.03	0.01	< 0.01	0.08	0.45	0.17
48	Mubende	0.33	0.07	0.02	0.14	0.02	0.26	< 0.01	< 0.01	0.68	0.73
49	Makerere	0.04	0.61	0.04	0.33	0.04	0.77	< 0.01	< 0.01	0.50	0.58
50	Nakifuma	0.04	0.61	0.04	0.33	0.04	0.77	< 0.01	< 0.01	0.90	0.56
51	Entebbe	0.04	0.61	0.04	0.33	0.04	0.77	< 0.01	< 0.01	0.73	0.47
52	Kituza	0.04	0.61	0.04	0.33	0.04	0.77	< 0.01	< 0.01	0.17	0.82
53	Entebbe	0.04	0.61	0.04	0.33	0.04	0.77	< 0.01	< 0.01	0.73	0.47
54	Jinja	0.01	0.02	< 0.01	0.80	0.10	0.20	< 0.01	< 0.01	0.67	0.78
55	Mbarara	0.02	0.30	0.10	< 0.01	0.27	0.76	< 0.01	0.08	0.19	0.86
56	Rubale	0.02	0.30	0.10	< 0.01	0.27	0.76	< 0.01	0.08	0.14	0.57
57	Kikunda	0.02	0.30	0.10	< 0.01	0.27	0.76	< 0.01	0.08	0.34	0.83
58	Bujumbura	0.19	0.44	0.03	0.12	0.37	0.10	< 0.01	0.01	0.39	0.03
59	Rubona	0.64	0.09	< 0.01	< 0.01	0.70	0.17	< 0.01	0.01	0.76	0.04
60	Kigali	0.04	0.14	0.32	*	0.14	0.08	< 0.01	0.01	0.39	0.03
61	Kamembe	0.30	< 0.01	< 0.01	*	0.92	0.28	< 0.01	0.01	0.16	0.08

62	Gisenyi	0.39	< 0.01	0.02	*	0.74	0.27	< 0.01	0.01	0.29	0.98
63	Gikongoro	0.76	0.11	< 0.01	*	0.17	0.12	< 0.01	0.01	0.76	0.04
64	Ruhengeri	0.04	< 0.01	0.32	*	0.14	0.08	< 0.01	0.01	0.10	0.32
65	Byumba	0.57	< 0.01	0.04	*	0.14	0.35	< 0.01	0.01	0.77	0.41
66	Arusha	< 0.01	0.85	0.30	0.01	0.83	0.03	< 0.01	< 0.01	< 0.01	< 0.01
67	Bukoba	0.08	0.49	0.97	*	0.25	0.81	< 0.01	< 0.01	0.06	0.93
68	Dar es salaam	0.42	0.03	0.35	0.63	0.32	0.82	< 0.01	< 0.01	0.03	0.38
69	Dodoma	0.21	< 0.01	0.53	0.11	0.73	0.70	< 0.01	< 0.01	0.54	0.22
70	Iringa	0.57	0.10	0.74	0.38	0.29	0.03	0.07	0.10	0.19	0.09
71	Kibaha	0.24	0.01	0.10	0.61	0.75	0.20	< 0.01	< 0.01	0.53	0.19
72	Kigoma	0.23	0.24	0.02	*	0.71	< 0.01	< 0.01	0.02	0.40	< 0.01
73	Lupiro	0.30	0.10	0.29	0.44	0.92	0.17	< 0.01	< 0.01	0.08	0.37
74	Mbeya	0.85	0.01	0.92	0.02	1.00	0.02	< 0.01	< 0.01	0.14	0.31
75	Morogoro	0.01	0.52	0.26	< 0.01	0.34	0.04	< 0.01	< 0.01	0.86	0.07
76	Moshi	0.01	0.90	0.08	0.31	0.46	0.29	< 0.01	< 0.01	< 0.01	0.58
77	Mtwara	0.81	0.20	0.60	0.87	0.88	0.88	< 0.01	0.15	0.04	0.06
78	Musoma	0.82	0.97	0.77	*	0.92	0.46	< 0.01	< 0.01	0.18	0.17
79	Mwanza	0.10	0.06	0.45	*	0.57	0.12	< 0.01	< 0.01	0.55	0.01
80	Pemba	0.13	0.52	0.16	0.62	0.51	0.81	< 0.01	< 0.01	0.86	< 0.01
81	Manyoni	0.12	0.11	0.07	0.06	0.46	0.04	< 0.01	< 0.01	0.32	0.71
82	Selous G.R	0.54	*	0.95	0.10	0.62	0.06	< 0.01	0.15	0.47	0.14
83	Sumbawanga	0.67	*	0.07	0.04	0.66	0.39	< 0.01	< 0.01	0.13	0.10
84	Tambora	0.09	*	< 0.01	0.03	0.02	0.62	< 0.01	< 0.01	0.74	0.57
85	Tanga	0.13	*	0.16	0.62	0.51	0.81	< 0.01	< 0.01	0.36	0.85
86	Zanzibar	0.42	*	0.35	0.63	0.35	0.83	< 0.01	< 0.01	0.17	0.04

Note: Computed P values greater than alpha (0.05) indicates no trend (not highlighted) while computed P values less than alpha (0.05) indicates presence of trend (highlighted in Yellow)

Appendix 6: Homogeneous sub-regions

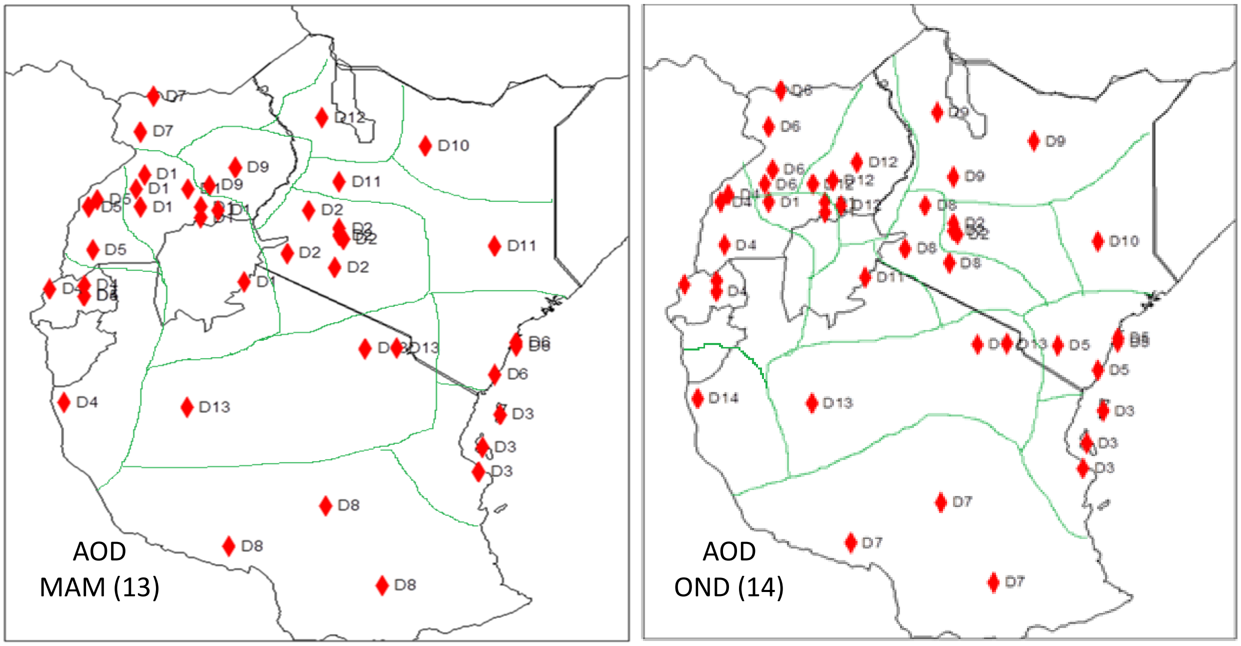

Fig 3 a: Homogeneous sub-regions obtained from daily AOD series

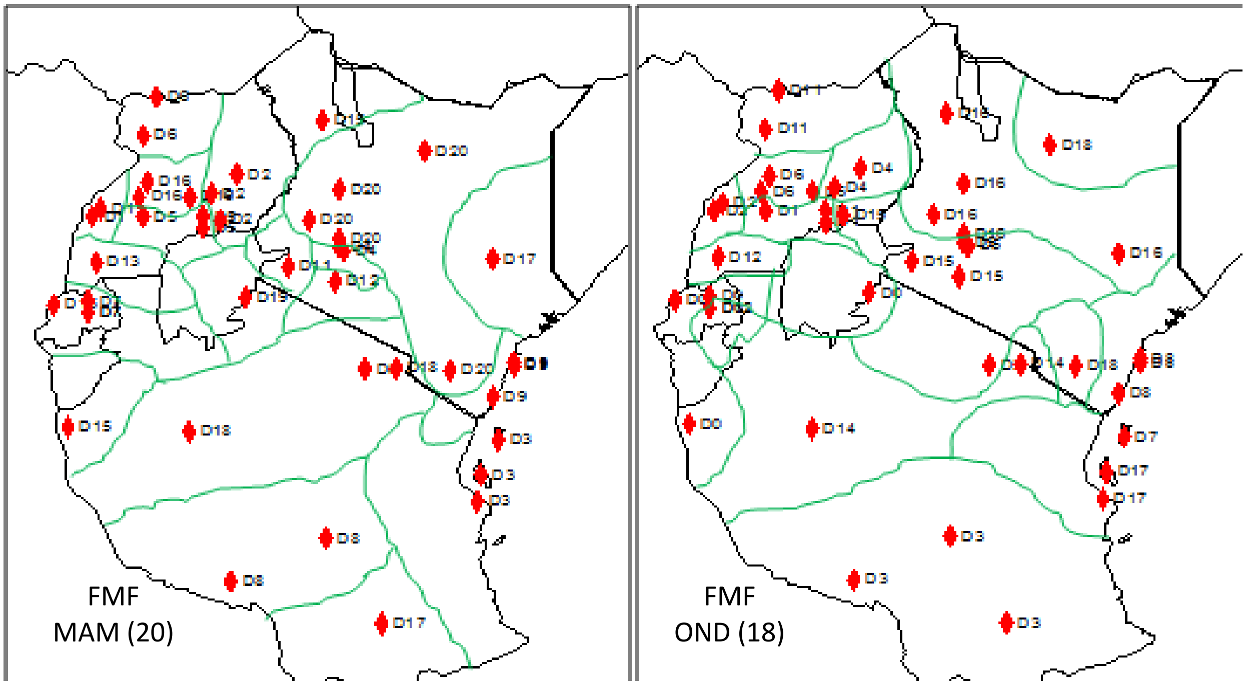

Fig 3 b: Homogeneous sub-regions obtained from daily FMF series

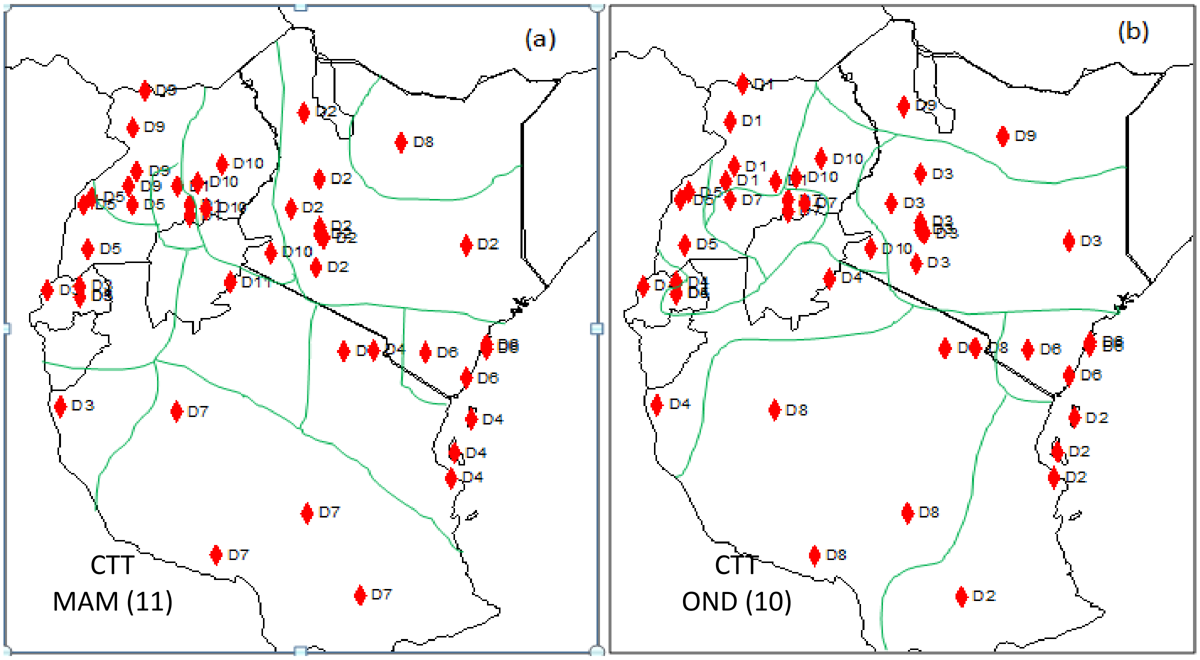

Fig 3 c: Homogeneous sub-regions obtained from daily CTT series

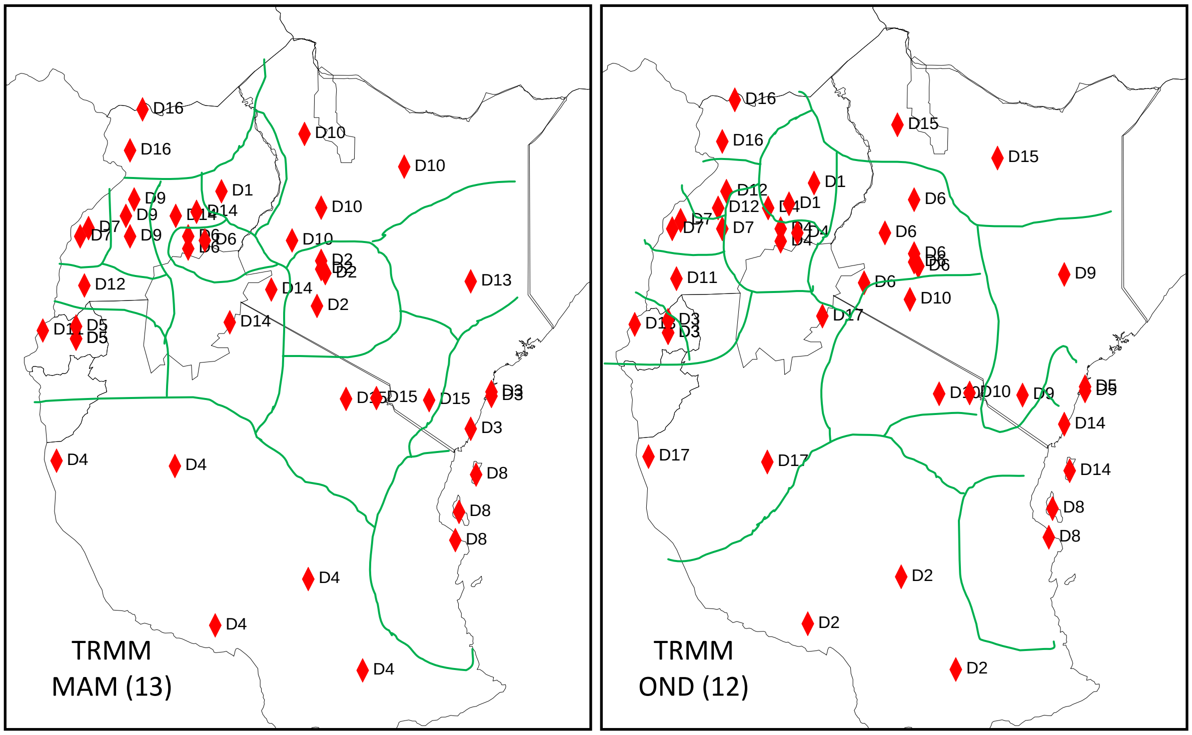

Fig 3 d: Homogeneous sub-regions obtained from daily TRMM series

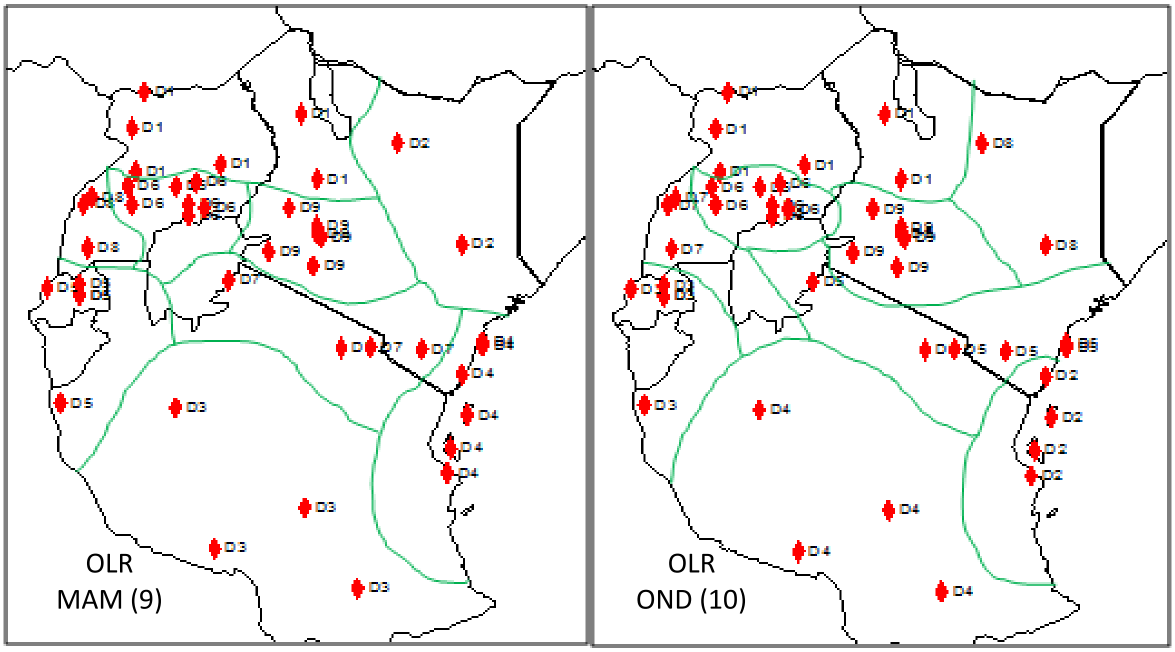

Fig 3 E: Homogeneous sub-regions obtained from daily OLR series

Appendix 7: Scree Parallel Plots

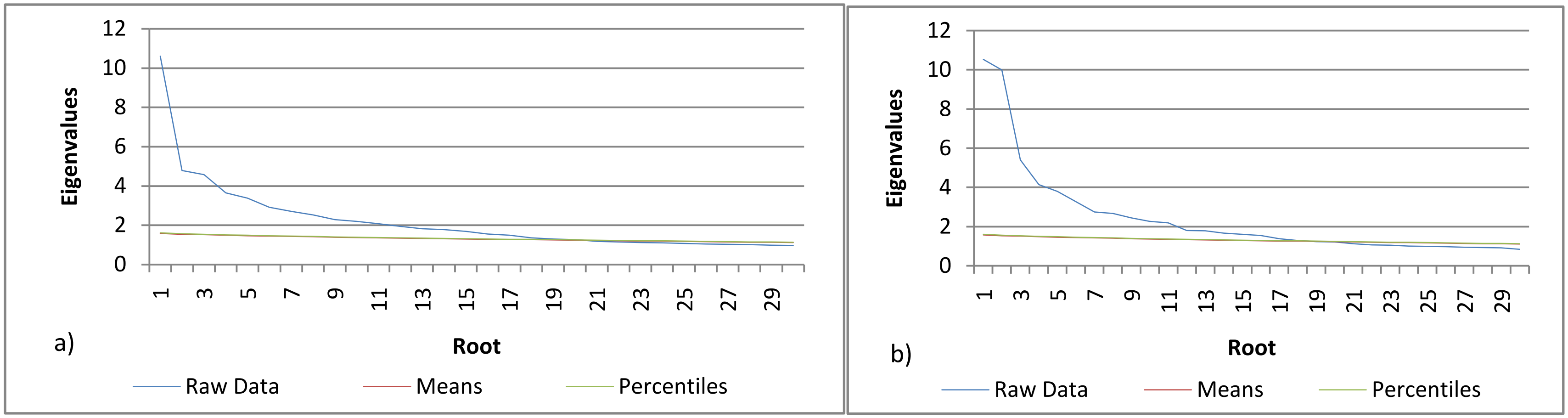

Fig. 5 a: A Scree parallel plot based on FMF Eigenvalues for observed (Raw), Means and 95th percentile (random) data during a) MAM b) OND season.

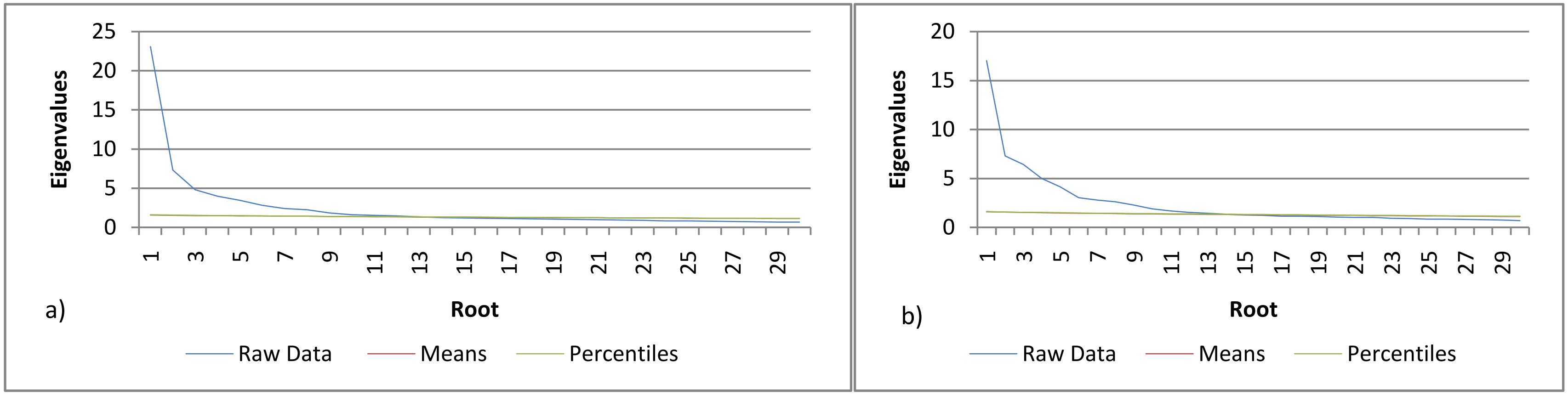

Fig. 5 b: A Scree parallel plot based on AOD Eigenvalues for observed (Raw), Means and 95th percentile (random) data during a) MAM b) OND season.

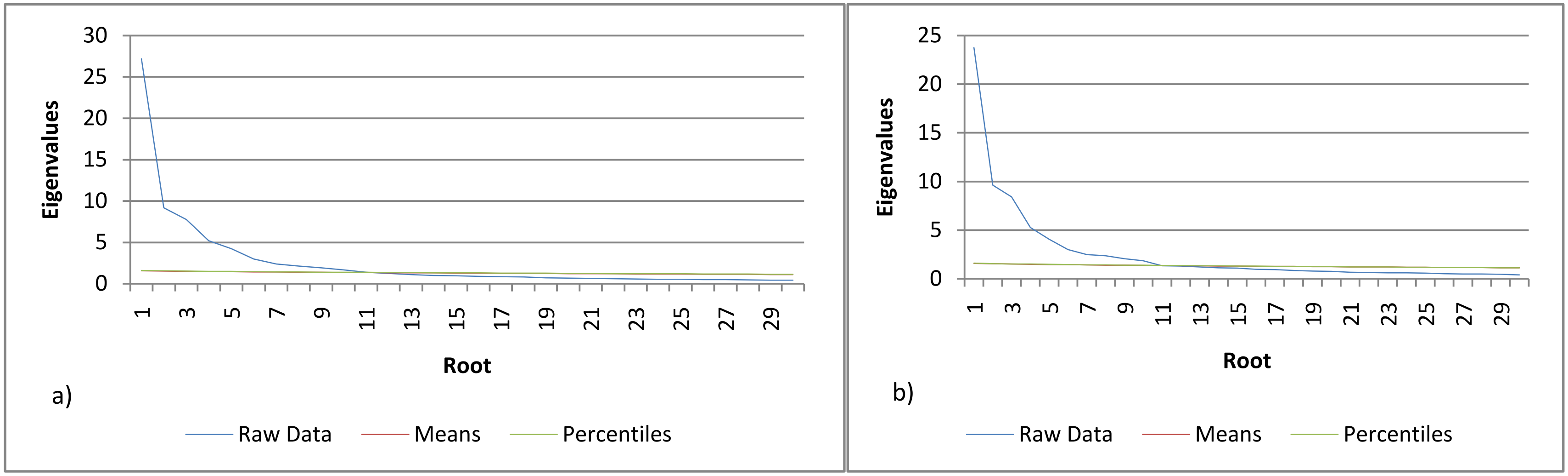

Fig. 5c: A Scree parallel plot based on CTT Eigenvalues for observed (Raw), Means and 95th percentile (random) data during a) MAM b) OND season.

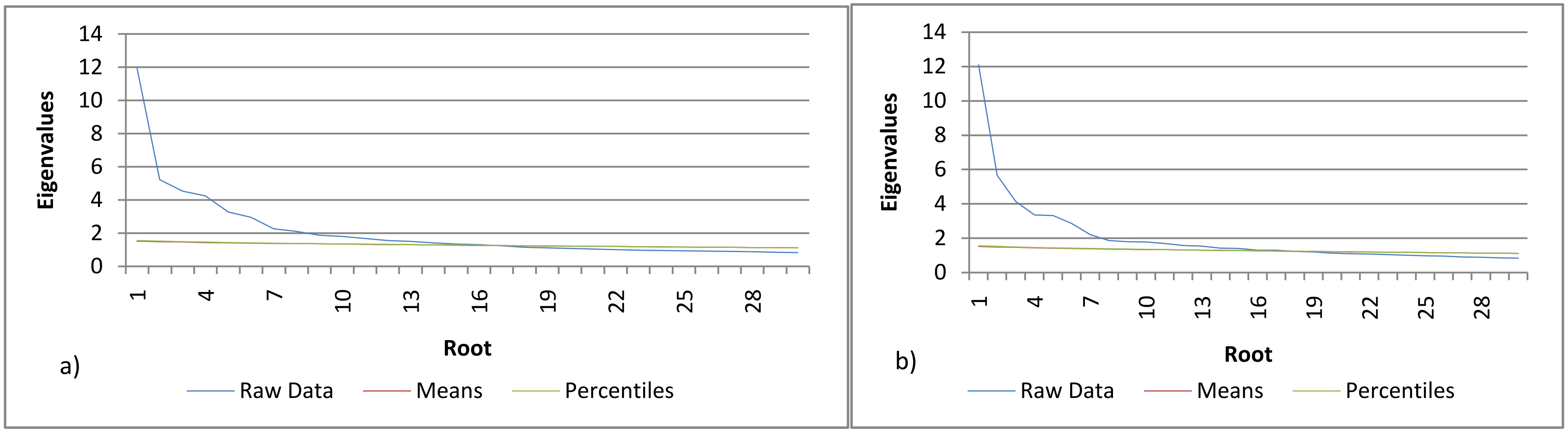

Fig. 5d: A Scree parallel plot based on TRMM 3B42 Eigenvalues for observed (Raw), Means and 95th percentile (random) data during a) MAM b) OND season.

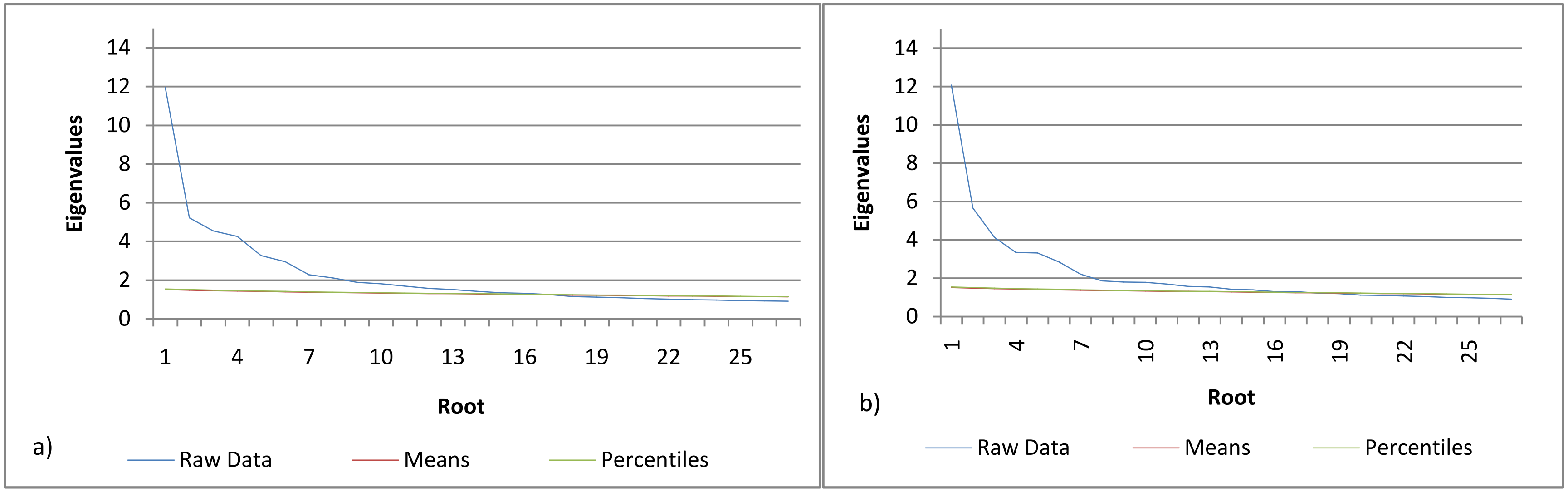

Fig. 5d: A Scree parallel plot based on OLR Eigenvalues for observed (Raw), Means and 95th percentile (random) data during a) MAM b) OND season

Appendix 8: Regions with Strong Factor Loadings (>0.75)

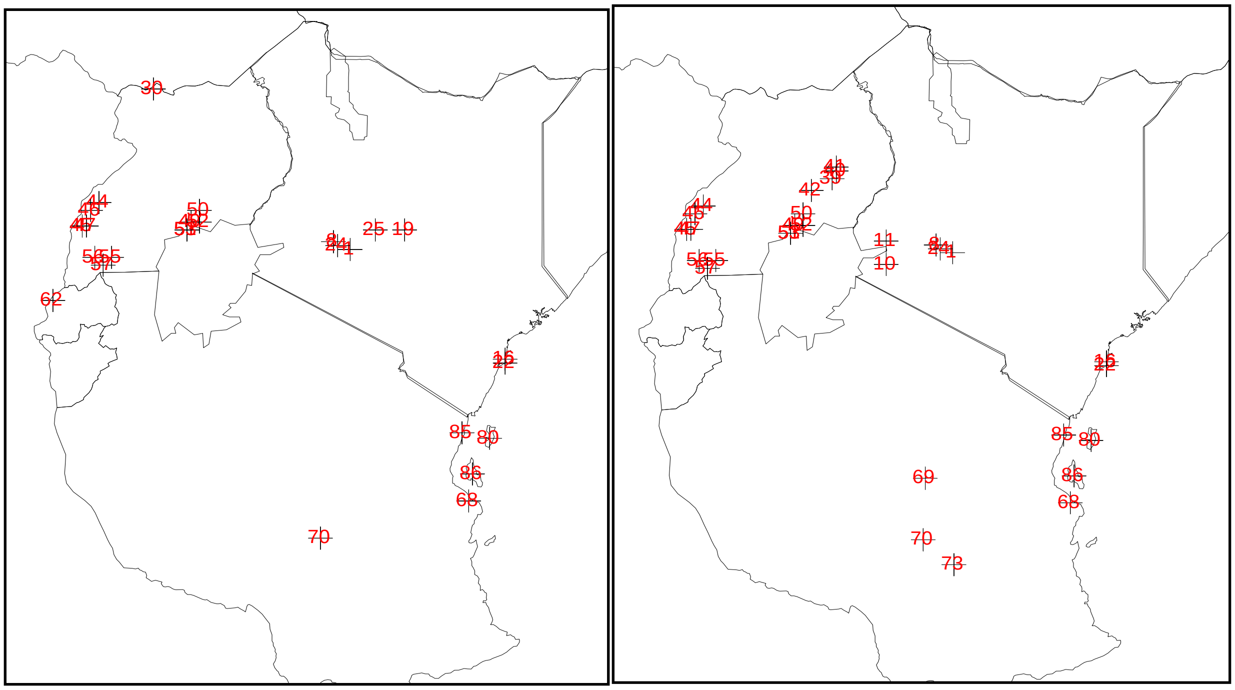

Fig. 7a: Strong Factor Loadings (> 0.75) after Varimax rotation obtained from daily AOD series during a) MAM and b) OND season

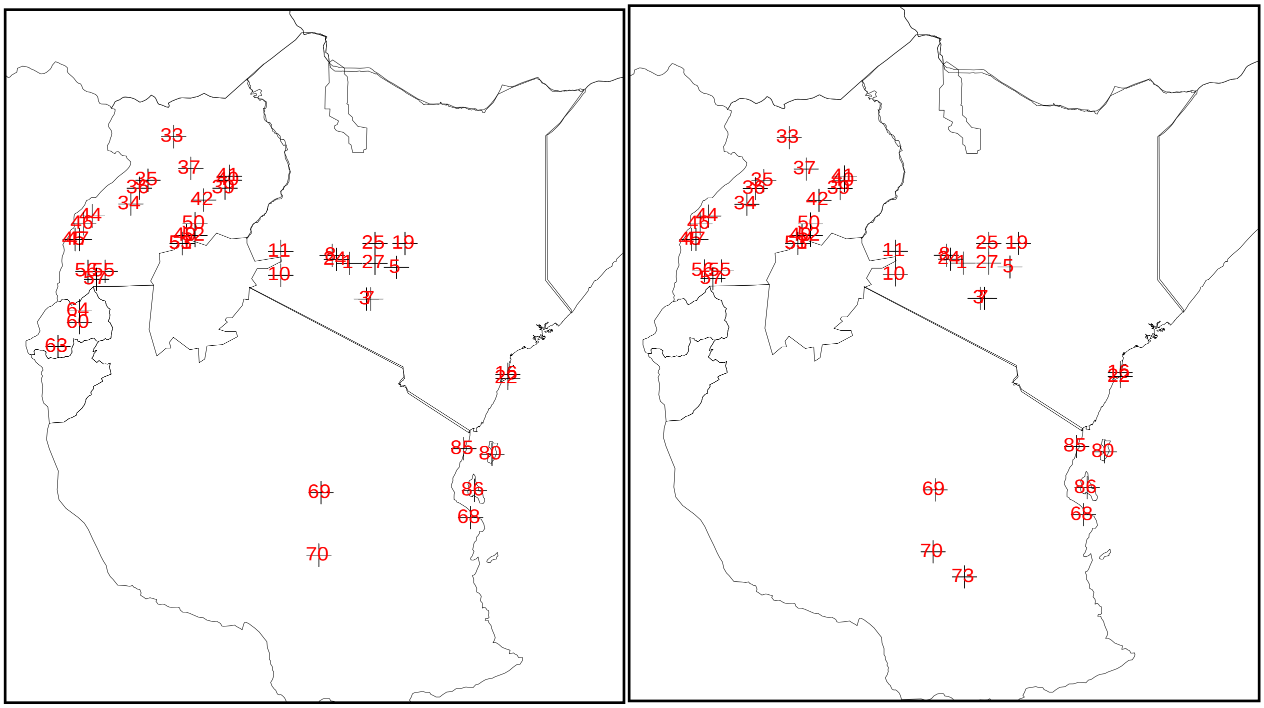

Fig. 7b: Strong Factor Loadings (> 0.75) after Varimax rotation obtained from daily FMF series during a) MAM and b) OND season

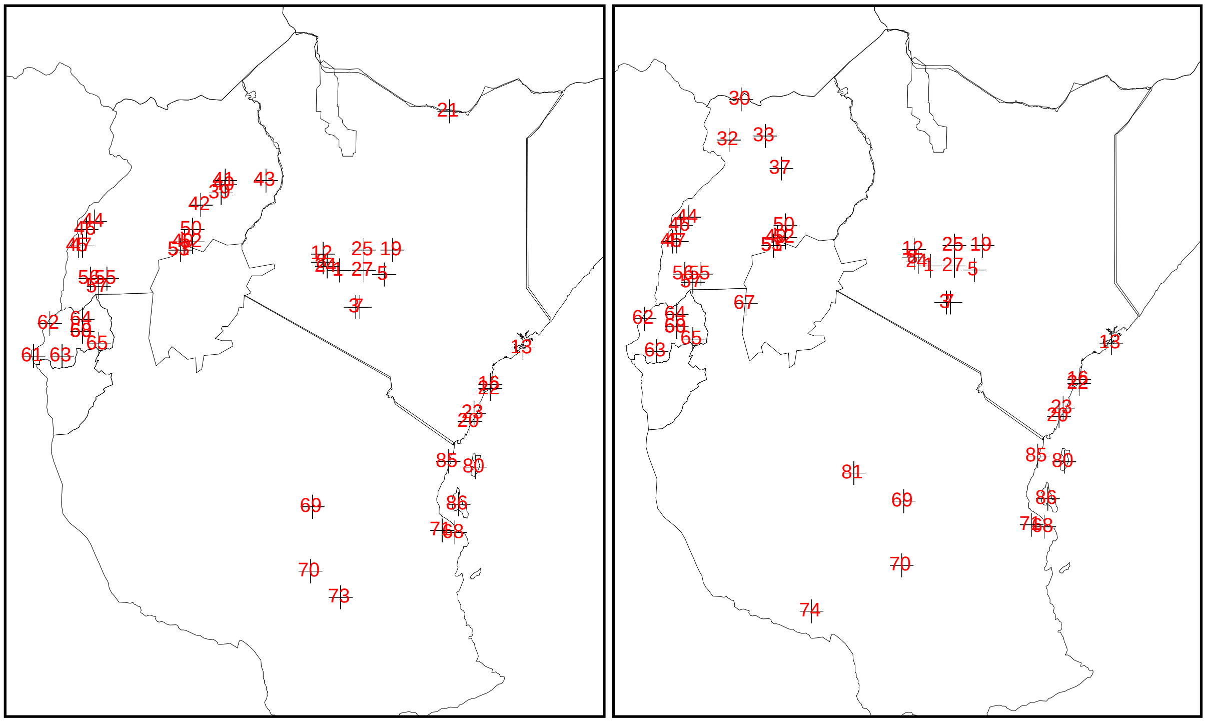

Fig. 7c: Strong Factor Loadings (> 0.75) after Varimax rotation obtained from daily CTT series during a) MAM and b) OND season

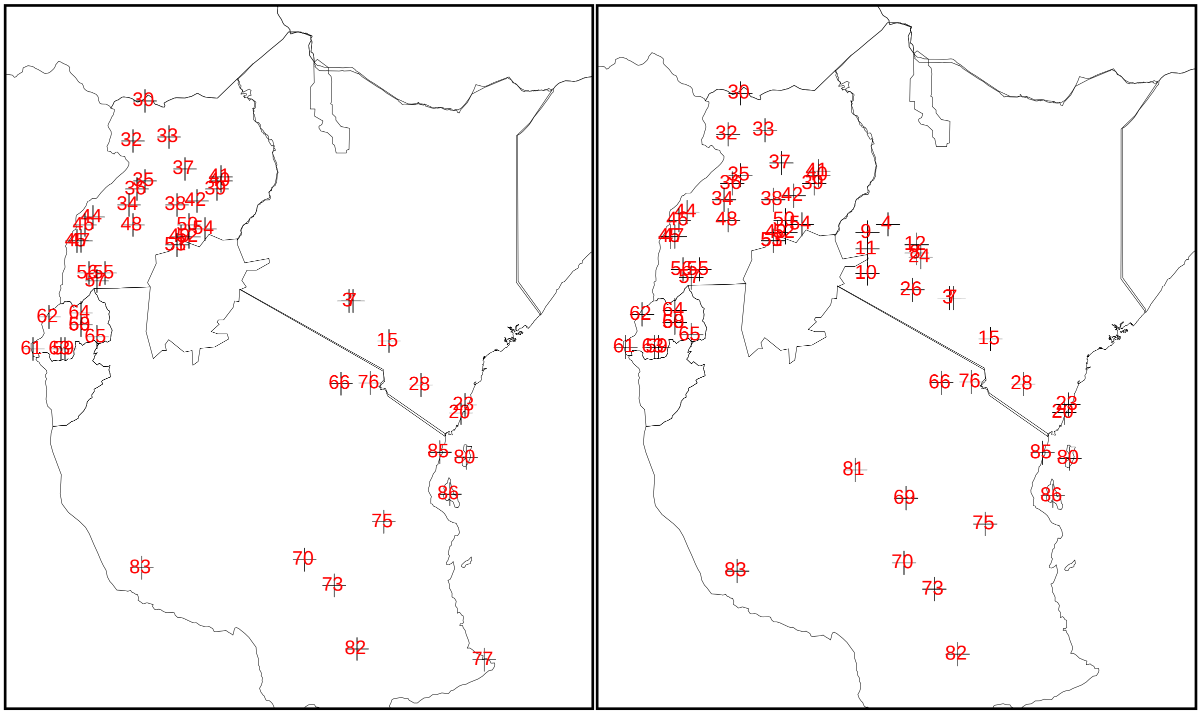

Fig. 7d: Strong Factor Loadings (> 0.75) after Varimax rotation obtained from daily OLR series during a) MAM and b) OND season

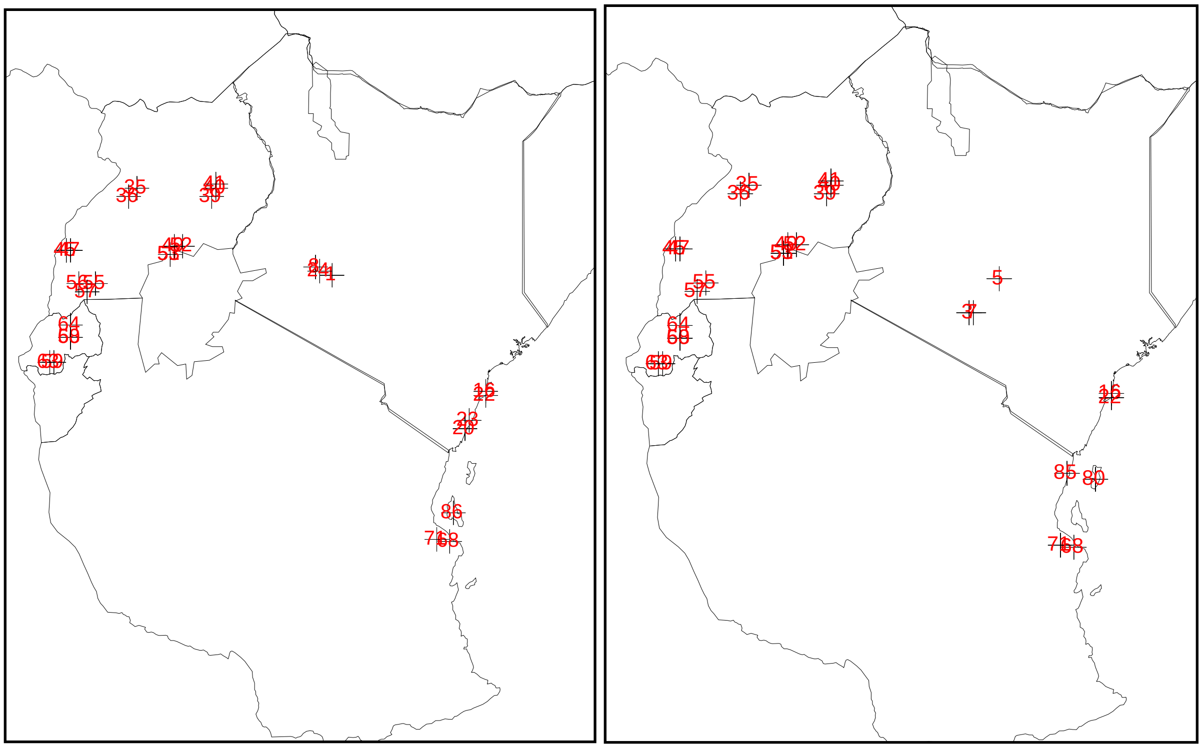

Fig. 7e: Strong Factor Loadings (> 0.75) after Varimax rotation obtained from daily TRMM (3b42) series during a) MAM and b) OND season

Appendix 9: Model Selection based on Stepwise Regression Method

a) MAM season

Entebbe	Estimate	Nakuru	Estimate	Zanzibar	Estimate	Kasese	Estimate	Kigali	Estimate
Intercept	36.49	Intercept	32.31	Intercept	68.12	Intercept	3.28	Intercept	17.57
Entebbe.olr	-0.08	Kitale.olr	-0.10	Zanzibar.olr	-0.24	Kasese.olr	-0.02	Kigali.olr	-0.05
Entebbe.ctt	-0.05	Kasese.aod	-2.90	Dar es Salaam.aod	13.33	Soroti.olr	-0.03	Entebbe.olr	-0.02
Moyale.olr	-0.04	Wadelai.ctt	0.03	Iringa.olr	-0.08	Kigali.olr	-0.02	Kitale.olr	-0.03
Moyale.ctt	0.05	Arusha.olr	-0.02	Mtwapa.fmf	7.38	Dodoma.ctt	0.02	Mwanza.ctt	0.04
Kigali.olr	-0.03	Entebbe.aod	-3.92	Kitale.olr	0.04	Iringa.aod	-3.30	Iringa.olr	0.02
Tabora.aod	-4.57	Dar es Salaam.fmf	-2.11	Kasese.aod	-6.56	Soroti.fmf	1.68	Kigali.ctt	-0.02
Malindi.fmf	3.97	Gulu.fmf	-1.58	Dodoma.ctt	0.05	Nakuru.aod	4.91	Nanyuki.fmf	-3.57
Nyeri.fmf	-3.03	Moyale.ctt	-0.02	Mbarara.ctt	-0.04	Moyale.olr	0.01	Dagoretti.fmf	2.76
Soroti.fmf	-2.91	Dagoretti.fmf	2.53	Kasese.fmf	2.86	Entebbe.ctt	0.02	Wadelai.ctt	0.02
Kisumu.fmf	3.00	Zanzibar.olr	-0.01	Malindi.aod	-8.35	Nakuru.fmf	1.47	Kasese.olr	-0.02
		Zanzibar.ctt	0.02	Manyoni.fmf	-3.31	Moyale.fmf	2.51	Moyale.fmf	2.99
						Dar es Salaam.fmf	1.33	Dodoma.fmf	-2.10

Malindi	Estimate	Masindi	Estimate	Mombasa	Estimate	Soroti	Estimate
Intercept	34.92	Intercept	18.99	Intercept	39.14	Intercept	10.27
Malindi.ctt	-0.10	Soroti.olr	-0.06	Zanzibar.olr	-0.07	Soroti.olr	-0.09
Arusha.olr	-0.12	Kasese.olr	-0.05	Malindi.ctt	-0.08	Dodoma.fmf	4.20
Iringa.olr	0.05	Kigali.ctt	0.02	Arusha.olr	-0.12	Moyale.ctt	0.03
Kitale.olr	0.05	Malindi.fmf	3.65	Kitale.olr	0.05	Entebbe.olr	-0.03
Zanzibar.olr	-0.04	Zanzibar.ctt	0.02	Iringa.olr	0.03	Kigali.ctt	0.03
Nakuru.ctt	0.04	Mtwapa.fmf	-2.54	Nakuru.aod	-9.94	Gulu.fmf	2.85
Entebbe.fmf	3.52	Entebbe.ctt	-0.02	Moyale.ctt	0.04	Nakuru.ctt	0.03
Soroti.ctt	-0.02	Entebbe.olr	0.02	Kigali.ctt	0.03	Dar es Salaam.fmf	-3.23
Nakuru.aod	-8.46	Malindi.ctt	-0.03	Wadelai.ctt	-0.02	Kigali.olr	-0.03
Entebbe.olr	-0.02	Arusha.olr	0.03			Zanzibar.ctt	0.02
Kigali.ctt	0.03	Kitale.olr	-0.02			Many.fmf	-1.90
Moyale.ctt	0.03	Lodwar.aod	-2.50			Dagoretti.aod	4.94
Dodoma.fmf	-3.11	Nanyuki.fmf	2.69			Entebbe.aod	-6.55
Gulu.fmf	-2.03	Dar es Salaam.fmf	1.84			Soroti.aod	6.10
						Nakuru.aod	-5.70
						Malindi.fmf	-3.11

b) OND season

Embu	Estimate	Malindi	Estimate	Entebbe	Estimate	Dagoreti	Estimate	Kasese	Estimate	Mbarara	Estimate
Intercept	82.01	Intercept	40.62	Intercept	46.55	Intercept	43.81	Intercept	5.01	Intercept	25.24
Arusha.olr	-0.16	Arusha.olr	-0.11	Soroti.olr	-0.08	Arusha.olr	-0.10	Mbarara.olr	-0.04	Mbarara.olr	-0.04
Moyale.olr	-0.07	Iringa.olr	0.02	Entebbe.ctt	-0.04	Kitale.olr	-0.08	Iringa.olr	0.01	Entebbe.olr	-0.02
Kitale.olr	-0.08	Malindi.ctt	-0.06	Arusha.olr	-0.03	Mbarara.aod	-4.41	Mbarara.ctt	0.02	Soroti.olr	-0.02
Iringa.olr	0.02	Entebbe.aod	-5.35	Mbarara.aod	6.24	Wadelai.aod	2.93	Kakamega.ctt	-0.03	Kigali.olr	-0.02
Nanyuki.aod	11.80	Nanyuki.fmf	3.33	Nyeri.fmf	2.87	Nanyuki.fmf	-3.10	Entebbe.ctt	0.02	Wadelai.ctt	-0.02
Entebbe.aod	-6.89	Nakuru.ctt	0.06	Tabora.aod	-7.53	Mbarara.olr	0.01	Entebbe.olr	-0.02	Entebbe.ctt	0.02
Lodwar.aod	-8.22	Entebbe.olr	-0.04	Entebbe.fmf	-2.97	Dago.aod	-5.60	Arusha.olr	0.02	Wadelai.aod	2.94
Dodoma.fmf	3.17	Wadelai.aod	-3.60	Soroti.aod	8.11	Kisumu.aod	5.34	Gulu.fmf	-1.74	Nanyuki.fmf	1.63
Malindi.ctt	-0.05	Kakamega.ctt	-0.03	Entebbe.aod	-7.95	Dodoma.fmf	-1.91	Dago.aod	3.35	Mbarara.aod	-2.15
Zanzibar.olr	0.04	Kigali.olr	0.02	Mbarara.olr	0.04	Tabora.aod	-5.03	Entebbe.aod	-3.70	Malindi.ctt	-0.02
Malindi.aod	-9.04	Kitale.olr	0.03	Entebbe.olr	-0.03	Nakuru.fmf	1.88	Nakuru.fmf	-1.52	Arusha.olr	0.02
Mbarara.ctt	0.03	Nyeri.fmf	-2.25	Kigali.olr	-0.02	Tang.fmf	-2.65	Wadelai.aod	2.35		
Soroti.olr	-0.04	Mbarara.fmf	-1.90	Malindi.fmf	-3.36						
Entebbe.olr	0.03	Mbarara.ctt	0.02	Kisumu.fmf	2.07						
Kisumu.fmf	-2.64	Moyale.ctt	-0.02								

Tanga	Estimate	Dar es Salaam	Estimate	Kigali	Estimate	Soroti	Estimate	Masindi	Estimate
Intercept	45.80	Intercept	64.51	Intercept	23.43	Intercept	33.51	Intercept	35.29
Zanzibar.olr	-0.12	Zanzibar.olr	-0.18	Kigali.olr	-0.04	Soroti.olr	-0.09	Soroti.olr	-0.09
Arusha.olr	-0.11	Iringa.olr	-0.06	Kitale.olr	-0.04	Kitale.olr	-0.05	Moyale.olr	-0.03
Kigali.olr	0.02	Dago.fmf	4.68	Tang.aod	5.84	Tabora.fmf	10.27	Iringa.olr	0.01
Kitale.olr	0.05	Lodwar.aod	8.02	Soroti.aod	6.63	Tabora.aod	4.58	Kisumu.fmf	2.06
Kisumu.aod	8.13	Soroti.aod	-6.43	Entebbe.aod	-4.04	Kisumu.aod	-3.73	Zanzibar.ctt	-0.02
Moyale.olr	-0.04	Soroti.fmf	3.01	Soroti.fmf	-2.29	Arusha.olr	0.03	Wadelai.ctt	-0.02
Kakamega.ctt	0.02	Mbarara.aod	-4.06	Kisumu.fmf	2.26	Zanzibar.olr	-0.02	Kakamega.ctt	0.02
Entebbe.aod	5.96	Dodoma.fmf	-2.35	Mbarara.olr	-0.01	Nakuru.fmf	1.75		
Mbarara.fmf	2.17								
Wadelai.aod	-2.91								

Appendix 10: Normality test of Multivariate Regression Analysis

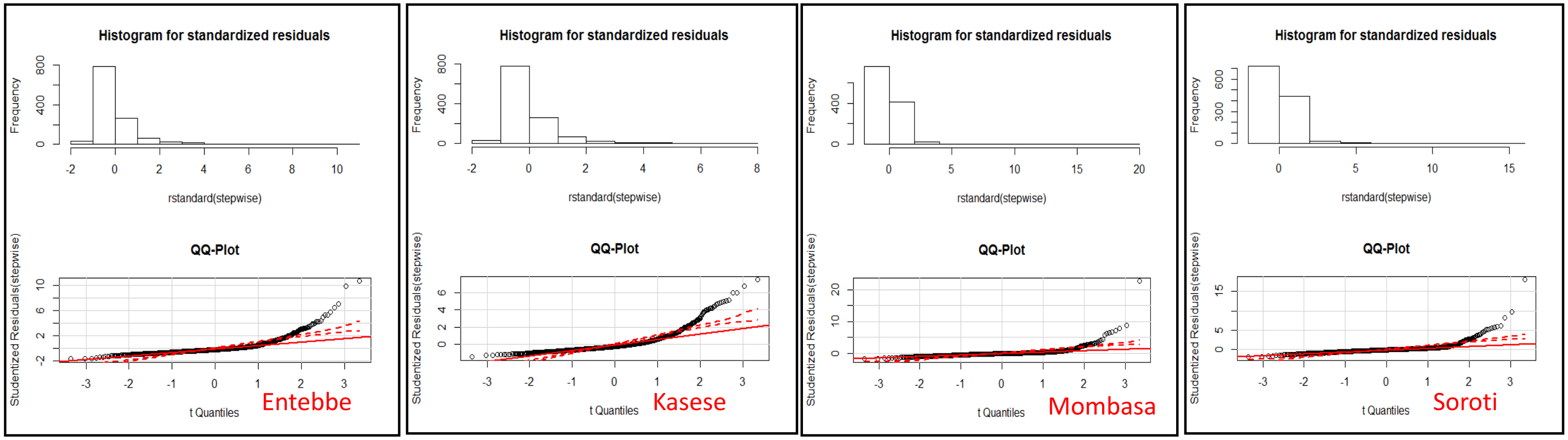

Fig. 9a: Normality Test Based on Histograms and QQ Plots for MAM season

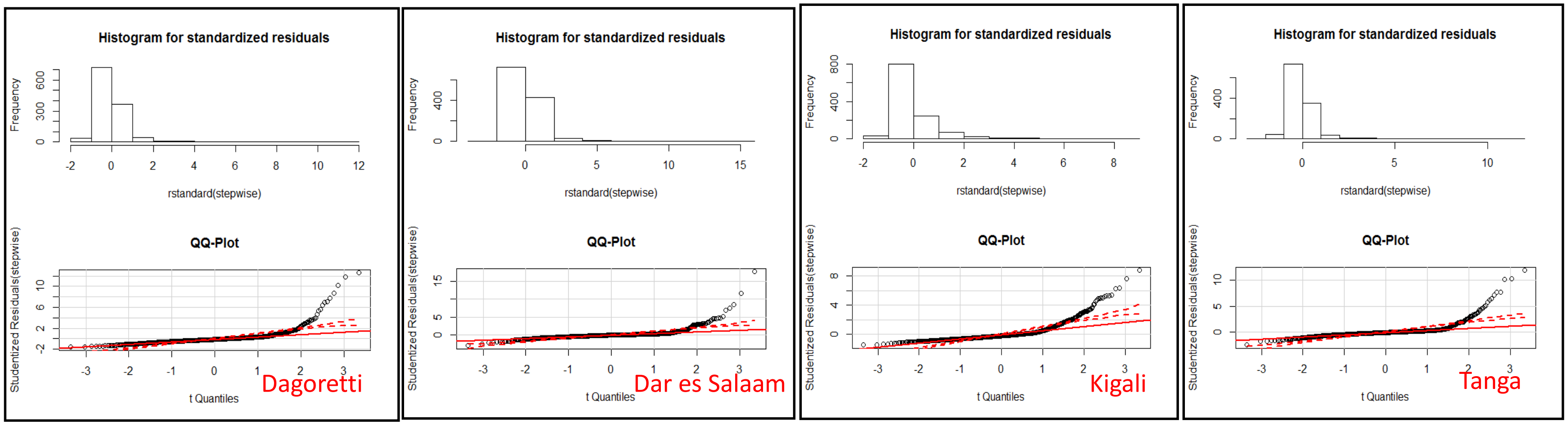

Fig. 9b: Normality Test Based on Histograms and QQ Plots for OND season

Appendix 11: The WRF ARW Modelling System Program Components

Adopted from http://www2.mmm.ucar.edu/wrf/users/docs/user_guide_V3/ARWUsersGuideV3.pdf

i. Overview

The Advanced Research WRF (ARW) modelling system has been in development for the past few years. The current release is Version 3, available since April 2008. The ARW is designed to be a flexible, state-of-the-art atmospheric simulation system that is portable and efficient on available parallel computing platforms. The ARW is suitable for use in a broad range of applications across scales ranging from meters to thousands of kilometers, including Idealized simulations (e.g. LES, convection, baroclinic waves); Parameterization research; Data assimilation research; Forecast research; Real-time NWP; Hurricane research; Regional climate research; Coupled-model applications and Teaching

The Mesoscale and Microscale Meteorology Division of NCAR is currently maintaining and supporting a subset of the overall WRF code (Version 3) that includes WRF Software Framework (WSF); Advanced Research WRF (ARW) dynamic solver, including one-way, two-way nesting and moving nest; The WRF Pre-processing System (WPS); WRF Data Assimilation (WRF-DA) system which currently supports 3DVAR 4DVAR, and hybrid data assimilation capabilities; Numerous physics packages contributed by WRF partners and the research community and several graphics programs and conversion programs for other graphics tools

The WRF modelling system software is in the public domain and is freely available for community use.

ii. The WRF Modelling System Program Components

The following figure shows the flowchart for the WRF Modelling System Version 3.

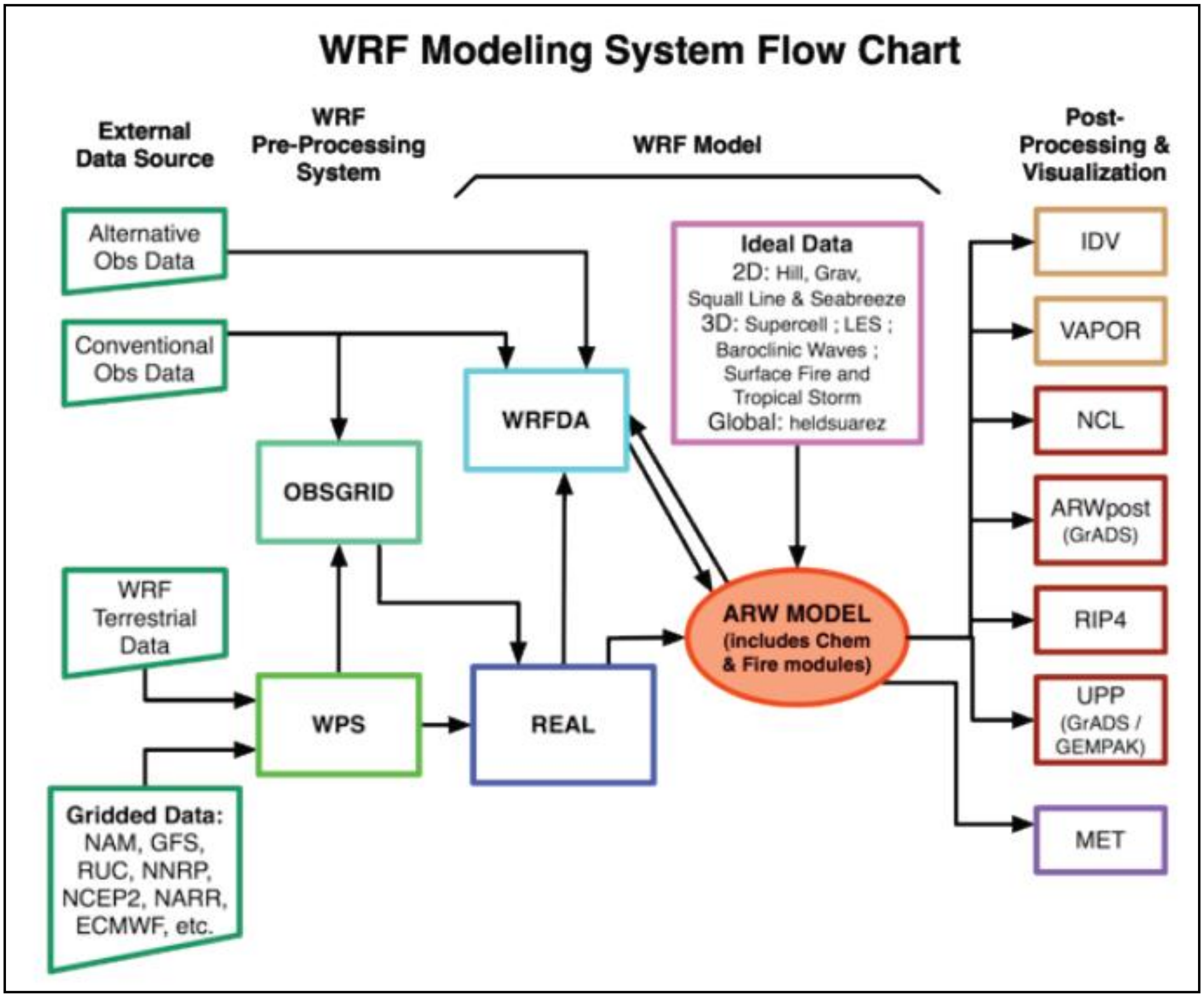

As shown in the diagram, the WRF Modelling System consists of the following major programs:

- The WRF Preprocessing System (WPS)
- WRF-DA
- ARW solver
- Post-processing & Visualization tools

a) The WRF Pre-processing System

This program is used primarily for real-data simulations. Its functions include 1) defining simulation domains; 2) interpolating terrestrial data (such as terrain, landuse, and soil types) to the simulation domain; and 3) degribbing and interpolating meteorological data from another model to this simulation domain. Its main features include:

- GRIB 1/2 meteorological data from various centers around the world
- USGS 24 category and MODIS 20 category land datasets; USGS GTOPO30 elevation dataset; Global 5-minutes United Nation FAO, and North-America STATSGO 30 sec soil category dataset; 10-min greenness fraction data based on AVHRR and 30-sec greenness fraction data based on 10 years MODIS; MODIS based leaf-area index; 0.15 degree monthly albedo and snow albedo data; and 1-degree deep soil temperature data; plus a few specialized datasets
- Map projections for 1) polar stereographic, 2) Lambert-Conformal, 3) Mercator and 4) latitude-longitude.
- Nesting
- User-interfaces to input other static data as well as met data

b) WRF-DA

This program is optional, but can be used to ingest observations into the interpolated analyses created by WPS. It can also be used to update WRF model's initial conditions when the WRF model is run in cycling mode. Its main features are as follows:

- It is based on an incremental variational data assimilation technique, and has both 3DVar and 4D-Var capabilities
- It also includes the capability of hybrid data assimilation (Variational + Ensemble)
- The conjugate gradient method is utilized to minimize the cost function in the analysis control variable space
- Analysis is performed on an un-staggered Arakawa A-grid
- Analysis increments are interpolated to staggered Arakawa C-grid and it gets added to the background (first guess) to get the final analysis of the WRF-model grid
- Conventional observation data input may be supplied either in ASCII format via the “obsproc” utility or “PREPBUFR” format.

- Multiple satellite observation data input may be supplied in BUFR format
- Multiple radar data (reflectivity & radial velocity) input is supplied through ASCII format
- Multiple outer loop to address the nonlinearity
- Capability to compute adjoint sensitivity
- Horizontal component of the background (first guess) error is represented via a recursive filter (for regional) or power spectrum (for global). The vertical component is applied through projections on climatologically generated averaged eigenvectors and its corresponding Eigen values
- Horizontal and vertical background errors are non-separable. Each eigenvector has its own horizontal climatologically-determined length scale
- Preconditioning of the background part of the cost function is done via the control variable transform U defined as B= UUT
- It includes the “gen_be” utility to generate the climatological background error covariance estimate via the NMC-method or ensemble perturbations
- A utility program to update WRF boundary condition file after WRF-DA

c) **ARW Solver**

This is the key component of the modelling system, which is composed of several initialization programs for idealized, and real-data simulations, and the numerical integration program. The key features of the WRF model include:

- Fully compressible nonhydrostatic equations with hydrostatic option
- Regional and global applications
- Complete Coriolis and curvature terms
- Two-way nesting with multiple nests and nest levels
- Concurrent one-way nesting with multiple nests and nest levels
- Offline one-way nesting with vertical nesting
- Moving nests (prescribed moves and vortex tracking)

- Mass-based terrain-following coordinate
- Vertical grid-spacing can vary with height
- Map-scale factors for these projections:
    - polar stereographic (conformal)
    - Lambert-conformal
    - Mercator (conformal)
    - Latitude and longitude, which can be rotated
- Arakawa C-grid staggering
- Runge-Kutta 2nd and 3rd order time integration options
- Scalar-conserving flux form for prognostic variables
- 2nd to 6th order advection options (horizontal and vertical)
- Monotonic transport and positive-definite advection option for moisture, scalar, tracer, and TKE
- Weighted Essentially Non-Oscillatory (WENO) advection option
- Time-split small step for acoustic and gravity-wave modes:
    - small step horizontally explicit, vertically implicit
    - divergence damping option and vertical time off-centering
    - external-mode filtering option
- Upper boundary absorption and Rayleigh damping
- Lateral boundary conditions
    - idealized cases: periodic, symmetric, and open radiative
    - real cases: specified with relaxation zone
- Full physics options for land-surface, planetary boundary layer, atmospheric and
- surface radiation, microphysics and cumulus convection

    - Ocean models
    - Grid analysis nudging using separate upper-air and surface data, and observation
- nudging
    - Spectral nudging
    - Digital filter initialization
- Adaptive time stepping
- Orographic gravity wave drag
- Stochastic kinetic-energy backscatter scheme
- A number of idealized examples

d) Graphics and Verification Tools

Several programs are supported, including RIP4 (based on NCAR Graphics), NCAR Graphics Command Language (NCL), and conversion programs for other readily available graphics packages like GrADS. Program VAPOR, **V**isualization and **A**nalysis **P**latform for **O**cean, Atmosphere, and Solar **R**esearchers (http://www.vapor.ucar.edu/), is a 3-dimensional data visualization tool, and it is developed and supported by the VAPOR team at NCAR (vapor@ucar.edu). Program MET, **M**odel **E**valuation **T**ools (http://www.dtcenter.org/met/users/), is developed and supported by the Developmental Testbed Center at NCAR (met_help@ucar.edu).

The details of these programs (with the exception of the MET program) are described more in the later chapters of this user's guide. See the above link for information about MET.